

## REPORT DOCUMENTATION PAGE

AFRL-SR-BL-TR-98-

athering  
action of  
ay, Suite

Public reporting burden for this collection of information is estimated to average 1 hour per response, including and maintaining the data needed, and completing and reviewing the collection of information. Send comments and suggestions for reducing this burden, to Washington Headquarters Services, Directorate 1204, Arlington, VA 22202-4302, and to the Office of Management and Budget, Paperwork Reduction Project (0

1. AGENCY USE ONLY (Leave Blank)	2. REPORT DATE 1993	3. REPC Final
----------------------------------	------------------------	------------------

## 4. TITLE AND SUBTITLE

Nonlinear Dynamics in a Two-Layer Model of Baroclinic Instability and the Effects of Varying Sidewall Boundary Conditions

## 5. FUNDING NUMBERS

## 6. AUTHORS

Michael David Mundt

## 7. PERFORMING ORGANIZATION NAME(S) AND ADDRESS(ES)

University of Colorado

## 8. PERFORMING ORGANIZATION REPORT NUMBER

## 9. SPONSORING/MONITORING AGENCY NAME(S) AND ADDRESS(ES)

AFOSR/NI

110 Duncan Avenue, Room B-115  
Bolling Air Force Base, DC 20332-8080

## 10. SPONSORING/MONITORING AGENCY REPORT NUMBER

## 11. SUPPLEMENTARY NOTES

## 12a. DISTRIBUTION AVAILABILITY STATEMENT

Approved for Public Release

## 12b. DISTRIBUTION CODE

## 13. ABSTRACT (Maximum 200 words)

See attachment

19980504 148

DATA QUALITY INSPECTED 4

## 14. SUBJECT TERMS

## 15. NUMBER OF PAGES

## 16. PRICE CODE

17. SECURITY CLASSIFICATION  
OF REPORT

Unclassified

18. SECURITY CLASSIFICATION  
OF THIS PAGE

Unclassified

19. SECURITY CLASSIFICATION  
OF ABSTRACT

Unclassified

## 20. LIMITATION OF ABSTRACT

UL

0465

**NONLINEAR DYNAMICS IN A TWO-LAYER MODEL OF  
BAROCLINIC INSTABILITY AND THE EFFECTS OF VARYING  
SIDEWALL BOUNDARY CONDITIONS**

AFRL-TR-98-0465 (AFSC)

This report has been reviewed and is  
approved for public release. The AFRL 190-12  
directive does not apply.

Michael David Mundt, Manager

by

**Michael David Mundt**

Graduate Research Assistant  
Department of Aerospace Engineering Sciences

*Colorado Center for Astrodynamics Research*

*University of Colorado      Boulder, Colorado*

1993

NONLINEAR DYNAMICS IN A TWO-LAYER MODEL OF BAROCLINIC INSTABILITY  
AND THE EFFECTS OF VARYING SIDEWALL BOUNDARY CONDITIONS

by

MICHAEL DAVID MUNDT

B.S., University of Colorado, 1989

M.S., University of Colorado, 1991

A thesis submitted to the  
Faculty of the Graduate School of the  
University of Colorado in partial fulfillment  
of the requirements for the degree of  
Doctor of Philosophy  
Department of Aerospace Engineering

1993

This thesis for the Doctor of Philosophy degree by

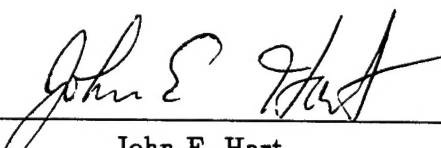
Michael David Mundt

has been approved for the

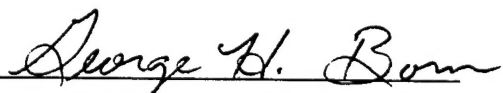
Department of

Aerospace Engineering

by



John E. Hart



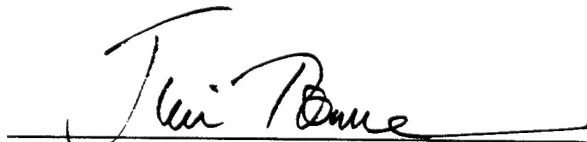
George H. Born



Lakshmi Kantha



Robert R. Leben



Juri Toomre

Date 7/15/93

Mundt, Michael David (Ph.D., Aerospace Engineering)

Nonlinear Dynamics in a Two-Layer Model of Baroclinic Instability and the Effects  
of Varying Sidewall Boundary Conditions

Thesis directed by Professor John E. Hart

The behavior of two-layer, quasi-geostrophic flow in a channel, which is subject to baroclinic instability, is investigated using a high-resolution numerical model. Solutions are obtained for both free-slip sidewalls (which allow tangential velocities but zero stress) and rigid sidewalls (which enforce zero velocity). Results for the slippery model are presented first, and the physics underlying the observed behavior is examined. As the Froude number  $F$  is increased, the system exhibits a transition from steady flow to periodic, quasi-periodic, and finally chaotic behavior. As  $F$  is increased to about five times the linear critical value, the motion becomes chaotic, and for even larger values of  $F$  it moves toward a "geostrophic turbulence" regime. The route to chaos is determined to be the breakdown of a two-torus.

A quasi-analytic method for predicting the instabilities of finite-amplitude baroclinic waves is then formulated, and the results are compared with the numerical solutions. This approach predicts the locations (in parameter space) where the equilibrium points of the system are unstable, and these correlate well with transitions in the numerical model. Surrogate models of the slippery case, obtained by computing the empirical orthogonal functions (EOFs) and using these as basis functions, are also generated. Such low-order models are used to better interpret the results and to examine the link between partial differential equations and low-dimensional dynamical systems. The empirical models provide a quantitatively accurate approximation of the full flow in steady, periodic, and simple quasi-periodic regimes; for more complex quasi-periodic and chaotic flows, the approach yields qualitative agreement. As the system approaches the region of geostrophic turbulence, the number of EOFs

required to accurately represent the flow rises rapidly. The EOFs are also shown to correlate well with the linear eigenfunctions of secondary instabilities in the slippery model.

For the rigid-wall geometry, the linear stability problem is first formulated and the results interpreted and compared to the free-slip case. The rigid case can be more or less stable than its slippery counterpart, depending on the magnitude of the bottom friction. In the region applicable to laboratory results, however, the neutral curves for both models are similar. Numerical solutions are then examined and compared to both the free-slip case and also to laboratory experiments. The onset of chaos occurs for very small or even negative supercriticality. The subcritical behavior observed in the model is determined to be due to wave-mean interactions. In general, the rigid-wall system is far more unstable and chaotic than the slippery model, counter to intuition but in better accord with laboratory (rigid wall) results. The route to chaos is again found to be the breakdown of a two-torus.

## DEDICATION

This thesis is dedicated to my parents, for always being there.

## ACKNOWLEDGEMENTS

Many people deserve thanks for assisting me in some way during the course of preparing my thesis. I would like to thank my thesis advisor, John Hart, for his patience and instruction and, most importantly, for teaching me how to do rigorous science. Robert Chase should be recognized, since without his encouragement I would never have attended graduate school in the first place. Bob Leben and Keith Julien provided me with helpful comments and advice on many topics during the writing of this thesis, and Nic Brummell deserves special thanks for his advice and generous assistance in computational matters. My office partners and friends Rob Olson, Chris Comp, and Steve Sayeedi provided me with endless entertainment and olfactory stimulation, and many others in the department supplied us with fodder for hours of scintillating conversation.

I want to acknowledge the support of a National Defense Science and Engineering Graduate fellowship for the majority of my tenure in graduate school. The assistance made it possible to freely explore my areas of interest, and my thesis is that much better as a result.

Finally, I wish to thank Alexandra Thomas for her wildly original and entertaining ideas concerning the expediting of graduation, and I want to thank my parents for their continued and unflinching support.

## CONTENTS

### Chapter

1	INTRODUCTION . . . . .	1
1.1	Low Rossby Number Flows . . . . .	4
1.2	Mechanisms of Baroclinic and Barotropic Instability . . . . .	6
1.3	Two Layer Model—Formulation . . . . .	9
1.4	Linear Theory . . . . .	14
1.5	Nonlinear Theory . . . . .	18
1.5.1	Energetics . . . . .	18
1.5.2	Types of Vacillations . . . . .	19
1.5.3	The Transition to Chaos . . . . .	22
1.6	Previous Results . . . . .	23
1.6.1	Single-Wave Models . . . . .	23
1.6.2	Multi-Wave Models . . . . .	25
1.6.3	Laboratory Experiments . . . . .	28
2	A STRESS-FREE MODEL OF BAROCLINIC INSTABILITY . . . . .	30
2.1	Stress-Free Sidewalls . . . . .	30
2.2	Numerical Method . . . . .	31
2.3	Model Formulation . . . . .	31
2.3.1	The Semi-Slippery Model . . . . .	31
2.3.2	The Slippery Model . . . . .	33
2.4	Model Verification . . . . .	35
2.5	Multiple States . . . . .	39
2.6	Results for the Semi-Slippery Model . . . . .	43

2.7	Results for the Slippery Model . . . . .	45
2.8	Discussion . . . . .	66
3	SECONDARY INSTABILITIES OF FINITE AMPLITUDE BARO-CLINIC WAVES . . . . .	67
3.1	Methodology . . . . .	67
3.2	Results for Slippery Model . . . . .	70
3.2.1	Fixed-Point Solutions . . . . .	70
3.2.2	Symmetric Steady-State—Symmetric Perturbation Field	74
3.2.3	Symmetric Steady-State—Asymmetric Perturbation Field	79
3.2.4	Spatio-Temporal Structure of Quasi-Linear Instabilities	83
3.2.5	Relating Fixed-Point Solutions to Mean Quantities . . .	84
3.3	Discussion . . . . .	90
4	EOF ANALYSES . . . . .	92
4.1	Definitions and Preliminary Remarks . . . . .	92
4.2	Methodology of Obtaining EOFs . . . . .	93
4.3	Approximate Dynamical Systems . . . . .	97
4.4	Practical Considerations . . . . .	99
4.5	The Relationship Between Spatial and Temporal Complexity .	100
4.6	Results for Slippery Model . . . . .	101
4.6.1	Symmetric Case . . . . .	101
4.6.2	Asymmetric Case . . . . .	109
4.7	Approximate Dynamical Systems for the Slippery Model . . .	116
4.7.1	Symmetric Case . . . . .	121
4.7.2	Asymmetric Case . . . . .	132
4.8	EOFs Versus Linear Eigenfunctions . . . . .	139
4.9	Discussion . . . . .	143

5 A RIGID-WALL MODEL OF BAROCLINIC INSTABILITY: THE LINEAR INSTABILITY PROBLEM . . . . .	144
5.1 Governing Equations . . . . .	144
5.2 Basic State . . . . .	145
5.3 Zonal Flow Boundary Conditions . . . . .	147
5.4 Linear Theory . . . . .	148
5.5 Results . . . . .	151
5.5.1 $U_{bc} \neq 0, U_{bt} = 0$ : . . . . .	151
5.5.2 $U_{bc} \neq 0, U_{bt} \neq 0$ : . . . . .	167
5.6 Discussion . . . . .	175
6 A RIGID-WALL MODEL OF BAROCLINIC INSTABILITY: NUMERICAL RESULTS . . . . .	177
6.1 Numerical Method . . . . .	177
6.2 Validation of Model . . . . .	178
6.3 Results . . . . .	179
6.4 Discussion . . . . .	189
6.5 Conclusions . . . . .	200
7 CONCLUSIONS . . . . .	204
Bibliography . . . . .	210
Appendix . . . . .	
A QUANTITIES OF FLOW ENERGETICS . . . . .	216
B DERIVATION OF ADDITIONAL CONDITIONS . . . . .	218
C RESULTS FOR SLIPPERY MODEL-SYMMETRIC STATE . . . . .	224
D SPATIAL SNAPSHOTS OF FULL SOLUTIONS OF SLIPPERY MODEL . . . . .	239
E SPATIAL SNAPSHOTS OF APPROXIMATE SOLUTIONS OF SLIPPERY MODEL . . . . .	252

F MEASURES OF CHAOS . . . . .	265
G THE RELATIONSHIP BETWEEN SPATIAL AND TEMPORAL COMPLEXITY . . . . .	272
H SOME DERIVATIONS CONCERNING THE RIGID-WALL, LIN- EAR INSTABILITY PROBLEM . . . . .	281
I NUMERICAL METHOD FOR RIGID-WALL FORMULATION . .	285

## TABLES

### Table

2.1	Convergence of rms deviation of baroclinic wavy kinetic energy versus model resolution . . . . .	38
2.2	Summary of instabilities and their associated symmetries. . . . .	41
3.1	Summary of instabilities for symmetric basic state, symmetric per- turbations . . . . .	78
3.2	Summary of instabilities for symmetric basic state, asymmetric per- turbations . . . . .	81
3.3	Ratio of means to rms deviations for K.E. quantities (symm. solution)	87
3.4	Ratio of means to rms deviations for K.E. quantities (asymm. so- lution) . . . . .	87
4.1	Performance comparison between full model and low-order EOF model, symm. case. . . . .	123
4.2	Performance comparison between full model and low-order <i>ad hoc</i> model, symm. case. . . . .	123
5.1	Contributions to $F_c$ for various values of $\Gamma$ , $Q = 0.001$ . . . . .	165
5.2	Contributions to $F_c$ for various values of $\Gamma$ , $Q = 10$ . . . . .	167
5.3	Contributions to $F_c$ for various values of $\Gamma$ , $Q = 0.1$ , $U_{bt} = 0$ . . . . .	174
5.4	Contributions to $F_c$ for various values of $\Gamma$ , $Q = 0.1$ , $U_{bt} \neq 0$ . . . . .	174
5.5	Contributions to $F_c$ for various values of $\Gamma$ , $Q = 10$ , $U_{bt} \neq 0$ . . . . .	175

## FIGURES

### Figure

1.1 Schematic of baroclinic instability. . . . .	7
1.2 Schematic of model geometry . . . . .	10
1.3 Energy-flow diagram . . . . .	20
2.1 Comparison of low-dimensional, spectral and pseudo-spectral slippery models. . . . .	36
2.2 Phase-space comparisons of low-dimensional, spectral and pseudo-spectral slippery models for $F = 30$ . . . . .	37
2.3 Wavenumber-space occupation of symmetric and antisymmetric sets. .	42
2.4 Behavior of Semi-Slippery Model for $8 \leq F \leq 40$ . . . . .	44
2.5 Behavior of Slippery Model for $8 \leq F \leq 40$ . . . . .	46
2.6 Energy transfer terms for asymmetric case, $F = 12$ . . . . .	49
2.7 Barotropic and Baroclinic components of $\sin(\pi y)$ zonal term vs. time, Asymm. case, $F=13$ . . . . .	51
2.8 Barotropic and Baroclinic components of $\sin(2\pi y)$ zonal term vs. time, Asymm. case, $F=13$ . . . . .	52
2.9 Zonally-integrated wavy kinetic energy vs. $y$ for several times, $T$ , over one cycle, $F = 13$ , Asymm. case . . . . .	53
2.10 Time return map and circle map for $\mathcal{U}_1$ term, asymmetric state, $F = 26$ . . . . .	56
2.11 Energy transfer terms for asymmetric case, $F = 26$ . . . . .	56
2.12 Phase-space plots of energy fluctuations, $F = 26$ , asymm. state . .	57

2.13 Phase-space plot, power spectrum, and return map of $\mathcal{U}_1$ coefficient, $F=30.5$ . . . . .	59
2.14 Phase-space plot, power spectrum, and return map of $\mathcal{U}_1$ coefficient, $F=30.9$ . . . . .	61
2.15 Phase-space plot, power spectrum, and return map of $\mathcal{U}_1$ coefficient, $F=40$ . . . . .	63
2.16 Power spectra of $\mathcal{U}_1$ coefficient for $F = 40, 70$ , and $100$ . . . . .	65
3.1 Steady-state Kinetic Energy vs. $F$ . . . . .	72
3.2 Steady-state $\Psi^2/2$ vs. $F$ . . . . .	73
3.3 Steady-state streamfunctions . . . . .	75
3.4 Wavenumber power spectrum for baroclinic wavy field, $F = 30$ . . . . .	76
3.5 Growth rates of unstable modes for symmetric perturbation field . . . . .	77
3.6 Growth rates of unstable modes for asymmetric perturbation field . . . . .	81
3.7 Eigenfunctions of barotropic and baroclinic wavy fields, $F=12$ , symmetric case . . . . .	84
3.8 Eigenfunctions of barotropic and baroclinic wavy fields, $F=24$ , symmetric case . . . . .	85
3.9 Eigenfunctions of barotropic and baroclinic wavy fields, $F=16$ , asymmetric case . . . . .	85
3.10 Comparison of mean and steady kinetic energies . . . . .	87
3.11 Mean fields at $F = 20$ for symmetric solution . . . . .	88
3.12 Mean fields at $F = 20$ for asymmetric solution . . . . .	88
3.13 Steady-state fields at $F = 20$ . . . . .	89
4.1 Number of EOFs needed to meet 99% variance threshold for Type-1 state . . . . .	102
4.2 Contour plots of means for all fields, symmetric state, $F = 8$ . . . . .	103
4.3 Normalized eigenvalue spectra for symmetric case . . . . .	105

4.4	Contour plots of EOFs for baroclinic wavy field, symmetric state, $F = 20$ . . . . .	105
4.5	Plots of EOFs for baroclinic zonal field, symmetric state, $F = 20$ . .	106
4.6	Contour plots of EOFs for baroclinic wavy field, symmetric state, $F = 32$ . . . . .	108
4.7	Plots of EOFs for baroclinic zonal field, symmetric state, $F = 32$ . .	108
4.8	Contour plots of EOFs for baroclinic wavy field, symmetric state, $F = 36$ . . . . .	110
4.9	Plots of EOFs for baroclinic zonal field, symmetric state, $F = 36$ . .	111
4.10	Number of EOFs needed to meet 99% variance threshold for asym- metric state . . . . .	112
4.11	Normalized eigenvalue spectra for asymmetric case . . . . .	114
4.12	Contour plots of EOFs for baroclinic wavy field, asymmetric state, $F = 20$ . . . . .	115
4.13	Plots of EOFs for baroclinic zonal field, asymmetric state, $F = 20$ . .	115
4.14	Contour plots of EOFs for baroclinic wavy field, asymmetric state, $F = 28$ . . . . .	117
4.15	Plots of EOFs for baroclinic zonal field, asymmetric state, $F = 28$ . .	118
4.16	Contour plots of EOFs for baroclinic wavy field, asymmetric state, $F = 32$ . . . . .	119
4.17	Plots of EOFs for baroclinic zonal field, asymmetric state, $F = 32$ . .	120
4.18	Phase-space comparisons of full and approximate models at $F = 20$ .	126
4.19	Comparison of the behaviors between the full and approximate models for $6 \leq F \leq 22$ . . . . .	128
4.20	Comparison of full and approximate models at $F = 36$ , symmetric case. . . . .	133

4.21 Comparison of full and approximate models at $F = 28$ , asymmetric case. . . . .	136
4.22 Comparison of full and approximate models at $F = 32$ , asymmetric case. . . . .	138
4.23 First two EOFs of barotropic and baroclinic wavy fields, $F=12$ , symmetric case . . . . .	140
4.24 First two EOFs of barotropic and baroclinic wavy fields, $F=24$ , symmetric case . . . . .	141
4.25 First two EOFs of barotropic and baroclinic wavy fields, $F=16$ , asymmetric case . . . . .	142
5.1 Basic state velocity profiles for various values of $\Gamma$ . . . . .	147
5.2 First four basis functions for the rigid, linear-instability problem. . . . .	150
5.3 Linear stability curves for slippery and rigid models, $\Gamma = 10^{1/2}$ . . . . .	153
5.4 Linear stability curves for slippery and rigid models, $\Gamma = 10$ . . . . .	153
5.5 Linear stability curves for slippery and rigid models, $\Gamma = 10^{3/2}$ . . . . .	154
5.6 Comparison of barotropic eigenfunction with basic state velocity profile, $Q = 10^{-4}, \Gamma = 10^{1/2}$ . . . . .	157
5.7 Comparison of barotropic eigenfunction with slippery case eigenfunction (i.e. $\cos(\pi y/2)$ ), $Q = 10^{-1}, \Gamma = 10^{3/2}$ . . . . .	157
5.8 Comparison of barotropic eigenfunction with slippery case eigenfunction (i.e. $\cos(\pi y/2)$ ) and basic state velocity profile, $Q = 10^{-1}, \Gamma = 10$ . . . . .	157
5.9 Generic energy transfer diagram for fluctuations. . . . .	162
5.10 Energy transfer diagram for fluctuations, $Q = 10^{3/2}, Q = 0.001$ . . . . .	162
5.11 Energy transfer diagram for fluctuations, $Q = 10, Q = 0.001$ . . . . .	163
5.12 Energy transfer diagram for fluctuations, $\Gamma = 10^{1/2}, Q = 0.001$ . . . . .	163

5.13 Meridional structure of barotropic and baroclinic wavy perturbations for several values of $\Gamma$ , $Q = 0.001$ . . . . .	166
5.14 Meridional structure of barotropic and baroclinic wavy perturbations for several values of $\Gamma$ , $Q = 10$ . . . . .	168
5.15 Linear stability curves for rigid model with $U_{bt} = 0$ and $U_{bt} \neq 0$ , $\Gamma = 10^{1/2}$ . . . . .	170
5.16 Linear stability curves for slippery and rigid models with $U_{bt} = 0$ and $U_{bt} \neq 0$ , $\Gamma = 10$ . . . . .	171
5.17 Linear stability curves for slippery and rigid models with $U_{bt} = 0$ and $U_{bt} \neq 0$ , $\Gamma = 10^{3/2}$ . . . . .	172
5.18 Eigenfunctions of barotropic perturbations with $U_{bt} = 0$ and $U_{bt} \neq 0$ , $\Gamma = 10$ , $Q = 0.1$ . . . . .	174
6.1 Calculated and observed linear eigenfunctions, $F = 1.68$ , $Q = 0.15$ .	180
6.2 Regime diagram for rigid-wall model with increasingly supercritical parameters. . . . .	181
6.3 Regime diagram for rigid-wall model with decreasingly supercritical and subcritical parameters. . . . .	182
6.4 Time traces of lowest zonal-correction modes, $F = 1.53$ , $Q = 0.10$ .	185
6.5 Time traces of selected lowest zonal-correction modes, $F = 1.60$ , $Q = 0.10$ . . . . .	186
6.6 Maximum return map of lowest symmetric baroclinic zonal correction, $F = 1.60$ . . . . .	186
6.7 Power spectrum of lowest symmetric baroclinic zonal correction, $F = 1.60$ . . . . .	187
6.8 Bifurcation structure near $F_c = 1.52$ for $Q = 0.1$ . . . . .	190
6.9 Bifurcation structure near $F_c = 1.81$ for $Q = 0.2$ . . . . .	191
6.10 Landau coefficient versus $Q$ . . . . .	195

6.11 Various bifurcation structures. . . . .	196
6.12 Contribution by nonlinear wave-zonal interactions to Landau coefficient, slippery case. . . . .	198
6.13 Contribution by nonlinear wave-zonal interactions to Landau coefficient, rigid case. . . . .	199
6.14 $v'_{bt} \tilde{\phi}_{bc}$ , slippery and rigid cases. . . . .	201
6.15 Zonal vorticity gradients, slippery and rigid cases. . . . .	201
6.16 Contributions to forcing of zonal correction equation, rigid case, $Q = 0.08$ . . . . .	202
C.1 Energy Flow Diagram for symmetric state, $F = 8$ . . . . .	225
C.2 Energy fluctuations vs. time for symmetric state, $F = 12$ . . . . .	227
C.3 $E(y)$ vs. $y$ for several times, $T$ , over one cycle, $F = 12$ . . . . .	227
C.4 Spatial power spectra of wavy fields, $F = 20$ , symmetric case. . . . .	228
C.5 $E(y)$ vs. $y$ for several times, $T$ , over one cycle, $F = 26$ . . . . .	230
C.6 Energy transfers vs. time for symmetric state, $F = 26$ . . . . .	230
C.7 Location of eddy center over two periods, $F=32$ , symmetric case, PSV regime. . . . .	232
C.8 $\sin(2\pi y)$ coefficient and power spectrum for layer 1, $F = 36$ . . . . .	233
C.9 Poincaré section of $\sin(2\pi y)$ coefficient for layer 1, $F = 36$ . . . . .	233
C.10 Phase-space plots of energy fluctuations, $F = 36$ . . . . .	234
C.11 Estimation of dominant PAV frequency at $F = 36$ . . . . .	237
D.1 Baroclinic wavy field over one period. $F = 20$ , symmetric solution, PAV regime. . . . .	240
D.2 Barotropic wavy field over one period. $F = 20$ , symmetric solution, PAV regime. . . . .	241
D.3 Baroclinic wavy field over one period. $F = 32$ , symmetric solution, PSV regime. . . . .	242

D.4 Barotropic wavy field over one period. $F = 32$ , symmetric solution, PSV regime. . . . .	243
D.5 Baroclinic wavy field at uncorrelated times. $F = 36$ , symmetric solution, quasi-periodic regime. . . . .	244
D.6 Barotropic wavy field at uncorrelated times. $F = 36$ , symmetric solution, quasi-periodic regime. . . . .	245
D.7 Baroclinic wavy field over one period. $F = 20$ , asymmetric solu- tion, PSV regime. . . . .	246
D.8 Barotropic wavy field over one period. $F = 20$ , asymmetric solu- tion, PSV regime. . . . .	247
D.9 Baroclinic wavy field at uncorrelated times. $F = 28$ , asymmetric solution, quasi-periodic regime. . . . .	248
D.10 Barotropic wavy field over one period. $F = 28$ , asymmetric solu- tion, quasi-periodic regime. . . . .	249
D.11 Baroclinic wavy field at uncorrelated times. $F = 32$ , asymmetric solution, chaotic regime. . . . .	250
D.12 Barotropic wavy field at uncorrelated times. $F = 32$ , asymmetric solution, chaotic regime. . . . .	251
E.1 Approximate baroclinic wavy field over one period. $F = 20$ , sym- metric solution, PAV regime. . . . .	253
E.2 Approximate barotropic wavy field over one period. $F = 20$ , sym- metric solution, PAV regime. . . . .	254
E.3 Approximate baroclinic wavy field over one period. $F = 32$ , sym- metric solution, PSV regime. . . . .	255
E.4 Approximate barotropic wavy field over one period. $F = 32$ , sym- metric solution, PSV regime. . . . .	256

E.5 Approximate baroclinic wavy field at uncorrelated times. $F = 36$ , symmetric solution, quasi-periodic regime. . . . .	257
E.6 Approximate barotropic wavy field at uncorrelated times. $F = 36$ , symmetric solution, quasi-periodic regime. . . . .	258
E.7 Approximate baroclinic wavy field over one period. $F = 20$ , asym- metric solution, PSV regime. . . . .	259
E.8 Approximate barotropic wavy field over one period. $F = 20$ , asym- metric solution, PSV regime. . . . .	260
E.9 Approximate baroclinic wavy field at uncorrelated times. $F = 28$ , asymmetric solution, quasi-periodic regime. . . . .	261
E.10 Approximate barotropic wavy field at uncorrelated times. $F = 28$ , asymmetric solution, quasi-periodic regime. . . . .	262
E.11 Approximate baroclinic wavy field at uncorrelated times. $F = 32$ , asymmetric solution, chaotic regime. . . . .	263
E.12 Approximate barotropic wavy field at uncorrelated times. $F = 32$ , asymmetric solution, chaotic regime. . . . .	264
G.1 Cumulative variance functions, $C(n)$ , for $\beta=2$ , $\alpha = 0, 1, \dots, 5$ , periodic temporal behavior. . . . .	277
G.2 $C(3)$ versus $\alpha$ for $\beta=2$ , periodic temporal behavior. . . . .	277
G.3 Scaling behavior of $C(3)$ versus mean wavenumber, $\bar{k}$ , for $\beta = 2$ , periodic temporal behavior. . . . .	278
G.4 $C(3)$ versus $\alpha$ for Lorenz time series. . . . .	280
G.5 Scaling behavior of $C(3)$ versus mean wavenumber, $\bar{k}$ , for Lorenz time series. . . . .	280

## CHAPTER 1

### INTRODUCTION

The atmosphere and oceans both exhibit behavior which spans a wide range of temporal and spatial scales, from dust devils with meter-long spatial scales and time scales on the order of minutes to planetary waves (in the atmosphere) or isolated eddies (in the ocean) that have time scales on the order of months. In the atmosphere, baroclinic instability is a phenomenon that occurs for large-scale flows (where the time scale of the flow is much longer than the rotation period of the Earth), and it is responsible for features such as mid-latitude cyclones and fronts. In the ocean, the Gulf of Mexico (among other areas) is known to shed eddies that possess time scales on the order of months. Detailed numerical models indicate that this eddy-shedding process is in large part due to baroclinic instability (Hurlburt and Thompson, 1980). Numerical investigations by Holland (1978), among others, indicate that baroclinic processes are also important in the generation of eddies in the general ocean circulation.

Quasi-geostrophic motion is defined to be that where horizontal pressure gradients nearly balance Coriolis forces, a situation which occurs for large-scale geophysical flows. The intent of this thesis is to investigate the dynamics of quasi-geostrophic flow in a channel geometry. This geometry is chosen to simulate a flow which is bounded by two constant-latitude lines. Depending on the boundary conditions implemented at the walls, the model can be applied either to an atmospheric or oceanic context, although the geometry is clearly oversimplified. Since the atmosphere contains no bounding "walls", stress-free boundary conditions are more applicable for this case and have been ubiquitously applied in previous studies. In

the oceans, however, there are sidewalls in the form of land, so that no-slip boundary conditions are more relevant. This latter situation is particularly interesting because no investigation of a rigid-wall formulation of quasi-geostrophic baroclinic chaos has been done for the type of model presented in this thesis.

There have been many studies of models, of varying complexity, with semi-stress-free walls (the term "semi" is used because the previously-studied systems typically have stress-free boundary conditions on the waves in the flow but have no-slip conditions on the zonally-averaged portion). Generally, the low-order systems that have been examined exhibit much different behavior than highly-resolved models. For instance, the transitions to more complex temporal behavior occur at much different values of supercriticality in simple models than in large numerical simulations (the supercriticality can be defined as  $(F - F_c)/F_c$ , where  $F$ , the Froude number, is the typical stability parameter, and  $F_c$  is the value of  $F$  at which linear instability first occurs). In addition, the behavior exhibited by these models has been shown to be very sensitive to the amount and type of dissipation used. Pedlosky and Frenzen (1980) show that, in their low-order model, small changes in the dissipation parameter can change the behavior of the flow from periodic to chaotic, and vice versa. Moreover, the inclusion of interfacial friction in a single-wave model eliminates the possibility of vacillatory solutions (Pedlosky and Polvani, 1987), while the same friction in a multiple-wave model tends to make oscillatory solutions steady (Klein and Pedlosky, 1992). Finally, comparison with analogous laboratory experiments has thus far been disappointing. The onset of complex spatio-temporal behavior in laboratory experiments occurs at substantially less supercritical parameter settings than in the numerical models. The *f*-plane experiments of Hart (1985) show the onset of chaos to occur at about unit supercriticality, while numerical experiments undertaken to examine an analogous situation (Cattaneo and Hart, 1990) do not

show chaotic behavior until supercriticality of order 4 or so is achieved. This suggests that the previous numerical investigations are missing a crucial portion of the important physics.

This thesis has several goals. The first objective is to better understand the effect of different boundary conditions on the solutions obtained. To this end, models with both consistently slippery and consistently rigid walls are investigated via high-resolution numerical simulations. The results are compared to previous numerical investigations using semi-stress-free walls. The second goal is to obtain results which better agree with laboratory experiments. The rigid-wall model is formulated especially for this reason, since the experiments carried out in a rotating cylinder necessarily possess a viscous sidewall. The final intent is to elucidate the physics underlying the various behavior exhibited by the numerical models.

The structure of the thesis is as follows. The remainder of Chapter 1 is devoted to an overview of baroclinic instability. The physics of this phenomenon are briefly reviewed, and the two-layer model is introduced. The linear theory of this model is then summarized, and some aspects of the nonlinear problem are discussed. Finally, the results of previous numerical and experimental investigations are reviewed. In Chapter 2, a model with fully stress-free boundaries is formulated and verified. The transition from steady flow to chaotic behavior in the model is then presented, and physical arguments are put forth to explain this change in behavior. Finally, the results are compared to those from a previous, semi-stress-free model. Chapter 3 is devoted to improving upon the predictions of linear theory. This is done with the afore-mentioned quasi-analytical approach, the essence of which is to use automated symbolic manipulation to compute secondary instabilities of the finite-amplitude, equilibrated primary instability. These predictions are then compared to the results of the full model discussed in Chapter 2. In Chapter 4, the method of Proper Orthogonal Decomposition is used to generate low-order models

to approximate the dynamics of the full numerical model in Chapter 2. The purpose of this endeavor is to understand the complexity of the flow in highly supercritical regimes and also to assess the degree to which complex spatio-temporal behavior can be explained by low-order dynamical systems. Next, Chapter 5 turns to a model with rigid walls and solves the linear stability problem for such a flow. The results are compared to results from a free-slip implementation, and the differences arising from the alteration of boundary conditions are explained. Chapter 6 examines the results from a numerical implementation of the rigid-wall model. The results are presented and interpreted. Comparisons of the behavior are made both with those for the slippery-wall model and also with laboratory experiments. Finally, Chapter 7 summarizes the results and presents some conclusions and ideas for further research.

### 1.1 Low Rossby Number Flows

The Rossby number of a geophysical flow, denoted  $R_o$ , is a nondimensional parameter that measures the ratio of the planetary rotation time scale (where the rotation rate is denoted as  $\Omega$ ) to the fluid's advective time scale, which is defined as  $L/U$  (where  $L$  is a characteristic length and  $U$  is a characteristic velocity).  $R_o$  is then defined as  $U/(2\Omega L)$ , and large-scale flows, such as those alluded to above, are those for which  $R_o \ll 1$ . For flows that satisfy this condition, a first-order approximation indicates that the horizontal flow is in geostrophic balance, in which horizontal pressure gradients balance the Coriolis force. In the vertical direction, the flow is in hydrostatic balance, which means that the vertical pressure gradient is balanced by the buoyancy force due to gravity.

The main limitation of the geostrophic approximation is that it is not prognostic, i.e. although the velocities are given unambiguously as a function of the pressure field, there is no way to discern the pressure field itself from the equations. The quasi-geostrophic approximation alleviates this difficulty by appealing to terms in

the governing equations that are on the order of  $R_o$ . The quasi-geostrophic relations can subsequently be cast entirely in terms of the  $O(1)$  pressure fields, thus yielding a closed system of equations that allows one to follow the temporal evolution of the flow. At any given time, the velocities are still evaluated geostrophically, so that the flow is in instantaneous geostrophic balance.

The seminal work of Charney (1947) and Eady (1949) showed that quasi-geostrophic waves of infinitesimal amplitude, when superposed on a zonal shear flow, could spontaneously grow by extracting energy from the background motion. Moreover, the fastest-growing wave in the Eady model possesses a wavelength on the order of 4,000 *km*, in good agreement with synoptic-scale disturbances in the Earth's atmosphere (Pedlosky, 1987).

There exist many examples which support the hypothesis that baroclinic instability assumes an active role in atmospheric dynamics. Webster and Keller (1975) have analyzed data acquired in the Southern Hemisphere, and the results indicate that there is evidence for both barotropic and baroclinic instabilities being responsible for the observed atmospheric variability. In addition, Hart (1976) has computed energy transfers for a low-order model of baroclinic instability, and the magnitudes of the mean energy transfers corroborate well with those observed in the Northern Hemisphere in January (Oort and Peixoto, 1974). Finally, polar projections of atmospheric flow (usually given by contour plots of isobars) have been presented which show great similarity to laboratory implementations of baroclinically unstable flows (Pfeffer and Chiang, 1967). With regard to the oceans, three-dimensional modeling of the Gulf Stream by Orlanski and Cox (1973) indicates that the meanders of the Gulf are likely the manifestation of baroclinically unstable waves. The results may possibly be valid for other oceanic western boundary currents. Furthermore, as previously stated, Hurlburt and Thompson (1980) explained the eddy shedding seen in the Gulf of Mexico to be attributable to baroclinic instability. Similar eddies

are generally seen in western boundary currents and thus may have a physically similar basis. In fact, the results of a generic, quasi-geostrophic ocean model studied by Holland (1978) indicate that baroclinic processes are important in generating mesoscale eddies.

## 1.2 Mechanisms of Baroclinic and Barotropic Instability

Although the models discussed herein are intended to simulate baroclinic instability, secondary instabilities of a barotropic nature can also arise. The mechanisms responsible for the two types of instabilities are, however, very different from one another, and it is instructive to briefly elucidate the physical processes responsible for each.

A schematic of a hypothetical geophysical flow situation is depicted in Figure 1.1. In the figure, the  $y$ -axis is directed north, while the  $z$ -axis points upward. The  $x$ -axis, then, is assumed to be directed into the page (toward the east). Suppose there is a basic zonal flow,  $U(y, z)$ , that is in geostrophic and hydrostatic balance. Then, by the use of the thermal wind relation (Pedlosky, 1987),

$$\frac{\partial U(y, z)}{\partial z} \propto -\frac{\partial \theta}{\partial y}, \quad (1.1)$$

where  $\theta$  is the potential temperature of the fluid, defined as

$$\theta = T \left( \frac{p_s}{p} \right)^{(\gamma-1)/\gamma}. \quad (1.2)$$

In the above equation,  $p_s$  is a reference pressure and  $\gamma$  is the specific heat ratio. The result of Equation 1.1 is that the constant potential temperature surfaces are necessarily arranged as shown in Figure 1.1, with  $\theta_2 > \theta_1$  required for static stability. The sloping distribution of  $\theta$  results in the condition that  $\partial U / \partial z \neq 0$ .

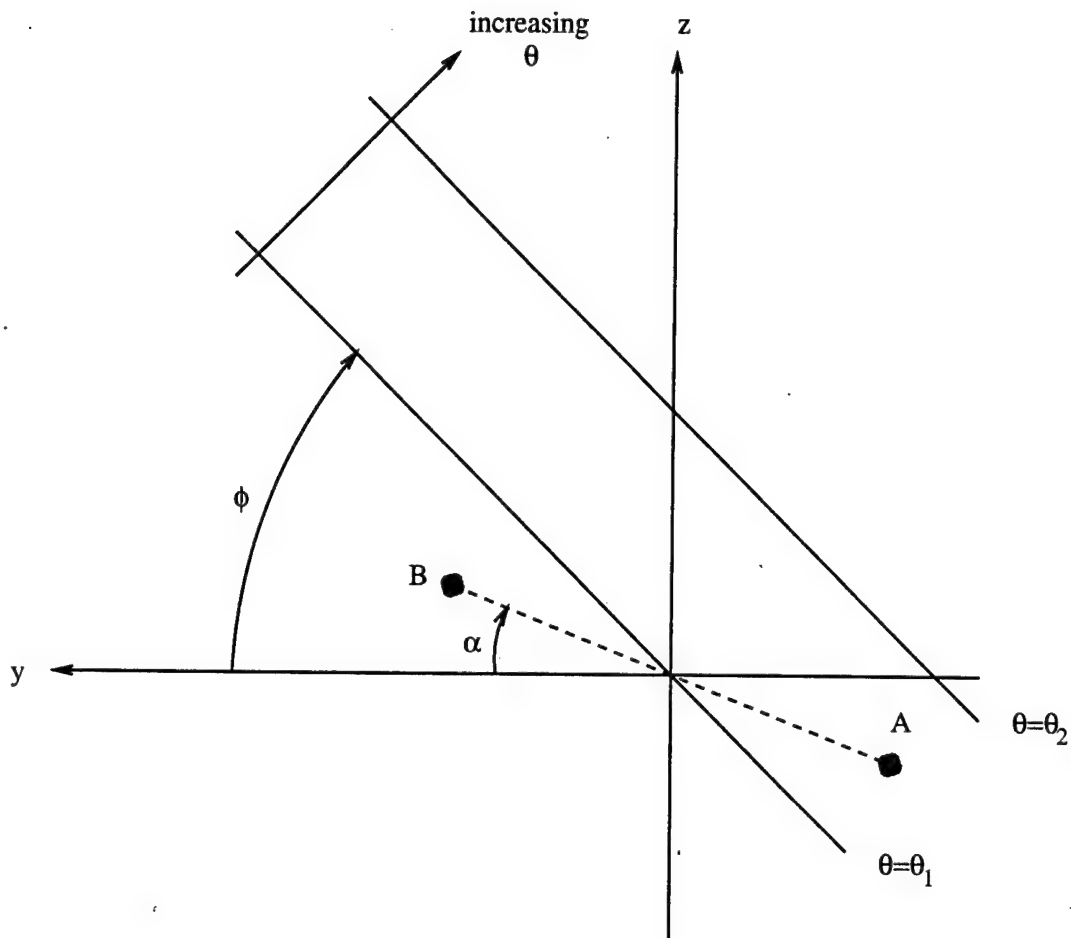


Figure 1.1: Schematic of baroclinic instability.

Now consider the movement of a fluid parcel from point A to point B along the dotted line shown. If the parcel moves adiabatically, then the restoring force on the parcel (i.e., the force which would move it back toward its original position at A and is proportional to the difference between the densities of parcel A at point B and parcel B at point B) is **negative** for  $0 < \alpha < \phi$ . Thus, for fluid parcel trajectories that occur within the wedge defined by the angle  $\phi$ , there is a net force tending to further accelerate the parcels away from their original position, resulting in an instability. This is known as a baroclinic instability, and it is really a form of thermal convection (i.e. "slantwise thermal convection") in which less dense fluid rises and denser fluid sinks. In addition, the energy for the instability arises from the **available potential energy** of the fluid, which is a result of the sloping of the constant potential temperature surfaces with respect to the constant pressure surfaces (which are nearly horizontal). It should be emphasized that the instability does **not** depend on the vertical Reynolds stresses,  $\overline{uw}$ .

Barotropic instability, conversely, does not depend on the vertical shear of the basic flow in a fundamental way. Instead, it depends on the meridional (or  $y$ -dependent) structure of the background state. If the zonal mean flow and the zonal vorticity gradient satisfy certain requirements, then the kinetic energy of the basic flow can be converted into perturbation energy. The important points to keep in mind are that the barotropic instability depends primarily on the meridional ( $y$ ), and not the vertical ( $z$ ), variation of  $U(y, z)$ , and also that a barotropic instability converts basic state kinetic energy directly into perturbation kinetic energy.

It is not difficult to imagine that, under certain circumstances,  $U$  might have the proper dependence of  $y$  and  $z$  such that the basic flow is unstable to both barotropic and baroclinic instabilities. In fact, the above situation does occur, and the energy flow mechanisms then become more complicated. For the numerical results presented herein, this process seems to be rather ubiquitous and will be

discussed in more detail later.

### 1.3 Two Layer Model—Formulation

In order to isolate the physics of baroclinic instability, it is desirable to simplify the situation as much as possible in order to eliminate extraneous effects. To accomplish this, layer models have been introduced and used extensively (see Pedlosky (1987) for a systematic derivation of layer models). In such a formulation, the stratification is simplified so that the system consists of two or more layers of fluid, each of which is constant density. If the Taylor-Proudman theorem applies, each layer exhibits behavior that is independent of height. Baroclinic effects, then, arise only through the differences in behavior between the various layers. This allows one to eliminate the complications that arise if one retains a system that allows density to vary continuously with height. The simplest model which still retains baroclinic effects, of course, is a two-layer model, and this formulation will form the basis of this endeavor. Flierl (1978) compared the results of two-layer models with continuously-stratified systems; he found that, despite the simplification inherent in a layer formulation, qualitative agreement with a model possessing continuous stratification was possible.

The model used herein is that which was introduced by Phillips (1954). The flow is defined in a rectangular channel, where  $x$  is the zonal direction and  $y$  is the meridional direction. Rotation may be present in the form of  $f$ -plane dynamics, where the rotation  $f = 2\Omega$  is constant; alternatively, a  $\beta$ -plane may exist, which is where  $f$  varies linearly with  $y$ , the purpose of which is to account for the sphericity of the Earth in a simple and approximate manner. In the investigations to follow, the  $f$ -plane assumption is used exclusively. The geometry of the numerical model is shown schematically in Figure 1.2.

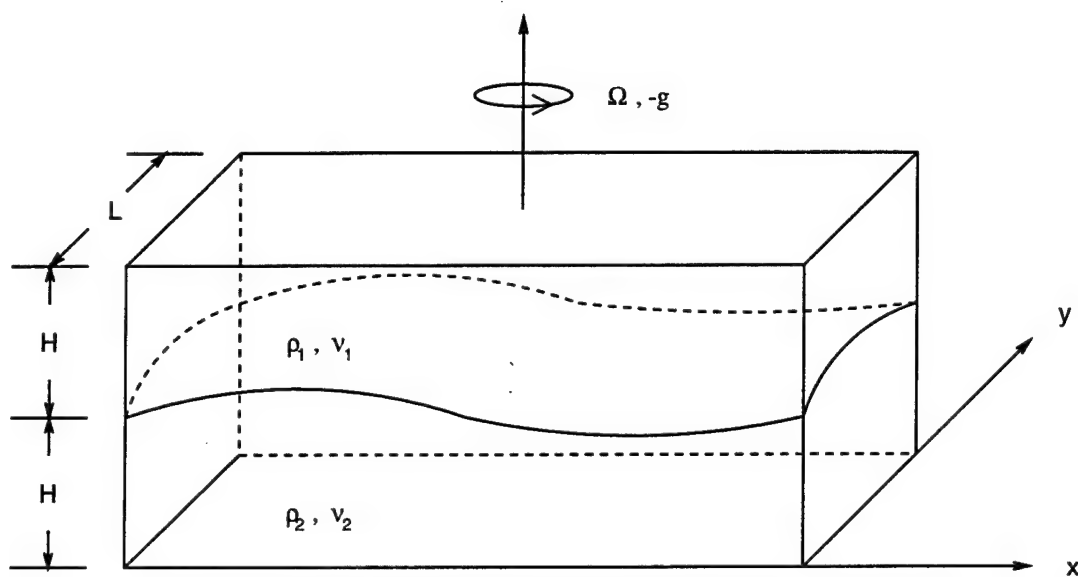


Figure 1.2: Schematic of model geometry

The flow is given by two potential vorticity equations

$$\begin{aligned} \left[ \frac{\partial}{\partial t} + J(P_k, \cdot) \right] [\nabla^2 P_k + F(-1)^k (P_1 - P_2)] &= -Q \nabla^2 P_k [(k-1)\chi + (2-k)] + \\ \frac{Q\chi(\nabla^2 P_1 - \nabla^2 P_2)(-1)^k}{1+\chi} &+ \frac{E}{R_o} \nabla^4 P_k, \end{aligned} \quad (1.3)$$

where  $k = 1, 2$ ,  $J(f, g) \equiv (\partial f / \partial x)(\partial g / \partial y) - (\partial f / \partial y)(\partial g / \partial x)$ , and  $P_k$  is the pressure in the  $k$ th layer. The meanings of the various terms deserve a brief explication. The second bracketed term on the left hand side of Equation 1.3 is the potential vorticity of the  $k$ th layer. This term is operated on by a time derivative and by a Jacobian. The Jacobian represents advection by the flow in each layer. On the right hand side of the equation, the first term is the Ekman damping at the top and bottom of the channel, while the second term represents interfacial Ekman friction; Ekman dissipation is actually a parametrization of the viscous effect on the flow by surfaces normal to the rotation vector. Finally, the last term on the right hand side represents lateral friction.

The parameters are as follows:  $F$  is the rotational Froude number,

$$F = \frac{2\Omega^2 L^2 (\rho_1 + \rho_2)}{g H (\rho_1 - \rho_2)}, \quad (1.4)$$

$Q$  is the bottom friction parameter,

$$Q = \frac{L \sqrt{\nu \Omega}}{H U} \quad (1.5)$$

$\chi$  is the viscosity ratio,

$$\chi = \sqrt{\frac{\nu_2}{\nu_1}}, \quad (1.6)$$

$E$  is the lateral Ekman number,

$$E = \frac{\nu}{2\Omega L^2}, \quad (1.7)$$

and  $R_o$  is the Rossby number,

$$R_o = \frac{U}{2\Omega L}. \quad (1.8)$$

In this thesis, all parameters will generally be held constant except for  $F$ . Then we will examine the transitions to more complex behavior as  $F$  is increased past its critical value (where instability first occurs). This operating scenario is somewhat different than some laboratory experiments, where  $Q$  is often varied while  $F$  is fixed.

The velocities in the two layers are evaluated geostrophically and are given by

$$u_k = -\frac{\partial P_k}{\partial y} \quad (1.9)$$

$$\text{and } v_k = \frac{\partial P_k}{\partial x}. \quad (1.10)$$

The height of the interface (from its rest value) is given by

$$h = R_o F (P_2 - P_1). \quad (1.11)$$

In the context of oceanic flows, the interface may be considered to be analogous to the thermocline, since there is a discontinuous density change across the interface (which can be related to a temperature difference).

The above-mentioned nondimensional parameters contain several dimensional constants:  $L$  is the width of the channel,  $H$  is the height of each resting layer

(which are assumed to be equal),  $U$  is a characteristic velocity,  $g$  is the gravitational constant, and  $\nu$  and  $\rho$  are the layer viscosities and densities, respectively. One other constant that does not explicitly appear in the equations is  $A$ , the aspect ratio of the channel, which is defined as the ratio of the length to the width. This parameter determines the physical geometry.

The boundary conditions can assume various forms depending on the specific treatment of the sidewalls. If a slippery-wall is implemented, the stress on the fluid at the walls must vanish, so that

$$\frac{\partial u'_k}{\partial y} = 0, \quad (1.12)$$

$$\frac{\partial \bar{u}_k}{\partial y} = 0, \quad (1.13)$$

where  $u_k$  is given by Equation 1.9 and the prime and overbar indicates wavy and zonally (i.e. downchannel) averaged velocities, respectively. Drazin and Reid (1981) give a more complete discussion of the slippery-wall condition in a slightly different context. In addition, there must be no flow through the walls, so that  $v_k = 0$  at these bounding walls, where  $v_k$  is given by Equation 1.10. For a rigid-wall channel (i.e. where the walls produce viscous effects), the boundary conditions are such that

$$u'_k = 0, \quad (1.14)$$

$$\bar{u}_k = 0, \quad (1.15)$$

and again  $v_k$  must be zero. The semi-stress-free models historically studied have utilized Equation 1.12 for the wavy portion of the flow and Equation 1.15 for the zonally-averaged quantity. In the absence of lateral friction, Pedlosky (1987) has shown that these are the proper boundary conditions, since the zonally-averaged velocity at the walls will decay to zero if not initially so.

One modification to Equation 1.3 which will be useful later is to cast the pressures in terms of their barotropic and baroclinic components. To do this, we first define

$$\Phi_{bt} \equiv P_1 + P_2, \text{ and} \quad (1.16)$$

$$\Phi_{bc} \equiv P_2 - P_1. \quad (1.17)$$

Then, Equation 1.3 becomes

$$\begin{aligned} \frac{\partial}{\partial t} \nabla^2 \Phi_{bt} - \frac{1}{2} J[\nabla^2 \Phi_{bt}, \Phi_{bt}] - \frac{1}{2} J[\nabla^2 \Phi_{bc}, \Phi_{bc}] = \\ -\frac{Q}{2} [(1 + \chi) \nabla^2 \Phi_{bt} + (1 - \chi) \nabla^2 \Phi_{bc}] + \frac{E}{R_o} \nabla^4 \Phi_{bt}, \end{aligned} \quad (1.18)$$

$$\begin{aligned} \frac{\partial}{\partial t} [\nabla^2 \Phi_{bc} - 2F\Phi_{bc}] - \frac{1}{2} J[\nabla^2 \Phi_{bc}, \Phi_{bt}] - \frac{1}{2} J[\nabla^2 \Phi_{bt}, \Phi_{bc}] - \\ FJ[\Phi_{bt}, \Phi_{bc}] = -\frac{Q}{2(\chi + 1)} [(1 - \chi^2) \nabla^2 \Phi_{bt} + (\chi^2 + 6\chi + 1) \nabla^2 \Phi_{bc}] + \\ \frac{E}{R_o} \nabla^4 \Phi_{bc}. \end{aligned} \quad (1.19)$$

The boundary conditions in terms of the barotropic and baroclinic velocities are identical to those for the layer velocities presented above.

#### 1.4 Linear Theory

The linear instability problem for the two-layer model described in the previous section is by now standard textbook fare (see, for example, Pedlosky (1987)). However, it is useful to quickly review the essentials of linear theory in order to establish a framework for the nonlinear theory to be discussed shortly.

Assume that a basic mean zonal flow, whose streamfunction is given by  $\Psi_n(y)$ , exists in both layers of the two-layer model described above. Next we suppose that there is a disturbance streamfunction of infinitesimal amplitude, denoted by

$\phi_n(x, y, t)$ , that exists in each layer. Then the total streamfunction in each layer is given by

$$P_n = \Psi_n(y) + \phi_n(x, y, t). \quad (1.20)$$

Substituting this into Equation 1.3, we obtain the following equation:

$$\begin{aligned} & \left[ \frac{\partial}{\partial t} + U_n \frac{\partial}{\partial x} \right] q_n + J(\phi_n, q_n) + \frac{\partial \phi_n}{\partial x} \frac{\partial \Pi_n}{\partial y} = \\ & -Q \nabla^2 (\Psi_n + \phi_n) [(n-1)\chi + (2-n)] + \\ & \frac{Q\chi [(\nabla^2(\Psi_1 + \phi_1) - \nabla^2(\Psi_2 + \phi_2))(-1)^n]}{(1+\chi)} + \frac{E}{R_o} \nabla^4 (\Psi_n + \phi_n), \end{aligned} \quad (1.21)$$

for  $n=1,2$ , where  $q_n$  is the perturbation potential vorticity and is defined as

$$q_n = \nabla^2 \phi_n - F(\phi_2 - \phi_1)(-1)^n, \quad (1.22)$$

$\Pi_n$  is the potential vorticity of the basic state and has a gradient given by

$$\frac{\partial \Pi_n}{\partial y} = -\frac{\partial^2 U_n}{\partial y^2} - F(U_1 - U_2)(-1)^n, \quad (1.23)$$

and  $U_n$  is the zonal basic state velocity in the  $n$ th layer, so that

$$U_n = -\frac{\partial \Psi_n}{\partial y}. \quad (1.24)$$

In order to formulate the linear stability problem, one first neglects terms that are nonlinear in  $\phi_n$ , so that the  $J(\phi_n, q_n)$  term is eliminated. Also, it is a great simplification to neglect the dissipative terms, i.e. the terms on the right hand side of

Equation 1.21. If this is done, the following inviscid, linear equation results for  $\phi_n$ :

$$[\frac{\partial}{\partial t} + U_n \frac{\partial}{\partial x}] q_n + \frac{\partial \phi_n}{\partial x} \frac{\partial \Pi_n}{\partial y} = 0. \quad (1.25)$$

In addition, the boundary conditions require that

$$\frac{\partial \phi_n}{\partial x} = 0, \quad y = 0, 1, \quad (1.26)$$

so that there is no flow through the walls at the boundaries.

Finally, if  $U_1$  and  $U_2$  are constants, then for stress-free boundaries a separable solution of the form

$$\phi_n = \text{Re} A_n \sin(l y) e^{ik(x-ct)} \quad (1.27)$$

can be sought, where  $\text{Re}$  denotes the real part is to be taken. If Equation 1.27 is substituted into Equation 1.25, the two following algebraic equations result for  $A_1$  and  $A_2$ :

$$[(c - U_1)(K^2 + F) + F(U_1 - U_2)]A_1 - F(c - U_1)A_2 = 0 \quad (1.28)$$

$$-F(c - U_2)A_1 + [(c - U_2)(K^2 + F) - F(U_1 - U_2)]A_2 = 0, \quad (1.29)$$

where  $K^2 \equiv k^2 + l^2$ . In order for  $A_1$  and  $A_2$  to have non-trivial solutions, the determinant of their coefficients must vanish. Doing this, we find that the value  $c$  is given by

$$c = \frac{U_1 + U_2}{2} \pm \left[ \frac{(U_2 - U_1)^2(K^2 - 2F)}{2(K^2 + 2F)} \right]^{1/2} \quad (1.30)$$

Instability then occurs for

$$F > F_c = \frac{K^2}{2}, \quad (1.31)$$

which is exactly the value of  $F$  that makes the imaginary part of  $c$  nonzero, thus yielding a wave whose amplitude grows exponentially with time.

Linear stability theory provides the value of  $F$  at which the first instability might spontaneously grow from some zonal background flow, here considered to be uniform. For example, for the slippery model to be investigated herein, the smallest allowable value of  $K^2$  occurs for  $k = \pi/2, l = \pi$  and is thus given by

$$K_{\min}^2 = \pi^2/4 + \pi^2 = 5\pi^2/4, \quad (1.32)$$

which corresponds to the wave  $e^{(i\pi x/2)} \sin(\pi y)$ . This yields a critical Froude number of  $F \approx 6.17$ , which corroborates very well with the onset of instability in the full numerical models when  $Q$  and  $E/R_o$  are small. The effect of friction on the neutral curves is to shift them upward by an amount that is  $O(Q^2)$ , so that the critical Froude number is given (Pedlosky, 1987) by

$$F_c = \frac{K^2}{2} + \frac{Q^2 K^2}{2k^2(U_1 - U_2)^2}. \quad (1.33)$$

For our investigations, which are carried out for small  $Q$ , the modification to the neutral curve is a wholly neglectable effect. Additionally, in a system allowing a continuous variation of wavelengths, very long waves (i.e.  $k \rightarrow 0$ ) are also stabilized by the effect of friction, but these waves are not allowed in the quantized-wavelength models presented herein.

There are two drawbacks to the linear theory presented above. First of

all, growth rates of a given wave perturbation are calculated from a given background flow that is zonal in nature. It does not apply to background flows that may themselves be wavy. The calculation of the linear stability of nonparallel flows is much more difficult and is discussed briefly by Pedlosky (1987). Second, and more importantly, linear theory only predicts whether a wave will initially grow from an infinitesimal amplitude. It makes no predictions regarding the asymptotic state of the system. Inevitably, the growth of the hypothesized wave will be halted by higher-order effects, and to address this issue we must return to the nonlinear problem.

## 1.5 Nonlinear Theory

Nonlinear effects become important when the wave field has grown large enough to influence, and indeed alter, the original zonal flow. In order to accurately determine the eventual fate of the system, these zonal flow alterations, and their subsequent return effect on the wave field (and *its* corresponding effect on the altered zonal field, *ad infinitum*) must be included via the nonlinear interactions. The resulting behavior of this nonlinear system can be quite complicated, exhibiting complex periodic, and even aperiodic, behavior. There are several topics of interest that are unique to the nonlinear regime, and these are discussed below.

**1.5.1 Energetics** In order to better characterize and understand the behavior of the quasi-geostrophic channel model, it is useful to derive energy equations for the flow. The procedure followed is similar to that of Holton (1972), who derives the energy equations for a continuously-stratified fluid. If Equation 1.3 is multiplied by  $-P_1$  and  $-P_2$  for  $k = 1, 2$ , respectively, one obtains equations for the time rate of change of the sum of the potential and kinetic energy in each layer. Equation 1.11 can then be differentiated with respect to time and multiplied by  $(P_2 - P_1)$ , which yields an equation for the time rate of change of potential energy. After some manipulation, the energy equations can be expressed in the following

format:

$$\frac{d\bar{P}}{dt} = \{\bar{K} \cdot \bar{P}\} + \{P' \cdot \bar{P}\}, \quad (1.34)$$

$$\frac{d\bar{K}}{dt} = \{K' \cdot \bar{K}\} - \{\bar{K} \cdot \bar{P}\} - \bar{F} + \bar{EI}, \quad (1.35)$$

$$\frac{dP'}{dt} = \{K' \cdot P'\} - \{P' \cdot \bar{P}\}, \quad (1.36)$$

$$\frac{dK'}{dt} = \{\bar{K} \cdot K'\} - \{K' \cdot P'\} - F', \quad (1.37)$$

where  $K$  denotes kinetic energy,  $P$  denotes potential energy, and the overbars and primes indicate zonal and wavy quantities, respectively. The energies are defined as follows:

$$P \equiv \frac{F}{2} \int \int (P_2 - P_1)^2 dx dy, \text{ and} \quad (1.38)$$

$$K \equiv \frac{1}{2} \sum_{i=1}^2 \int \int \left[ \left( \frac{\partial P_i}{\partial x} \right)^2 + \left( \frac{\partial P_i}{\partial y} \right)^2 \right] dx dy. \quad (1.39)$$

The transfer of energy from one type to another is indicated by the terms of the form  $\{A \cdot B\}$ , which is positive when energy is being transferred from  $A$  to  $B$ . Additionally,  $F'$  and  $\bar{F}$  indicate frictional dissipation of the wavy and zonal fields, respectively, and  $\bar{EI}$  represents the energy input to the system required to maintain the basic zonal flow. The actual form of each term is generally long and not very illuminating, and for these reasons an exposition of them is relegated to Appendix A. However, it is useful to represent the energetics in graphical form. Figure 1.3 displays a visual representation of the energetics of the flow field, following Hart (1976). This approach will be extremely helpful when deducing the behavior of the model presented in Chapter 2.

**1.5.2 Types of Vacillations** Several types of vacillations (or nonlinear periodic oscillations) in quasi-geostrophic flows have been identified, both experimentally and numerically. The first, and simplest, type is amplitude vacillation

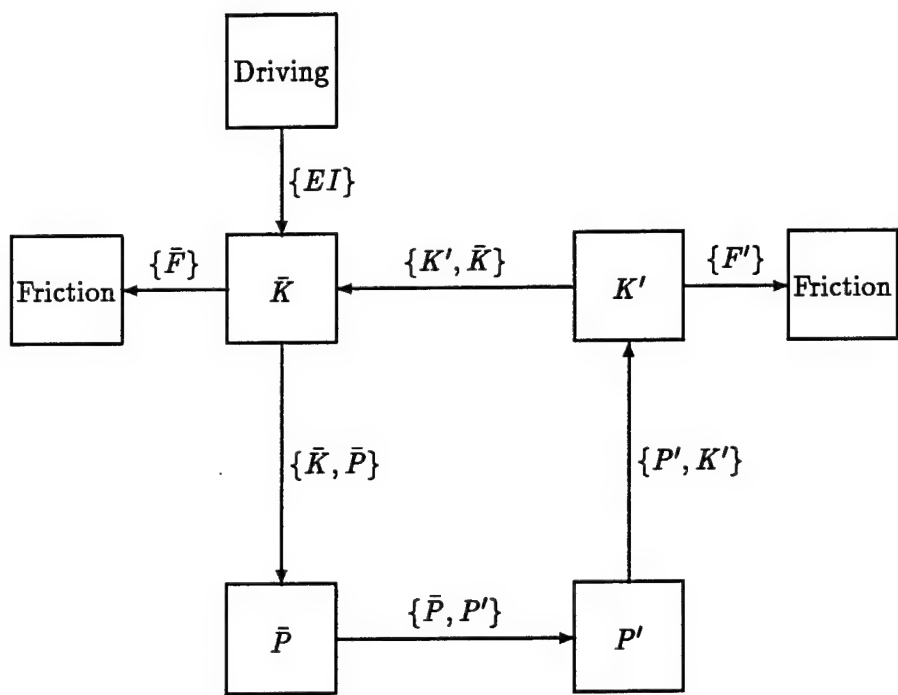


Figure 1.3: Energy-flow diagram

(AV), which involves energy transfers mainly from zonal available potential energy to eddy available potential energy to eddy kinetic energy ( $\bar{P} \rightarrow P' \rightarrow K'$ ) (Pfeffer and Chiang, 1967; Pfeffer et al., 1974). Amplitude vacillation, then, is primarily a baroclinic mechanism, following the same energy path as that described for baroclinic instability itself. When nonlinear effects are included, the wavy kinetic energy grows while the zonal potential energy is depleted and vice versa, thus maintaining a periodic energy transfer between the two flow components. In the AV regime, the spatial structures of the waves are largely constant and thus do not change shape over the course of a vacillation cycle.

Structural vacillation, conversely, is characterized by changes in the spatial structure of the wave field. The spatial variations cause fluctuations primarily in the meridional distribution of wave energy, but with little change in the overall wave energy (Pfeffer and Chiang, 1967; Pfeffer et al., 1980; Weng et al., 1986). Because the wave shape changes with time, the Reynolds stresses are important in structural vacillation (Pfeffer et al., 1980). Equivalently, the exchange of kinetic energy between the zonal and wavy portions of the flow (i.e.  $\bar{K} \rightarrow K'$ ) seems to be of consequence, implying that the vacillation is caused (or at least characterized) by a barotropic instability. Holton (1972) shows that the kinetic energy transfer term, denoted by  $\{K' \cdot \bar{K}\}$  can be written for a continuously-stratified flow as

$$\{K' \cdot \bar{K}\} = \int_V \bar{\psi} \frac{\partial^2 M}{\partial y^2} dV, \quad (1.40)$$

where  $\psi$  is the zonal streamfunction,  $M = \overline{u'v'}$ ,  $u'$  and  $v'$  are the eddy velocities, the overbar denotes a zonal average, and the integral is taken over the volume of the fluid. This relation, which is extrapolated to a two-layer flow in Appendix A, indicates that changes in the zonal average of the horizontal Reynolds stress of the wave field (which would result from a change in its spatial structure), and which generally yield

a nonzero meridional second derivative of this quantity, result in fluctuations of the barotropic energy transfer term. Thus, shape changes in the wavy field can produce Reynolds stresses, which in turn may generate a barotropic energy transfer.

Two other types of vacillation, which although they are not found in the  $f$ -plane numerical results presented herein, are briefly worth mentioning. Wavenumber vacillation (Pfeffer and Fowlis, 1968) is described by the periodic exchange of the stream function between two waves with different zonal wavenumbers. This vacillation can arise from the dispersion of two waves of constant amplitude, thus giving the impression of a wave field whose energy vacillates in time but is actually constant. Additionally, the source of such behavior may arise from a mixed-wave state whose origin is a double Hopf bifurcation (Hart, 1981). Finally, Ohlsen and Hart (1989b) describe a type of interference vacillation on a  $\beta$ -plane by which two waves can interact, via nonlinear couplings of their sidebands, to produce a low-frequency zonal flow oscillation.

**1.5.3 The Transition to Chaos** A well-established and ubiquitous occurrence in nonlinear systems is chaos, which is sometimes described as deterministic stochasticity. Chaos is characterized by irregular and aperiodic behavior in time (and sometimes in space), although it is not generally identified with fully-developed turbulence. There are two common routes to chaos that have historically been found in both numerical and laboratory experiments of baroclinic instability: quasi-periodicity (Farmer et al., 1982) and period-doubling (Hart, 1985). Quasi-periodic motions refers to a time-dependent fluctuation that consists of two or more independent frequencies whose ratios are irrational numbers. Ruelle and Takens (1971) proved that, if a three-frequency, quasi-periodic system is perturbed very slightly, it usually breaks down into chaotic behavior. More generally, a two-torus can directly break down into chaotic behavior without intervening three-torus motion (Berge et al., 1984).

Period-doubling behavior was first elucidated by Feigenbaum (1978). In this scenario, one begins with a periodic signal characterized by a dominant frequency,  $f_0$ . As the relevant driving parameter is increased, the fundamental period of the signal successively doubles, which equivalently results in the appearance of frequencies  $f_0/2$ ,  $f_0/4$ ,  $f_0/8$ , etc. Moreover, an infinite number of period-doublings occur within a finite parameter range, and the doublings follow well-defined scaling relations (Berge et al., 1984). At the completion of the period-doubling cascade, chaotic behavior ensues. As with quasi-periodicity, the period-doubling route to chaos, and the predicted scaling relations, have been observed experimentally.

There exist many numerical algorithms with which to characterize and quantify the ostensibly-chaotic behavior of a given system. The interested reader will find a summary of the methods used in this thesis in Appendix F.

## 1.6 Previous Results

**1.6.1 Single-Wave Models** Pedlosky (1970,1971,1972) was the first to systematically include the effects of the nonlinear interactions on the baroclinic wave field. His weakly nonlinear analysis was predicated on the assumption that the flow was only slightly supercritical with respect to the first unstable wave, i.e.

$$F = F_c + \Delta, \quad (1.41)$$

where  $F_c$  is the critical Froude number (given by Equation 1.31 for the inviscid case and by Equation 1.33 for nonzero dissipation) and  $\Delta$  is the supercriticality, where  $\Delta \ll F_c$ . When the system is only slightly above the stability threshold for the primary unstable wave, the remaining waves are linearly stable and wave-wave interactions are negligible. This result formally arises from his perturbation theory. Thus, the retention of a single wavy mode is sufficient to characterize the structure of the perturbation. Pedlosky's expansion included a correction to the initial zonal

flow that eventually becomes significant and halts the growth of the initial wave perturbation. However, the asymptotic behavior of the system was found to be highly dependent on the magnitude of the dissipation parameter,  $Q$ . For  $Q = O(1)$ , the system eventually equilibrates to a nonzero steady state. For  $Q = 0$ , the wave field and the zonal flow correction both oscillate with periods and amplitudes that are dependent upon the initial conditions. This is to be expected, since there is no viscosity to erase the system's memory of its initial state. Finally, for  $Q = O(|\Delta|^{1/2})$ , the system exhibits oscillatory behavior with oscillations that are independent of the initial conditions. Pedlosky (1971) notes the resemblance of these oscillations to the amplitude vacillation found in rotating annulus experiments and described by Pfeffer and Chiang (1967).

In a later paper, Pedlosky and Frenzen (1980) reported the existence of chaotic behavior in the weakly nonlinear model. The model was somewhat modified from the previous analyses to include multiple zonal correction modes, but qualitatively similar results can be obtained by retaining only a single zonal correction. For values of  $Q$  that lie between those which produce steady solutions and those which produce periodic behavior, the wavy and zonal fields can oscillate chaotically. As Pedlosky and Frenzen note, the most striking point to note is that the complex behavior results not from a highly turbulent flow regime but rather from a system that has a simple spatial dependence and also is only very slightly supercritical. They also indicate that the results are very sensitive to the value of the dissipation parameter. Pedlosky and Polvani (1987) found that the type of behavior exhibited by a single-wave model is critically related to the type, as well as the amplitude, of the dissipation included in the governing equations. When they made the damping proportional to the potential vorticity, the solutions became steady for all parameter values.

Hart (1986) examined the behavior of a single-wave model with a generic

zonal flow correction in cylindrical geometry, which is analogous to an experimental setup. He retained one wave and several zonal flow correction terms. It was found, for  $f$ -plane motions, that there was some qualitative similarity between the model behavior and the experimental behavior inasmuch as both exhibited a truncated period-doubling route to chaos. However, the value of  $F$  for which the flow became chaotic was much lower in the experiments than in the model, and the vacillation periods differed by about 40%. This would suggest that the single-wave model is missing some crucial physics.

The behavior exhibited by the single-wave model is important because the model is deduced from first principles and not from an arbitrary spectral truncation of the streamfunctions. Thus, the system is rigorously valid in the asymptotic limit  $\Delta \rightarrow 0$ . However, it is not clear if the behavior of the single-wave model at larger supercriticality is even qualitatively, much less quantitatively, similar to that which would be shown by a model which retains many spatial modes and is thus capable of representing much more complex spatial behavior.

**1.6.2 Multi-Wave Models** Boville (1980) considered the problem of quasi-geostrophic flow in a channel on an  $f$ -plane. He represented the streamfunctions with 8 zonal harmonics and 16 meridional modes, yielding a system with 128 waves in each layer. The full model displayed behavior that differed substantially from that of the single-wave model; for instance, the transition to oscillatory flow required a larger supercriticality for the multi-wave implementation than for the single-wave representation. In addition, Boville discovered that the inclusion of zonal harmonics was more critical to the behavior than the inclusion of multiple meridional modes. This seems to suggest the inadequacy of single-wave models for any point in parameter space not near the neutral curve. Shortly after his  $f$ -plane treatise, Boville (1981) considered motions on a  $\beta$ -plane. It was again found that substantial differences existed between a modestly-resolved model (with the same

number of modes as the *f*-plane case) and a single-wave model, again casting the latter's validity for finite supercriticality into doubt. Boville (1982) considered the  $\beta$ -plane channel flow in a highly supercritical, and thus very nonlinear, regime. He found that the model, which now consisted of 16 zonal harmonics and 16 meridional wavenumbers (or 256 wavenumber pairs in each layer), exhibited both amplitude and structural vacillation, depending on the exact parameters chosen. Most importantly, Boville stated that the wave-wave interactions comprised a substantial portion of the energy conversions, justifying the inclusion of multiple waves into the model. Later, Klein and Pedlosky (1986) considered *f*-plane dynamics with a similar resolution as that of Boville. They reported that the behavior of the system, with increasing supercriticality, would generally proceed from steady to periodic to aperiodic behavior, although they noted many exceptions to this overall trend. In addition, they too reported that the inclusion of many zonal harmonics was imperative to the qualitative nature of the solution. They concluded that "the crucial role of the zonal harmonics is to allow a sufficiently accurate description of the meridional structure of the basic wave so that the correction to the zonal flow may be calculated directly". In other words, the higher wave-wave interactions are thought to act indirectly to regulate the meridional structure of the primary wave, which is subsequently imperative in generating the proper wave-mean flow interaction. Investigating the system in a different geometry, Yoshida and Hart (1986) considered a spectral model of quasi-geostrophic flow in a cylinder. They represented the stream-functions with 10 zonal harmonics and 12 (or more) radial modes. Consistent with the previous studies, they found significant differences in behavior between their full numerical model and the corresponding single-wave model. In addition, the model exhibited both period-doubling and quasi-periodic routes to chaos. Cattaneo and Hart (1990) used a resolution of 49 x 49 (or approximately 2500 wavenumber pairs in each layer) to study *f*-plane dynamics in a channel. Their model exhibited the

following transition: steady flow, periodic amplitude vacillation (PAV)→periodic structural vacillation (PSV)→quasi-periodicity→chaos. Chaotic behavior ensued at about  $O(4)$  supercriticality. As a final example, Klein and Pedlosky (1992) recently used a spectral model with a resolution of up to  $49 \times 49$  to examine the effects of different dissipation mechanisms. Two important results from their paper are noted here. First, the choice of dissipation parameterization greatly affected the results obtained; the inclusion of interfacial Ekman friction generated results that tended to be more stable than those obtained with only solid-surface Ekman friction (e.g. steady solutions instead of periodic flow). The other important result is that, for large supercriticality, there is a barotropic fluctuation superimposed on the initial baroclinic vacillation. Moreover, the appearance of this vacillation coincides with the Froude number at which the second harmonic of the fundamental wave possesses a linear growth rate larger than that of the fundamental itself. This behavior is similar to that observed in this study (in which a higher resolution has been used). Unfortunately, Klein and Pedlosky did not perform extensive numerical integrations in order to ascertain the exact nature of the solutions as a function of  $F$ , negating the possibility of a direct comparison with the results to be presented herein.

The results of all of the afore-mentioned models, with the exception of Cattaneo and Hart (1990) and Klein and Pedlosky (1992), are obscured by the question of convergence. Additionally, all of the models neglect the effect of lateral friction at the sidewalls and thus inconsistently incorporate free-slip conditions on the waves but no-slip conditions on the zonal flow at the sidewalls. As will be shown in the next chapter, for the channel flow model at large supercriticality, the number of Fourier modes required to achieve quantitative convergence is more than an order of magnitude greater than the highest resolution used in most of the previously-discussed simulations. In addition, Klein and Pedlosky (1992) did not perform extensive calculations at high resolution, so that their findings are certainly very sparse. Thus, while

the results are certainly an improvement on the prognostics generated by single-wave models, it is dangerous to put too much faith in them. Moreover, the behavior of some of the models exhibit a return to simpler behavior as the supercriticality is increased. This is certainly not seen in experiments (Hart, 1985; Ohlsen and Hart, 1989a), where the complexity of the flow increases with increasing supercriticality and decreasing friction. Furthermore, even high-resolution models show substantial differences in behavior, in terms of the supercriticality at which chaos first occurs, when compared to laboratory experiments. This would suggest that the previous models may be missing a crucial portion of the physics, in addition to lacking adequate resolution.

**1.6.3 Laboratory Experiments** Two types of laboratory experiments have been performed and analyzed extensively in an effort to model baroclinic instability. The first consists of a rotating annulus which has a relatively hot outer (equatorward) boundary and a relatively cold inner (poleward) boundary (see Hide and Mason (1975) for a comprehensive review). As the relevant parameters (i.e. rotation rate and temperature gradient) are modified, the system first undergoes a transition from axisymmetric flow to amplitude vacillation (Pfeffer and Chiang, 1967; Pfeffer et al., 1974), which is essentially a baroclinic phenomenon. At higher supercriticality, the amplitude vacillation yields to structural vacillation (Pfeffer et al., 1980). Finally, at even more supercritical settings, the flow becomes irregular (both temporally and spatially) and enters into the regime of geostrophic turbulence. At least some of the so-called turbulence can be analyzed in terms of low-dimensional chaotic dynamics. Read (1992) and Read et al. (1992) present data which indicates that particular vacillatory states give way to chaotic states which can be characterized as evolution on a low-dimensional attractor. For some parameter settings, the transition to chaos was via quasi-periodicity, while for others it seemed to be via intermittency (which is a third type of transition to chaos and has not been otherwise

documented for baroclinic flows).

Of greater interest here is the two-layer experiment initiated by Hart (1972) (see review by Hart (1979)), which can be directly compared to numerical two-layer investigations. The experimental configuration is very similar to the theoretical model described in Section 1.3, with the exception that the experimental geometry is cylindrical. In any case, the various states observed in the annulus experiment are also observed in the two-layer flow, including steady waves, amplitude vacillation, structural vacillation, and irregular (i.e. chaotic) flow (Hart, 1972; Hart, 1976; Hart, 1985; Ohlsen and Hart, 1989a). Both  $f$ -plane and  $\beta$ -plane experiments display a period-doubling route to chaos. However, both experiments show only two doublings before becoming chaotic. One possible explanation for this may simply be measurement limitations. Since the successive period-doubled regimes occur in successively smaller windows of parameter space, the ability of experiments to access and measure these states is difficult. However, the apparent period-doubling may be the onset of a quasi-periodic flow with frequencies possessing a ratio very close to 2. This idea has consequences for the results to be presented later.

The two-layer experiment is especially appealing because it can be modeled relatively easily, thus allowing comparison between theory and experiment. However, the test of the efficacy of weakly nonlinear theory has not been fruitful due to the theory's validity only very close to the neutral curve, a region which is not easily accessible experimentally. In addition, it is not evident that the region of convergence of weakly nonlinear theory includes behavior other than steady waves anyhow. Establishing a correspondence between theory and experiment is an ongoing task, and in the remaining chapters, some effort to forge this link will be undertaken.

## CHAPTER 2

### A STRESS-FREE MODEL OF BAROCLINIC INSTABILITY

The purpose of this chapter is to introduce and examine the results of a two-layer model of baroclinic instability with fully-slippery walls. The motivation for investigating such a situation is first discussed briefly. Next, the general numerical method used to treat such models is summarized. A fully-stress-free model is then introduced and described; the model results are validated by a comparison with a low-order spectral model. Finally, the results of the full numerical simulations are described and compared to previous results utilizing mixed boundary conditions (which will be referred to as "semi-slippery").

#### 2.1 Stress-Free Sidewalls

Previous numerical models of two-layer baroclinic instability have utilized mixed boundary conditions at the sidewalls: stress-free conditions are imposed on the wavy portions, while a no-slip requirement is mandated for the zonal corrections. These conditions are valid in the absence of lateral friction (Pedlosky, 1987), but in the numerical models lateral friction is needed to halt the cascade of enstrophy to higher wavenumbers. Aside from numerical reasons, the shortcoming of the above approach is that, physically, there is no reason to expect that the walls would affect one portion of the flow differently than another. Apart from the fact that it is internally consistent, the use of fully stress-free conditions at these bounding walls is more analogous to the atmosphere, which has no natural boundaries. In addition, although laboratory experiments necessarily have viscous sidewalls, the onset of instability in such experiments agrees very well with linear theory based

on a slippery-wall assumption (Hart, 1972). Thus, it was previously hoped that the results would be applicable to laboratory experiments in the nonlinear regime as well.

## 2.2 Numerical Method

The numerical method used for the slippery model is described in detail by Cattaneo and Hart (1990) (hereafter referred to as CH), but it is useful to briefly summarize it here. CH actually investigated the results of a semi-slippery implementation, but the general method for both the semi-slippery and the fully stress-free models is essentially equivalent (with the exception of the implementation of the specific boundary conditions). The scheme used is a Fourier pseudo-spectral method; the advantages of a such a method are both its speed and accuracy. With this type of algorithm, the linear terms in the equation are computed in spectral space, while the nonlinear terms are computed in physical space. Furthermore, the linear terms are found using a centered Crank-Nicholson scheme, while the nonlinear terms are updated with a 3-level Adams-Bashforth method. CH note that pseudo-spectral methods introduce aliasing when nonlinear terms are evaluated. To eliminate this problem, a standard dealiasing scheme based on the 2/3 rule is adopted (Canuto et al., 1988).

## 2.3 Model Formulation

**2.3.1 The Semi-Slippery Model** In their paper, CH developed a high-resolution numerical model of the two-layer flow described in the previous chapter. They expand the pressures in the two layers as

$$\begin{aligned}
 P_k(x, y, t) = & \mp y + \sum_{n=1}^{\infty} \sum_{j=1}^{\infty} \phi_{k_n j}(t) e^{2i n \pi x / A} \sin(j \pi y) + \\
 & \sum_{j'=1}^{\infty} \hat{\phi}_{k_j j'}(t) \cos(j' \pi y), \quad k = 1, 2,
 \end{aligned} \tag{2.1}$$

where the  $\mp y$  term indicates a uniform basic state and the constant  $A$  is the ratio of the length of the channel to its width. As stated by CH, the expansion is consistent with slippery boundary conditions for the wavy terms but not for the zonal flow. In other words,  $\partial u_k / \partial y |_{y=0,1} = -\partial^2 P_k / \partial y^2 |_{y=0,1}$  is not necessarily zero since the expansion for the zonal portion of the streamfunction is in terms of  $\cos(j'\pi y)$  terms. The boundary conditions, then, are not truly slippery in the sense the stress vanishes at the walls. In fact, the use of cosines indicates that the zonally-averaged velocity is zero at the walls, which is consistent with a rigid-wall (i.e. viscous) boundary condition.

Following Phillips (1954), one can derive a circulation condition for  $\partial \bar{u}_k / \partial t$ , where the overbar denotes an average in  $x$ . Details of the derivation are given in Appendix B. In the absence of lateral friction,  $\bar{u}_k$  decays very rapidly from a given initial value and can then essentially be considered zero for all time. However, when lateral friction exists, Equations B.7,8 are necessary to determine the fate of  $\bar{u}_k$ . The model is thus inconsistent because it incorporates lateral friction but uses an expansion that results in the trivial relation  $\bar{u}_k = 0$ . As a mitigating factor, CH anticipated such effects of the order of  $E/(R_o Q) \approx 1/300 \ll 1$ , possibly rendering the inconsistency unimportant. However, we shall see shortly that there are some significant differences between the purely stress-free results and those of CH, a result which emphasizes again the critical role that subtle changes in boundary conditions can have on the baroclinic chaos problem.

Another complication with the CH model concerns the effect of wave-wave interactions. The Jacobian terms in Equation 1.3 generate wave-wave interactions, which in turn alter the zonal flow. The meridional dependence of these interactions can be written schematically as

$$\sin(k\pi y) \cos(k'\pi y) = \frac{1}{2}[\sin((k+k')\pi y) + \sin((k-k')\pi y)], \quad (2.2)$$

so that wave-wave interactions have a meridional dependence that can be expanded in terms of sines. The functional representation is consistent with the expansion for the wavy terms but not for that of the zonal flow. Therefore, wave-wave interactions couple non-locally in Fourier space to the zonal flow. Because

$$I[k, j'] = \int_0^1 \sin(k\pi y) \cos(j'\pi y) dy = \frac{k((-1)^{k+j'} - 1)}{j'^2 - k^2} \quad (2.3)$$

where  $k$  is the cross-stream wavenumber for the wavy mode and  $j'$  is the cross-stream wavenumber for the zonal mode, for  $k$  odd there is coupling to all cross-stream wavenumbers for which  $j'$  is even, and for  $k$  even there is coupling to all wavenumbers with  $j'$  odd. There is thus slower convergence in spectral space than is optimal, requiring the introduction of substantial lateral friction in order to maintain good spectral convergence. However, it is precisely the presence of lateral friction in the sidewall boundary conditions which invalidates the expansion.

**2.3.2 The Slippery Model** The slippery model was formulated in order to correct the various deficiencies in the semi-slippery model and to see if better agreement with experiment might be found. In order to ensure that there are stress-free conditions at the walls, the zonally averaged pressures at the walls ( $y = 0, 1$ ) are expanded as sine functions. Thus,  $-\partial^2 P_k / \partial y^2 = \partial u_k / \partial y = 0$  at the walls, where  $k$  indicates the layer. In addition, with this type of expansion, Equation 2.2 indicates that the nonlinear interactions will have direct projections on the meridional structure, thus eliminating the problems associated with projecting

sine functions onto a cosine basis, as Equation 2.3 indicates. Finally, the proper circulation condition is included in the model. The derivation of this condition, which is a method by which to close the secondary circulation (induced by the Ekman layers) in terms of the primary circulation, is contained in Appendix B, along with the derivation of the mass conservation stipulation. It provides a constraint on the evolution of the zonally-averaged velocities at the walls,  $\bar{u}_k$ . To properly account for these requirements, the following expansion is used:

$$P_k(x, y, t) = \mp y + \sum_{n=1}^{\infty} \sum_{j=1}^{\infty} \phi_{k_n j}(t) e^{2in\pi x/A} \sin(j\pi y) + \sum_{j'=1}^{\infty} \hat{\phi}_{k_j}(t) \sin(j'\pi y) + \mathcal{U}_k(t)(y - 1/2) \mp \mathcal{D}(t)/2. \quad (2.4)$$

Because of the nature of the expansion, there is a complete set of cosine functions to describe  $u_k = -\partial P_k / \partial y$  (the zero wavenumber component arises from the second to last term in Equation 2.4). In addition, the no-stress stipulation is automatically satisfied, and the nonlinear interactions project directly onto the original functional expansion. Thus, it only remains to express the circulation condition and mass conservation requirement in terms of the quantities given in Equation 2.4, a full treatment of which is given in Appendix B. Owing to the nature of the chosen expansion, the  $\mathcal{U}_k(t)$  terms decouple from the  $\mathcal{D}(t)$  term, and the resulting relations are given by Equations B.13,14,15. These equations yield three additional constraints to the system described by Equation 1.3.

The implementation of the extra boundary conditions, in terms of numerical coding, is relatively straightforward but tedious. Note that Equations B.13,14,15 couple all of the zonal coefficients together. Previously, because of the Fourier representation of the pressure fields, the solution matrix for the coefficients was diagonal, so that one needed only to solve a multiplicity of scalar equations to update the time coefficients. Now, however, a sparse matrix must be solved for the zonal terms in

the model. In order to keep numerical errors to a minimum, the matrix solution is obtained in double precision at every time step.

## 2.4 Model Verification

Virtually all of the subroutines are identical to those used for the semi-slippery model, eliminating the necessity to comprehensively re-check each portion of the code. It was decided that the most efficient way to check the modified code was to test the results for a low resolution run against a low-order, fully spectral model. The spectral code assumed a spatial dependence in each layer that consisted of the following waves:  $\sin(\pi y) \cos(\pi x/2)$ ,  $\sin(\pi y) \sin(\pi x/2)$ , and  $\sin(2\pi y)$ . This resulted in six equations for the two layers, and when added to the two equations for  $U_1$  and  $U_2$ , resulted in a cumulative total of eight equations. The pseudo-spectral code was run at a resolution of 8x9, which is the lowest resolution at which aliasing effects can be removed. Although this resolution contains more wavenumbers than the spectral model, all waves except those listed above were zeroed out at each time step, resulting in a good approximation to the spectral model. The results are shown in Figure 2.1. The single line indicates the steady regime, while the double lines indicate the envelope of periodic solutions. There is essentially exact agreement between the two models. Figure 2.2 compares the phase-space diagrams between the two models for  $F = 30$ . The x-axis displays the barotropic wave amplitude, while the y-axis represents the baroclinic wave amplitude. The attractors are indistinguishable, which further indicates that the pseudo-spectral model is operating correctly.

The other requirement from the model was that it be convergent in the sense that results are independent of resolution. Convergence tests were performed on the asymmetric state for three resolutions: 96x49, 128x65, and 192x97. In addition, for each resolution, results were obtained for  $F = 8, 16, 26$ , and 40 (these values of  $F$  were chosen to sample the system over the spectrum of temporal behavior). The

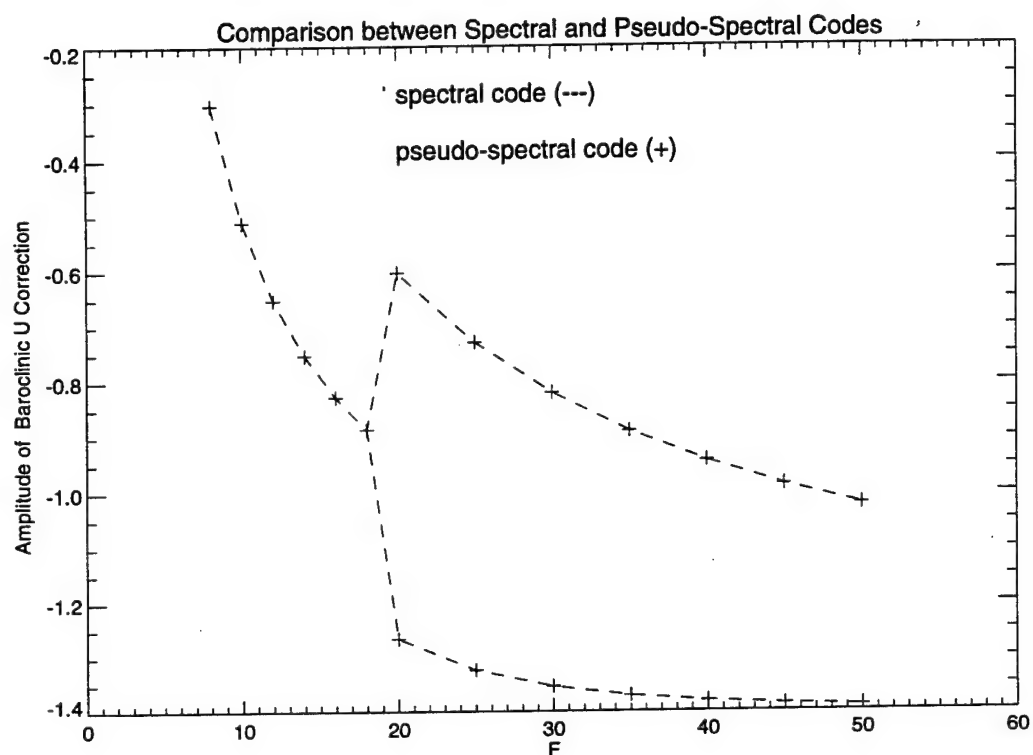


Figure 2.1. Comparison of low-dimensional, spectral and pseudo-spectral slippery models for  $8 \leq F \leq 50$ . The single line indicates the steady regime, while the double lines indicate the envelope of periodic solutions.

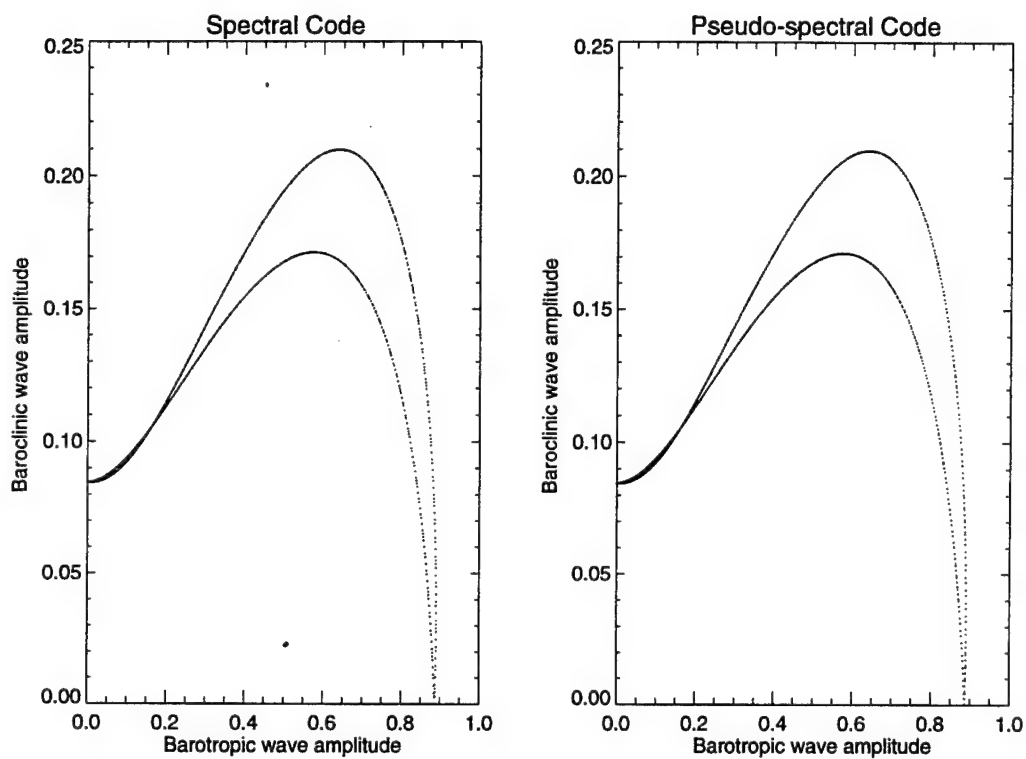


Figure 2.2. Phase-space comparisons of low-dimensional, spectral and pseudo-spectral slippery models for  $F = 30$ . The x-axis is the barotropic wave amplitude, and the y-axis is the baroclinic wave amplitude.

asymmetric state was chosen because of its more complicated time dependence. All resolutions showed similar qualitative behavior with regard to the type of motion displayed (i.e. steady, periodic, chaotic) for a given value of  $F$ . In other words, the transition points (in terms of  $F$ ) between different types of behavior were the same for all three resolutions. However, it was desired that the agreement be quantitative as well. To ascertain whether or not there in fact was quantitative agreement, the wavy baroclinic kinetic energy in the asymmetric state was used as a proxy measurement. The kinetic energy was used to ensure that the signal chosen contained input from many wavenumbers and thus represented the overall behavior of the system. Its mean and root-mean-square (rms) deviation were computed for  $F = 8, 16, 26$ , and  $40$  for all three resolutions. The results were then differenced to determine the percent change in mean and rms deviation between successive resolutions. The percentage changes in the mean are extremely small and average about 3%. Table 2.1 shows the successive percentage change in rms deviation, which is a better measure of the differences between resolutions.

Table 2.1. Convergence of rms deviation of baroclinic wavy kinetic energy versus resolution for various values of  $F$ .

Froude Number	Percent change in rms deviation between 96x49 and 128x65 resolution	Percent change in rms deviation between 128x65 and 192x97 resolution
8	n/a	n/a
16	21.9 %	-4.06 %
26	-100.5 %	21.6 %
40	-6.15 %	3.41 %

The rms deviations do show some differences as a function of resolution. However, the changes between the 128x65 case and the 192x97 case are minimal, with an average difference of around 9%. In addition, the time behavior for  $F \geq 24$  is not strictly periodic, so that very long time averages would be necessary in order to get an extremely accurate estimate of the rms deviation. Consequently, some of

the differences can be attributed to sampling for only a finite time. However, the differences in rms deviation at  $F = 26$  are sufficiently large to suggest a real difference in behavior. The probable cause of this is the nature of the quasi-periodic behavior that exists at  $F = 26$ ; the mode-locking that occurs sporadically as a function of  $F$  in this regime makes the system very sensitive (quantitatively) to small changes in parameters and/or resolution. An interesting item to note is that the chaotic regime is more robust than the quasi-periodic regime in the sense that its quantitative behavior changes very little with resolution. Overall, the differences between the 128x65 and 192x97 resolutions are small, and it was thus decided that the 128x65 resolution would be adequate to achieve a valid set of results in the expected states.

## 2.5 Multiple States

Various symmetries can exist in the channel model, and the successive breaking of symmetries correlates with the onset of more complex (e.g. chaotic) motion in the flow. Identifying these symmetries is therefore crucial to understanding the changes in behavior that the system undergoes as parameters are varied. The first is a vertical symmetry. If the viscosities in the two layers are equal (i.e.  $\chi = 1$ ) and there is no barotropic, or depth-averaged, basic zonal flow, then there exist wavy solutions which also generate no barotropic zonal corrections, thus preserving the vertical symmetry. In this case, the instability is termed **zonoclinic**, since only the baroclinic zonal corrections are entrained. If the barotropic wavy field is purely real (i.e. in the x-direction it consists only of cosine functions) and the baroclinic wavy field is purely imaginary (only sine functions), or vice versa, then a zonoclinic instability is guaranteed. This is clearly a special requirement on the spectral occupation of the wavy fields. In contrast to the zonoclinic instability, another type entrains only the barotropic zonal corrections and is thus termed **zonotropic**. The presence of a zonotropic instability breaks the vertical symmetry of the problem, and it is

generated when the barotropic and baroclinic fields are both complex-valued. However, the meridional modes of the wavy fields must be related in a specific manner such that no baroclinic zonal corrections are generated by the nonlinear terms.

The other important symmetry in the problem involves the occupation, in wavenumber space, of the wavy fields, a symmetry which leads to the presence of “multiple states”. CH elucidated the idea of multiple states in channel flows constrained to be quasi-geostrophic. They observe that there exist certain subsets of wavenumbers that do not propagate information outside of the subsets. These wavenumber subsets are then invariant under the action of the nonlinear operators in Equation 1.3. They discuss one type of invariant subset that is particularly important. If there is energy in any zonal modes that are even with respect to the cross-stream midpoint of the channel then all wavenumber pairs can contain energy; this state is termed “asymmetric” (because the zonal flow velocity is then asymmetric about the mid-plane of the flow). However, if only the zonal modes that are odd with respect to the midpoint contain energy, then a “countable infinity of distinct wave states are possible” (Cattaneo and Hart, 1990) and the state is termed “symmetric”. The symmetric state results from flows that have shift-reflect symmetry in physical space (i.e. if one chooses a point, shifts by one-half the channel length, and reflects about the midpoint, the flow velocity is the same as at the original point). In terms of the wavenumbers themselves, if the gravest zonal ( $k_x$ ) and meridional ( $k_y$ ) wavenumbers are defined to be 1, then symmetric waves have the property that  $k_x + k_y$  is even. Figure 2.3 displays the symmetric state in wavenumber space. The wavenumber pairs denoted with a lowercase ‘a’ are the antisymmetric wavenumbers; these have the property that  $k_x + k_y$  is odd. Each forms a “checkerboard” in wavenumber space. The antisymmetric state, however, is not invariant under the action of the nonlinear operators, and it interacts to affect the symmetric state. When this happens, an asymmetric state is generated, since all wavenumbers

now possess nonzero energy.

These symmetries are important because all of the instabilities observed in the numerical solutions appear to be one of four types: symmetric zonoclinic, symmetric zonotropic, antisymmetric zonoclinic, and antisymmetric zonotropic. Thus, each instability is associated with a symmetry breaking of a particular type. The instabilities and their symmetries are summarized in Table 2.2. The second column indicates the symmetry of the waves, while the third column describes the symmetry of the zonal correction. The fourth column indicates whether each symmetry is preserved under the action of the nonlinear operators in the governing equations. Finally, the last column indicates the behavior generally exhibited by each type in the absence of other instabilities. The PAV behavior is associated with zonoclinic instabilities because the wavy fields do not change shape over time, while the PSV behavior is associated with zonotropic instabilities since the waves do change shape over the course of one vacillation cycle (resulting from the complex-valued nature of the wavy fields themselves). Because the antisymmetric wavenumber symmetry cannot be preserved under the action of the nonlinear terms, the resulting state is asymmetric. Therefore, when referring to a stability that is initially antisymmetric, the term “asymmetric” will also be used interchangeably.

Table 2.2: Summary of instabilities and their associated symmetries.

Type of Instability	Wavy and Zonal Symmetry	Type of Zonal Correction	Preserves Wave #/Z.C. Symmetry?	Typical Finite Amp. Behavior
symmetric zonoclinic	symmetric	baroclinic	yes/yes	PAV
antisymmetric zonoclinic	antisymmetric	baroclinic	no/yes	PAV
symmetric zonotropic	symmetric	barotropic	yes/no	PSV
antisymmetric zonotropic	antisymmetric	barotropic	no/no	PSV

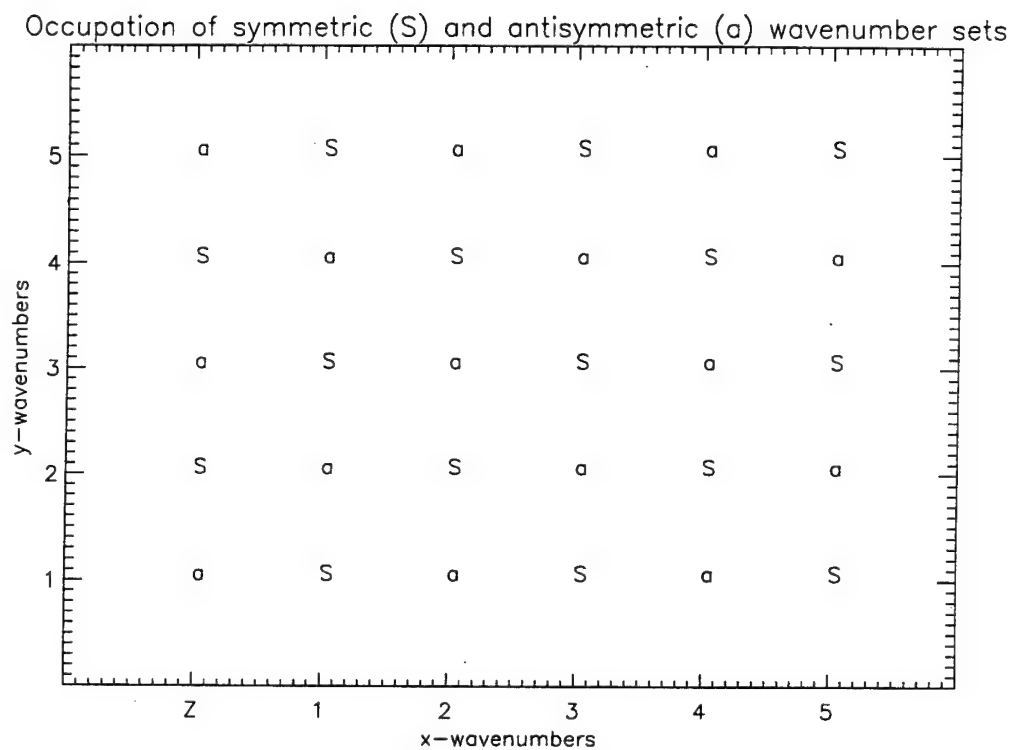


Figure 2.3. Wavenumber-space occupation of symmetric and antisymmetric sets. The 'Z' indicates the zonal correction terms.

## 2.6 Results for the Semi-Slippery Model

Some results from our calculations with the CH semi-slippery model are shown below. For the numerical runs, parameters were set to the following values:

$$Q = 0.06, \quad (2.5)$$

$$\chi = 1.0,$$

$$E/R_o = 0.0002,$$

$$A = 4,$$

$$8 \leq F \leq 40.$$

The parameter values are the same used by CH except for  $\chi$ , which they set equal to 0.9. For the equal-viscosity case studied here, the wave disturbances are stationary instead of travelling (as is found for  $\chi \neq 1$ ). A resolution of 96x49 was used, again consistent with CH. This resolution was found to provide convergent behavior for the model. Numerical runs were performed for both the symmetric and asymmetric states for the Froude number range listed above.  $F$  values were increased in increments of 2. The overall results are shown in Figure 2.4.

As is evident from the figure, the symmetric case makes a transition from steady to periodic behavior (i.e. periodic amplitude vacillation) at  $F \approx 16$ . Then, at  $F \approx 26$ , there is a transition from PAV to PSV. This state persists until  $F = 40$ , where the study was terminated. In addition, if the symmetric state is perturbed with asymmetric perturbations, for  $F \geq 12$  it will evolve toward the asymmetric solution. For  $F < 12$ , however, the asymmetric state decays and approaches the symmetric steady solution.

The asymmetric state shows slightly more complicated behavior. At  $F \approx 12$ , the asymmetric case goes from a steady solution directly to PSV, which persists

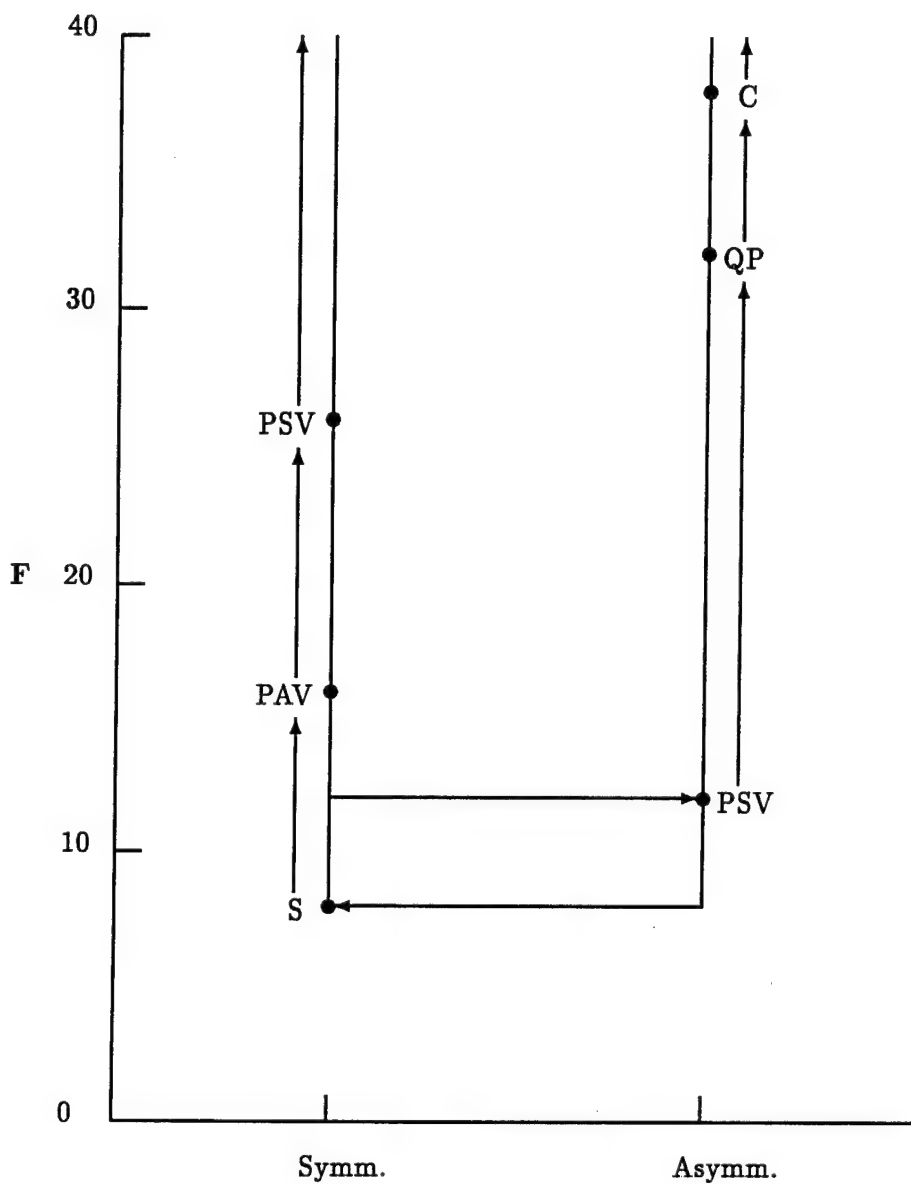


Figure 2.4. Behavior of Semi-Slippery Model for  $8 \leq F \leq 40$ . The vertical arrows indicate the range of  $F$  over which a particular type of behavior is realized. The horizontal arrows indicate the direction of transition between symmetric and asymmetric states (i.e. the asymmetric state decays to the symmetric state for  $F < 12$ , and the symmetric state, when perturbed, becomes asymmetric for  $F \geq 12$ ).  $S$  = steady, PAV = periodic amplitude vacillation, PSV = periodic structural vacillation, QP = quasi-periodic, C = chaotic.

until  $F \approx 32$ . The solution then becomes quasi-periodic for  $32 \leq F \leq 38$ . Finally, for  $F \geq 38 \approx 5F_c$ , the system becomes chaotic. Thus, the semi-slippery model displays one of the quintessential routes to chaos, that of the breakdown of a torus (Berge et al., 1984).

In summary, the semi-slippery model shows profound differences between the behaviors of the symmetric and asymmetric states. In addition, the symmetric state is unstable with respect to asymmetric perturbations for all values of  $F$  except those near the onset of initial instability. This would seem to indicate that the symmetric solution cannot be realized in any “real” (e.g. experimental or geophysical) flow. Finally, the temporal behavior of both states is relatively simple, with chaos occurring only for large values of  $F$ . As stated in the introduction, this is relatively disappointing in comparison to experimental results; although the experiments are performed in a cylindrical geometry, the laboratory flow becomes chaotic for  $F \geq 12 \approx 1.6F_c$  (Hart, 1985).

## 2.7 Results for the Slipping Model

Numerical runs were made for  $8 \leq F \leq 40$  (in increments of 2) for both the symmetric and asymmetric cases, with the system parameters set equal to the values shown in Equation 2.5. The general behavior as a function of  $F$  is shown in Figure 2.5.

When compared to the results of the semi-slippery model, the slipping model displays similar qualitative behavior, but there are some significant differences in the transition points. The results are indeed sensitive to the boundary conditions implemented. For example, in the symmetric state, the semi-slippery model never becomes quasi-periodic for  $F \leq 40$ , while the fully-slipping results display this behavior for  $F \geq 34$ . In addition, for both the symmetric and asymmetric solutions, transitions to more complex temporal behavior occur at lower values of  $F$  than the

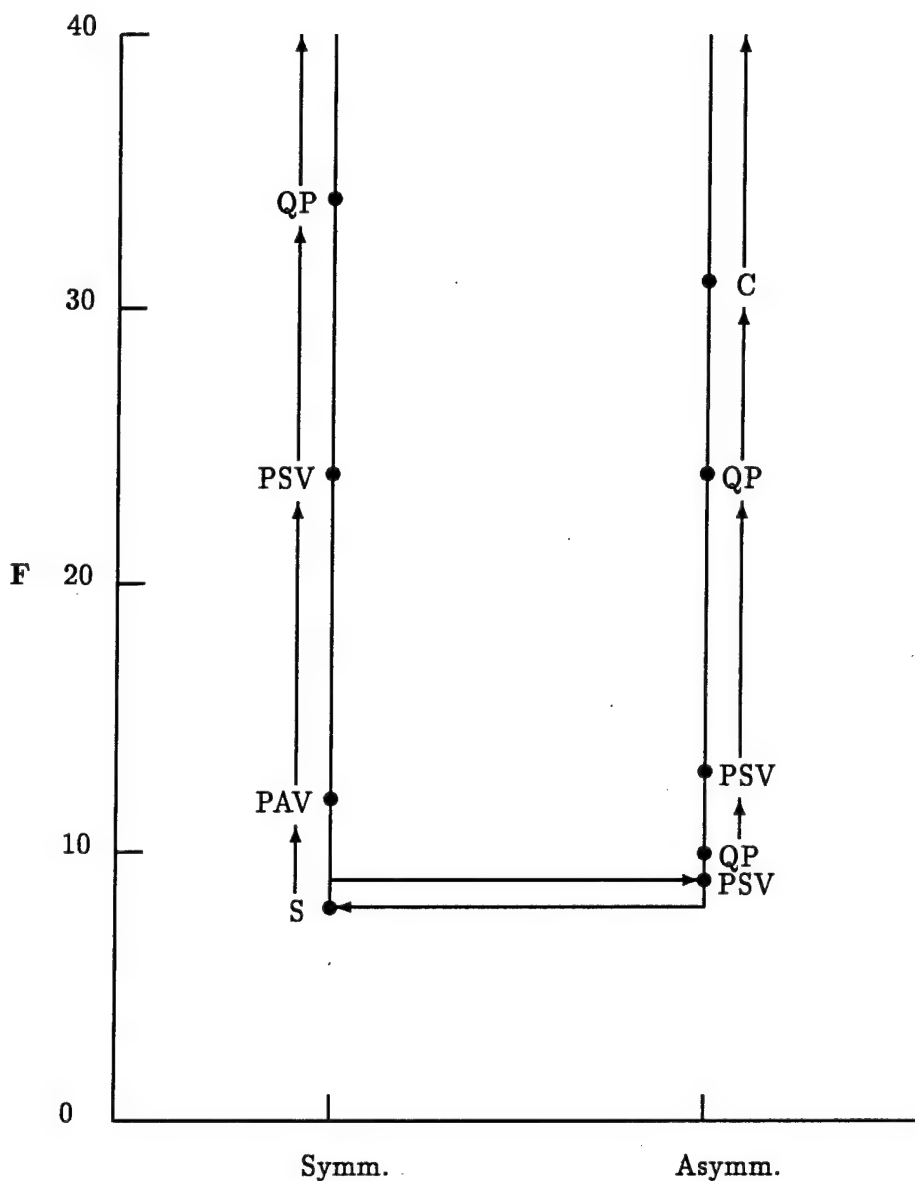


Figure 2.5. Behavior of Slippery Model for  $8 \leq F \leq 40$ . The vertical arrows indicate the range of  $F$  over which a particular type of behavior is realized. The horizontal arrows indicate the direction of transition between symmetric and asymmetric states (i.e. the asymmetric state decays to the symmetric state for  $F < 9$ , and the symmetric state, when perturbed, becomes asymmetric for  $F \geq 9$ ).  $S$  = steady, PAV = periodic amplitude vacillation, PSV = periodic structural vacillation, QP = quasi-periodic, C = chaotic.

comparable transitions in the semi-slippery case.

The symmetric solution exhibits steady-behavior just above the onset of instability. At slightly larger values of  $F$ , it enters a regime of periodic amplitude vacillation. The energetics in this regime exhibit the classic baroclinic signature (see Section 1.5.2). At still higher values of  $F$ , a barotropic instability causes a transition to structural vacillation. As the supercriticality is increased further, there is eventually a mixing between the PAV and PSV which results in a quasi-periodic flow. Since the symmetric solution is unstable and performs a transition to the asymmetric state over almost all values of  $F$  considered, the asymmetric state is the only realizable flow in a laboratory setting. In order to keep this discussion concise, a detailed summary of the symmetric state's behavior has been relegated to Appendix C and only the asymmetric solutions will be discussed further in this chapter.

The energy diagram introduced in Section 1.5.1 is useful for showing the mean energies of the system, but the energy fluctuations have proven to be much more revealing in understanding the behavior at a particular parameter setting. For brevity, important results in the mean energy cycle will be simply stated rather than graphically illustrated. The asymmetric state first comes into existence at  $F = 9$ . The mean energies of the asymmetric state are much the same as those in the symmetric regime. A useful quantity is the percentage ratio of the mean barotropic energy transfer to the mean baroclinic energy transfer, which we define as  $\mathcal{R}$ , where

$$\mathcal{R} (\%) = 100 \frac{\{\bar{K} \cdot K'\}}{\{P' \cdot K'\}}, \quad (2.6)$$

At  $F = 9$ ,  $\mathcal{R}$  is about 6.9%, similar to the symmetric state at  $F = 8$ . The growth rate of the instability is extremely small at this value of  $F$ , and it subsequently takes many oscillations for this state to "equilibrate". In addition, the amplitude

of the vacillation is very small, so that the state could be described as quasi-steady. An examination of the energetics indicates that the behavior is a form of PAV, since there is no barotropic zonal correction term involved (which means that the barotropic zonal kinetic energy is zero).

At  $F = 10$ , the solution becomes quasi-periodic. The value of  $\mathcal{R}$  has grown to 11.6%. Figure 2.6 shows the energy transfers as a function of time. The behavior is largely the same as the symmetric solution at  $F = 12$ , but with an additional modulation that results in quasi-periodic behavior. Nonetheless, the system still appears to be exhibiting amplitude vacillation, and the baroclinic energy transfer terms have rms deviations an order of magnitude larger than the barotropic transfer term. In addition, the barotropic zonal kinetic energy is still zero (as it was for  $F = 9$ ). Finally, an examination of the power spectra of the zonal coefficients indicates that the quasi-periodicity arises as a result of the previous solution at  $F = 9$  interacting with the symmetric PAV solution. Thus, the difference between the symmetric and asymmetric solutions at this parameter setting seems to be that the asymmetric instability interacts just slightly with the original symmetric solution, producing a weak, quasi-periodic modulation of the flow.

At  $F = 13$ , the asymmetric case enters a regime of periodic structural vacillation, and the value of  $\mathcal{R}$  is now 13.7%. The cause of this dynamical behavior is a barotropic instability, just as in the symmetric state. This can be seen in Figure 2.7, which displays the barotropic and baroclinic  $\sin(\pi y)$  coefficients as a function of time. The barotropic portion of this coefficient grows with time until it reaches a simple periodic regime; the baroclinic component, conversely, decays to zero. In addition, this PSV regime possesses the property that the **symmetric** modes retain only a **baroclinic component**. Figure 2.8 displays the barotropic and baroclinic  $\sin(2\pi y)$  zonal components. The barotropic portion decays to zero, while the baroclinic portion alters in response to the instability and eventually reaches a periodic state.

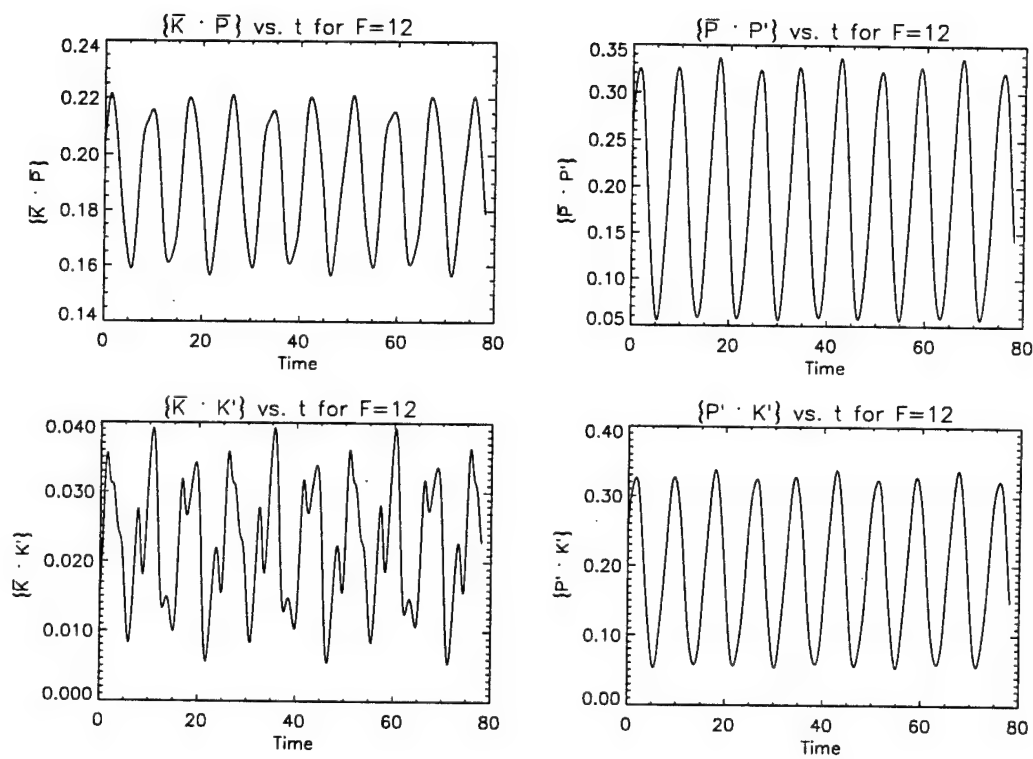


Figure 2.6: Energy transfer terms for asymmetric case,  $F = 12$

Thus, the baroclinic nature of the flow is maintained in the symmetric modes, while the antisymmetric modes reflect the barotropic component. For clarity, the symmetric modes are those for which the sum of the  $x$ -wavenumber and  $y$ -wavenumber are even, while the antisymmetric modes are those for which the sum is odd. However, the asymmetric state generally includes all waves, since it encompasses the symmetric as well as the antisymmetric modes.

As is the case for the symmetric solution, profound changes arise in the fluctuations of the various energies and also the energy transfer terms between PAV and PSV. That the state can be characterized as structural vacillation is evidenced by Figure 2.9, which displays the meridional kinetic energy (for the upper layer) vs. time. The shape of the distribution clearly changes in shape as well as in amplitude, in contrast to the distribution of kinetic energy for  $F = 12$ , which retains its shape over the course of one vacillation cycle. The phase relationships between the energies are different in the asymmetric PSV regime than for the symmetric regime. The zonal potential and wavy potential energies are approximately in phase, as are the zonal and wavy kinetic energies. Moreover, these pairs are approximately out of phase with each other. This may be contrasted with the behavior of the symmetric case at  $F = 26$ , where the zonal energies are in phase with each other and exactly out of phase with the wavy kinetic energy. The clue to the origin of this difference seems to be contained in the magnitudes of the rms deviations of the energy transfer terms. Although, for  $F = 13$ , the system is in a structural vacillation regime that is generally characterized by a domination of barotropic energy transfers, the rms deviations of both the barotropic and the baroclinic transfer terms are approximately equal at this parameter setting. Recall that for the symmetric state at  $F = 26$ , the barotropic energy transfer dominates. Thus, it seems that the exact phase relationships between the various energies depend on the magnitudes of the transfers between these energies. In contrast to the amplitude vacillation regime,

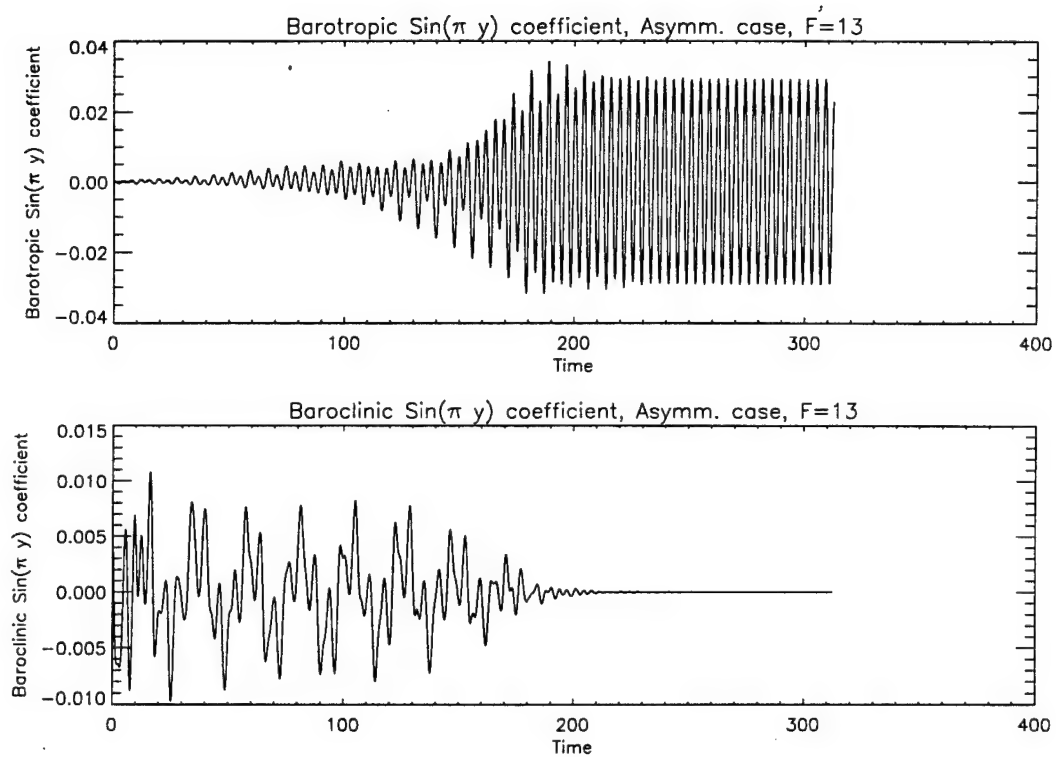


Figure 2.7. Barotropic and Baroclinic components of  $\text{sin}(\pi y)$  zonal term vs. time, Asymm. case,  $F=13$

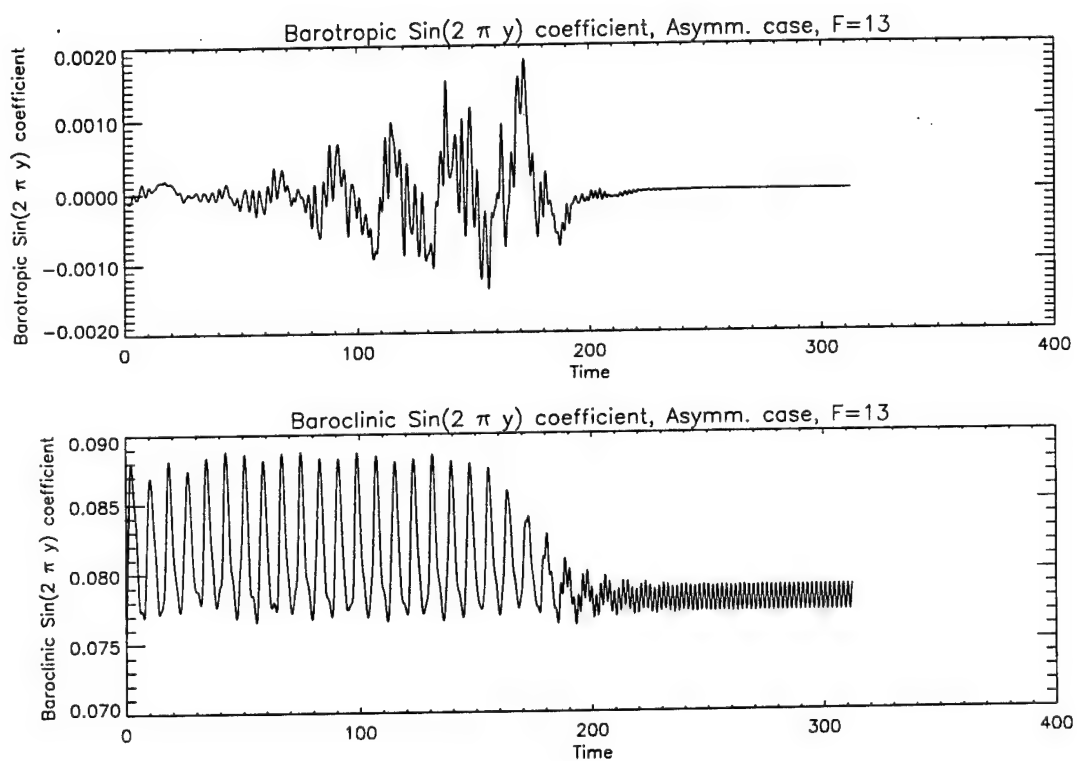


Figure 2.8. Barotropic and Baroclinic components of  $\text{sin}(2\pi y)$  zonal term vs. time, Asymm. case,  $F=13$

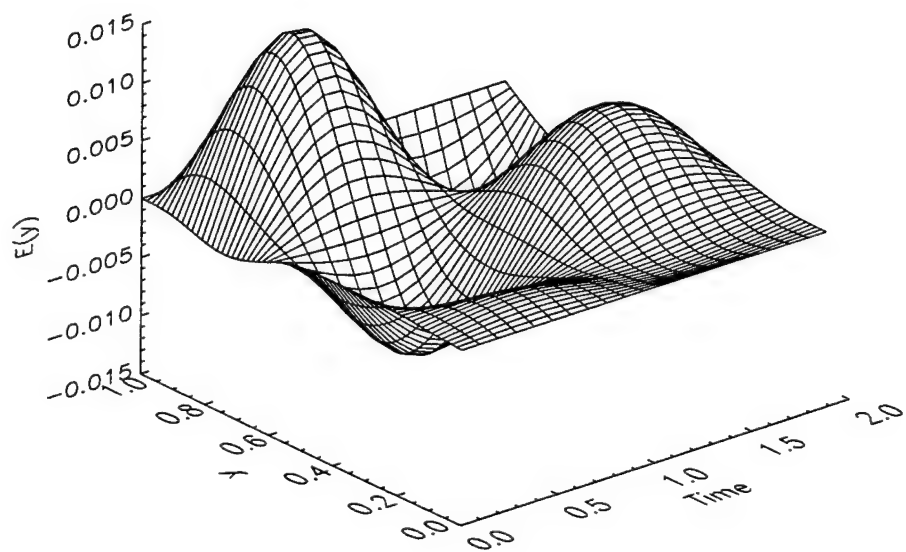


Figure 2.9. Zonally-integrated wavy kinetic energy,  $E(y)$ , vs.  $y$  for several times,  $T$ , over one cycle,  $F = 13$ , Asymm. case

which is characterized largely by baroclinic transfers and fixed relationships between the various potential and kinetic energies, the PSV phenomenon is more complex and, in a sense, more generic than PAV.

There is, however, some commonality between the various PSV solutions. The dominant frequency for the  $\sin(2\pi y)$  coefficient at  $F = 13$  is about 0.53 nondimensional frequency units, compared to the peak frequency of 0.38 frequency units for the symmetric solution at  $F = 26$ . The discrepancy is not as large as it seems, because the frequency tends to decrease with increasing  $F$ , so that the two are probably comparable at equal values of  $F$ . Thus, PSV seems to be generally associated with higher-frequency oscillations than does PAV.

The transition from PAV (actually, the quasi-periodic state) to PSV is very abrupt. This is in contrast to the results of a low-order model studied by Weng et al. (1986), who observe a slow transition in which a mixed vacillation occurs between the two regimes. They do not comment as to whether the mixed vacillation is periodic or quasi-periodic.

The spatial dependence of the flow at  $F = 20$ , near the upper limit of the PSV regime, is shown in Figures D.7,8. The counter-rotating eddy feature common to PSV behavior is clear in the baroclinic field, although the spatial representation of the flow is much different than in the symmetric regime. The barotropic field shows less of this counter-rotating tendency. Instead, it appears that eddies move meridionally in more of a "zig-zag" manner from the top of the flow domain to the bottom. Thus, the barotropic field also shows structural differences from the barotropic PSV solution in the symmetric regime.

The next parameter setting to examine is  $F = 26$ , just after the asymmetric state has become quasi-periodic. The value of  $\mathcal{R}$  has increased to 26.2%, so that the mean barotropic energy transfer continues to grow (relative to the mean baroclinic

energy transfer) with increasing  $F$ . The time return map of the  $U_1$  coefficient is exhibited in Figure 2.10a (the time return map is essentially the same as the maximum return map, but it measures the time between successive maxima). Figure 2.10b, which displays a circle map constructed from the time return map, displays slight noninvertibility near  $\theta_n = 2$ , a necessary condition for chaos (Baker and Gollub, 1990). Thus, the system is near the onset of chaos but is still exhibiting regular (i.e. non-chaotic) behavior.

The origin of the observed behavior is essentially the same as the transition to quasi-periodicity in the symmetric solution—i.e., mixing of baroclinic and barotropic instabilities. Figure 2.11 displays the energy transfers versus time. In contrast to the flow at  $F = 20$ , the baroclinic transfer terms are larger than the barotropic transfer term, implying that the quasi-periodic behavior arises from the interaction of a baroclinic instability with a barotropic instability (however, unlike the symmetric solution, the baroclinic instability in this situation is **asymmetric**). This is evidenced by the fact that the asymmetric, baroclinic zonal terms, which are nonexistent at  $F = 20$ , grow to a finite value at  $F = 24$ . Additionally, the dominant temporal frequencies of the baroclinic  $\sin(\pi y)$  zonal term and the baroclinic  $\sin(2\pi y)$  zonal term are 0.150 and 0.116 nondimensional frequency units, respectively. These values correspond to the respective oscillation frequencies in the earlier QP regime, which is governed by baroclinic instabilities. It can thus be concluded that the quasi-periodic behavior arises as the result of competition between barotropic and baroclinic instabilities (just as in the symmetric state), and it is also clear that the baroclinic instabilities are qualitatively similar to those that govern amplitude vacillation, so that it is likely the same instability experiencing a resurgence.

One final aspect to examine at  $F = 26$  is the phase relationships between the energies, which are displayed in Figure 2.12. Although the behavior is not strictly periodic, the relative phases of the energies are much like that found in a

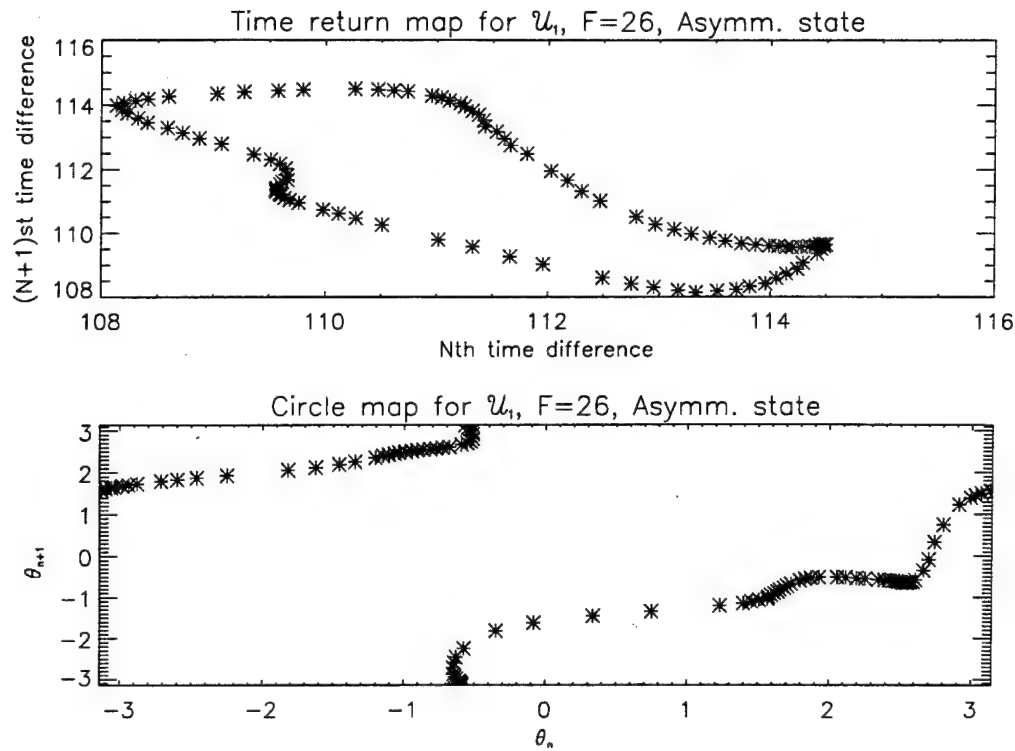


Figure 2.10. (a) Time return map and (b) circle map for  $U_1$  term, asymmetric state,  $F = 26$ .

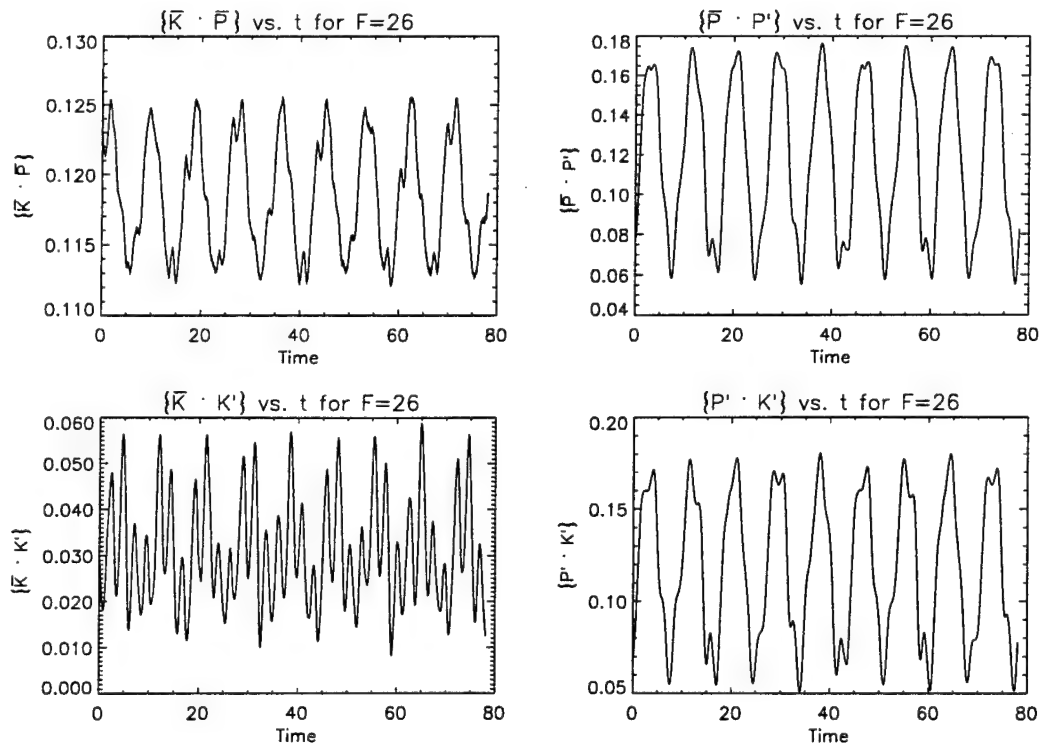


Figure 2.11: Energy transfer terms for asymmetric case,  $F = 26$

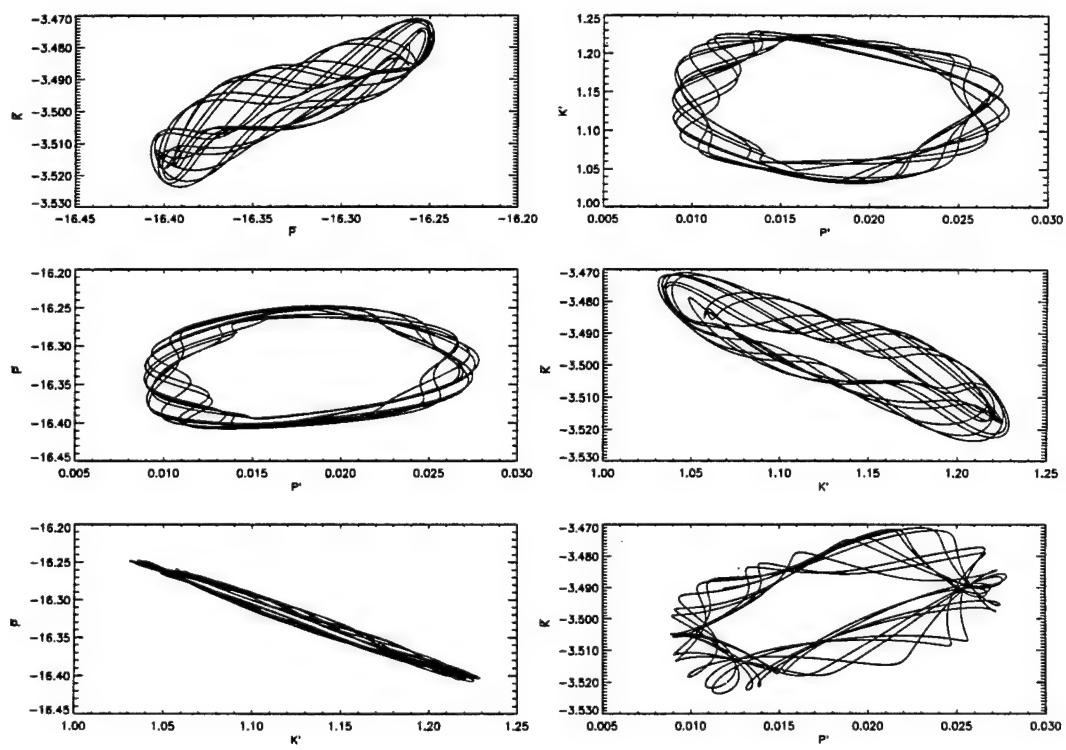


Figure 2.12: Phase-space plots of energy fluctuations,  $F = 26$ , asymmm. state

pure amplitude vacillation. Specifically,  $\bar{P}$  and  $\bar{K}$  are in phase with one another and out of phase with  $K'$ ; additionally,  $P'$  is ninety degrees out of phase with  $K'$ . These are the energy cycles observed in a purely baroclinic flow. Thus, the barotropic instability simply acts to modulate this transfer of energy, adding complexity to the temporal behavior of the flow in the process.

Between  $F = 24$  and  $F = 30$ , the system alternates between phase-locked states (which are multiply-periodic) and quasi-periodicity. An example of the flow fields in a quasi-periodic state, at  $F = 28$ , is shown in Figures D.9,10. In contrast to the symmetric regime's quasi-periodic flow, the spatial dependence is much more complicated than that exhibited for PSV, although the baroclinic field still shows some features of counter-rotation. There exist many transient, small-scale features, especially in the baroclinic field. The lack of correspondence with the pure PSV behavior is not surprising, since previously it was stated that baroclinic energy transfers dominate the quasi-periodic behavior. Thus, the spatial dependence is likely a complex amalgamation of both PAV and PSV fields.

At  $F \approx 30.9$ , the system becomes chaotic. To understand the mechanics of the transition, the behavior at  $F = 30.5$  is used as a reference. Figure 2.13a displays a phase-space plot of the  $\mathcal{U}_1$  coefficient at  $F = 30.5$ , which is plotted against itself using the method of time delays, as well as the power spectrum of the time series shown in Figure 2.13b. The phase space plot shows a very orderly attractor, while the power spectrum consists of several distinct peaks and a relatively small noise floor, implying quasi-periodicity.

A time return map constructed from the same time series is shown in Figure 2.13c. The return map further indicates that the system is quasi-periodic. To confirm this numerically, one can normally resort to calculating the largest Lyapunov exponent of the system (see Appendix F). If it is positive, then the system is by definition chaotic; if it is zero, the dynamics are quasi-periodic. However, calculations of this

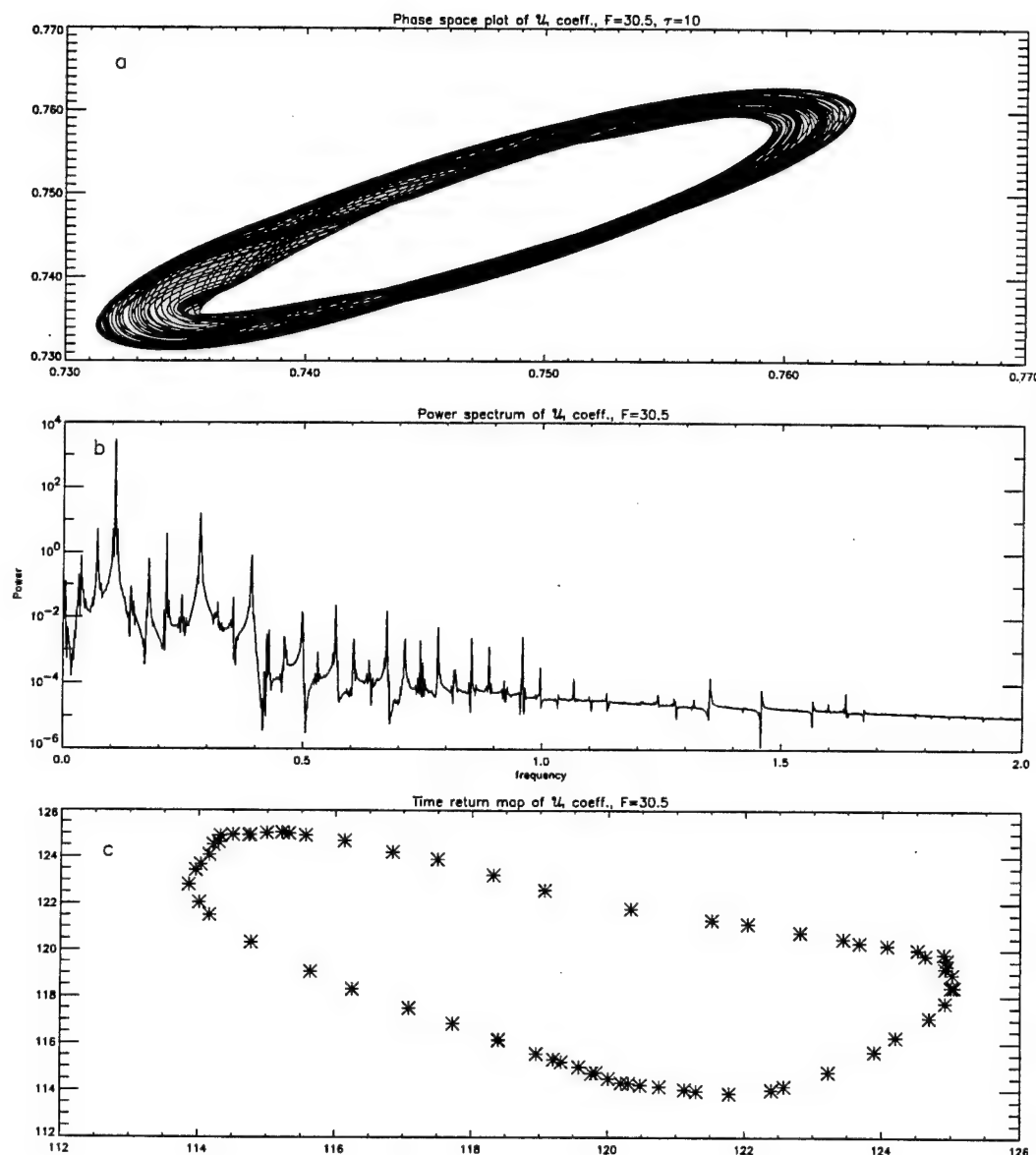


Figure 2.13.  $F = 30.5$ . (a) Phase-space plot of  $U_1$  coefficient vs. itself with a time delay of .078 seconds. (b) Power spectrum of the same time series. (c) Time return map constructed from  $U_1$  time series.

type failed to unambiguously determine whether or not the dynamics at  $F = 30.5$  are chaotic (the calculations revealed a positive, but very small, exponent, which is not numerically significant). As a last option, a nonlinear prediction algorithm developed by Farmer and Sidorowich (1987) was used in order to determine whether the predictability extent was finite or infinite, the former indicating a chaotic system. For the flow at  $F = 30.5$ , the prediction error does not grow with time. Thus, the system is quasi-periodic and not chaotic. The results at  $F = 30.5$  can now be contrasted with those at  $F = 30.9$ . The phase-space plot and power spectrum of the  $U_1$  coefficient are displayed in Figure 2.14a,b. The phase-space trajectory is somewhat more convoluted than was the case for  $F = 30.5$ , and the power spectrum shows a broadening of the major peaks (a hallmark of the transition to chaos). In addition, the time return map constructed from the  $U_1$  time series, and shown in Figure 2.14c, is no longer a simple curve. Finally, a use of the nonlinear prediction algorithm indicates that the prediction now grows with time, albeit slowly. The fact that the error grows at such a slow rate, and even seems to oscillate in phase with the actual signal, indicates that the dynamics are still largely determined by the quasi-periodic portion of the dynamics. This is also apparent when one examines the energetics of the flow. There is almost no change in the relative magnitudes of the fluctuations of the energies or the energy transfer terms between the quasi-periodic and chaotic states. Since the onset of chaotic behavior is not reflected in a quantitative change in the energetics of the flow, what causes the chaos? According to the Ruelle-Takens scenario discussed in Section 1.5.3, the introduction of a third incommensurate frequency to a quasi-periodic flow generally results in an unstable situation. It would seem reasonable to conclude that a new instability becomes sufficiently potent to interact with the quasi-periodic flow, resulting in incipient chaos. However, since there is no newly-detectable peak in the power spectrum at  $F = 30.9$ , the amplitude of the instability must be relatively weak.

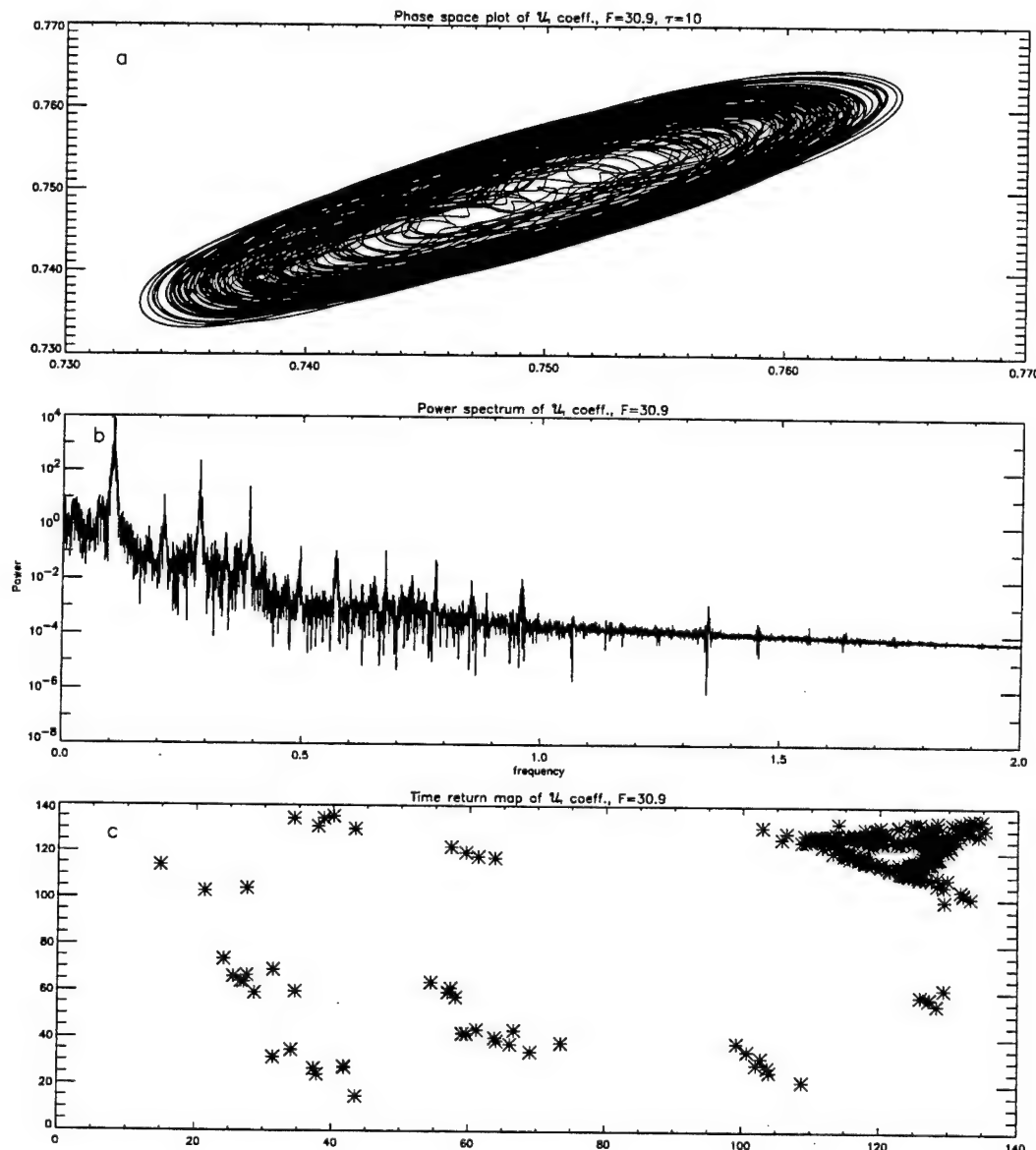


Figure 2.14.  $F = 30.9$ . (a) Phase-space plot of  $U_1$  coefficient vs. itself with a time delay of .078 seconds. (b) Power spectrum of the same time series. (c) Time return map constructed from  $U_1$  time series.

Spatial fields at  $F = 32$ , just above the onset of chaos, are displayed in Figures D.11,12. The spatial dependence is not much more convoluted than that at  $F = 28$ , nor is there a shift toward domination by smaller scales. Rather, the same basic spatial structures are now simply modulated chaotically in time. This indicates that the final transition, from quasi-periodicity to chaos, is more important temporally, leaving the spatial behavior of the fields statistically intact.

The system becomes chaotic quickly. Estimates of correlation dimension of the attractor (see discussion in Appendix F) produce the correct value of two for the quasi-periodic behavior at  $F = 30.5$ , but the results are inconclusive for the attractor at  $F = 30.9$ , which must necessarily have a dimension greater than two. More specifically, there is an absence of a scaling region over which the dimension can be estimated. However, the dimension at any length scale never exceeds about 3.5, indicating the attractor dimension most likely lies between three and four, a reasonable conclusion to draw considering the nascent chaotic behavior under consideration. Given that it is impractical (from a data-gathering standpoint) to estimate the attractor dimension with any certainty at  $F = 30.9$  (and Lyapunov exponents are also impractical, as Eckmann and Ruelle (1992) have asserted that the estimation of these requires even more data than does a dimension calculation), it is certainly not feasible to calculate the dimension at higher values of  $F$ , where one would intuitively expect behavior that is more chaotic than that at lower  $F$ . However, it is possible to make a rough visual assessment by viewing the attractor, power spectrum, and return map. Figure 2.15 displays these for the  $\mathcal{U}_1$  coefficient at  $F = 40$ .

The phase-space plot is much more convoluted and shows much less of the quasi-periodic dynamics than is evident at  $F = 30.9$ . The power spectrum and return maps corroborate this; there is no well-defined peak in the power spectrum, and the return map shows no low-dimensional structure. It is thus certainly reasonable to assume that further increases in  $F$  would lead the system to a state of

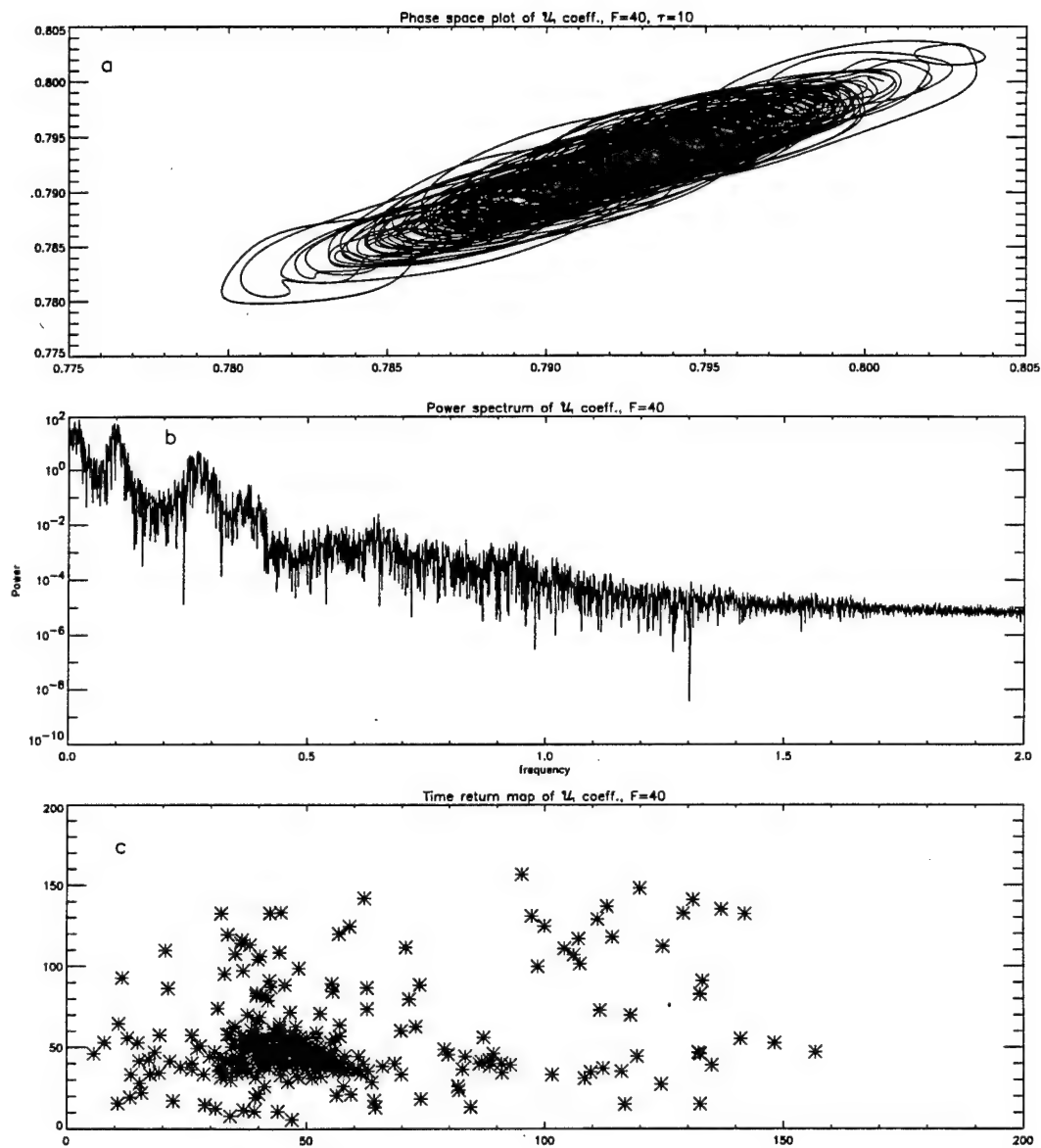


Figure 2.15.  $F = 40$ . (a) Phase-space plot of  $U_1$  coefficient vs. itself with a time delay of .078 seconds. (b) Power spectrum of the same time series. (c) Time return map constructed from  $U_1$  time series.

geostrophic turbulence, where the spatial and temporal dynamics possess self-similar power spectra over a range of scales. To ascertain this, three numerical runs were made at a resolution of 256x129:  $F = 40, 70$ , and  $100$ . The numerical results presented herein have self-similar spatial spectra at all three parameter settings and are therefore not shown. The integrated, squared streamfunction as a function of wavenumber possessed a slope of approximately  $-8$  to  $-9$ , on a log-log scale, for all cases considered, however. The temporal power spectra of the  $U_1$  coefficient at these parameter settings are shown in Figure 2.16. As  $F$  increases, the spectral peaks become broader and less apparent. At  $F = 100$ , only the dominant PAV peak, at about 0.1 frequency units, remains visible, and the power appears to decay algebraically (linear on the log-log scale used) with a slope of approximately  $-3.3$ . This agrees with the experiments of Buzyna et al. (1984), who examined the transition to geostrophic turbulence in a heated, rotating annulus. In the turbulent regime, they found both the spatial and temporal power spectra to possess self-similarity. The wavenumber spectra showed a slope ranging from  $-2.4$  to  $-4.8$ , depending on the thermal Rossby number; the frequency spectra exhibited a slope of approximately  $-4$ , which was not sensitive to parameter changes. In addition, the temporal spectra in the transition regime between ordered and turbulent flow displayed the same broadening and eventual disappearance of prominent spectral peaks as that seen in Figure 2.16.

Judging from these results, the dynamics seen just above the transition to chaos bridge the gap between perfectly ordered flow (e.g. periodic) and turbulent processes. However, there is a very rapid transition, once the flow becomes chaotic, to very complicated spatial and temporal dependence; the system does not remain on a low-dimensional (i.e. almost quasi-periodic) attractor for long. Guckenheimer and Buzyna (1983) attempted to compute attractor dimension in the geostrophic turbulence regime for the experiment alluded to above. They found no evidence for

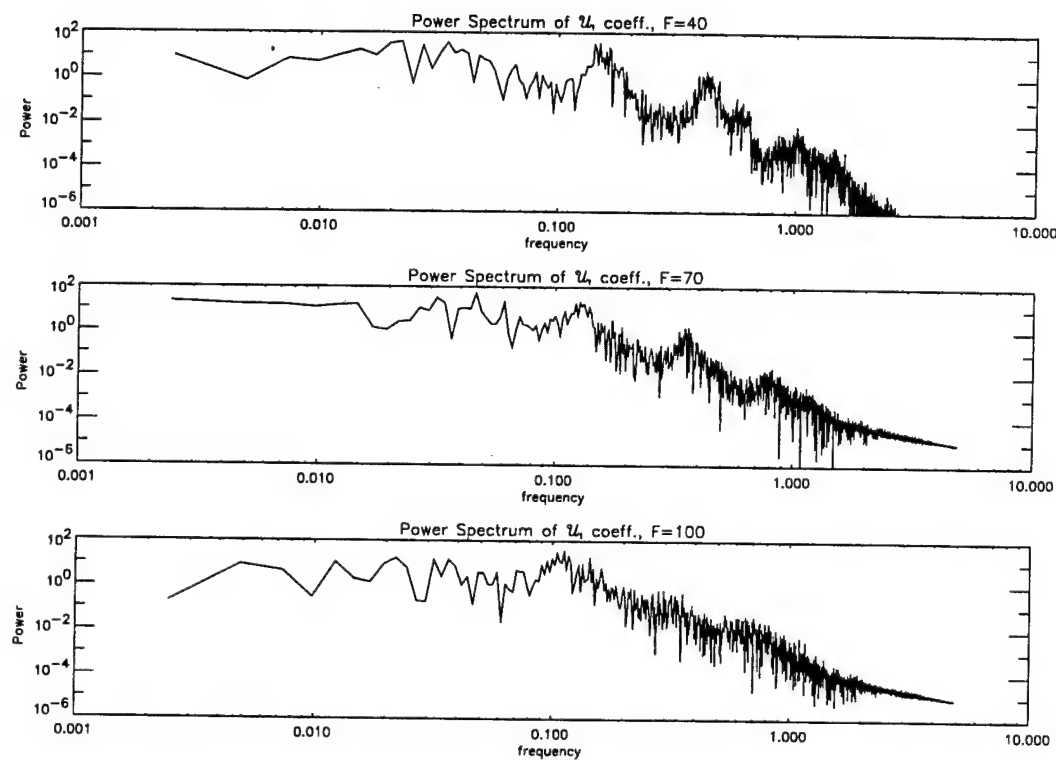


Figure 2.16: Power spectra of  $U_1$  coefficient for  $F = 40, 70$ , and  $100$ .

attractors of less than dimension 7. This result has important implications for the behavior of the actual atmosphere, which is thus presumably operating at a level of supercriticality at least comparable to that in the model presented herein.

In summary, the asymmetric regime shows more complex behavior than the symmetric state. The initial transition to the asymmetric solution occurs at  $F = 9$  in the form of PSV. At  $F = 10$ , a symmetric, baroclinic, secondary instability results in a quasi-periodic oscillation that persists until  $F = 13$ . At this point, structural vacillation, much like that seen in the symmetric state, occurs. This persists until  $F = 24$ , at which point an asymmetric, baroclinic, secondary instability interacts with the PSV oscillation to produce quasi-periodic behavior. In addition, the quasi-periodic flow is dominated by baroclinic energy transfers, in contrast to the symmetric state quasi-periodicity, which is dominated by barotropic energy transfers. Finally, for  $F \geq 30.9$ , the system becomes chaotic, and as  $F$  increases above this threshold, any evidence for evolution on a very-low-dimensional attractor disappears.

## 2.8 Discussion

The formulation and investigation of a two-layer model of baroclinic instability with fully-stress-free sidewalls has been carried out. The results show significant discrepancies with a mixed-boundary-condition model formulated by CH. The asymmetric regime shows a transition from periodic flow to quasi-periodicity to chaos. In addition, after the onset of chaos, the spatio-temporal behavior quickly becomes complicated. Numerical results at large values of  $F$  ( $\approx 100$ ) show a transition to self-similar spatial and temporal spectra, which would seem to indicate that the flow is becoming turbulent. The numerical results, which become chaotic at  $F \approx 5F_c$ , are disappointing in comparison to laboratory experiments, which show a transition to chaos at  $F \approx 1.6F_c$ .

## CHAPTER 3

### SECONDARY INSTABILITIES OF FINITE AMPLITUDE BAROCLINIC WAVES

It is of great interest to understand the regime diagram shown in Figure 2.4 from an analytical standpoint. This would aid in comprehending the transition from simple flow to more complex spatial and temporal behavior. Linear theory, however, is only capable of predicting the growth of single-wave perturbations on the zonal mean flow and is thus useless in understanding secondary instabilities such as PAV and PSV. Busse and Or (1986) and Or and Busse (1987) have had success with what will be termed a “quasi-linear” analysis. They utilized this analysis to examine secondary instabilities in convection in a rotating annulus. In the quasi-linear method, the state of the system due to the primary instability is directly calculated. The presence of secondary instabilities of this equilibrated state are then ascertained. This chapter introduces the methodology of this approach. The method is then applied to the stress-free model discussed in Chapter 2, and comparisons with those results are made.

#### 3.1 Methodology

Conceptually, the implementation of such an analysis is straightforward. In a practical sense, however, it is rather difficult, and it would be virtually impossible without a symbolic manipulator such as *Mathematica* (Wolfram, 1991). We proceed by defining the barotropic and baroclinic streamfunctions as

$$\Phi_{bt} \equiv P_1 + P_2, \quad (3.1)$$

$$\Phi_{bc} \equiv P_2 - P_1, \quad (3.2)$$

respectively (as was done previously in Equations 1.12,13), and expand them as the finite sums

$$\begin{aligned}\Phi_{bt} &= \sum_{j=1}^N \sum_{k=1}^{N-j+1} \sin(k\pi y)[A_{jk}(t) \cos(j\pi x/2) + B_{jk}(t) \sin(j\pi x/2)] + \\ &\quad \sum_{l=1}^N B'_l(t) \sin(l\pi y) + \mathcal{U}_{bt}(t)(y - 1/2),\end{aligned}\tag{3.3}$$

$$\begin{aligned}\Phi_{bc} &= \sum_{j=1}^N \sum_{k=1}^{N-j+1} \sin(k\pi y)[C_{jk}(t) \cos(j\pi x/2) + D_{jk}(t) \sin(j\pi x/2)] + \\ &\quad \sum_{l=1}^N D'_l(t) \sin(l\pi y) + \mathcal{U}_{bc}(t)(y - 1/2) + \mathcal{D}(t) + 2y.\end{aligned}\tag{3.4}$$

Then one can insert these into Equations 1.14,15 and exploit the orthogonality of the above trigonometric functions to obtain a spectral model with approximately  $2(N + 1)^2$  time-dependent coefficients (note that a triangular truncation in wavenumber space is used). Once this spectral model has been obtained, a Newton-Raphson method can be used in order to find the fixed points of the spectral equations, i.e. those values of  $A_{jk}$ ,  $B_{jk}$ ,  $D_{jk}$ ,  $D'_{jk}$ ,  $B'_l$ ,  $D'_l$ ,  $\mathcal{U}_{bc}$ ,  $\mathcal{U}_{bt}$ , and  $\mathcal{D}$  for which the time derivatives  $dA_{jk}/dt$ ,  $dB_{jk}/dt$ ,  $dC_{jk}/dt$ ,  $dD_{jk}/dt$ ,  $dB'_l/dt$ ,  $dD'_l/dt$ ,  $d\mathcal{U}_{bc}/dt$ ,  $d\mathcal{U}_{bt}/dt$ , and  $d\mathcal{D}/dt$  are identically zero. The fixed point solution yields the steady-state of the system for a given set of parameters. Once this has been obtained, one can then examine the stability of the time-independent state by considering small perturbations from equilibrium. To accomplish this, we write the total barotropic and baroclinic streamfunctions, respectively, as

$$\begin{aligned}\Phi_{bt} &= \sum_{j=1}^N \sum_{k=1}^{N-j+1} \sin(k\pi y)[(A_{jk,f} + \hat{A}_{jk}(t)) \cos(j\pi x/2) + \\ &\quad (B_{jk,f} + \hat{B}_{jk}(t)) \sin(j\pi x/2)] + \sum_{l=1}^N (B'_{l,f} + \hat{B}'_l(t)) \sin(l\pi y) + \\ &\quad (\mathcal{U}_{bt,f} + \hat{\mathcal{U}}_{bt}(t))(y - 1/2),\end{aligned}\tag{3.5}$$

$$\begin{aligned}
\Phi_{bc} = & \sum_{j=1}^N \sum_{k=1}^{N-j+1} \sin(k\pi y) [(C_{jk,f} + \hat{C}_{jk}(t)) \cos(j\pi x/2) + \\
& (D_{jk,f} + \hat{D}_{jk}(t)) \sin(j\pi x/2)] + \sum_{l=1}^N (D'_{l,f} + \hat{D}'_l(t)) \sin(l\pi y) + \\
& (\mathcal{U}_{bc,f} + \hat{\mathcal{U}}_{bc}(t))(y - 1/2) + (\mathcal{D}_f + \hat{\mathcal{D}}(t)) + 2y,
\end{aligned} \tag{3.6}$$

where the  $f$  subscript indicates those coefficients which are the fixed point values and the  $\hat{\cdot}$  symbol indicates perturbation quantities. The total streamfunctions above are defined as the sum of the steady-state streamfunctions and the perturbation streamfunctions (i.e.  $\Phi_{bt} \equiv \Phi_{bt,f} + \hat{\Phi}_{bt}$ , etc.). The expansions given by Equations 3.5 and 3.6 can then be substituted into a linearized form of Equations 1.14,15, which, after some simplification, can be written as

$$\begin{aligned}
& \partial \nabla^2 \hat{\Phi}_{bt} / \partial t - 1/2 [J(\nabla^2 \hat{\Phi}_{bt}, \Phi_{bt,f}) + J(\nabla^2 \Phi_{bt,f}, \\
& \hat{\Phi}_{bt}) + J(\nabla^2 \hat{\Phi}_{bc}, \Phi_{bc,f}) + J(\nabla^2 \Phi_{bc,f}, \hat{\Phi}_{bc})] = \\
& -Q/2[(1+\chi)\nabla^2 \hat{\Phi}_{bt} + (1-\chi)\nabla^2 \hat{\Phi}_{bc}] + E/R_o \nabla^4 \hat{\Phi}_{bt},
\end{aligned} \tag{3.7}$$

$$\begin{aligned}
& \partial / \partial t [\nabla^2 \hat{\Phi}_{bc} - 2F \hat{\Phi}_{bc}] - 1/2 [J(\nabla^2 \hat{\Phi}_{bc}, \Phi_{bt,f}) + \\
& J(\nabla^2 \Phi_{bc,f}, \hat{\Phi}_{bt}) + J(\nabla^2 \hat{\Phi}_{bt}, \Phi_{bc,f}) + \\
& J(\nabla^2 \Phi_{bt,f}, \hat{\Phi}_{bc})] - F[J(\hat{\Phi}_{bt}, \Phi_{bc,f}) + J(\Phi_{bt,f}, \hat{\Phi}_{bc})] = \\
& -Q/(2(\chi+1))[(1-\chi^2)\nabla^2 \hat{\Phi}_{bt} + (\chi^2 + 6\chi + 1)\nabla^2 \hat{\Phi}_{bc}] + \\
& E/R_o \nabla^4 \hat{\Phi}_{bc}.
\end{aligned} \tag{3.8}$$

The above equations are linear in  $\hat{\Phi}_{bt}$  and  $\hat{\Phi}_{bc}$  once  $\Phi_{bt,f}$  and  $\Phi_{bc,f}$  are known. In addition, we assume that the perturbation functions possess a structure similar to the original stream functions (see Equations 3.5,6) above, so that the perturbation equations can also be cast in terms of a spectral model. The spectral model then consists of a set of linear, constant coefficient, ordinary differential equations, and

perturbations from the steady state will then grow or decay exponentially. Thus, we can assume that each variable has a solution that is proportional to  $e^{\lambda t}$ , and the task as stated is reduced to an eigenvalue problem. Using *Mathematica*, one can solve for the spectrum of eigenvalues,  $\{\lambda_i\}$ , and their corresponding eigenvectors. This yields, respectively, the growth rates of any unstable modes as well as their spatial structure.

### 3.2 Results for Slippery Model

**3.2.1 Fixed-Point Solutions** For the set of parameters considered in this study, only a single, symmetric fixed-point solution was found; this is the same result that was found for the full numerical model presented in Chapter 2. In other words, obtaining a solution for an asymmetric set of equations resulted in the asymmetric modes having values of zero. This finding suggests that there may be no asymmetric fixed point solution, stable or unstable. Thus, in the discussion that follows, it is implied that any steady solution referred to is a symmetric steady-state.

The symmetric case is comprised of wavenumbers for which the sum of the x-wavenumber and y-wavenumber is even (i.e.  $j + k = 2, 4, 6, \dots$ , or  $l = 2, 4, 6, \dots$ ). Due to computer limitations, especially the large memory overhead that symbolic manipulations require, the largest attainable value of  $N$  in Equations 3.3,4 is  $N = 8$ , despite the fact that for the symmetric state all wavenumbers with  $j + k = 3, 5, 7, \dots$  or  $l = 1, 3, 5, \dots$  are excluded *a priori* (Or and Busse (1987) use a similar resolution). Thus, the total number of equations, which is approximately  $(N + 1)^2 = 81$ , is much fewer than the  $O(10^4)$  equations used in the full numerical model. However, as will be shown below, there is good qualitative agreement between the behavior of the full numerical model and the instabilities calculated by the analytic, quasi-linear model. This gives confidence that at least the initial instabilities of steady, finite-amplitude baroclinic waves are predicted well by a model with  $N = 8$ .

Figure 3.1 shows the steady-state, area-integrated kinetic energy vs.  $F$  for the various components of the stream functions: the baroclinic zonal and wavy portions, and the barotropic wavy portion. For all the results presented herein, the barotropic zonal kinetic energy has a steady-state value of 0, and it is therefore not plotted. The figure also displays these energies as a function of  $N$ , which is proportional to the number of modes in the system. It is evident that this energy converges fairly rapidly to some asymptotic value despite the fact that the resolution (in terms of the number of modes) is relatively small. The baroclinic wavy kinetic energy shows a lesser tendency toward convergence but still does not change drastically between  $N = 6$  and  $N = 8$ . Figure 3.2 shows the steady-state values of  $1/2$  the area-integrated, squared streamfunction for the various components listed above. For the baroclinic wavy and zonal components, this quantity is proportional (by a factor of  $F$ ) to the available wavy and zonal potential energy, respectively. As above, the barotropic zonal field has a steady-state value of zero. This quantity  $\int \Psi^2/2dA$  also shows good convergence as a function of  $N$ , with the baroclinic wavy component again the least-convergent member. Taken together, the results presented in Figures 3.1 and 3.2 indicate that a relatively modest resolution is capable of displaying a reasonably accurate steady solution of the full equations.

The quasi-linear model yields the structure of the steady-state solutions, which are primary instabilities of the zonal flow, for a chosen set of parameters. Figure 3.3 displays the steady solutions for  $F = 7, 10, 20$ , and  $30$  for the barotropic wavy mode, the baroclinic wavy mode, and the baroclinic zonal mode, respectively. The barotropic zonal mode has a steady-state amplitude that is identically zero and is therefore not plotted. The steady, barotropic, wavy field essentially remains the same over the range of Froude numbers. It resembles the lowest possible wave and the one that first becomes unstable. The baroclinic zonal field also remains essentially constant for  $7 \leq F \leq 30$  and is largely comprised of the  $(y - 1/2)$  term, as

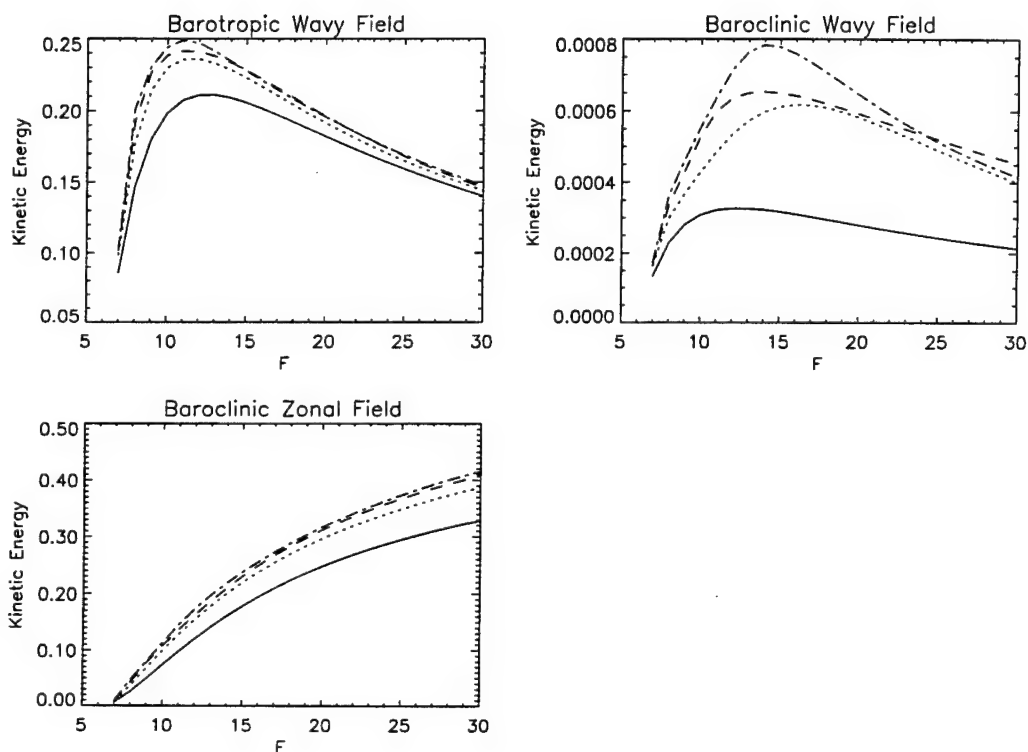


Figure 3.1. Steady-state Kinetic Energy vs.  $F$  for the barotropic and baroclinic wavy and zonal components. The solid line is for  $N=2$ , the dotted line is for  $N=4$ , the dashed line is for  $N=6$ , and the dot-dashed line is for  $N=8$ .

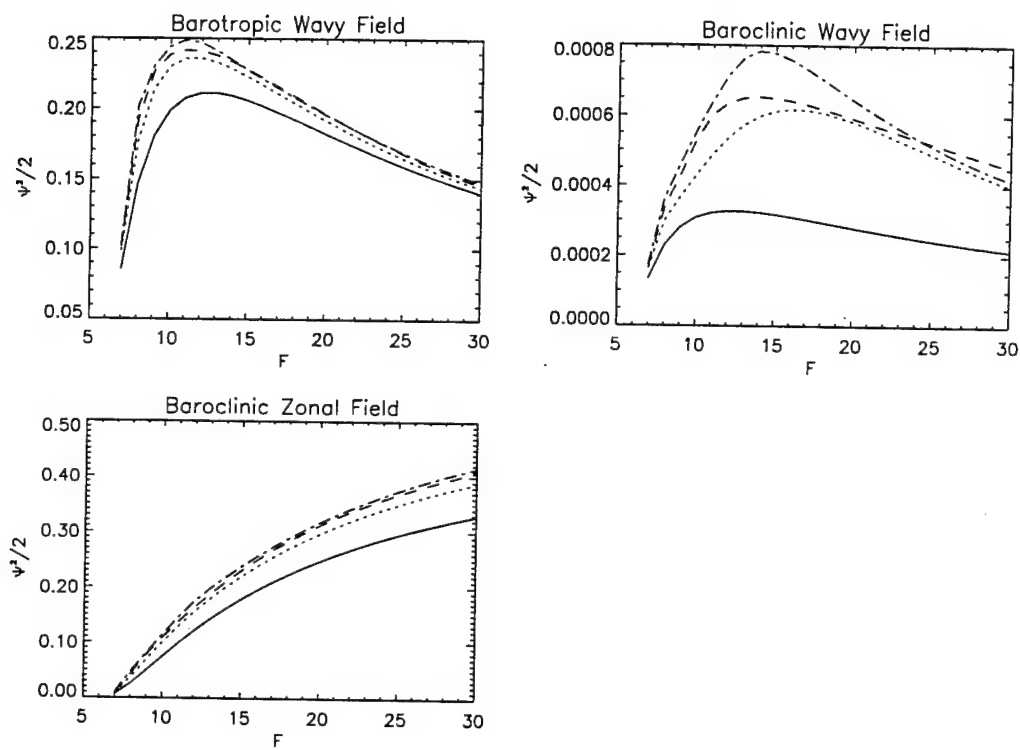


Figure 3.2. Steady-state  $\Psi^2/2$  vs.  $F$  for the barotropic and baroclinic wavy and zonal components. The line types are the same as for Figure 3.1.

can be seen from Figure 3.3. The baroclinic wavy field, on the other hand, is built from a mixture of wavenumbers, although an examination of Figure 3.4, which shows the wavenumber power spectrum of the baroclinic wavy field at  $F = 30$ , indicates that the  $j = 1, k = 1$  and  $j = 2, k = 2$  waves give the largest contributions. This result, incidentally, indicates the inherent deficiencies in single-wave models, even for modest supercriticality.

### 3.2.2 Symmetric Steady-State–Symmetric Perturbation Field

Once the nonlinear, symmetric, steady-state solutions have been found, the next task is to establish the stability of the time-independent fields as a function of  $F$  and to examine the nature of any instabilities that may occur. Perturbations can be symmetric or asymmetric in nature (see Table 2.2); this subsection considers symmetric perturbations, while the next treats asymmetric perturbations. Figure 3.5 shows the real part of the positive eigenvalues as a function of the Froude number,  $F$ , which varies from 7 to 30. The eigenvalues are all complex. Since from the previous chapter it was demonstrated that the important system transitions occur for  $F \leq 30$ , it is probably neither useful nor particularly accurate to compute eigenvalues for larger values of  $F$ . There are seven unstable modes that occur in the range  $7 \leq F \leq 30$ , as shown in Figure 3.5. The first instability occurs at  $F = 9$  and becomes stable again for  $F = 10$ . This is most probably a spurious instability, as such behavior does not occur in the numerical model (by spurious it is meant that the instability would disappear for larger  $N$ ). Nonetheless, both this instability and that at  $F = 12$  are zonoclinic, in which the barotropic zonal mode does not participate.

Although the steady-state provides a meridional shear that in turn allows for a zonotropic instability, the shear is evidently weak enough that the system is still more prone to a secondary zonoclinic instability. At  $F = 15$ , another mode becomes unstable. This is also a zonoclinic instability and is very similar to the first two. However, the structures of the growing modes appear to be dominated by

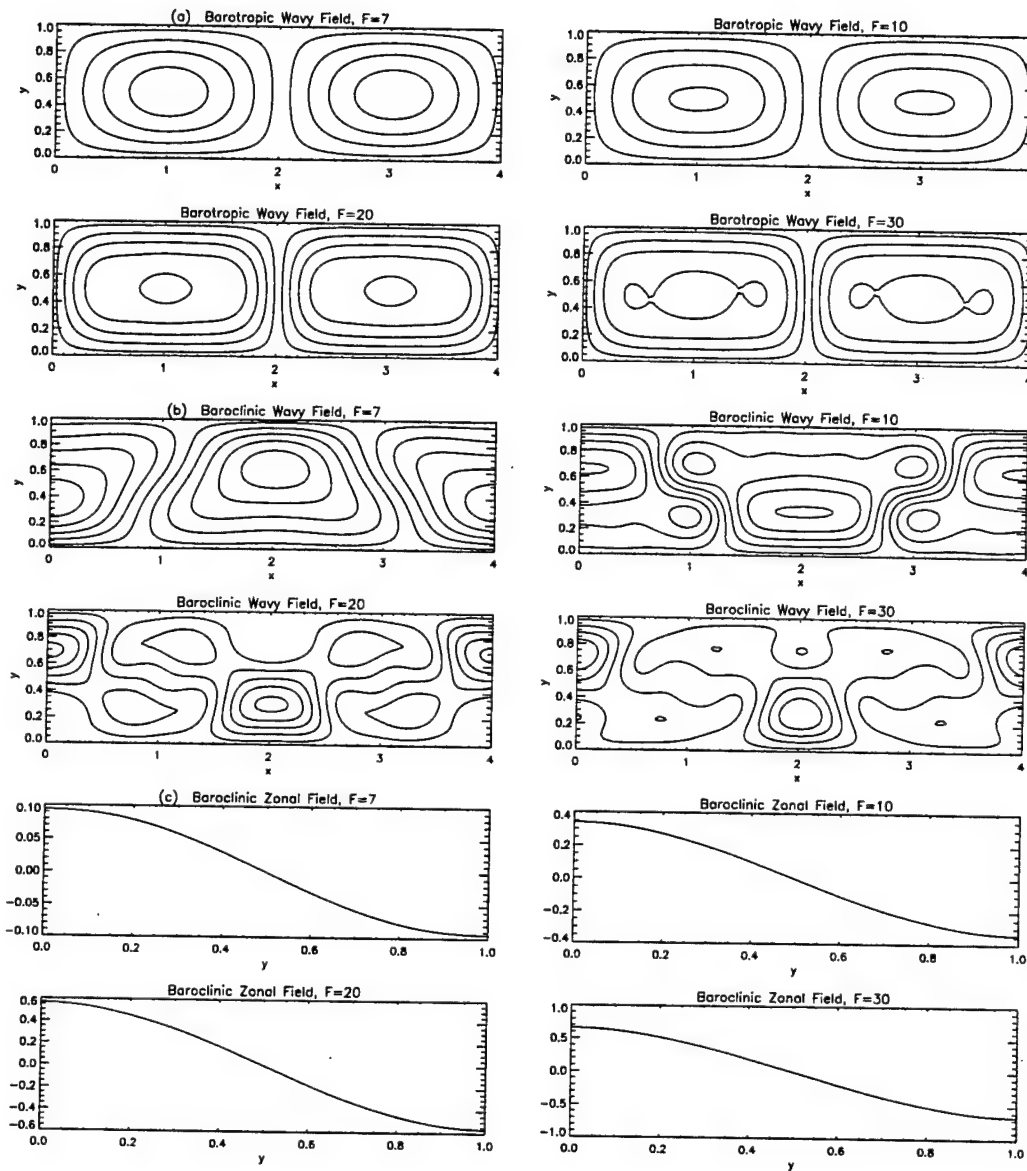


Figure 3.3. (a) Steady-state barotropic wavy streamfunctions for  $F=7$ , 10, 20, and 30. The x (zonal) and y (meridional) directions are indicated. (b) Steady-state baroclinic wavy streamfunctions for  $F=7$ , 10, 20, and 30. The x (zonal) and y (meridional) directions are indicated. (c) Cross-section of steady-state baroclinic zonal streamfunctions for  $F=7$ , 10, 20, and 30. The y (meridional) direction is indicated.

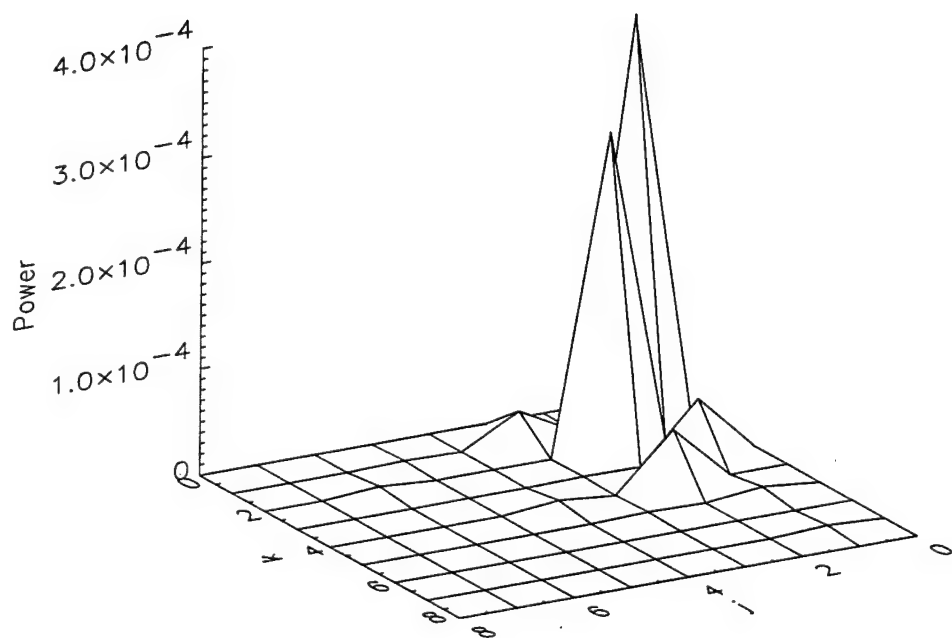


Figure 3.4. Wavenumber power spectrum for baroclinic wavy field,  $F=30$ . The spectrum is dominated by the  $j = 1, k = 1$ , and  $j = 2, k = 2$  waves.

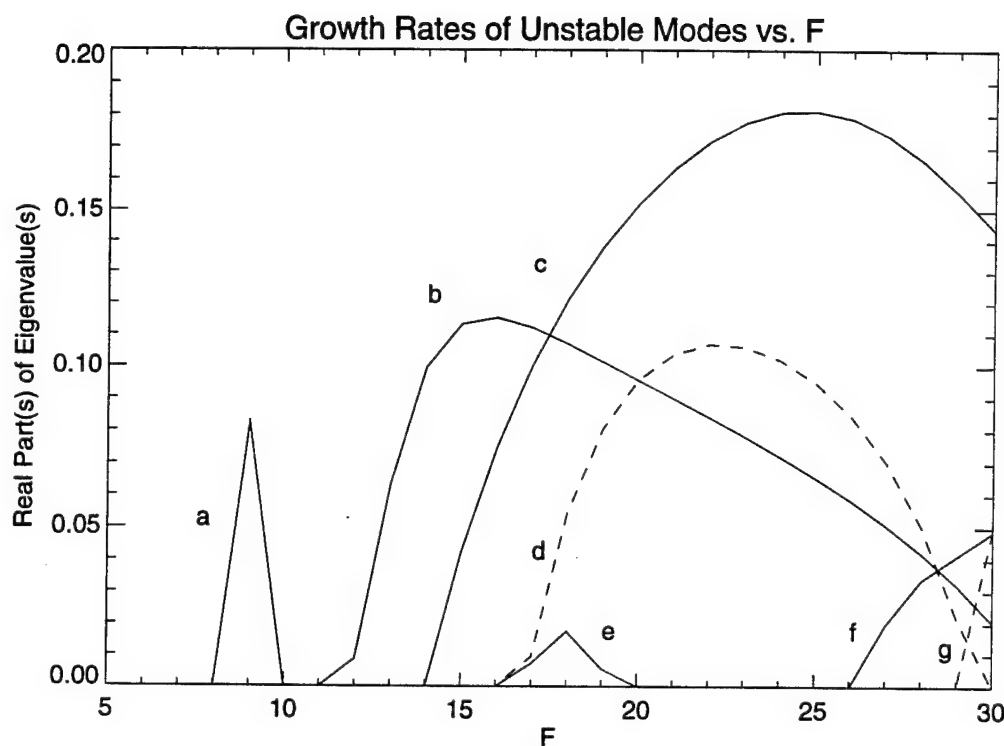


Figure 3.5. Growth rates of unstable modes as a function of  $F$  (symmetric state, symmetric perturbation field,  $7 \leq F \leq 30$ ). The solid lines indicate zonoclinic instabilities, while the dashed line signify zonotropic instabilities.

higher wavenumbers than those present in the first two instabilities. At  $F = 17$ , two more instabilities are born, one of which is short-lived. The one with the smaller growth rate (that quickly dies out) is another baroclinic instability. However, the faster-growing mode is a zonotropic instability. Finally, the instability at  $F = 27$  is another zonoclinic instability, and that at  $F = 30$  is another zonotropic instability. The instabilities are summarized in Table 3.1.

Table 3.1. Summary of instabilities for symmetric basic state, symmetric perturbations. The type and symmetry of each instability is listed as a function of the initial value of  $F$  at which the instability is born. The label column indicates the respective curve in the figure.

Label	Froude Number	Type of Instability	Symmetry
a	9	Zonoclinic	Symmetric
b	12	Zonoclinic	Symmetric
c	15	Zonoclinic	Symmetric
d	17	Zonotropic	Symmetric
e	17	Zonoclinic	Symmetric
f	27	Zonoclinic	Symmetric
g	30	Zonotropic	Symmetric

Qualitatively, the sequence of instabilities agrees with the results from the numerical model discussed in Chapter 2. Figure 2.4 shows that the symmetric state undergoes three major changes. The first change occurs between  $F = 10$  and  $F = 12$ , where the model undergoes a transition from steady flow to periodic amplitude vacillation. In the numerical model (as discussed in Chapter 2), no barotropic zonal oscillations occur in this parameter range. At about  $F = 24$ , the barotropic zonal field grows from zero and oscillates about a small, finite value. From this value of  $F$  until  $F = 36$ , the system displays PSV. At  $F = 36$ , the system becomes quasi-periodic. This agrees qualitatively with the scenario presented in Table 3.1 and Figure 3.5. The first type of instability to occur is a symmetric, zonoclinic instability. At higher supercriticality, a symmetric, zonotropic instability occurs. Following this, there is a succession of both types of instabilities at still larger values of  $F$ .

At this resolution, the growth rate of the zonotropic instability never exceeds that of the primary zonoclinic instability. This does not necessarily imply, however, that the preferred state of the system is the one with the largest growth rate. Therefore, PSV is not ruled out in the reduced model presented here. It also seems plausible, as discussed in Chapter 2, that the quasi-periodicity arises from some type of competition or mixed state between instabilities. The drawback to this analysis, of course, is that instabilities are only computed with respect to the steady state, while in the full numerical model, instabilities at higher  $F$  must occur on top of time-dependent (i.e. vacillating) states.

All of the growing modes shown in Figure 3.5 have complex eigenvalues, which implies that the modes oscillate as they grow. We can compare the frequency in the PAV regime in the full numerical model with the oscillatory frequency of the first growing mode, which occurs at  $F = 12$ . This period of vacillation in the symmetric PAV regime is approximately 8.00 nondimensional time units. From the quasi-linear model, the period is calculated to be about 8.63 nondimensional time units. Thus, the modestly-resolved, quasi-linear model appears to predict correctly the frequency of the amplitude vacillation quite well. To compare the PSV frequency, the quasi-linear frequency was obtained at two places—at  $F = 17$ , where the instability first occurs, and also at  $F = 24$ , which is where the numerical model first displays PSV. At  $F = 17$ , the oscillation period is 2.18 time units, while at  $F = 24$  it is 2.69 time units. The PSV vacillation period for the full model is 2.54 time units. Thus, there is good agreement for the PSV oscillation frequency as well.

### 3.2.3 Symmetric Steady-State—Asymmetric Perturbation Field

The other case to be considered is that of a symmetric steady-state with an asymmetric perturbation field. Because the asymmetric perturbation field requires a larger number of equations than does the symmetric case, the resolution is constrained by computer memory limitations to be  $N = 6$ , which results in approximately

$(N + 1)^2 = 49$  modes for the steady state and about  $2(N + 1)^2 = 98$  modes for the perturbations.

Figure 3.6 shows the real parts of the eigenvalues of the growing modes for  $7 \leq F \leq 30$ . Again, the eigenvalues are all complex, which results in oscillatory instabilities, but the imaginary parts are not shown. Table 3.2 summarizes the type of each instability displayed in Figure 3.6. The first instability occurs at  $F = 9$  and is a symmetric, zonoclinic instability. The disturbance is symmetric because only the symmetric wavenumbers yield a nonzero contribution to the growing modes. At  $F = 11$ , there are two more instabilities. The first unstable mode (i.e. the one that eventually achieves a larger maximum growth rate) is an asymmetric, zonoclinic instability. The second instability is an asymmetric, zonotropic instability. These instabilities are termed asymmetric because only those wavenumbers which are deemed asymmetric (i.e. the sum of the x-wavenumber and the y-wavenumber is odd) give nonzero contributions to the instability. At  $F = 20$  occurs another zonoclinic, asymmetric instability which never achieves a very large growth rate. Another pair of instabilities occurs at  $F = 24$ . The slower-growing mode is a symmetric, zonoclinic instability. The faster-growing mode is an asymmetric, zonotropic instability. At  $F = 26$ , a symmetric, zonotropic instability occurs, while yet another asymmetric, zonotropic instability comes into existence at  $F = 29$ . Finally, for  $F = 30$ , there is an asymmetric, zonoclinic instability. It is important to note that the zonotropic instability born at  $F = 24$  eventually dominates in terms of growth rate. This is in sharp contrast to the symmetric case, where the growth rate of the zonotropic instabilities never exceeds that of the largest zonoclinic instability.

Although for this case the resolution of the quasi-linear model is lower than desirable, there is nonetheless good qualitative agreement with the numerical model. From Figure 2.4, recall that the full asymmetric solution undergoes several significant transitions in behavior. For  $9 \leq F \leq 10$ , the system is governed by an asymmetric,

Table 3.2. Summary of instabilities for symmetric basic state, asymmetric perturbations. The type and symmetry of each instability is listed as a function of the initial value of  $F$  at which the instability is born. The label column indicates the respective curve in the figure.

Label	Froude Number	Type of Instability	Symmetry
a	9	Zonoclinic	Symmetric
b	11	Zonoclinic	Asymmetric
c	11	Zonotropic	Asymmetric
d	20	Zonoclinic	Asymmetric
e	24	Zonoclinic	Symmetric
f	24	Zonotropic	Asymmetric
g	26	Zonotropic	Symmetric
h	29	Zonotropic	Asymmetric
i	30	Zonoclinic	Asymmetric

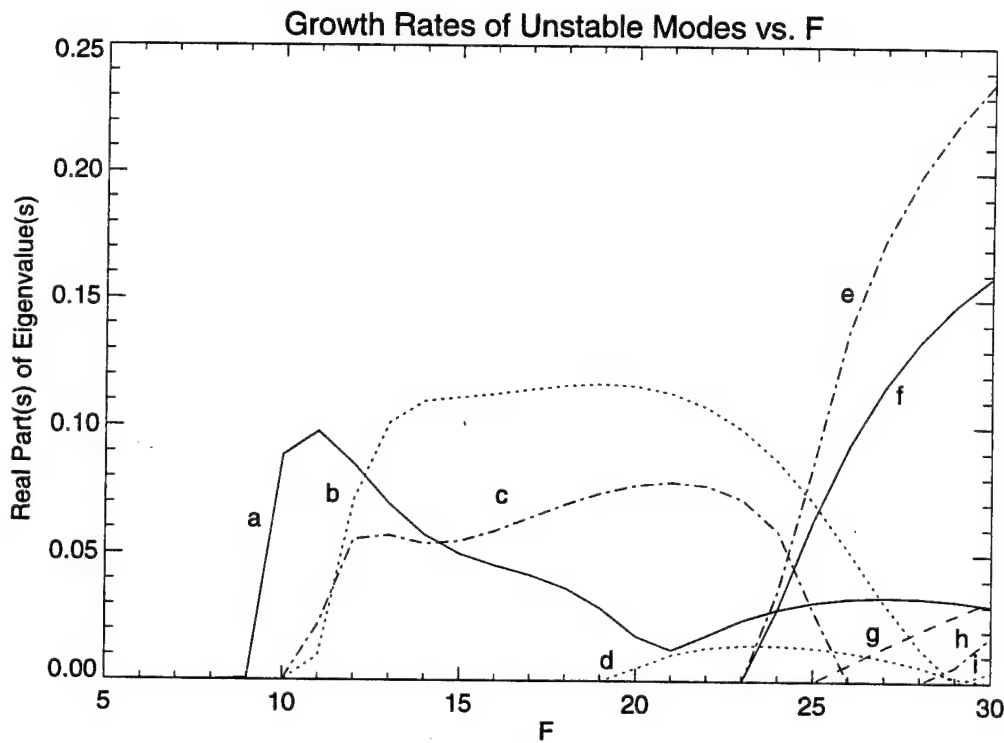


Figure 3.6. Growth rates of unstable modes as a function of  $F$  (symmetric state, asymmetric perturbation field,  $7 \leq F \leq 30$ ). The line-type legend is as follows: solid line, zonoclinic symmetric instabilities; dashed line, zonotropic symmetric instabilities; dotted line, zonoclinic asymmetric instabilities; dot-dashed line, zonotropic asymmetric instabilities.

zonoclinic instability. Then, for  $10 < F \leq 13$ , the system is quasi-periodic, with the behavior ostensibly caused by the weak interaction of the asymmetric, zonoclinic instability with a symmetric, zonoclinic instability. This behavior corresponds, with reference to the quasi-linear results, to the instabilities at  $F = 9$  and (the faster-growing one) at  $F = 11$ . Next, for  $13 < F \leq 24$ , the full model is dominated by a zonotropic instability that results in PSV. This correlates well with the emergence of the second instability at  $F = 11$ . Additionally, this instability decays by  $F = 26$ , at which point the two instabilities born at  $F = 24$  both achieve large growth rates. Note that the full model undergoes a transition to quasi-periodicity at  $F = 24$ . These secondary instability calculations again suggest that this is the result of competition between zonotropic and zonoclinic instabilities. Eventually, this interaction, possibly coupled with interaction amongst the plethora of other instabilities generated at higher values of  $F$ , likely result in the chaotic behavior found for  $F \geq 30.9$ . The quasi-linear theory, however, provides a clue to the nature of the behavior found in the full model by revealing the types of secondary instabilities that may occur in the system.

As with the symmetric state, the oscillating frequencies of the unstable modes compare favorably with the time scales inherent in the full, numerical model. At  $F = 9$ , where the full model exhibits a weak PAV phenomenon, the dominant period is approximately 7.3 time units. The unstable eigenmode that corresponds to this state is the asymmetric, zonoclinic instability born at  $F = 11$  in the quasi-linear model, and its period is about 4.4 time units. Better agreement is obtained by comparing the vacillation frequency in the more robust PSV state at  $F = 13$  with the zonotropic, asymmetric instability which is born at  $F = 11$ . The vacillation period of the  $\sin(\pi y)$  coefficient in the numerical model is about 3.8 nondimensional time units, while the quasi-linear theory yields a period of 4.8 time units at  $F = 13$ .

### 3.2.4 Spatio-Temporal Structure of Quasi-Linear Instabilities

The instabilities discussed in the previous sections have a spatial dependence that oscillates and grows with time. More specifically, one can associate one part of the instability with a  $\cos(\lambda_j t) e^{\lambda_j r t}$  term and the other portion of the instability with  $\sin(\lambda_j t) e^{\lambda_j r t}$ , where the  $r$  and  $i$  subscripts indicate, respectively, the real and imaginary parts. The superposition of these temporal functions, multiplied by their respective spatial dependence, yield the spatio-temporal behavior of the growing (and oscillating) disturbance. Additionally, one can make the two spatial functions associated with the given instability orthogonal in the sense that they have no mean projection onto each other. This is done by finding the eigenvectors of the covariance matrix of the spatial functions; the eigenvectors are then linear combinations of the original functions that are also orthogonal. The primary reason for doing this will be obvious in the next chapter, where direct comparisons are made with the empirical orthogonal functions (EOFs) of the full, nonlinear solutions, but it is nonetheless instructive to examine these orthogonal spatial instabilities at this point.

The first solution to examine is the initial symmetric, zonoclinic instability in the symmetric perturbation case, which occurs at  $F = 12$ . Figure 3.7 shows the barotropic and baroclinic wavy field orthogonal functions of the initial symmetric, zonoclinic instability in the symmetric perturbation case, which occurs at  $F = 12$ . The structures are of course not comprised of single waves, but rather are constructed from many different wavenumbers. For the structures shown in Figure 3.7, the first eigenfunction in each field accounts for about 95% of the total variance of the instability, while the second eigenfunction contributes the remaining 5%. In Figure 3.8, the eigenfunctions for the initial symmetric, zonotropic instability (which occurs at  $F = 17$ ) are displayed for  $F = 24$ . These are much different than those shown in Figure 3.7; in this case, the first eigenfunctions of each field possess only about 60% of the total variance. In addition, the spatial eigenfunctions themselves are

rather complicated. This is of great consequence and will be discussed in detail in Chapter 4, but for now it is sufficient to note that this result is consistent with the observation of counter-rotating eddies observed in the PSV regime (which is associated with the onset of a zonotropic instability). The eigenfunctions for the initial zonotropic asymmetric instability (which occurs at  $F = 11$ ) are displayed at  $F = 16$  in Figure 3.9. In this situation, the first barotropic eigenfunction accounts for 82% of the total variance, while the first baroclinic eigenfunction accounts for about 63% of its total variance. The primary eigenfunctions are both dominated by a wavenumber-2 disturbance, while the secondary eigenfunctions are rather more convoluted.

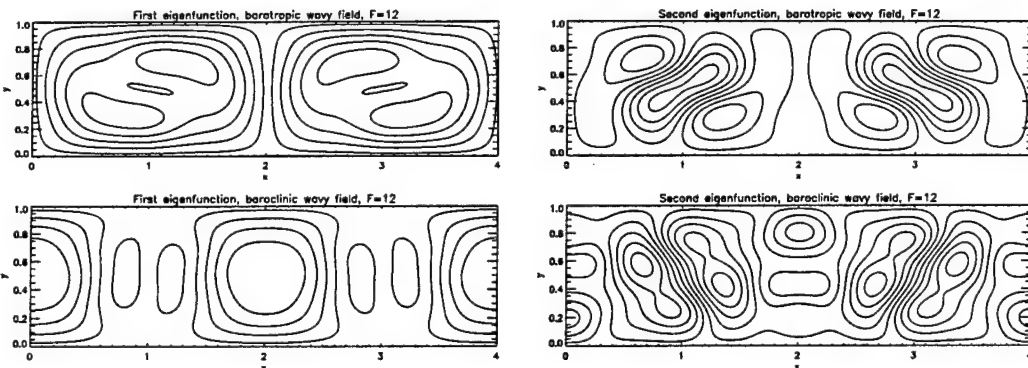


Figure 3.7. Eigenfunctions of barotropic and baroclinic wavy fields,  $F=12$ , symmetric case

**3.2.5 Relating Fixed-Point Solutions to Mean Quantities** During the course of this investigation, it was observed that the time-averaged (hereafter denoted as “mean”) quantities in the numerical model seem to be very closely related to the fixed point solutions from the quasi-linear analysis, both in magnitude and spatial structure. For instance, Figure 3.10 compares mean kinetic energies (from the results presented in Chapter 2) versus fixed-point kinetic energies for the barotropic wavy component, the baroclinic wavy component, and also for the baroclinic zonal

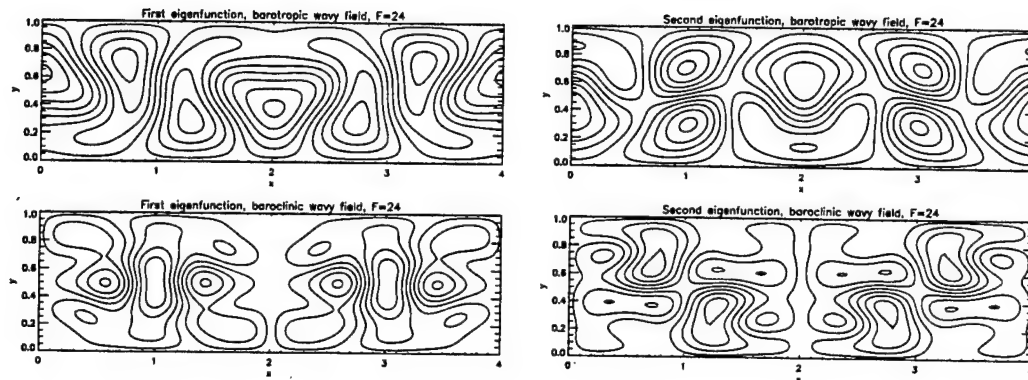


Figure 3.8. Eigenfunctions of barotropic and baroclinic wavy fields,  $F=24$ , symmetric case

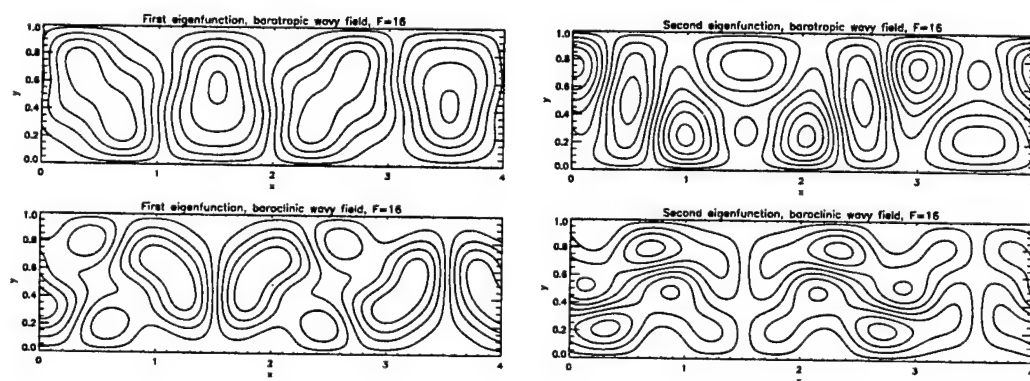


Figure 3.9. Eigenfunctions of barotropic and baroclinic wavy fields,  $F=16$ , asymmetric case

component. The mean barotropic zonal component has a fixed-point value of 0 for all  $F$  and is not shown. Nonetheless, there is very good agreement between the two quantities (i.e. mean fields versus steady-state fields) with the exception of the baroclinic wavy energy. However, this is a small quantity, and the nature of the discrepancy will hopefully be elucidated below.

If the barotropic and baroclinic fields are written as follows,

$$\Phi_{bt}(x, y, t) = \phi_{bt,mean}(x, y) + \phi_{bt}(x, y, t) \quad (3.9)$$

$$\Phi_{bc}(x, y, t) = \phi_{bc,mean}(x, y) + \phi_{bc}(x, y, t), \quad (3.10)$$

(i.e. the total field is written as the sum of a mean part, which is not a function of time, and a fluctuating, time-dependent portion), and if these expansions are then substituted into the governing equations, Eqns. 1.14,15, the resulting equations would describe the time evolution of  $\phi_{bt}$  and  $\phi_{bc}$ . In addition, there would be nonlinear terms of three types: those involving two mean quantities, those involving a mean quantity with a perturbation quantity, and those involving two perturbation quantities. If the system were such that  $\|\phi_{bt,mean}(x, y)\| \gg \|\phi_{bt}(x, y, t)\|$  and  $\|\phi_{bc,mean}(x, y)\| \gg \|\phi_{bc}(x, y, t)\|$ , where  $\|f\|$  indicates some suitable norm such as  $(\iint f^2 dx dy)^{1/2}$ , then one could neglect, to a first approximation, any term containing a perturbation quantity. What would remain, then, would be equations that balance nonlinear interactions of the mean quantities with dissipation of mean quantities. By definition, then, the mean fields would be the steady-state solutions of the equations.

This seems to be the scenario that occurs in this model. Tables 3.3,4 show, for the symmetric and asymmetric solutions, respectively, the ratio of the mean kinetic energies for the various zonal and wavy components to the standard deviations of the actual kinetic energies. When this ratio is large, the scenario hypothesized

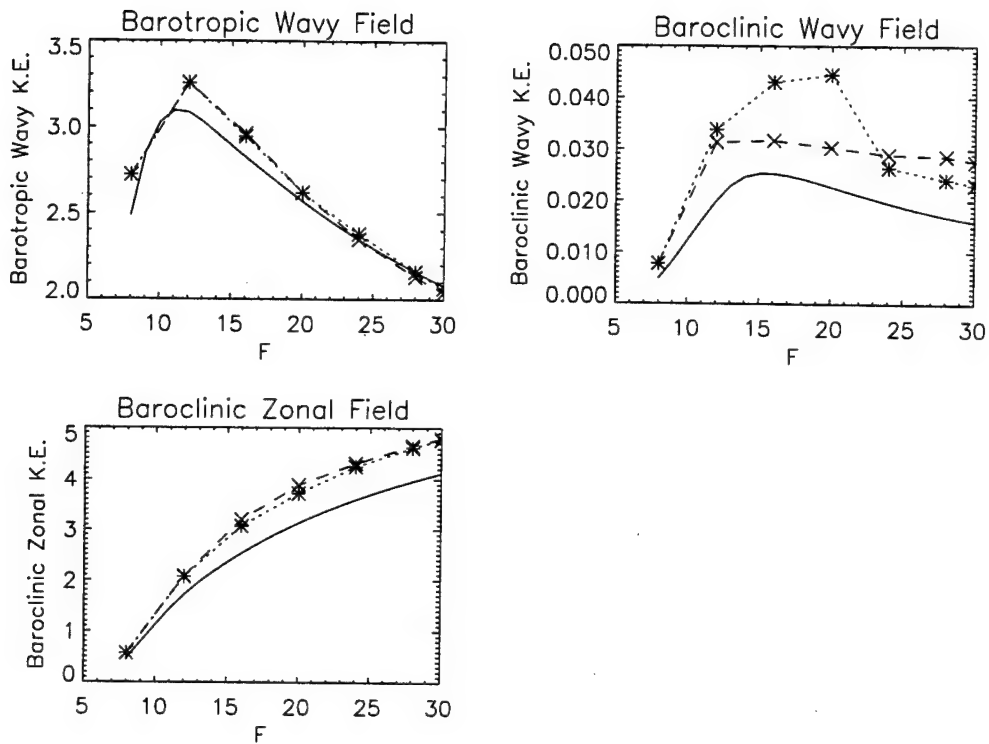


Figure 3.10. Comparison of mean and steady kinetic energies of barotropic wavy component, baroclinic wavy component, and baroclinic zonal component. The solid line indicates the steady values, the dotted line and asterisks indicate the symmetric state means, and the dashed line and X's indicate the asymmetric state means.

Table 3.3. Ratio of means to rms deviations for kinetic energy quantities of the various wavy and zonal portions of the stream function (symmetric solution)

F	Barotropic wavy	Baroclinic Wavy	Baroclinic Zonal
12	9.70	2.51	16.0
20	4.70	1.73	10.4
28	445	20.4	4650

Table 3.4. Ratio of means to rms deviations for kinetic energy quantities of the various wavy and zonal portions of the stream function (asymmetric solution)

F	Barotropic wavy	Baroclinic Wavy	Baroclinic Zonal
12	12.2	3.25	20.1
20	729	10.3	1890
28	12.1	4.49	35.2

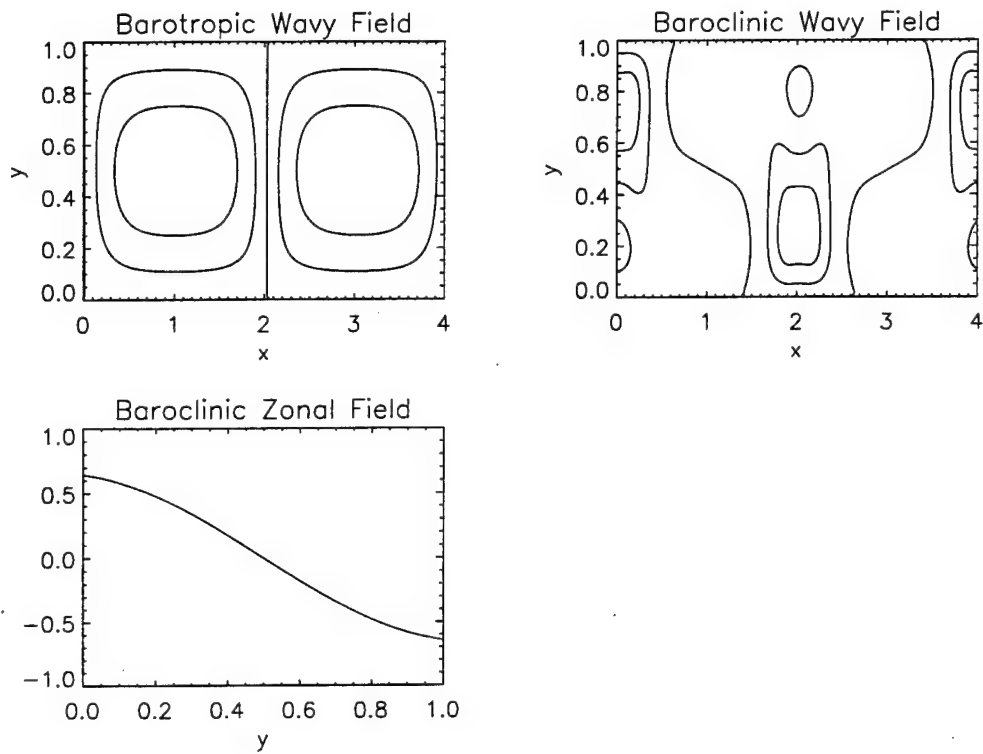


Figure 3.11: Mean fields at  $F = 20$  for symmetric solution

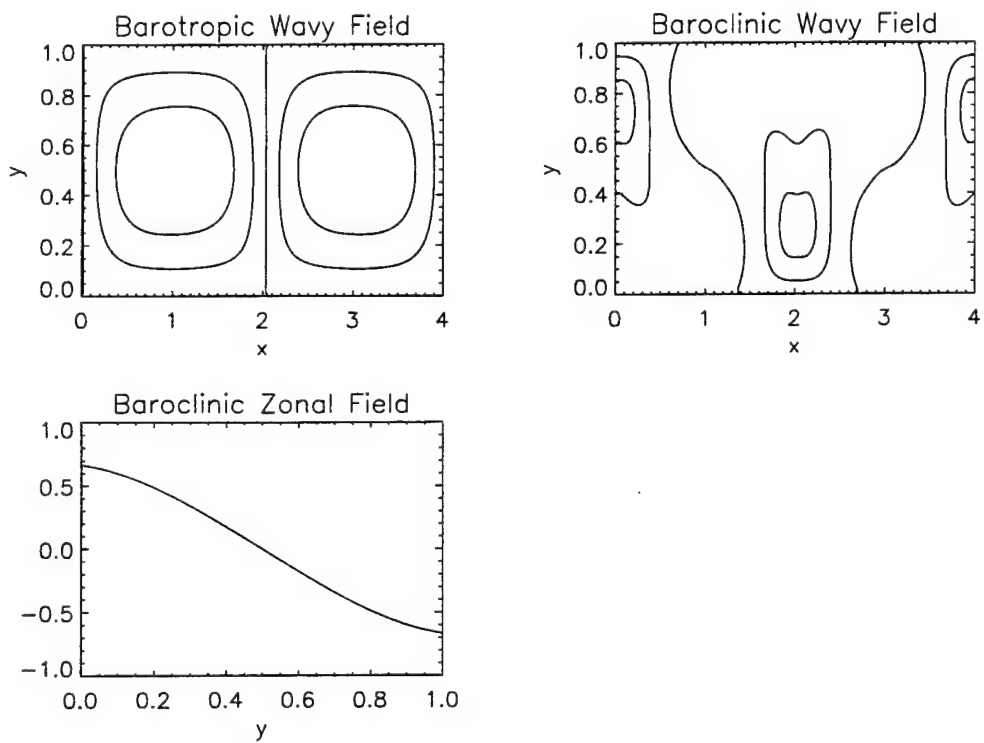


Figure 3.12: Mean fields at  $F = 20$  for asymmetric solution

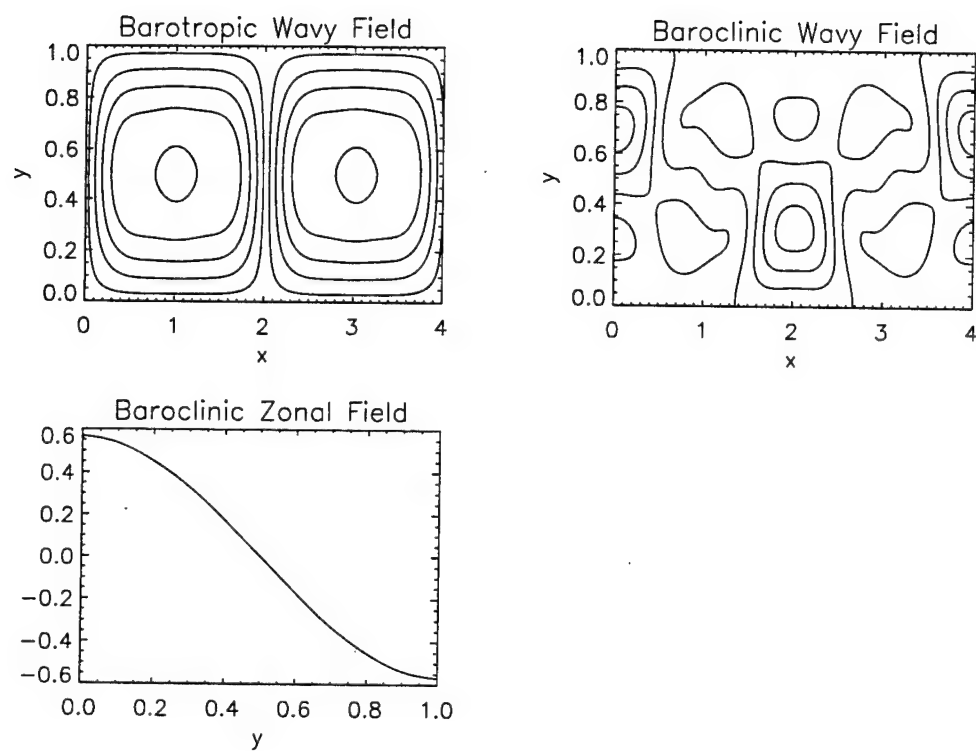


Figure 3.13: Steady-state fields at  $F = 20$

above holds to a rough approximation. When the ratio becomes  $O(1)$ , the concept breaks down and one cannot necessarily expect the mean energies to reflect the steady-state values. Note that the ratio for the baroclinic wavy component is often close to unity. This partially explains the discrepancies in Figure 3.10, although the differences in the baroclinic zonal kinetic energy, for example, cannot be explained by this phenomenon. Finally, it is interesting to note the correlation in spatial structure between the mean and steady-state quantities. Contour plots of the mean streamfields at  $F = 20$  are displayed in Figure 3.11 for the symmetric solution and in Figure 3.12 for the asymmetric solution. These should be compared to the output of the analytical model, which is displayed in Figure 3.13. There is good agreement in the spatial structure of the streamfunctions, despite the fact that there are noticeable differences in the magnitudes of the fields. Although this is an *a posteriori* explanation of the situation, it nonetheless indicates that the particular, steady-state low-order model presented here can predict the mean states of the highly-resolved numerical model with good accuracy.

### 3.3 Discussion

By utilizing a quasi-linear model, where the steady solution of the full set of nonlinear equations is first obtained, followed by an analysis of the stability of this steady state, the limited predictions made by classical linear instability theory can be extended. Due to computer limitations, our quasi-linear approach is limited to approximately  $O(10^2)$  degrees of freedom. However, the kinetic and potential energies show convergent properties even for this modestly-resolved system, allowing successful comparisons with the full numerical results.

For the steady solutions, the barotropic wavy and baroclinic zonal components are comprised largely of single wavenumber pairs even for large supercriticality. In contrast, the baroclinic wavy field is represented by many different wave numbers,

which likely explains the inability of single-wave models to predict the experimental behavior of the two-layer system. Despite its relative complexity, though, the steady baroclinic wavy field has an approximately-constant shape for  $10 \leq F \leq 30$ .

When a symmetric perturbation field is applied to the steady-state solution, the resulting instabilities qualitatively agree with the results found in the highly-resolved numerical model. In the quasi-linear model, the first instability is zonoclinic, which is later followed by a zonotropic instability. This agrees with the numerical results. In addition, the oscillatory frequency of both the zonoclinic and zonotropic disturbances correspond very well to the dominant frequencies in the PAV and PSV regimes, respectively, of the numerical model, thus suggesting that the PAV and PSV oscillations have their origin as instabilities of the nonlinear steady waves.

For an asymmetric perturbation field, the secondary bifurcations also agree with the regime diagram of the full numerical code. The initial instability is zonoclinic and is later followed by a zonotropic instability. The predicted oscillatory frequency in the PSV regime is well predicted by the quasi-linear model.

Due to the fact that the barotropic wavy and baroclinic zonal mean (i.e. time-averaged) fields are much larger than the corresponding fluctuating quantities, the mean quantities are good approximations to the fixed-point values, both in amplitude and spatial structure. Although the mean baroclinic wavy field does not agree as well in amplitude with its steady-state value, the spatial structure is very similar. This suggests that the steady-state quantities can be deduced to some extent simply by extracting the mean quantities from the numerical model, and vice versa. Unfortunately, this is not an *a priori* deduction but rather an *a posteriori* observation.

## CHAPTER 4

### EOF ANALYSES

This chapter first introduces the concept of empirical orthogonal functions (hereafter denoted as EOFs) and explains their value in studying the models presented herein. EOFs are then computed for the full numerical solutions found in Chapter 2, and the results of these computations are discussed. Next, EOFs are used to construct low-order dynamical systems, and their resulting behavior is compared to the full solutions. Finally, the correspondence between the eigenfunctions of secondary instabilities (discussed in Chapter 3) and the EOFs themselves is investigated.

#### 4.1 Definitions and Preliminary Remarks

The concept of utilizing EOFs as an analytical tool dates back well over a century (see Priesendorfer (1988) for a brief historical overview). The technique is also referred to as Principal Component Analysis (PCA) (Priesendorfer, 1988) and Proper Orthogonal Decomposition (POD) (Lumley, 1970), and the various naming conventions will be considered identical for this discussion. The modern form of the methodology is based on the Karhunen-Loeve (KL) procedure (Loeve, 1955).

The crux of the KL procedure, which directly produces the EOFs, can be summarily described as follows. Given some field  $\Phi$ , which is a function of space,  $\vec{x}$ , and time,  $t$ , one can write the unknown function  $\Phi$  as

$$\Phi(\vec{x}, t) = \sum_{i=1}^N a_i(t) \phi_i(\vec{x}), \quad (4.1)$$

where  $N$  may be arbitrarily large in order that  $\Phi$  is faithfully reproduced. In addition,

for any particular value of  $N$ , denoted by  $\hat{N}$ , we desire the discrepancy between the original field and the approximation obtained by including  $\hat{N}$  modes to be as small as possible. In essence, then, the KL procedure optimally compresses the information contained in  $\Phi(\vec{x}, t)$ , thus yielding a measure of the complexity of the original field.

The relatively recent discovery of chaos, and its possible link to fluid turbulence, has resulted in strong interest in utilizing the KL procedure to analyze and characterize fluid flows, although Lumley (1967) actually advocated the procedure over two decades ago for analyzing turbulence. A plethora of examples has appeared in recent literature. Sirovich and Rodriguez (1987) and Rodriguez and Sirovich (1990) utilized the method in order to investigate solutions to the Ginzburg-Landau equation, a one-dimensional PDE. Sirovich (1989) and Deane and Sirovich (1991) also used the technique to analyze data from a numerical model of Rayleigh-Benard convection, while Sirovich et al. (1990b) exploited the KL procedure to study coherent structures in turbulent channel flow. While all of the the above references utilized numerical data in order to extract the EOFs, there have been studies involving experimental data as well. Aubry et al. (1988, 1989) exploited the KL procedure to study turbulent boundary layers near a wall by utilizing experimental data; and Sirovich et al. (1990a) used experimentally-obtained data to extract EOFs from a jet flow. Finally, Deane et al. (1991) applied the methodology to irregular flow domains by considering both the flow around a cylinder and also flow in a periodically grooved channel.

#### 4.2 Methodology of Obtaining EOFs

The following derivation of the method follows Priesendorfer (1988) and is a relatively non-mathematical treatment. Consider a field  $\Phi(t, x)$  that is a function of one space variable,  $x$ , and time,  $t$ . The one-dimensional formulation in space is done only for ease of understanding, and the following analysis can be generalized

by making space a vector field. Additionally, in order to formulate the problem in matrix form, both time and space will be considered discrete, i.e.  $x = 1, \dots, p$ ,  $t = 1, \dots, n$ , so that  $\Phi(t, x)$  is now represented as an  $n \times p$  matrix, denoted as  $\Phi$ . It is also assumed that at any value of  $x$ , the temporal mean, given by

$$\bar{\Phi}(x) = \sum_{t=1}^N \Phi(t, x), \quad (4.2)$$

is zero. Denoting the set of spatial values at any given time,  $t$ , by the  $px1$ -dimensional matrix  $\phi(t) = [\phi(1), \dots, \phi(p)]^T$ , one can define the projection of  $\phi(t)$  onto some arbitrary  $p \times 1$ -dimensional matrix,  $\mathbf{e} = [e(1), \dots, e(p)]^T$ , as

$$(\phi, \mathbf{e}) = \phi^T(t)\mathbf{e} = \mathbf{e}^T\phi(t) = \sum_{x=1}^p \Phi(x, t)e(x), \quad (4.3)$$

where  $\mathbf{e}$  is normalized so that  $\mathbf{e}^T\mathbf{e} = 1$ . A scalar function of the vector  $\mathbf{e}$ , called  $\Psi(\mathbf{e})$ , is now defined as

$$\Psi(\mathbf{e}) = \sum_{t=1}^n [\phi^T(t)\mathbf{e}]^2 = \sum_{t=1}^n [\mathbf{e}^T\phi(t)] [\phi^T(t)\mathbf{e}], \quad (4.4)$$

which can be rewritten as

$$\Psi(\mathbf{e}) = \mathbf{e}^T \left[ \sum_{t=1}^n \phi(t)\phi^T(t) \right] \mathbf{e}. \quad (4.5)$$

When scaled by a factor of  $n^{-1}$ ,  $\Psi(\mathbf{e})$  simply measures the mean projection of  $\Phi(x, t)$  onto  $\mathbf{e}$ , or how well  $\mathbf{e}$  is “aligned” with the data in  $\Phi$ . Finally, if one defines the  $pxp$  scatter matrix (which is actually a covariance matrix),  $\mathbf{S}$ , as

$$\mathbf{S} = \sum_{t=1}^n \phi(t)\phi^T(t) = \Phi^T\Phi, \quad (4.6)$$

Equation 4.5 can be written as

$$\Psi(\mathbf{e}) = \mathbf{e}^T \mathbf{S} \mathbf{e}. \quad (4.7)$$

Note that  $\mathbf{S}$  is a symmetric matrix, and  $S_{ij}$  measures the temporal covariance between the  $i$ th and  $j$ th spatial points.

To complete the procedure, we now wish to find the values of  $\mathbf{e}$  for which  $\Psi(\mathbf{e})$  has local extrema. This determines those values of  $\mathbf{e}$  along which  $\Phi$  tends to be oriented. After several steps, it can be shown that the determination of these special values of  $\mathbf{e}$  is reduced to an eigenvalue problem, i.e.

$$\mathbf{S} \mathbf{e} = \lambda \mathbf{e}. \quad (4.8)$$

Thus one obtains a hierarchy of eigenvectors and corresponding eigenvalues, each set of which satisfies the extrema requirement. In addition, it can be shown that the eigenvectors are orthogonal to each other, i.e.  $\mathbf{e}_j^T \mathbf{e}_k = \delta_{jk}$ , where  $\delta_{jk}$  is the Kronecker delta. If one orders the eigenvalues such that  $\lambda_1 \geq \lambda_2 \geq \dots \geq \lambda_p \geq 0$ , then the following interpretation can be made:  $\mathbf{e}_1$  is the direction along which  $\Psi$  is maximized;  $\mathbf{e}_2$  is the direction along which  $\Psi$  is maximized, given that  $\mathbf{e}_2$  is orthogonal to  $\mathbf{e}_1$ ;  $\mathbf{e}_3$  is the direction along which  $\Psi$  is maximized, with the stipulation that  $\mathbf{e}_3$  is orthogonal to both  $\mathbf{e}_1$  and  $\mathbf{e}_2$ ; etc.

The data matrix  $\Phi$  can now be written in terms of the new basis defined by the  $\mathbf{e}_j$ , which can be written in matrix form as  $\mathbf{E} \equiv [\mathbf{e}_1 \dots \mathbf{e}_p]$ . Thus, we write

$$\Phi = \mathbf{A} \mathbf{E}^T, \quad (4.9)$$

where  $\mathbf{A} \equiv [\mathbf{a}_1 \dots \mathbf{a}_p]$  is an as-yet-undefined amplitude matrix. In order to find  $\mathbf{A}$ , one can post-multiply Equation 4.9 by  $\mathbf{E}$ , which, after noting that  $\mathbf{E}^T \mathbf{E} = \mathbf{I}$  (the

identity matrix), can be simplified to yield

$$\mathbf{A} = \Phi \mathbf{E}. \quad (4.10)$$

Thus, the original field can now be completely expanded in terms of the new basis functions and amplitudes as

$$\Phi(t, x) = \sum_{j=1}^p a_j(t) e_j(x), \quad (4.11)$$

where  $t = 1, \dots, n$  and  $x = 1, \dots, p$ . The KL procedure can be thought of as rotating the data set such that it lies along a new coordinate system, where the axes of the new coordinate system are given by the eigenvectors, and the projection of  $\Phi$  onto these new axes is represented as amplitude coefficients.

There are other interesting features of the KL procedure that merit some brief attention. First, if one regards the quantity  $\Phi^2$  as representing an “energy”, then by the following relation,

$$\sum_{x=1}^p \sum_{t=1}^n \Phi^2(t, x) = \sum_{k=1}^p \lambda_k, \quad (4.12)$$

so that the time- and space-integrated “energy” is simply the sum of the eigenvalues. A related interpretation states that the average percentage of energy possessed by the  $j$ th eigenfunction is  $\lambda_j / (\lambda_1 + \dots + \lambda_p)$  (Rodriguez and Sirovich, 1990). Additionally, if one approximates the rotated system given by Equation 4.11 with  $m$  modes, with  $m < p$ , such that

$$\Phi(t, x) \approx \Phi_m(t, x) = \sum_{j=1}^m a_j(t) e_j(x), \quad (4.13)$$

then the error between  $\Phi$  and  $\Phi_m$  is a minimum for that value of  $m$ . More specifically, denoting the error as

$$\epsilon_m = \langle \|\Phi - \Phi_m\|^2 \rangle, \quad (4.14)$$

where

$$\|f^2\| \equiv \sum_{x=1}^p f^2(t, x) \quad (4.15)$$

and  $\langle \rangle$  denotes an average over the time variable, this error is a minimum for any  $m$ . Equivalently, the  $m$  eigenfunctions approximate as closely as possible (based on the norm presented in Equation 4.15) the original field,  $\Phi$  (Sirovich et al., 1990a). Sirovich (1991) has also shown that the representational entropy is also minimized for any  $m$  if one uses the EOFs as the basis set, as is shown in Equation 4.13.

### 4.3 Approximate Dynamical Systems

Typically, partial differential equations are solved by using a finite grid in the spatial domain and/or treating the spatial dependence as a sum of Fourier (or similar) modes. Moreover, the number of grid points or modes, which measures the number of degrees of freedom of the system, is often large—the slippery model possesses about  $10^4$  degrees of freedom. This is at odds, however, with the temporal behavior of the flow, which exhibits periodic, quasi-periodic, and chaotic (i.e. weakly turbulent) behavior. Taken together, these two observations indicate that most of the spatial modes must be slaved to one another, so that there are effectively many fewer degrees of freedom in the flow than an estimate based on the number of grid points would indicate. In turn, this implies that it may be possible to formulate a system that exploits the slaving of variables and is thus lower-dimensional than, but (approximately) equivalent to, the original system.

Sirovich (1989) discusses a systematic method for executing the above procedure, which is in effect a modified Galerkin method that utilizes the EOFs as basis functions. First, denote the governing equations of some dynamical system by

$$\frac{\partial \vec{v}}{\partial t} = \vec{F}(\vec{v}), \quad (4.16)$$

where  $\vec{v}$  is the dependent variable and  $\vec{F}$  is some operator particular to the exact equations under consideration (cf. Equation 1.3). If one then utilizes some subset of the KL eigenfunctions and projects  $\vec{v}$  onto this subset, one obtains

$$\vec{v}_N = P_N \vec{v} = \sum_{j=1}^N a_j(t) \mathbf{e}_j, \quad (4.17)$$

where  $P_N$  is a projection operator and  $N$  is some integer whose value will be discussed below. The intent is to approximate  $\vec{v}$  with some small error by expanding it in terms of the empirical eigenfunctions. After doing this, one substitutes the expansion given by Equation 4.17 into Equation 4.16 and projects the resulting equation onto the empirical eigenfunctions themselves, i.e.

$$\left( \mathbf{e}_j, \frac{\partial}{\partial t} \vec{v}_N - \vec{F}(\vec{v}_N) \right) = 0, \quad j = 1, \dots, N, \quad (4.18)$$

where the  $( \cdot, \cdot )$  indicates the projection function (or an inner product) defined by Equation 4.3. The result is a system of  $N$  ordinary differential equations for the  $a_j(t)$  denoted by

$$\frac{d\vec{a}}{dt} = \vec{G}(\vec{a}), \quad (4.19)$$

where  $\vec{a}$  is the approximate state vector ( $\vec{a} = (a_1, \dots, a_N)$ ). Thus, by utilizing the empirical orthogonal functions, one can reduce one or more partial differential equations

into a set of ordinary differential equations of order  $N$ , where  $N$  is possibly much smaller than the state space of the original PDEs. A methodology is now needed for choosing an adequate value of  $N$  such that the approximate dynamical system given by Equation 4.19 mimics the behavior of the original equations. Rodriguez and Sirovich (1990) invoke an *ad hoc* rule, demanding that  $N$  be chosen such that

$$\sum_{j=1}^N \lambda_j / \sum_{i=1}^p \lambda_i > .99, \quad (4.20)$$

so that the retained eigenfunctions capture, on average, at least 99% of the energy of the flow. This criterion will, in general, also be adopted for the analyses presented herein.

#### 4.4 Practical Considerations

The field  $\Phi(t, x)$  must in practice be represented by an  $n \times p$  matrix, where  $n$  is the temporal index and  $p$  is the spatial index. Typically, the number of spatial points is very large, with  $p$  ranging from  $O(10^3)$  to  $O(10^4)$ . Since the spatial index is so large, computational limits put constraints on the maximum allowable value of  $n$ . On the other hand, the number of nonzero eigenvalues obtainable from an  $n \times p$  matrix is  $\min(n, p)$ , so that if  $n < p$ , the eigenfunctions do not form a complete basis for  $\Phi(t, x)$ . These two facts would seem to render the KL procedure impotent for systems with large values of  $p$ . However, Sirovich (1987) has alleviated this problem by introducing the **method of snapshots**. In essence, the method simply consists of taking a large enough number of temporal samples (at all the spatial points) such that the spectrum of eigenvalues is convergent. For systems that exhibit relatively low-dimensional behavior, the number of snapshots,  $n$ , need only be large enough such that  $n \gg N$ , where  $N$  is given by Equation 4.20 and gives a measure of the speed at which the eigenvalues approach zero (and hence, by conjecture, a relative measure of the dimension of the system). For the models considered herein, a value

of  $n$  of  $O(10^2)$  has proven to be sufficient, and the resulting matrix dimensions of  $O(10^2) \times O(10^3 - 10^4)$  are easily manageable by current computing standards.

The other consideration is that of when to obtain the temporal snapshots. For a system exhibiting chaotic behavior, Rodriguez and Sirovich (1990) advocate using snapshots obtained at uncorrelated times, which ensures that the information contained within a given ensemble of snapshots is maximized. A more general criterion is that one would like to have a representative sample of all the different states the system can assume. Thus, for periodic behavior, it is only necessary to sample over one period of the flow. For quasi-periodic and chaotic flows, sampling at uncorrelated times is probably a near-optimal strategy, as it ensures capturing the flow at many locations on the attractor.

#### 4.5 The Relationship Between Spatial and Temporal Complexity

One question largely left unanswered in the literature is the relationship between the number of EOFs required to represent a flow and the spatio-temporal complexity of that flow. In other words, it is not clear how the spatial and temporal portions of the system interact to affect, and effect, the EOF spectrum. To understand this phenomenon, a simple model has been formulated and examined; the results of this are discussed in detail in Appendix G. The main conclusion drawn from this analysis is that the EOF spectrum depends directly on the spatio-temporal coupling of the field. If either the spatial complexity or the temporal complexity is small (e.g. the temporal field is steady or varies sinusoidally), then the number of EOFs necessary to capture the spatio-temporal variability is also small. The requirement of a large number of temporal-spatial modes is the result of the interaction of the two domains. This conclusion will be borne out in the results presented below.

## 4.6 Results for Slippery Model

**4.6.1 Symmetric Case** As was shown in Chapter 2, the solutions of the symmetric state are relatively simple; therefore, the results provide a natural benchmark against which to measure more complicated behavior. The EOF spectrum was found at values of  $F$  ranging from 8 to 40 in increments of 4. Figure 4.1 displays the number of EOFs required to meet the 99% variance threshold, using both pressure (i.e. stream function) and vorticity, as a function of  $F$ . For the pressure EOFs, there are obvious discontinuities in the number of EOFS required in different regimes. For  $8 \leq F < 24$ , the system is in a PAV regime, and fewer than 10 total EOFs are required. However, for  $24 \leq F < 36$ , the system exhibits structural vacillation, and the number of modes required almost doubles. This indicates that the PSV regime is more “complex” than the PAV regime. For  $36 \leq F \leq 40$ , the system is quasi-periodic, and the required number of EOFS again jumps substantially, with virtually twice as many modes needed in the quasi-periodic regime as in the PSV state. Furthermore, in the quasi-periodic regime the number of required modes increases with  $F$ . Finally, the required number of vorticity EOFs is always greater than the required number of streamfunction EOFS, and their ratio varies between two and three. This is consistent with the results shown in Appendix G, since in spectral space the vorticity, denoted as  $\omega(k)$ , is  $k^2\psi(k)$ , where  $\psi(k)$  is the streamfunction as a function of the wavenumber,  $k$ . Thus, the EOFs are calculated on statistics that decay with a slope of  $-\gamma$  ( $\gamma$  being some unknown constant) for streamfunction and a slope of  $-\gamma + 4$  for vorticity.

There are four distinct dynamical regimes in the symmetric state. The first is the steady-state regime. For this case, there are no EOFs to extract—there is only a mean spatial structure for each pertinent variable. Figure 4.2 displays the mean fields obtained at  $F = 8$ , near the onset of the initial wavy instability (the barotropic zonal field is nonexistent at this point). The barotropic wavy field can almost entirely

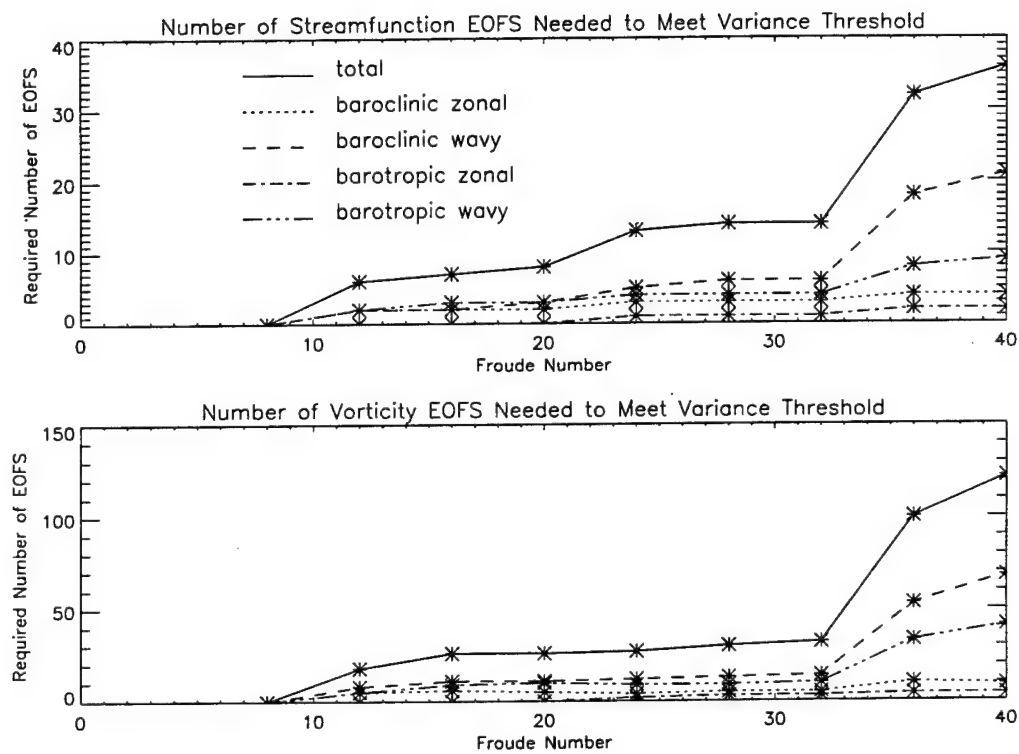


Figure 4.1. Number of EOFs needed to meet 99% variance threshold for Type-1 state. Results are shown using both stream function and vorticity as generating fields. Required number of EOFs are shown for each component of the flow in addition to the total number.

be described by the function  $\sin(\pi x/2) \sin \pi y$ , while the baroclinic zonal field is well-approximated by  $\sin 2\pi y$ . Both of these are the lowest-wavenumber modes for their respective fields. However, the baroclinic wavy field is clearly an amalgamation of several waves. Recall that the validity of single-wave models (discussed in Chapter 1) hinges on the assumption that the fields be confined to a single-wave disturbance. The lack of prognostic ability of single-wave models is to be expected given these results.

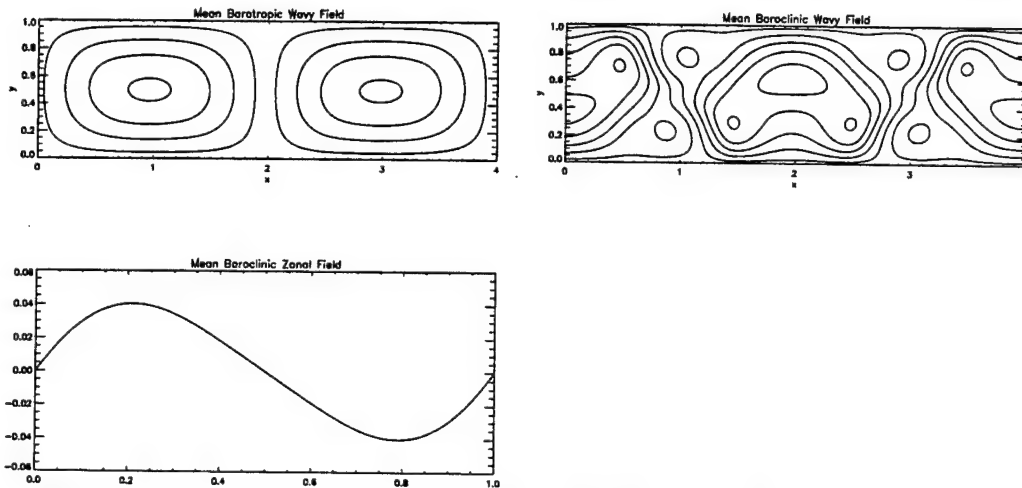


Figure 4.2: Contour plots of means for all fields, symmetric state,  $F = 8$ .

The next state to examine is at  $F = 20$ , in the PAV regime. Figure 4.3 displays the sorted, normalized eigenvalues, based on the streamfunctions, (or percent of the total variance captured by each EOF), for the baroclinic wavy and zonal components. The percent variance captured by each successive EOF falls off approximately exponentially, eventually reaching a noise floor at which the percent variance shows no further decay with increasing mode number. At this parameter setting, eight total EOFs are required to meet the variance threshold. Figure 4.4 displays contour plots of the EOFs for the baroclinic wavy stream function, along with their respective percent variance contributions. The EOFs are composed of many wavenumber pairs, indicating that the flow would not be well described by a simple Galerkin truncation. Figure 4.5 displays plots of the EOFs for the baroclinic

zonal flow. In contrast to the wavy fields, the EOFs here are simple and appear to be comprised of the two lowest symmetric zonal modes,  $\sin 2\pi y$  and  $\sin 4\pi y$ . Thus the coherent structures of the zonal field, at least in the PAV regime, are equivalent to the linear eigenfunctions.

The scenario for  $F = 32$ , in the PSV regime, is quite different from that of PAV at  $F = 20$ . The eigenvalue spectra for the baroclinic fields are shown in Figure 4.3. The spectrum for the wavy field has a curious step-like feature; this indicates eigenvalue pairing. Eigenvalue pairing occurs when traveling-wave phenomena are being investigated, as it takes two EOFs to represent the advance of the wave's phase with time. In this situation there are no waves traveling downstream. However, as seen in Figures D.3,4, the structural vacillation regime is characterized by two counter-rotating eddies, each comprising the entire meridional field and half of the zonal domain. Thus, the pairing of eigenvalues occurs when this rotation (which is really a form of a traveling wave) is decomposed into orthogonal functions.

The contour plots of the EOFs of the baroclinic wavy field are shown in Figure 4.6, and the structure of the EOFs shows the pairing of coherent structures. Where the first mode of each pair tends to have eddies oriented in a particular configuration, the second tends to possess eddies of the same spatial scale but rotated through some angle so as to change their orientation. This allows the rotation of both the barotropic and baroclinic fields with time. Figure 4.7 displays the EOFs for the baroclinic zonal field. The baroclinic zonal flow requires three EOFs to meet the variance requirement, and their corresponding spatial structure is now relatively complicated (compared to  $F = 20$ ).

The use of empirical orthogonal functions elucidates several salient points regarding the physics of the problem. First, amplitude vacillation is spatially "simpler" than structural vacillation and thus requires fewer spatial modes for adequate representation. Also, the pairing of eigenvalues in the EOF decomposition indicates

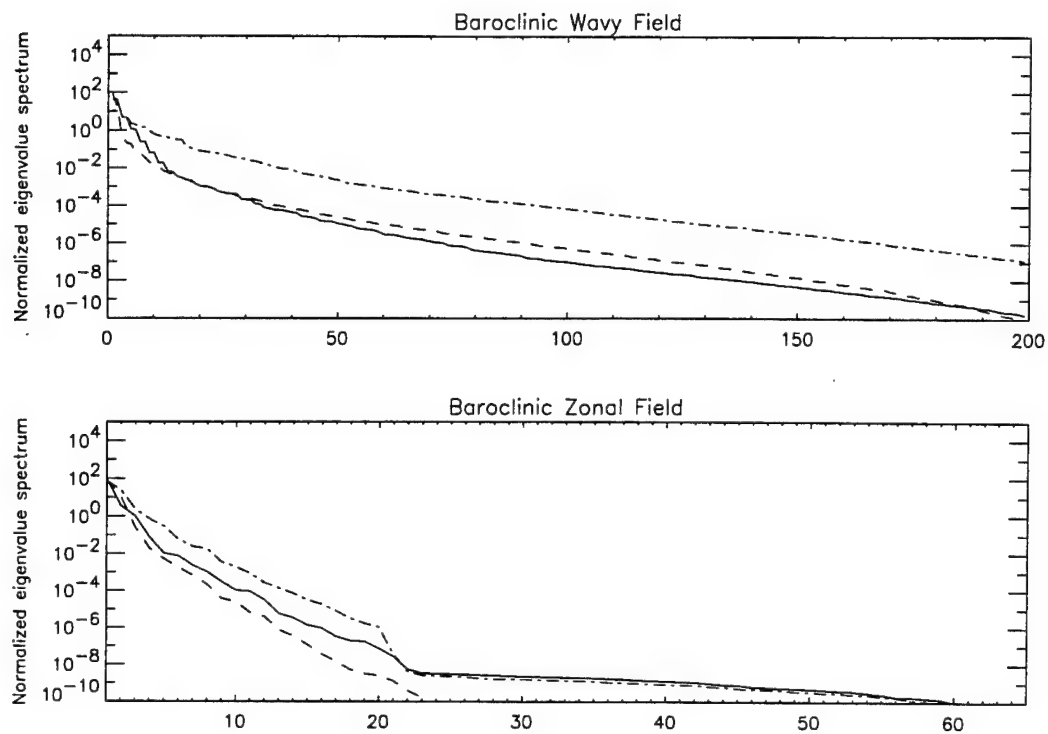


Figure 4.3. Normalized eigenvalue spectra for symmetric case. The dashed line corresponds to  $F = 20$  (PAV); the solid line corresponds to  $F = 32$  (PSV); the dot-dashed line corresponds to  $F = 36$  (QP).

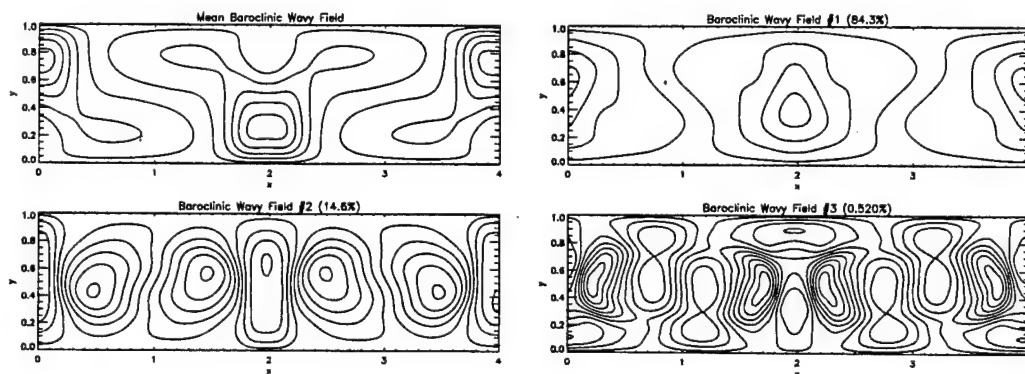


Figure 4.4. Contour plots of EOFs for baroclinic wavy field, symmetric state,  $F = 20$ .

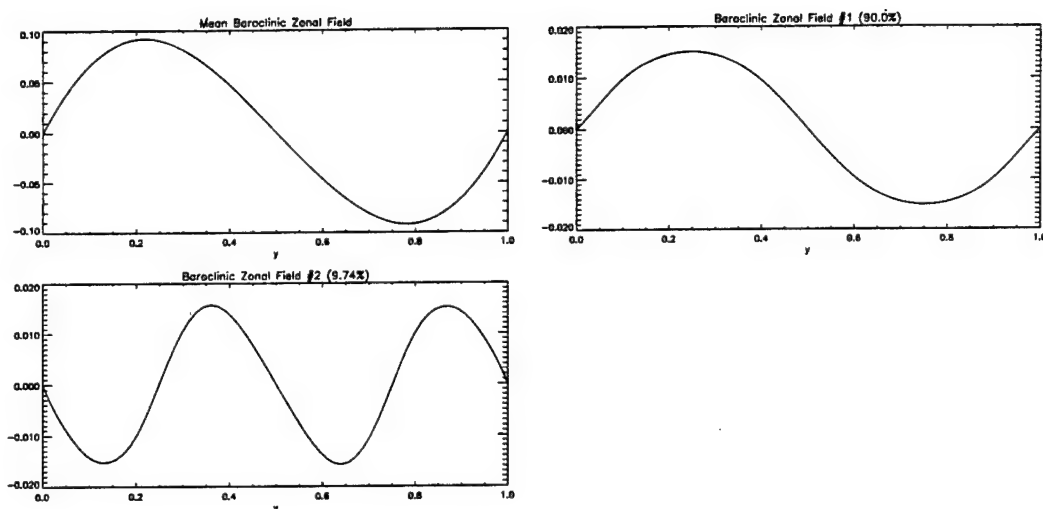


Figure 4.5. Contour plots of EOFs for baroclinic zonal field, symmetric state,  $F = 20$ .

the presence of traveling waves for the PSV case. An examination of the spatial structure of the EOFs (and a comparison to the full flow field) reveals that the modes travel in a circulating pattern rather than zonally. This observation is consistent with the idea that the structural vacillation phenomenon is characterized by the meridional shift of kinetic energy. The circular motion of the eddy fields simply propagates kinetic energy from one side of the channel to the other in a periodic fashion.

The final case to examine for the symmetric solution is  $F = 36$ , where the behavior is quasi-periodic in time. At this parameter setting, a total of 32 EOFs are needed to meet the 99% variance threshold. Figure 4.3 displays the EOF spectra for the baroclinic fields. There is now little pairing of EOFs in the wavy fields; the baroclinic field retains a few pairs in the higher-energy modes, but this does not persist for the smaller-energy EOFs. This corroborates the results presented in Chapter 2—essentially that the quasi-periodic regime appears to represent a mixing between amplitude vacillation and structural vacillation, so that the EOFs (and the corresponding eigenvalue spectrum) would be expected to possess properties of both vacillation states. In addition, Figure 4.3 shows that the eigenvalue spectra of the wavy fields decay much less rapidly than do the wavy-field spectra in the periodic cases, and they never actually reach a noise floor. Thus, the spatial complexity is much higher than in the periodic flows. Figure 4.8 displays the EOFs for the wavy baroclinic field. The coherent structures are similar to but not identical to those for the PSV case at  $F = 32$ . The first four EOFs are very similar to those at  $F = 32$ , but the next two are different; they are not obviously similar to the higher energy modes at  $F = 20$ , either. However, the barotropic wavy modes show similarities both to those found in the PSV regime and also those found in the PAV regime; this supports the mixing concept. Reflecting the slower decay of variance, the first six baroclinic fields possess about 92% of the total energy, but the remaining energy

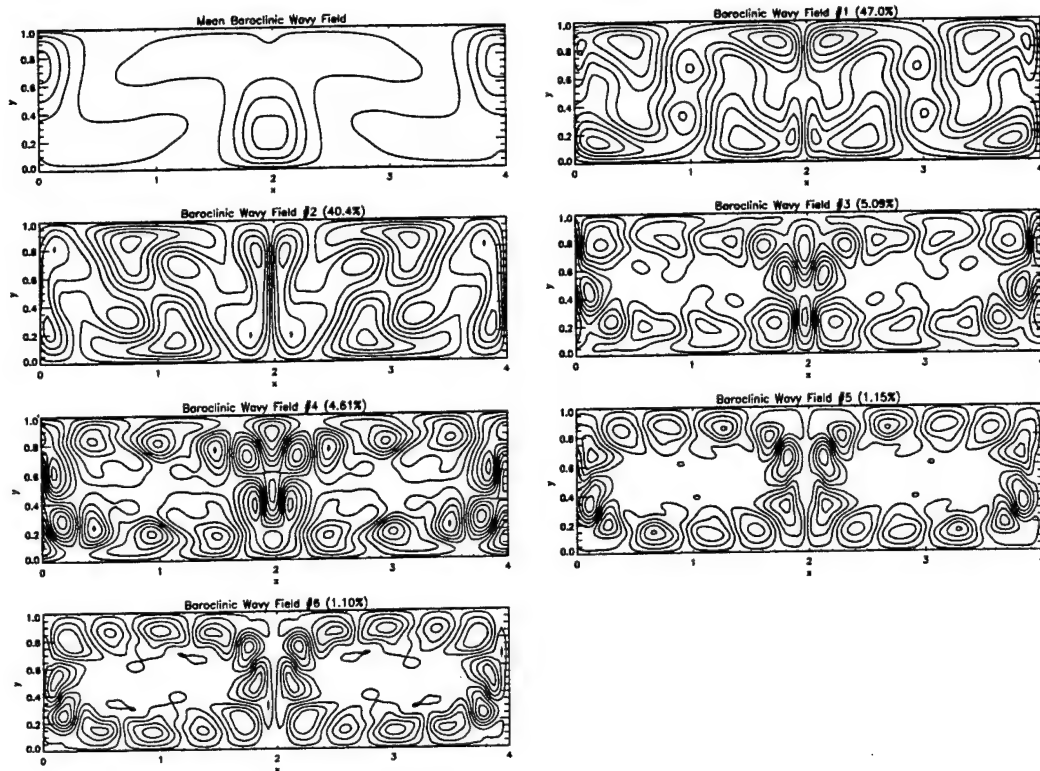


Figure 4.6. Contour plots of EOFs for baroclinic wavy field, symmetric state,  $F = 32$ .

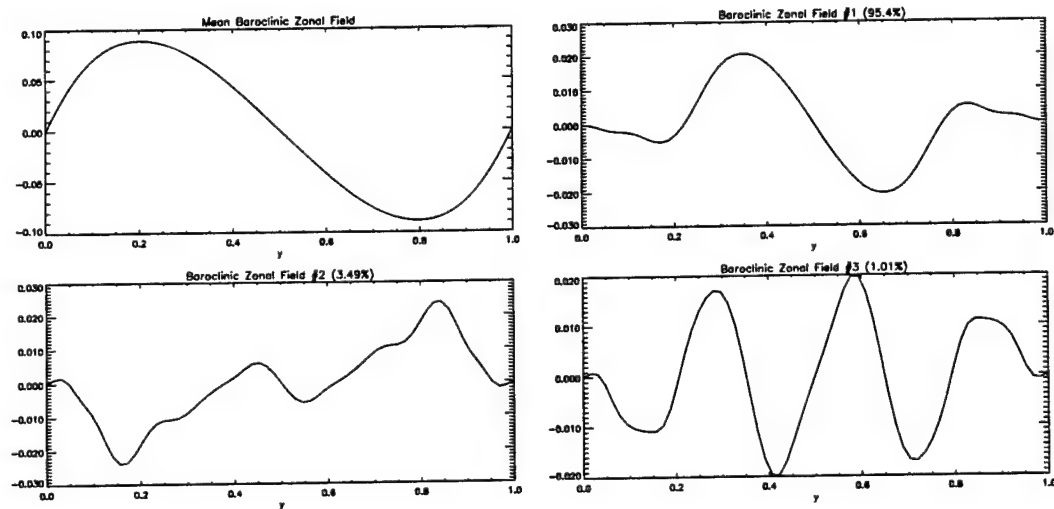


Figure 4.7. Contour plots of EOFs for baroclinic zonal field, symmetric state,  $F = 32$ .

is partitioned among many low-energy modes. Figure 4.9 displays the zonal EOFs. These are similar to those found at  $F = 32$ , with the exception that the energy of the baroclinic zonal field is primarily partitioned among the first two modes rather than only the first EOF.

**4.6.2 Asymmetric Case** With reference to Figure 2.4, there exist three distinct regimes of interest for the asymmetric solution. The first is the PSV regime that occurs for  $14 \leq F < 24$ ; the second is the quasi-periodic regime for  $24 \leq F < 30.9$ ; the final regime is the chaotic regime that exists over the range  $30.9 \leq F \leq 40$ . As Figure 2.4 clearly indicates, there are small regions of both PSV and quasi-periodic behavior for  $F < 14$ , but these regions occur over very small ranges of  $F$  and are not included in this analysis.

Figure 4.10 displays the number of EOFs required to meet the 99% variance threshold, using both stream function and vorticity measures, as a function of  $F$ . The general increase in EOFs needed versus temporal complexity is similar to that seen in the symmetric case. The PSV regime, sampled in Figure 4.10 at  $F = 16$  and  $F = 20$ , requires the fewest number of EOFs. The quasi-periodic region, which is represented by the data for  $F = 24$  and  $F = 28$ , requires a much larger number of EOFs to meet the variance threshold. A large fraction of the increase is due to the baroclinic wavy field. Finally, the data for  $F \geq 30$  is in the chaotic regime and requires the largest number of EOFs for representation. Because of the complex spatio-temporal behavior at the higher values of  $F$ , the number of vorticity EOFs required should be construed as a lower bound, since no unequivocal convergence of the required number was observed as the number of samples was increased (however, the number of streamfunction EOFs is accurate).

The first parameter setting to be investigated is  $F = 20$ , in the PSV regime and near the transition to quasi-periodic flow. Figure 4.11 displays the eigenvalue spectrum for the flow's baroclinic components. In this regime, 12 total EOFs are

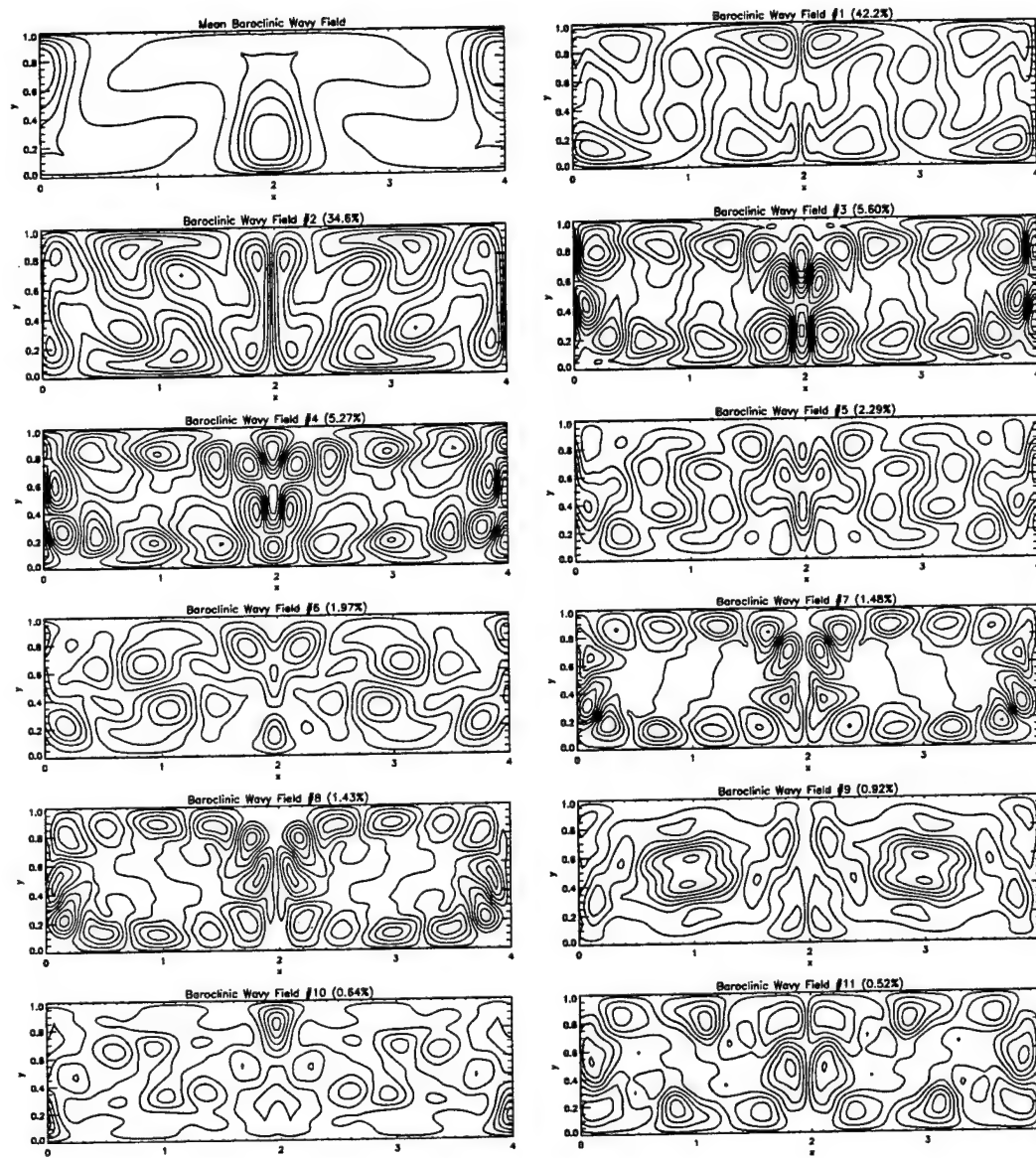


Figure 4.8. Contour plots of EOFs for baroclinic wavy field, symmetric state,  $F = 36$ .

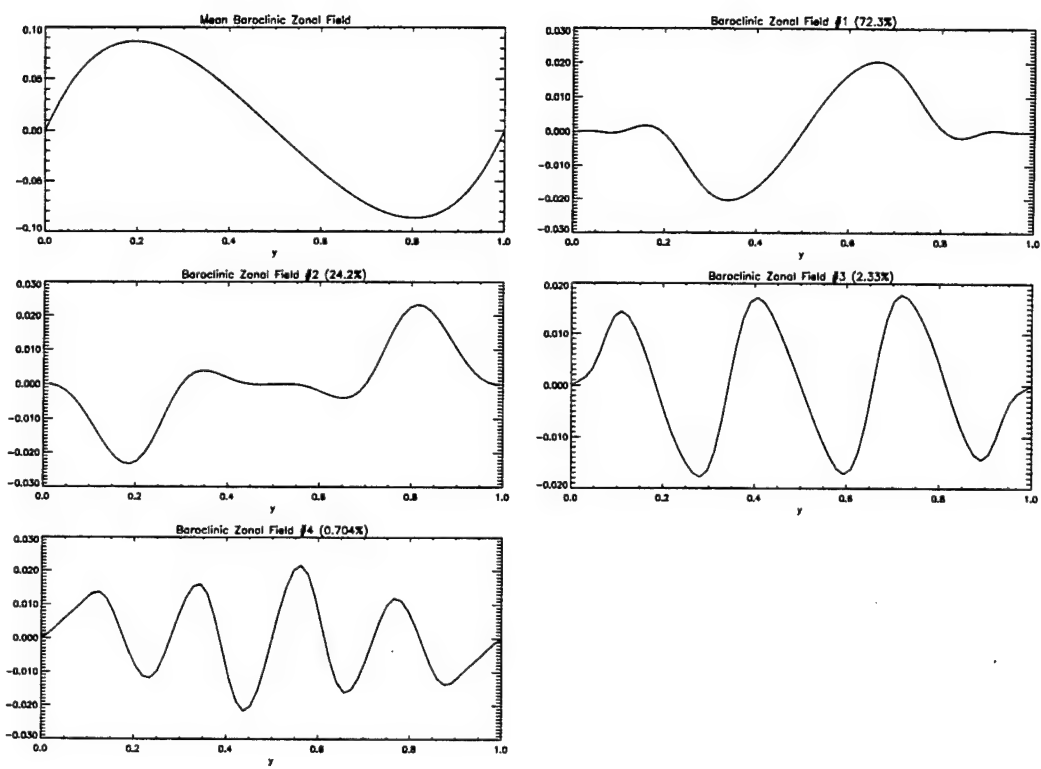


Figure 4.9. Contour plots of EOFs for baroclinic zonal field, symmetric state,  $F = 36$ .

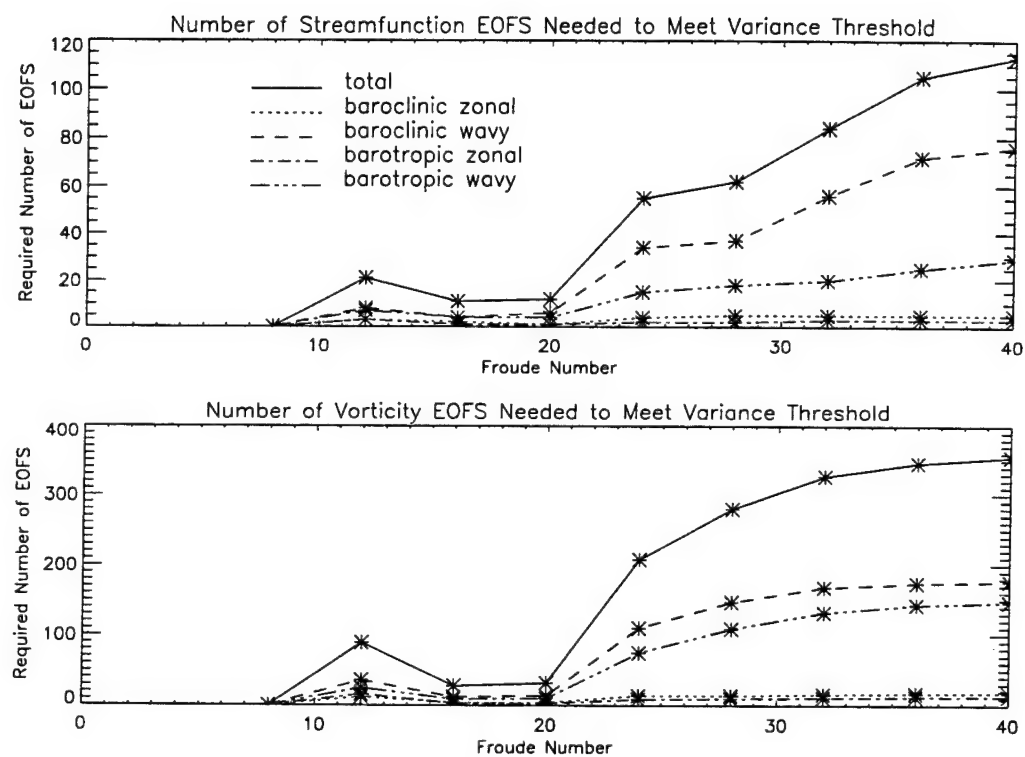


Figure 4.10. Number of EOFs needed to meet 99% variance threshold for asymmetric state. Results are shown using both stream function and vorticity as generating fields. Required number of EOFs are shown for each component of the flow in addition to the total number.

needed to meet the 99% variance threshold. The “step-wise” appearance in the wavy fields’ spectra is similar to the results for the symmetric PSV behavior and also indicates a traveling wave phenomenon in the form of counter-rotating eddies. In addition, the number of EOFs required is similar to the symmetric PSV solution. Figure 4.12 displays the EOFs for the baroclinic wavy field, from which it can be seen that the counter-rotating behavior is evident in the structure of the spatial functions. The structure of the EOFs is qualitatively, but not quantitatively, similar to the EOFs in the symmetric PSV regime, indicating that there are substantive differences between the symmetric and asymmetric solutions. The baroclinic zonal EOFs are shown in Figure 4.13. The baroclinic zonal structure is an admixture of waves and is somewhat different from the leading EOF in the symmetric PSV regime (see Figure 4.7). The barotropic field, in contrast to the symmetric state at  $F = 32$ , is dominated by the lowest asymmetric zonal term (i.e.  $\sin(\pi y)$ ).

The eigenvalue spectrum for  $F = 28$ , where the system exhibits quasi-periodicity, is shown in Figure 4.11. To meet the 99% variance criterion, 62 EOFs are required, and 37 of these are from the baroclinic wavy field. As with the symmetric results, the wavy eigenvalue spectra fall off much less rapidly in the quasi-periodic regime than in the periodic regions. Additionally, the spectra for this asymmetric QP behavior fall off less rapidly than even the symmetric QP solution, indicating that the asymmetric quasi-periodicity is of a more complex nature than that of the symmetric case. This is corroborated by examining the actual EOFs; the first eleven for baroclinic wavy field are shown in Figure 4.14 and account for 90% of the total variance. The spatial fields are extremely complicated, and a glance at the percentage of variance captured by each reveals that no single spatial scale dominates the flow. In addition, there is little vestige of the counter-rotating eddy structure seen in the PSV regime. The barotropic zonal flow is largely unchanged; the first EOF now simply captures slightly less of the total variance than previously. However, the baroclinic

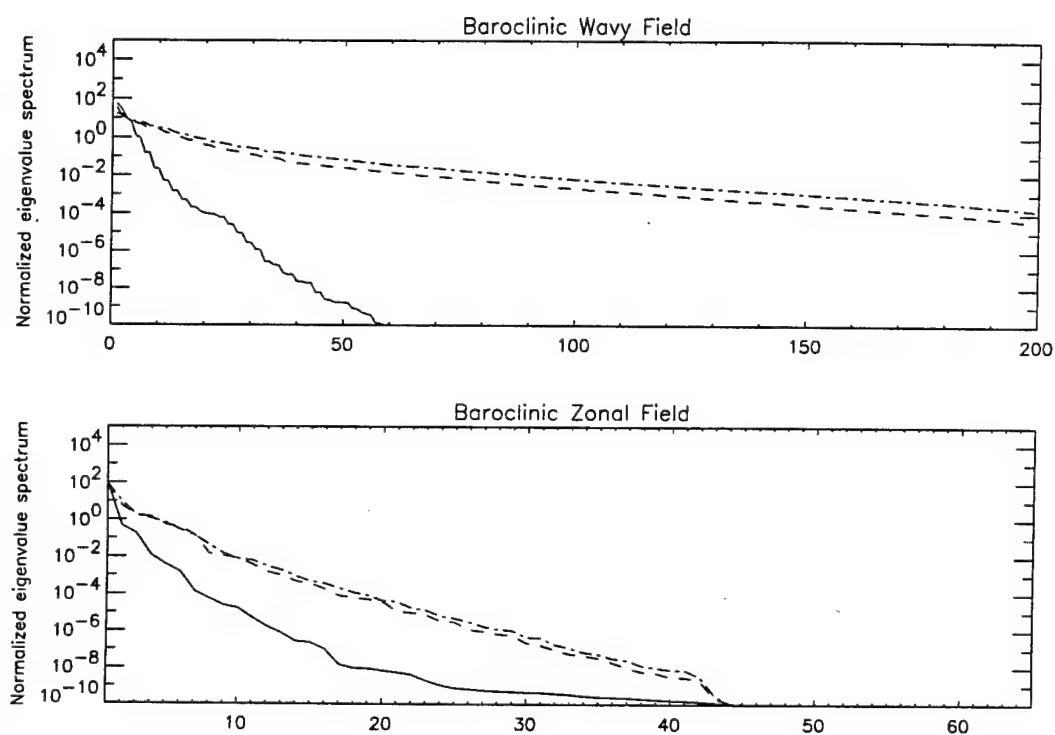


Figure 4.11. Normalized eigenvalue spectra for asymmetric case. The solid line corresponds to  $F = 20$  (PSV); the dashed line corresponds to  $F = 28$  (QP); the dot-dashed line corresponds to  $F = 32$  (Chaotic).

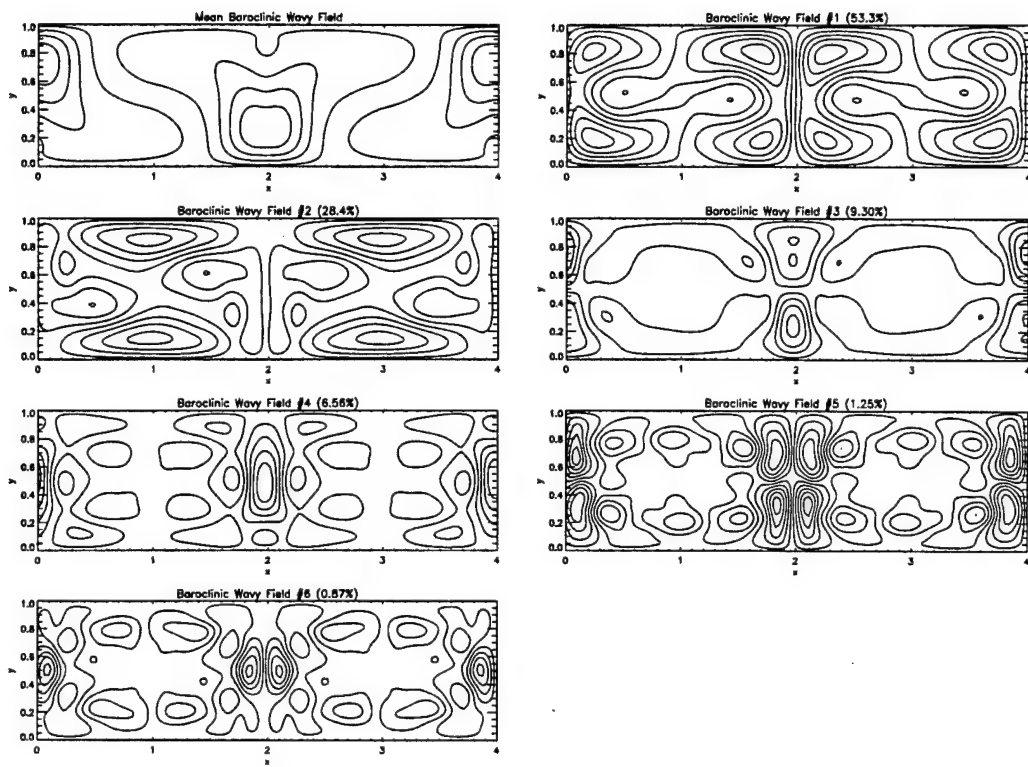


Figure 4.12. Contour plots of EOFs for baroclinic wavy field, asymmetric state,  $F = 20$ .

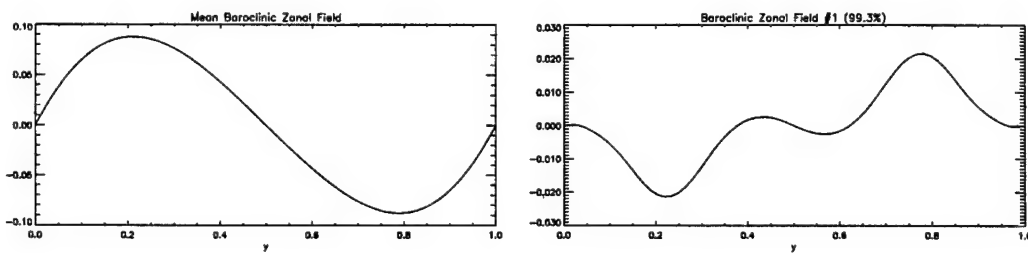


Figure 4.13. Contour plots of EOFs for baroclinic zonal field, asymmetric state,  $F = 20$ .

zonal flow EOFs, shown in Figure 4.15, show substantial differences from the PSV results at  $F = 20$ . The lowest asymmetric mode (i.e.  $\sin \pi y$ ) dominates the first EOF; this is consistent with the asymmetric, baroclinic instability which correlates with the onset of the quasi-periodic behavior. The second mode is comprised largely of the lowest symmetric linear eigenfunction,  $\sin(2\pi y)$ . The lower-energy EOFs are mixtures of other eigenfunctions and become increasingly convoluted.

The final parameter setting to examine for the asymmetric solution is at  $F = 32$ , in the chaotic regime. About 87 EOFs are required to meet the 99% variance requirement, with 60 needed for the baroclinic wavy field alone. The only significant change between the quasi-periodic solution and the chaotic solution is that the required number of baroclinic wavy EOFs increases by about 50%. Figure 4.11 displays the normalized eigenvalue spectra at  $F = 32$ . There is little change from the results at  $F = 28$ , except that the baroclinic wavy spectrum falls off even less rapidly than in the quasi-periodic regime.

The first eleven EOFs for the baroclinic wavy field are shown in Figure 4.16. Again, little is changed from  $F = 28$ , except that the dominant EOFs capture relatively less of the total energy as the complexity of the flow increases. For example, the first 11 baroclinic wavy fields only represent about 80% of the total energy, compared to 90% at  $F = 28$ . Especially for the baroclinic wavy field, a large portion of the energy is partitioned into a multitude of low-energy modes, which explains the need for such a large number of EOFs to meet the variance threshold requirement. Finally, Figure 4.17 displays the baroclinic zonal EOFs, the first two of which are also largely unchanged from  $F = 28$ .

#### 4.7 Approximate Dynamical Systems for the Slippery Model

The EOFs found in the previous section can be exploited, via the methodology presented in Section 4.3, in order to produce low-order sets of ODEs that mimic

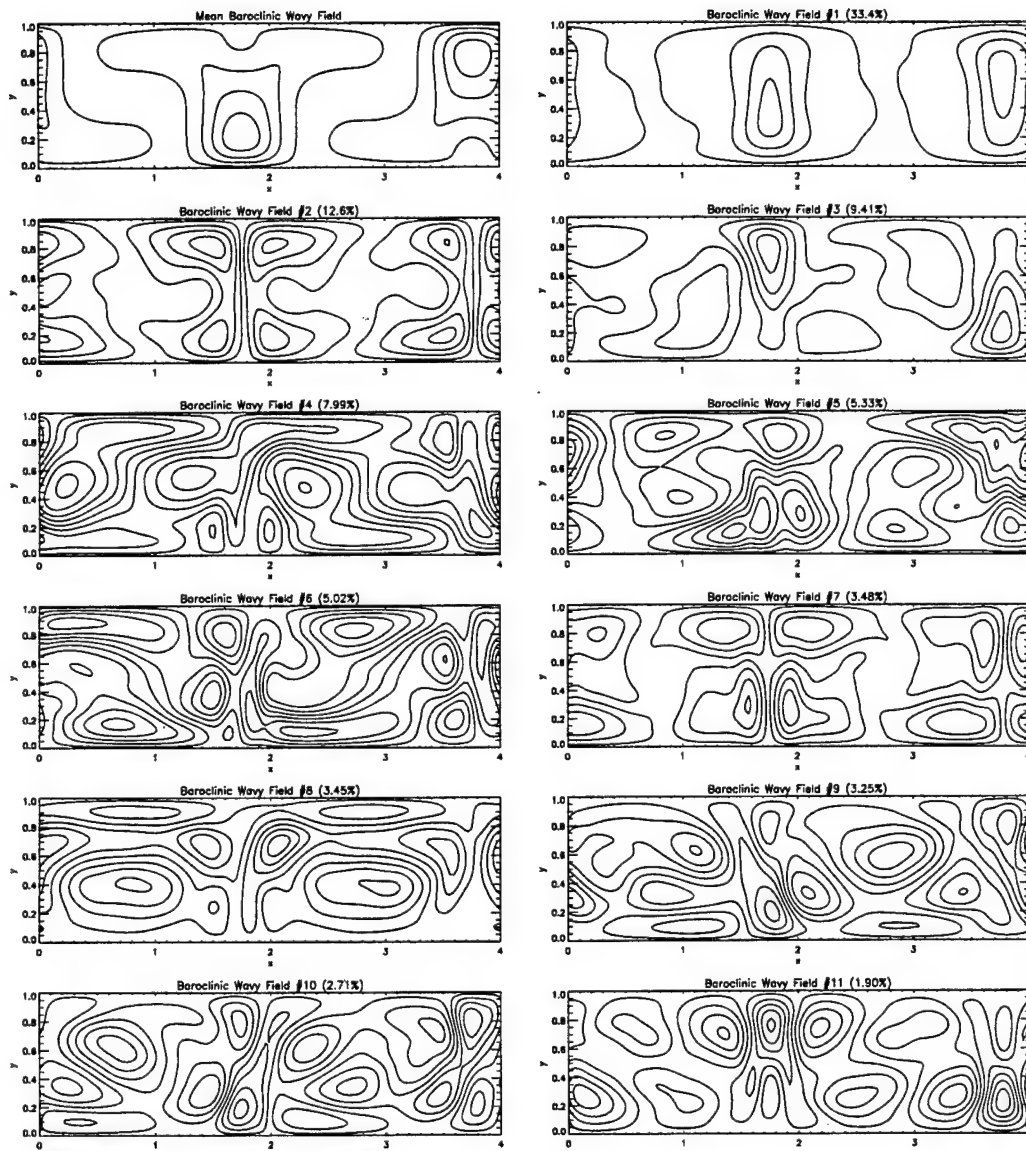


Figure 4.14. Contour plots of EOFs for baroclinic wavy field, asymmetric state,  $F = 28$ .

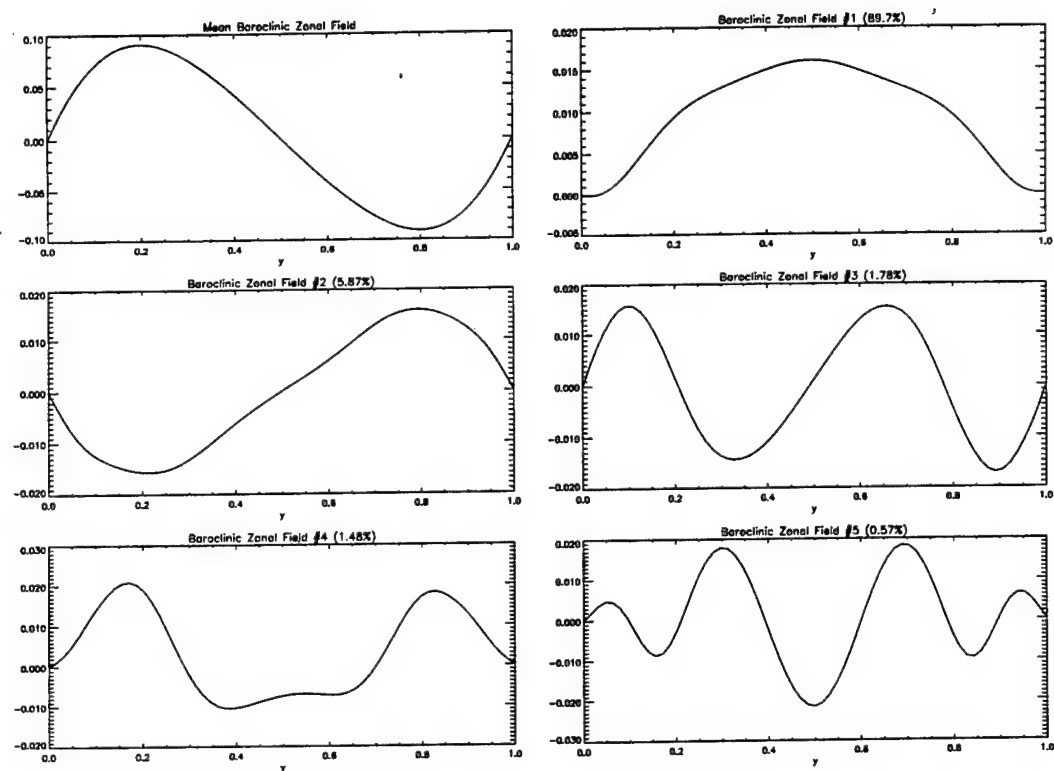


Figure 4.15. Contour plots of EOFs for baroclinic zonal field, asymmetric state,  $F = 28$ .

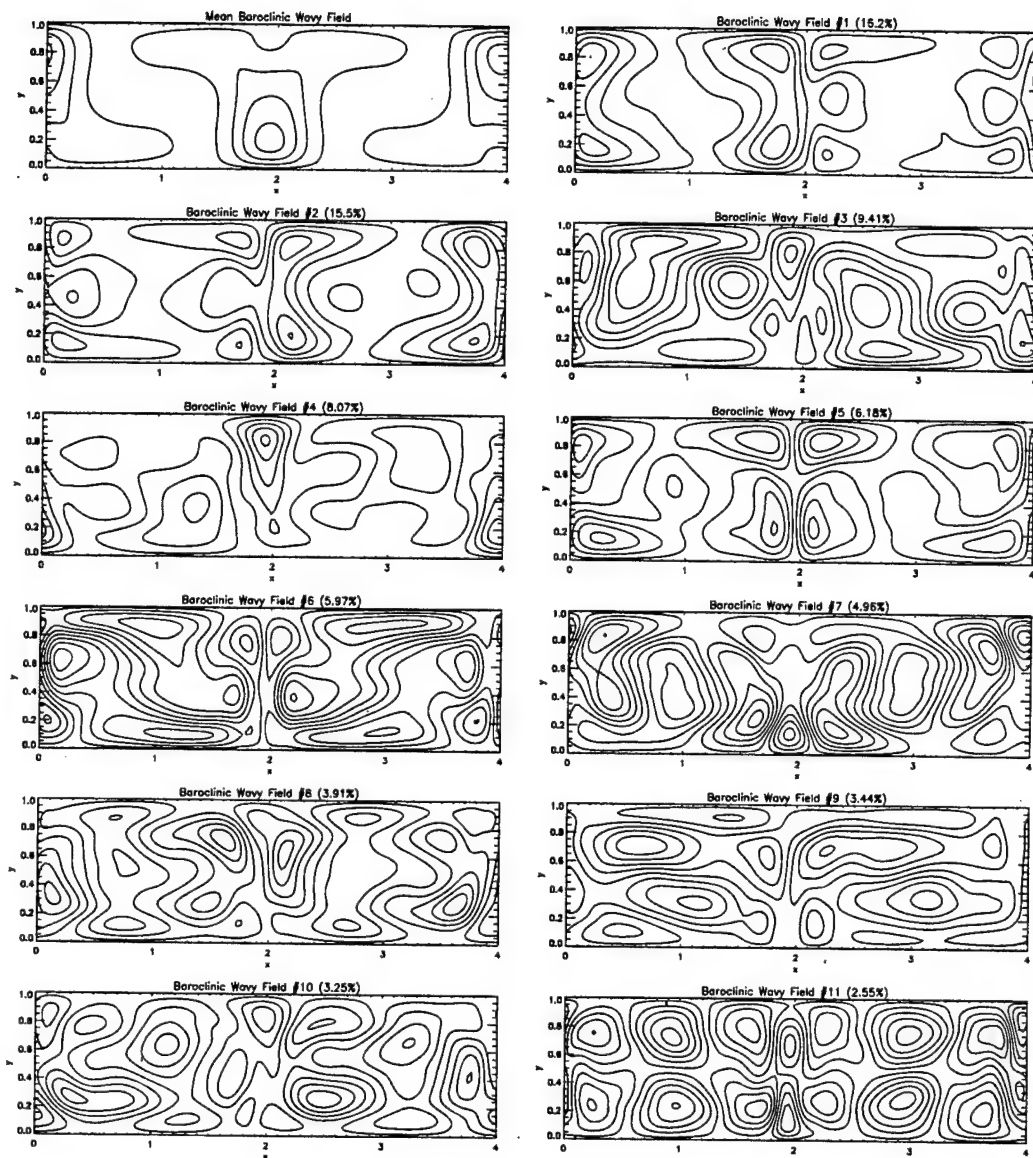


Figure 4.16. Contour plots of EOFs for baroclinic wavy field, asymmetric state,  $F = 32$ .

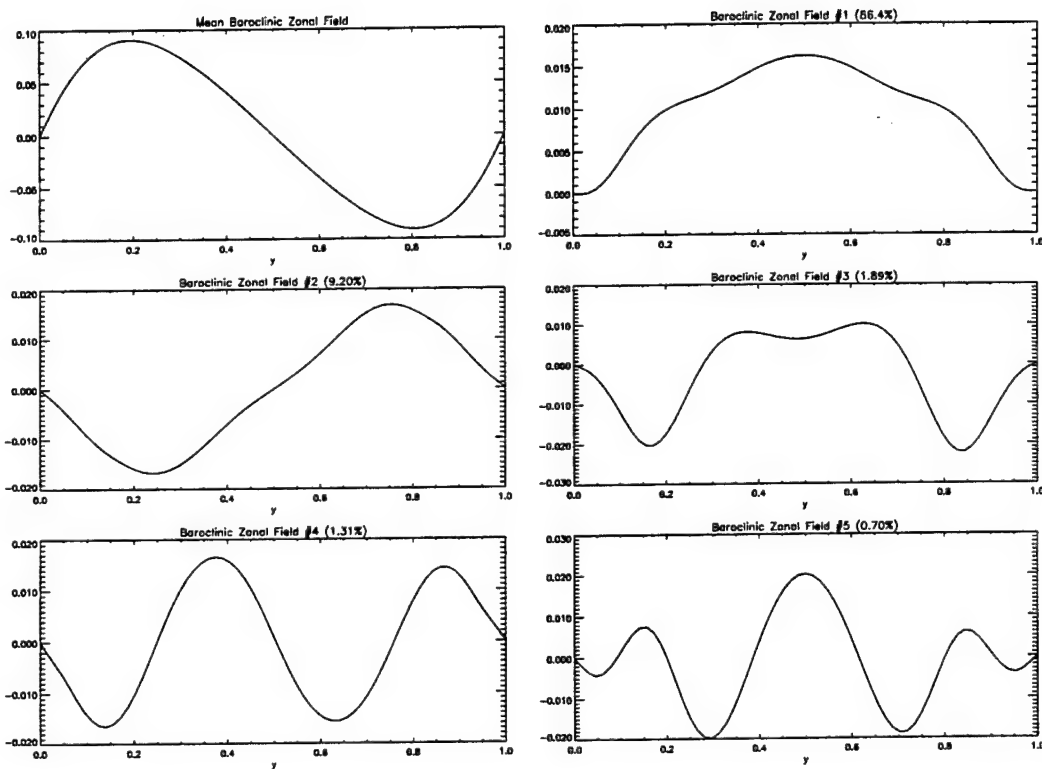


Figure 4.17. Contour plots of EOFs for baroclinic zonal field, asymmetric state,  $F = 32$ .

the original model (which is equivalent to  $O(10^4)$  ODEs). There is substantial motivation for doing this. For instance, the low-order set of ODEs is much more quickly integrated (numerically) on a computer. This allows a more thorough investigation of solutions, since much more data can be obtained in an equivalent amount of computer time. The resulting data can also be compressed for storage using the EOFs. Additionally, the ability to represent a result from a complex model with a relatively simple system places an upper bound on the “complexity” of the original solution. This yields physical insight as to the number of important degrees of freedom in the problem. Although, for example, it requires all of the EOFs to exactly represent a given flow field, the results of the previous section have shown that the field can be almost fully represented by a much smaller number of EOFs.

**4.7.1 Symmetric Case** The first parameter setting to investigate is  $F = 8$ . For this value of  $F$ , as previously noted, the behavior is steady, so that only mean fields exist. However, in order to “test” the concept of obtaining ODEs from PDEs via EOFs, the mean fields can be assumed to possess time-dependent coefficients; then ODEs can be obtained for these coefficients, which should relax to unity upon integration in time. Doing this, one finds that the wavy and zonal fields do indeed approach unity with an error of about 1%, and the velocity correction term also approaches its proper value within an error of about 3%.

This low-order model can now be used to answer other pertinent questions. First, how well does the model perform at “off-reference” values of  $F$  (i.e. values of  $F$  other than that at which the model was constructed)? Second, how well does its performance, with reference to the full numerical model, compare to a low-order model based on the gravest linear eigenfunctions? For comparison, the low-order system which was used for model verification (see Section 2.5) was again used (this will be referred to as the *ad hoc* model). This model retains two wavy modes each ( $\sin(\pi x/2) \sin \pi y$  and  $\cos(\pi x/2) \sin \pi y$ ) for both the barotropic and baroclinic wave

fields, one zonal mode ( $\sin 2\pi y$ ) for the baroclinic zonal field, and the the baroclinic velocity correction,  $U_2 - U_1$ . Referring to Figure 4.2, both the barotropic wavy and baroclinic zonal fields are well represented by this choice of functions, but the actual baroclinic wavy field is much richer in structure than a single wave. Nonetheless, both low-order models predict the critical Froude number for the onset of instability to within less than 1% error. However, neither model predicts time-dependent behavior to occur before  $F \approx 20$ , while the full model becomes oscillatory at  $F = 12$ . Both models thus fail at predicting the onset of amplitude vacillation. To compare results in the steady regime, Table 4.1 displays a comparison of behavior between the full model and the EOF approximate model, while Table 4.2 displays a comparison between the full model and the *ad hoc* low-order model. The quantity used for comparison is one-half the area-integrated square of the stream function (i.e.  $1/2 \int_A \Psi^2 dA$ ) for each of the three fields. The *ad hoc* model performs abysmally at both  $F = 8$  and  $F = 10$ , underestimating the magnitude of each field by an average of about 40% of its true value (and performing worst with the value of the baroclinic wavy field). However, when the actual spatial structure of the baroclinic waves are accounted for, a low-order model (i.e. the EOF model) does fairly well at predicting the behavior over a range of  $F$ . As Table 4.1 shows, the errors are negligible at  $F = 8$ , where the model is derived, and acceptable at  $F = 10$ . Again, the baroclinic wavy field shows the worst correspondence, and an examination of the full-model solution indicates that this is due to further changes in the shape of this quantity. Therefore, the full model's steady-state can be well described by a low-order dynamical system, but the spatial structures cannot be assumed *a priori*, at least with any validity. Instead, the approximate model must be constructed from results gleaned from the full code.

The next approximate system constructed is at  $F = 20$ , near the upper end of the PAV regime. As Figure 4.1 demonstrates, relatively few EOFs are required

Table 4.1. Performance comparison between full model and low-order EOF model, symm. case. The quantity used for comparison is one-half the area-integrated squared streamfunction,  $1/2 \int_A \Psi^2 dA$ , and the numbers represent the percentage error in this quantity.

Froude Number	Barotropic Wavy Field	Baroclinic Wavy Field	Baroclinic Zonal Field
8	1.6 %	-.45 %	-3.2 %
10	-5.9 %	-30.8 %	4.5 %

Table 4.2. Performance comparison between full model and low-order *ad hoc* model, symm. case. The quantity used for comparison is one-half the area-integrated squared streamfunction,  $1/2 \int_A \Psi^2 dA$ , and the numbers represent the percentage error in this quantity.

Froude Number	Barotropic Wavy Field	Baroclinic Wavy Field	Baroclinic Zonal Field
8	-33.5 %	-48.5 %	-53.5 %
10	-22.8 %	-59.2 %	-42.6 %

to meet the 99% variance threshold at this Froude number. To help ensure that the system exhibited a stable limit cycle, the transient-sampling approach advocated by Deane et al. (1991) was used. At this parameter setting, it requires three barotropic wavy modes, three baroclinic wavy modes, and two baroclinic zonal modes to represent 99% percent of the total energy, on average. This alone results in eight required equations. In addition, in order to attempt to use the resulting system at other values of  $F$ , the means have temporal coefficients attached to them so that their magnitude is allowed to vary with  $F$ . Finally, an equation for  $\mathcal{U}_{bc}$  is needed, bringing the total to twelve equations. When these are integrated, the resulting system does exhibit periodic behavior: the typical error in the mean and rms deviation of the  $1/2 \int_A \Psi^2 dA$  diagnostic for each of the three fields is 15%. More specifically, the rms deviations are all too large. In addition, the period of the oscillation is about 10% too high.

This result is acceptable, but it can be improved upon if the following conjecture is made—that the higher-wavenumber, low-energy modes act primarily as energy sinks. These modes are linearly stable and would not spontaneously arise on their own; however, the presence of the large-scale, high-energy structures causes them to persist, where they act to funnel energy away from the large-scale modes. However, the very process of obtaining EOFs is concerned with extracting the high-energy behavior and ignoring those modes which contribute little to the overall energy balance. The idea, then, is to parameterize the effect of these modes by assuming they act only in a dissipative manner. Using this premise, the ODE representing the lowest-energy mode for each field can be damped by some extra amount to be determined empirically. Assuming that one of these hypothetical modes is represented by the time coefficient  $a_i$ , and is governed by a differential equation for  $da_i/dt$ , one simply adds the quantity  $-\rho a_i$  to the right hand side of the equation.

The initial values of  $\rho$  were chosen such that they were on the order of the original dissipation values; then the error (which is defined as the sum of the percentage errors in mean and rms deviation for each field using the metric shown in Table 4.1) was simply tracked as  $\rho$  was varied. The value  $\rho = .295$  was found to be optimal, resulting in a total error of 13.7%, much lower than the 90% error obtained for  $\rho = 0$ . In addition, the frequency of oscillation is now accurate to within less than 3%.

Using  $\rho = .295$ , the results from the full model can be directly compared with those from the 12-ODE approximation. Figure 4.18 shows phase-space comparisons for selected pairs of the three  $1/2 \int_A \Psi^2 dA$  quantities, referred to as "energy" in the figure. The agreement in both the size and shape of the attractor is very good.

The agreement in area-integrated quantities is necessary but not sufficient to show that the spatial dependence is the same between the two models. This may not occur if the various time coefficients possess different phase relationships in the approximate model than they do in the full model, a discrepancy which may not be apparent in comparing quantities with only temporal dependence. However, as Figures E.1,2 show, the spatial dependence of each of the wavy fields compares very favorably with the "exact" solution, shown in Figures D.1,2 (the phase of the approximate fields slightly lags that of the exact fields). The essential features of each of the variables are captured, despite the fact that the spatial dependence is highly non-trivial. Thus, the approximate model is highly successful in replicating the behavior of the full numerical integration for  $F = 20$ .

One hope of creating approximate models is that systems derived at one parameter value can be used to also approximate the results at other parameter values. Otherwise, a new approximate model must be constructed at each parameter value that one wishes to study. It is the alteration of spatial structure as a function of parameter changes that dictates whether or not the same model can be successfully

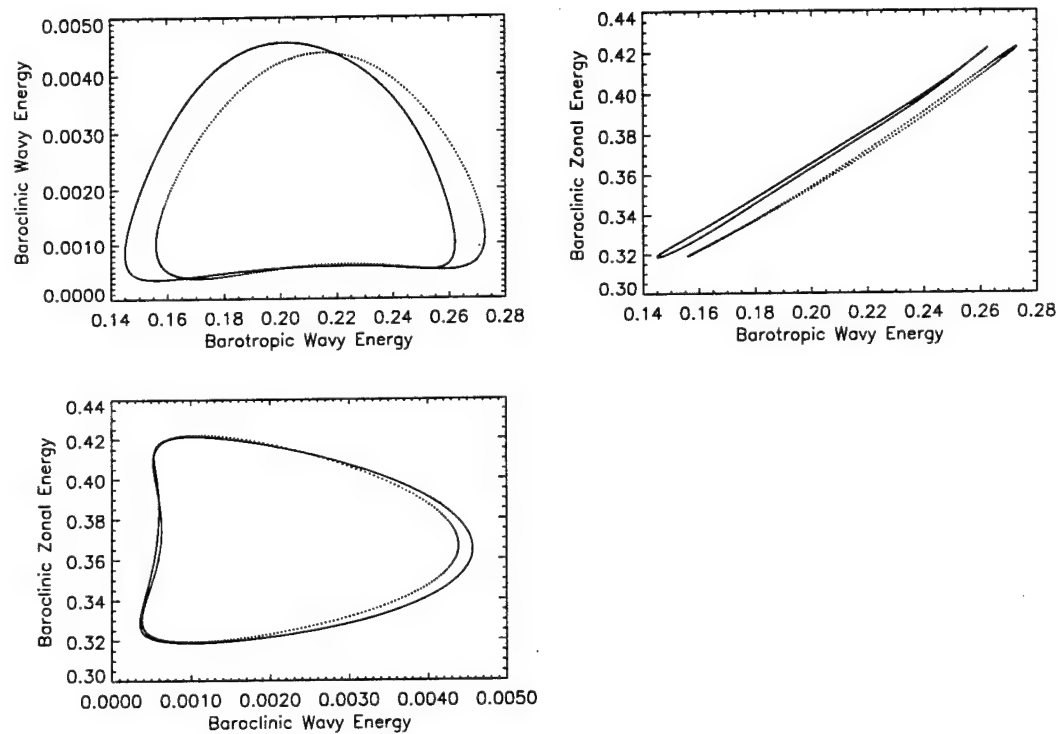


Figure 4.18. Phase-space comparisons of full and approximate models at  $F = 20$ . The solid line indicates the full-model results, while the dotted line signifies the results of the approximate, 12-equation model.

utilized for a range of parameter values. If the spatial field changes slowly with, for example,  $F$ , then the same set of equations can probably do an adequate job of mimicking the flow's real behavior over a reasonable range in  $F$ . As can be seen from Figure 4.10, the number of EOFs needed in the PAV regime is relatively constant, so that one may also expect the shape of the EOFs to be relatively constant, further implying that the model derived at  $F = 20$  may be valid over the entire realm of PAV. To measure the correspondence between the actual result and the approximate result, the quantity  $\mathcal{X} \equiv 1/2 \int_A \Psi^2 dA$  was used. Figure 4.19 displays comparisons between the approximate and full models in the range  $6 \leq F \leq 22$  for all three variables. The outer lines indicate the envelope of the (periodic) solution, while the middle line indicates the mean value. The agreement is reasonably good considering that the mean baroclinic field changes appreciably with  $F$ . In addition, the approximate model makes the transition from steady zonal flow to steady waves at  $F \approx 5.8$ , which compares well to the theoretical value of  $F \approx 6.2$ ; furthermore, the transition from steady to periodic behavior occurs at about  $F = 12$  for both models. Therefore, the approximate model is successful in predicting both the onset of instability and the onset of periodic behavior. This is in sharp contrast to the four-equation model extracted from the steady state at  $F = 8$  and the low-dimensional Lorenz-type model. Finally, the EOF model is successful in its approximation of the mean and rms deviation of the three variables over the entire PAV regime, with the correspondence worsening as  $F$  becomes further away from its reference value of 20. The baroclinic wavy field is the least accurate, and presumably this error occurs because the baroclinic field changes shape substantially with  $F$ . However, its amplitude is small enough relative to the other variables that both the barotropic wavy and baroclinic zonal fields remain largely accurate for the entire range of  $F$ .

One shortcoming is that this model is incapable of predicting the onset of PSV that occurs at  $F \approx 24$ . This is because the spatial structure in the PSV regime

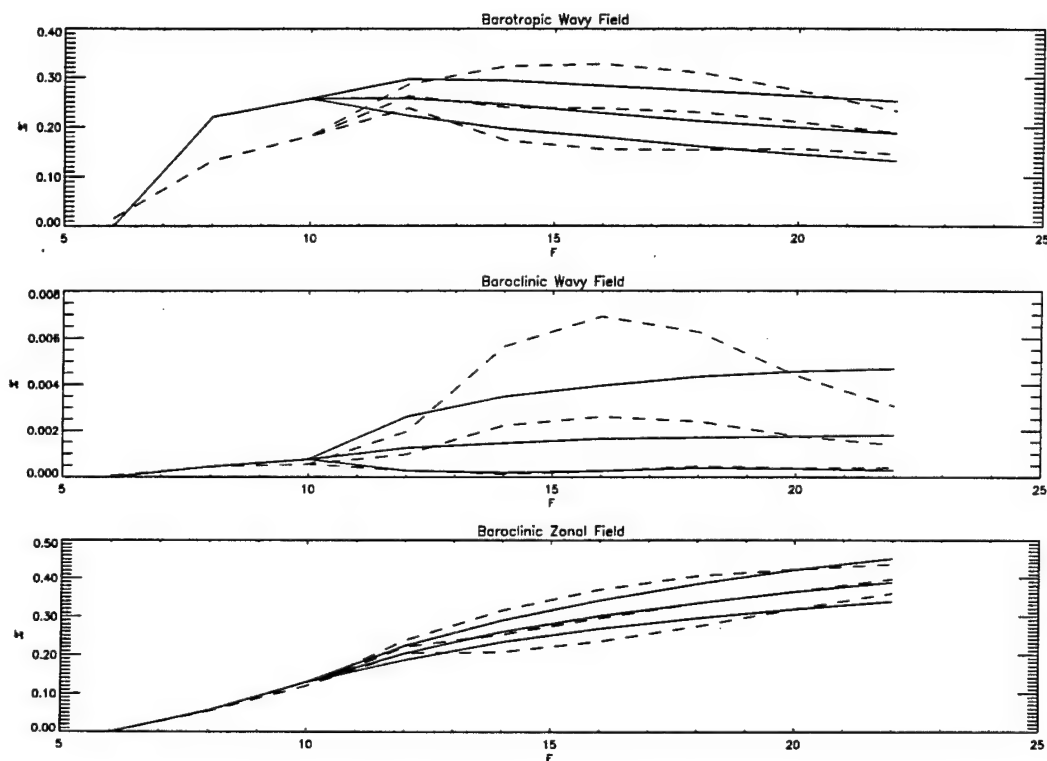


Figure 4.19. Comparison of the behaviors between the full and approximate models for  $6 \leq F \leq 22$ . The outer lines indicate the envelope of the periodic behavior, while the center lines indicate the mean value. The solid line indicates the full-model results, while the dashed line signifies the results of the approximate, 12-equation model. The ordinate is  $\mathcal{X} = 1/2 \int_A \Psi^2 dA$ .

is more complicated than that in the realm of PAV, so that the included spatial fields are incapable of representing the PSV phenomenon. Instead, the 12-mode model becomes quasi-periodic at  $F \approx 26$ .

The next approximate dynamical system was constructed to capture the PSV phenomenon that occurs between  $F = 24$  and  $F = 34$ . The EOFs were obtained at  $F = 32$ , near the upper end of the PSV regime. The dynamical system for this setting is comprised of 15 ODEs (4 for the barotropic wavy field, 2 for the barotropic zonal field, 6 for the baroclinic wavy field, and 3 for the baroclinic zonal field, including the velocity correction equation). One additional modification that is made is to subtract the mean of the baroclinic velocity correction ( $U_2 - U_1$ ) from its fluctuating component. This is helpful because the rms deviation about the mean is about  $10^{-3}$  as large as the mean itself, and the separation of the two keeps integration errors to a minimum. When the system is integrated, the behavior simulates structural vacillation well, except the amplitudes are again too large. Thus, an *ad hoc* dissipation parameter was again used, except for the wavy fields it was applied to the lowest-energy pair of modes, since the EOFs act in a pairwise manner to produce traveling disturbances. The optimal value was found to be  $\rho \approx 0.30$ , which produces an average error in the four rms deviations and means of 25%. Almost all of the error is in the baroclinic zonal term, whose amplitude is about two times its nominal value. The dominant frequency of oscillation is in error by only about 1%, a negligible amount. In the structural regime all rms deviations are very small, and the matter of prime importance is to create correct phase relationships between the various modes such that the spatial dependence is replicated. Figures E.3,4 display the behavior of the fields over one period, which can be compared to the full-model behavior shown in Figures D.3,4 (the phases between the approximate and actual fields are again different). As with the PAV case, there is very good correspondence between the full and approximate solutions, which indicates that the approximate

model, while slightly amiss in amplitude, nonetheless generates the correct phase relations between the variables to produce accurate spatial fields.

Finally, the changes in rms deviations and means of the various flow quantities are almost negligible over the range in  $F$  for which PSV exists, so that the model trivially yields accurate predictions over a range in  $F$ . One important aspect to note is that the model does not predict the transition from PAV to PSV at  $F \approx 24$ , nor does it reflect PAV behavior for  $F < 24$ . This is due to the fact that the spatial fields for PAV are not contained in those seen in PSV, and vice versa. Thus, neither approximate system contains the information needed to display the alternate behavior. This is unfortunate, because it means that the model derived at  $F = 32$  is useless outside of a narrow range in  $F$  for which structural vacillation occurs, and the model derived at  $F = 20$  is useful only until PSV becomes dominant.

The last approximate system to be constructed is for the quasi-periodic regime that exists for  $34 \leq F \leq 40$ . In the middle of this regime, at  $F = 36$ , Figure 4.1 indicates that 32 EOFs are needed to meet the 99% variance threshold. Instead of obtaining a 32-dimensional system, it was decided to attempt to extract the essential features of the flow from a lower-dimensional model. Thus, a total of 16 equations were used: 4 for the barotropic wavy field, 2 for the barotropic zonal field, 6 for the baroclinic wavy field, and 3 for the baroclinic zonal field (as well as the requisite baroclinic correction equation). The percent of total variance captured by these EOFs is approximately 97%, 100%, 92%, and 99%, respectively, so that only the baroclinic wavy field is significantly truncated.

When the resulting system is integrated, the system exhibits quasi-periodic transients but eventually "blows up." In order to stabilize the system, ad hoc dissipation again was used. However, in contrast to the approximate systems in the periodic regimes, adding extra damping to only the lowest-energy modes does not yield impressive results. Quasi-periodic states are obtained for proper values of the

damping coefficient, but the amplitudes of the lower-energy modes are too high. The probable cause of this is the slower fall-off of variance in the EOF spectrum (in comparison to the periodic cases), which in turn results in a lack of dominance by the leading one or two modes. In order to mitigate this problem, a more sophisticated form of dissipation was used. Following Smith et al. (1991), dissipation was added to every mode in the form

$$\frac{da_i}{dt} \propto -\rho M^\alpha a_i. \quad (4.21)$$

In this equation,  $\rho$  is an arbitrary scale factor,  $M$  is the mode number (e.g.  $M = 1$  corresponds to the largest-energy mode), and  $\alpha$  is a scaling constant. For example, then, the differential equation for the sixth baroclinic wavy mode will be damped by the additional amount  $\rho 6^\alpha a_6$ . The representation given by Equation 4.21 has the effect of damping all the modes, but it preys most on the lower-energy, higher- $M$  modes, similar to the simple damping used in the periodic systems. In this analysis,  $\alpha = 2$  was chosen essentially arbitrarily, although the results do not seem to depend very strongly on this parameter.

A range of  $\rho$  values was found to yield a system that exhibits quasi-periodic behavior;  $\rho = 0.002$  gave the best correspondence with the actual flow. Retaining such a small number of modes virtually ensures that quantitative correspondence between the full and approximate fields is impossible, but qualitative agreement is a reasonable expectation, and this is indeed the case. Figure 4.20 displays the barotropic wavy  $\int \Psi^2 / 2 dA$  for the actual and approximate systems. The rms deviation of the approximate system is too large, but the behavior is qualitatively similar. In addition, the dominant frequencies of the two differ by only about 4%. Agreement between other quantities of interest is similar. Thus, a relatively low-dimensional dynamical system qualitatively captures the mixing between barotropic and baroclinic

instabilities that results in quasi-periodic behavior. A final analysis can be made by comparing the spatio-temporal behavior of the approximate fields, shown in Figures E.5,6, with the full solutions shown in Figures D.5,6. The agreement for this model is also very good, which is not too surprising since the behavior is much like the PSV state at  $F = 32$ .

One item worth mentioning is that larger amounts of damping result in the system returning to a PSV-type behavior. Thus, the equations seem to embody the behavior that occurs at smaller supercriticality than that at which the equations were derived. A direct test of this was not possible, however, since the resulting equations were too large to leave  $F$  as a free parameter. Also, higher-order systems were tried, but the difficulty in resolving the lower-energy modes, even with 300 temporal samples, resulted in numerical errors that prevented any significant improvement in model accuracy. In this case at least, the simplest model proved also to be the most accurate.

**4.7.2 Asymmetric Case** Approximate dynamical systems were constructed for three settings in the asymmetric regime: one in the PSV regime, one in the quasi-periodic region, and one where the flow is fully chaotic. The PSV system was derived at  $F = 20$ , near the transition to quasi-periodicity. The results are very similar to the approximate system obtained in the symmetric PSV regime. The number of equations used was 4 for the barotropic wavy field, 1 for the barotropic zonal field, 6 for the baroclinic wavy field, and 1 for the baroclinic zonal field (i.e. the number needed to meet the 99% variance criterion), along with the baroclinic velocity correction equation. This resulted in a system of 15 ODEs. Simple damping of the last pair of modes of each of the wavy fields was again necessary in order to obtain reasonable amplitudes. For a damping value of  $\rho = 0.2$ , the average error in the means and standard deviations of the  $\int \Psi^2 / 2dA$  values is about 25%, comparable to the symmetric-case results. However, in this instance, the barotropic wavy field

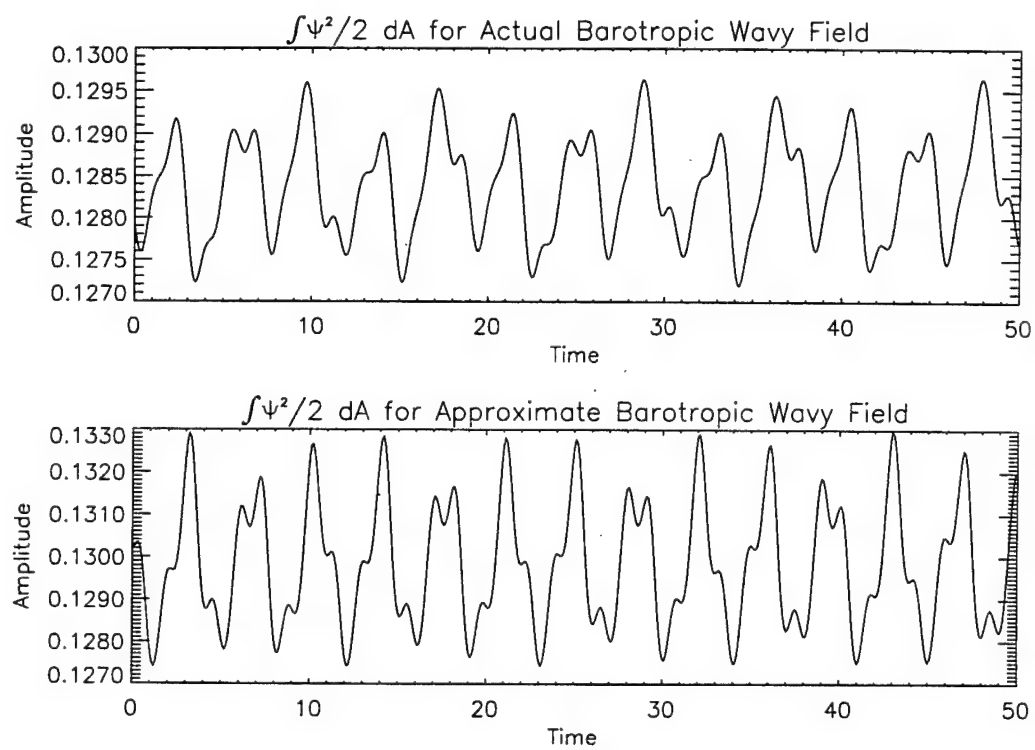


Figure 4.20. Comparison of  $\int \Psi^2/2 dA$  of barotropic wavy field between full and approximate models.  $F = 36$ , symmetric case.

rms deviation is in error by the greatest amount, being approximately two times too large. The apparent culprit is the subtle phase relationship between the various modes; the rms deviation of the above area-integrated quantity is actually smaller than the rms deviations of the individual modes, indicating that the phases of the various modes must be correctly aligned in order to produce a signal of the proper amplitude. Regardless, the approximate system does a credible job of reproducing the spatial and temporal behavior of the original flow. This can be seen in Figures E.7,8, which show the temporal evolution of the wavy fields for the approximate system (the full fields lag the approximate fields by about five frames). There is very close correspondence with the full flow shown in Figures D.7,8 (note that the phases between the full and approximate results are shifted with respect to each other). Thus, although the energy amplitudes of the approximate system are slightly askew, the spatial behavior of the flow is left intact.

The second case considered is at  $F = 28$ , in the quasi-periodic regime. The crucial difference between this quasi-periodic case and the one seen in the symmetric state is the “complexity” of the system as quantified by the number of EOFs required to meet the 99% variance threshold. In both cases, the number of zonal EOFs required is small ( $\leq 5$ ); however, in the symmetric solution, 8 barotropic wavy EOFs and 18 baroclinic wavy EOFs are needed, while the asymmetric solution requires 18 barotropic wavy EOFs and 37 baroclinic wavy EOFs. Thus, the asymmetric regime requires about twice as many modes. Consequently, the approximate dynamical system needs to be that much larger in order to capture the essential dynamics. Unfortunately, however, the implementation used here to obtain the ODEs is very memory- and time-intensive computationally. It is simply not possible to represent the baroclinic wavy field with, for example, 30 modes. Therefore, the correspondence between the full and approximate systems is more qualitative than quantitative. The final choice for the approximate system includes 8 barotropic wavy modes,

2 barotropic zonal modes, 12 baroclinic wavy modes, 4 baroclinic zonal modes, a velocity correction term, and a mass correction term (this must now be included since it is nonzero in the full model), for a total of 28 equations. The baroclinic wavy field is clearly the most under-represented, with the first 12 modes accounting for about 90% of the total variance; the first 8 barotropic wavy modes account for 95% of its total variance, while both sets of zonal EOFs meet the original 99% threshold. The damping is again spread over the entire set of EOFs, just as was done with the symmetric quasi-periodic solution, with  $\alpha = 2$  and  $\rho = 0.0002$ . A comparison of the actual time series of the barotropic wavy  $\int \Psi^2/2 dA$  with its reconstructed evolution is given in Figure 4.21. The figure shows that the rms deviation of the reconstructed time series is too small relative to the actual time trace. Additionally, although the dominant frequency in the power spectrum of the reconstructed time series is the same as that of the full model, there is also a prominent high-frequency oscillation that doesn't appear in the original time series. This is possibly because the components related to the structural vacillation, which indeed are of a higher frequency, are not suppressed enough in the approximate model. A final comparison may be made by examining Figures E.9,10, which display, respectively, the baroclinic and barotropic wavy fields at uncorrelated times. The spatial scales are certainly the same as those seen in the full model (see Figures D.9,10), and there appears to be some quantitative correspondence in the actual spatial patterns. Overall, however, this approximate model should be taken as more of a qualitative reflection of the dynamics of the asymmetric, quasi-periodic solution.

The final case to examine is in the chaotic regime at  $F = 32$ , which is just slightly above the quasi-periodic-chaotic transition point. At this value of  $F$ , a total of approximately 90 EOFs are required to meet the variance threshold. However, the construction of a set of 90 ODEs is obviously far beyond the capacity of even a relatively fast computer, at least given the algorithms used for this analysis. It should

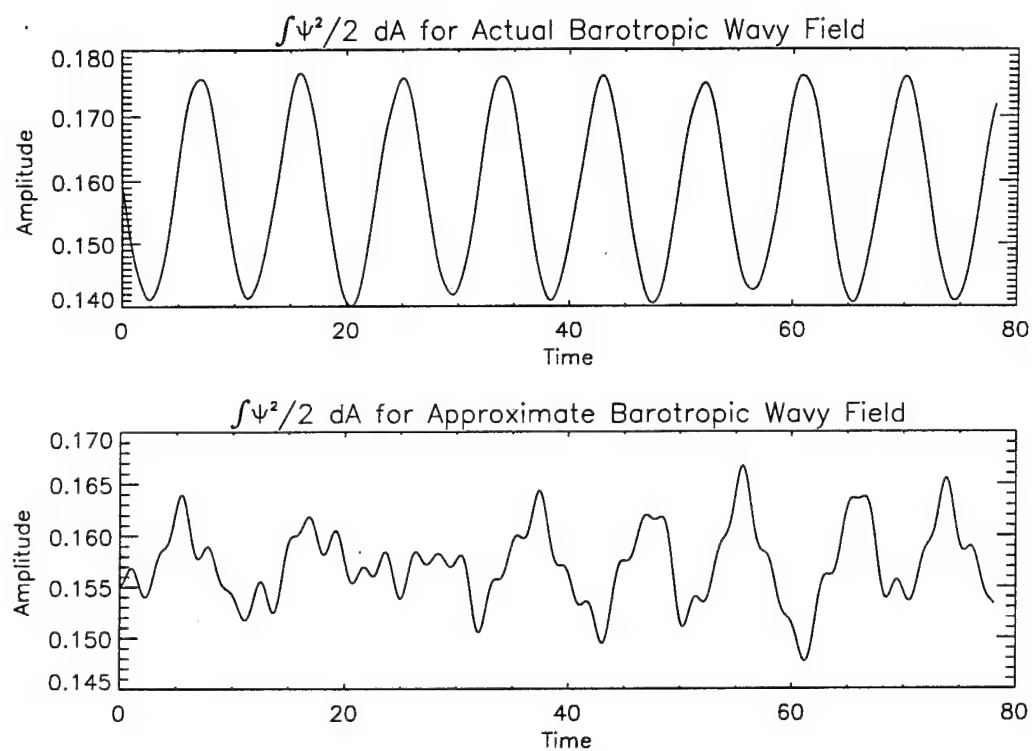


Figure 4.21. Comparison of  $\int \Psi^2/2 dA$  of barotropic wavy field between full and approximate models.  $F = 28$ , asymmetric case.

be noted that the time required to perform an  $N^2$ -mode simulation with a pseudo-spectral code is approximately  $O(N^3)$ . For a fully spectral model, however, the time is proportional to  $O(N^6)$ . For large enough values of  $N$ , the spectral approach therefore becomes self-defeating. Thus, several smaller systems of various sizes were attempted. The final system used was equivalent to that constructed at  $F = 28$ , in the quasi-periodic region: 8 barotropic wavy modes, 12 baroclinic wavy modes, 2 barotropic zonal modes, 4 baroclinic zonal modes, 1 baroclinic velocity correction, and 1 mass correction term, yielding a total of 28 equations. Again, the baroclinic wavy field is the least resolved, with the first 12 modes accounting for slightly more than 80% of the total variance. Damping equivalent to that used for  $F = 28$  was implemented, with  $\alpha = 2$  and  $\rho = 0.0002$ . A comparison of the actual time series of the barotropic wavy  $\int \Psi^2 / 2 dA$  with its reconstructed evolution is given in Figure 4.22. The rms deviations are similar, but the presence of the higher-frequency is again too prominent in the approximate system in comparison to the full results. In addition, other quantities of the approximate system, such as the baroclinic wavy component, have rms deviations twice as large as in the full model.

A visual comparison can be made by examining the evolution of the approximate spatial fields, shown in Figures E.11,12, with the full solutions displayed in Figures D.11,12. The baroclinic field displays the correct scales, if not the same quantitative behavior, but the approximate barotropic field seems to be dominated by a wavenumber-2 disturbance. The full solution, conversely, tends to exhibit smaller scale disturbances. In summary, the agreement between full and approximate solutions in the more complex instances is not exemplary. There is some qualitative corroboration in terms of spatial and temporal scales, but the precise interactions are not well preserved. This is not unexpected in light of the severe truncations necessary to obtain a system that is of a manageable size.

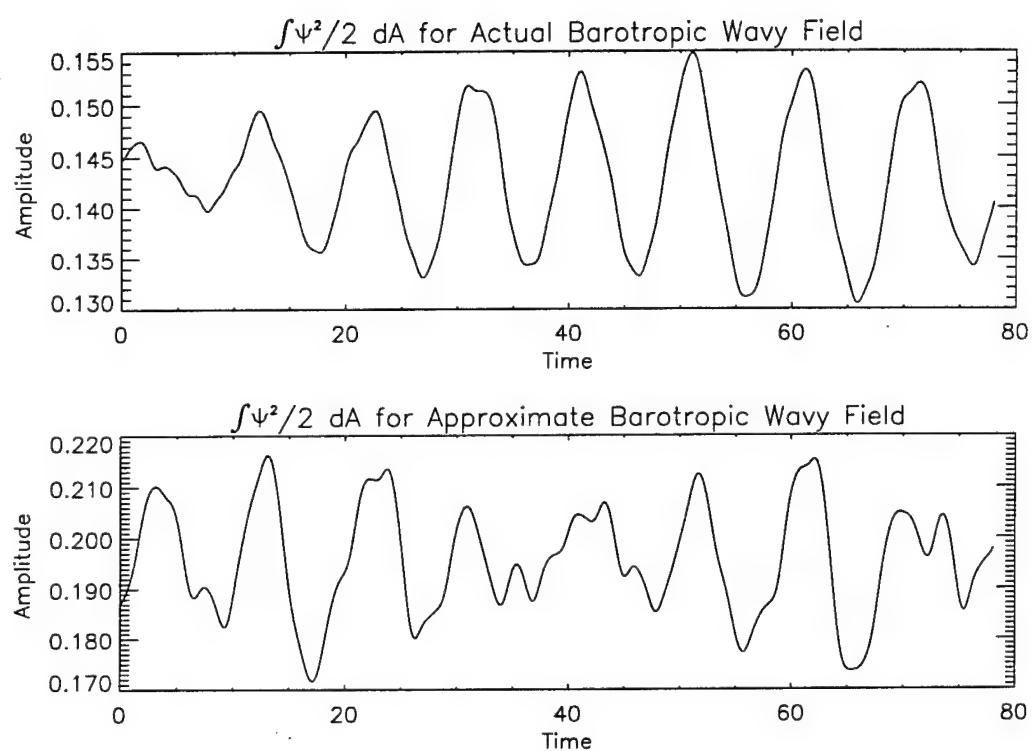


Figure 4.22. Comparison of  $\int \Psi^2/2 dA$  of barotropic wavy field between full and approximate models.  $F = 32$ , asymmetric case.

#### 4.8 EOFs Versus Linear Eigenfunctions

One final analysis that can be performed with the EOFs is to compare them to the linear eigenfunctions displayed at the end of Chapter 3. It is conceivable that the linear disturbances, although necessarily modified by the nonlinear terms, may remain the dominant spatial structure of the flow at finite amplitude. This corroboration is of importance for at least two reasons. First of all, it gives a physical basis to the computed EOFs. In addition, it allows one to know the EOFs *a priori*, so that one may use them in a low-order analytical formulation. This is currently not possible with the numerically-obtained EOFs. The technique is most applicable at the onset of a primary instability, or where the full model is in a purely periodic state.

Figure 3.7 shows the eigenfunctions at the onset of symmetric PAV, which for the quasi-linear calculations (done in Chapter 3) occurs at  $F = 12$ . For the full model, the onset is also at  $F = 12$ . Figure 4.23 displays the first two EOFs of both the barotropic wavy field and the baroclinic wavy field at  $F = 12$  in the symmetric state. The first two modes in each field account for 99% of the total variance of their respective fields. Correlation coefficients were calculated for each mode. For the barotropic field, the coefficients are 0.98 and 0.86 for the first two eigenfunctions, respectively; for the baroclinic field, the coefficients are 0.97 and 0.93. This indicates that the linear eigenfunctions are indeed the main contributors to the spatial dependence of the flow, being modified only slightly by the nonlinearities.

The onset of symmetric PSV occurs at  $F = 24$ , and Figure 4.24 displays the EOFs at this parameter value. The quasi-linear analysis indicates the onset of PSV to occur at  $F = 17$ ; the corresponding linear eigenfunctions due to this instability, calculated at  $F = 24$  for comparison, are shown in Figure 3.8. Again, there is very good agreement between the two resulting spatial maps. The correlation coefficients for the barotropic field are 0.96 and 0.94, while those for the baroclinic field are

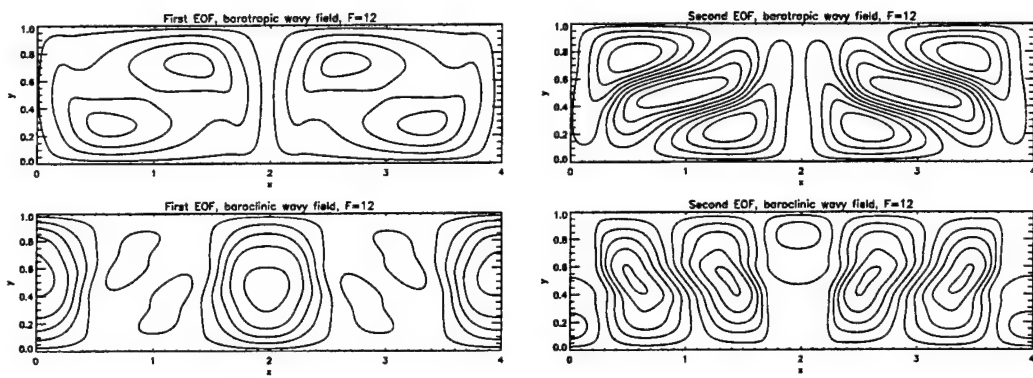


Figure 4.23. First two EOFs of barotropic and baroclinic wavy fields,  $F=12$ , symmetric case

0.80 and 0.79. The coefficients for the barotropic field compare to those in the PAV regime, while those for the baroclinic field are only slightly worse. However, the agreement should not be expected to be as good, because the first two barotropic wavy EOFs account for 98% of the total variance of that field, while the two primary baroclinic wavy EOFs only account for 93% of the total variance of their field. This indicates that the nonlinear terms act to entrain other modes as well, so that the linear eigenfunctions are not the only spatial fields participating in the vacillation. These results also indicate that the counter-rotating eddy structure is firmly entrenched in the linear eigenfunctions themselves and is not purely a consequence of the nonlinearity.

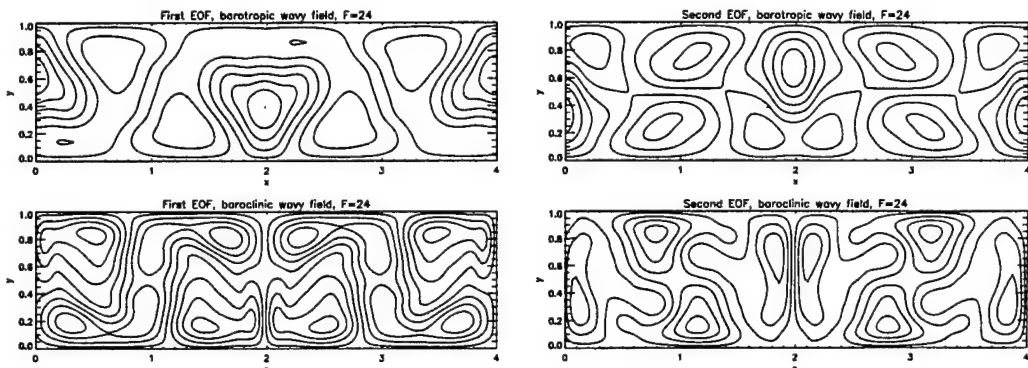


Figure 4.24. First two EOFs of barotropic and baroclinic wavy fields,  $F=24$ , symmetric case

Finally, a comparison can be made in the asymmetric regime. The quasi-linear analysis indicates that the initial asymmetric PSV instability occurs at  $F = 11$ , and Figure 3.9 shows the linear eigenfunctions from this instability at  $F = 16$ . The numerical model first exhibits asymmetric PSV at  $F = 13$ . EOFs were computed just slightly above this parameter value, at  $F = 16$ , and the first two of each wavy field are displayed in Figure 4.25. The first two barotropic EOFs represent 98% of the total variance, while the first two baroclinic EOFs represent only 88% of the

total variance. After a correction is made for the arbitrary phase shift between the fields, the correlation coefficients are calculated to be 0.94 and 0.73 for the barotropic fields, and 0.76 and 0.72 for the baroclinic fields. The agreement is thus not quite as good as for the symmetric PSV regime, but it nonetheless indicates that the full model's behavior in the asymmetric regime is partially described by the linear eigenfunctions. The agreement may not be as favorable because the resolution used by the quasi-linear analysis for the asymmetric solution is smaller than that used for the symmetric state.

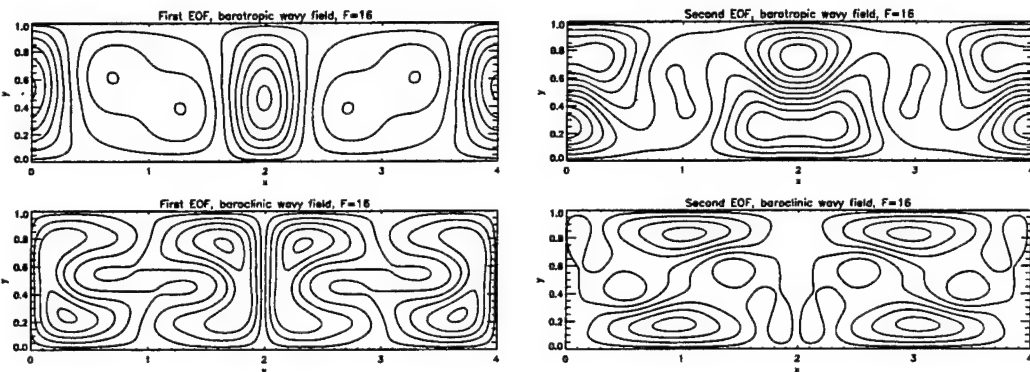


Figure 4.25. First two EOFs of barotropic and baroclinic wavy fields,  $F=16$ , asymmetric case

In summary, the linear eigenfunctions correlate well with the EOFs calculated from the full model. This indicates that the nonlinearities act only to slightly modify these instabilities. One could possibly exploit this information to construct low-order analytical models that could be used to at least study PAV and PSV. It is not, however, clear whether one could improve upon the models generated using EOF basis functions, since these pseudo-optimally represent the **actual** flow field.

#### 4.9 Discussion

The use of EOFs provides one with a measure of the spatio-temporal "complexity" of the system under consideration. Furthermore, this complexity, as measured by the number of EOFs needed to meet a particular variance threshold, is proportional to the temporal complexity of the flow (which also results in an increase in spatial complexity). Nonetheless, the actual number of spatio-temporal pairs needed can be quite astonishing, even for non-chaotic flows. The use of EOFs is also useful for extracting some of the relevant physics of the problem. For example, the pairing of eigenvalues seen in the PSV regimes indicates traveling wave phenomena in the form of counter-rotating eddies, which subsequently helps to explain the periodic, spatial transfer of energy that occurs in these regimes.

EOFs were also used to create approximate dynamical systems which mimic the original flow, but with far fewer degrees of freedom. For the purely periodic and simpler quasi-periodic cases, the method is shown to be quite viable, yielding results very close to the original solutions. The result is qualitatively successful in the more complicated quasi-periodic and chaotic regimes, but the large number of modes required to meet the 99% variance threshold is a barrier to obtaining a quantitatively-accurate model. The idea of inertial manifolds discussed by Sirovich et al. (1990c) is a possible solution to this computational problem, but it would require a comprehensive investigation in order to assess the viability of such an approach. Nonetheless, the results are still useful for the insight they give into the complexity of these highly-supercritical flows, and they also reveal the limitations of low-dimensional dynamical systems as paradigms for understanding such behavior.

Finally, the primary EOFs at the onset of both PAV and PSV behavior are shown to correlate very highly with the linear eigenfunctions of the associated instabilities. This indicates that the flow, at least in the periodic regimes, is largely influenced by the structures of the secondary instabilities.

## CHAPTER 5

### A RIGID-WALL MODEL OF BAROCLINIC INSTABILITY: THE LINEAR INSTABILITY PROBLEM

This chapter describes the two-layer, quasi-geostrophic model with rigid (i.e. no-slip) sidewalls. First, the governing equations are re-introduced with slightly different notation. Next, the exact basic-state solution and the boundary conditions are discussed. Finally, a solution method to the linear stability of the basic flow is formulated and its results interpreted.

#### 5.1 Governing Equations

The equations governing the rigid model are identical to those governing the slippery version. However, the notation used is slightly different, and it is useful to briefly clarify the alterations. The barotropic and baroclinic streamfunctions can be written (similar but not identical to the form in Equations 1.16,17) as

$$\Phi_{bt} = \frac{1}{2}(P_1 + P_2), \quad (5.1)$$

$$\Phi_{bc} = \frac{1}{2}(P_1 - P_2), \quad (5.2)$$

respectively. The vorticity equations, then, are nearly equivalent to Equations 1.18,19 and are written as follows:

$$\begin{aligned} \frac{\partial}{\partial t} \nabla^2 \Phi_{bt} - J[\nabla^2 \Phi_{bt}, \Phi_{bt}] - J[\nabla^2 \Phi_{bc}, \Phi_{bc}] = \\ -\frac{Q}{2}[(1 + \chi) \nabla^2 \Phi_{bt} - (1 - \chi) \nabla^2 \Phi_{bc}] + \frac{E}{R_o} \nabla^4 \Phi_{bt}, \end{aligned} \quad (5.3)$$

$$\frac{\partial}{\partial t} [\nabla^2 \Phi_{bc} - 2F \Phi_{bc}] - J[\nabla^2 \Phi_{bc}, \Phi_{bt}] - J[\nabla^2 \Phi_{bt}, \Phi_{bc}] -$$

$$2FJ[\Phi_{bt}, \Phi_{bc}] = -\frac{Q}{2(\chi+1)} [-(1-\chi^2)\nabla^2\Phi_{bt} + (\chi^2 + 6\chi + 1)\nabla^2\Phi_{bc}] + \frac{E}{R_o}\nabla^4\Phi_{bc}. \quad (5.4)$$

The physical meanings of the various terms are unchanged from Chapter 1.

In order to preserve the aspect ratio used in the slippery code while also facilitating computational solutions, the domain of the flow for the rigid code is  $0 \leq x \leq 8$ ,  $-1 \leq y \leq 1$  (the domain for the slippery code, recall, is  $0 \leq x \leq 4$ ,  $0 \leq y \leq 1$ ). The boundary conditions are

$$u_{bt} = v_{bt} = 0, \quad (5.5)$$

$$u_{bc} = v_{bc} = 0, \quad (5.6)$$

at  $y = \pm 1$ .

## 5.2 Basic State

For the slippery model, the simplest flow that satisfies the equations is  $u = C$ , where  $C$  is an arbitrary constant. Thus, the basic flow has no dependence on either  $x$  or  $y$ . For the rigid model, however, the requirement that  $u = 0$  at the walls indicates that the velocity must have some meridional dependence on  $y$  (unless  $u=0$  everywhere, which is rather uninteresting). The exact solution can be obtained by examining Equations 5.3,4. If one dictates that there be no barotropic basic state, then only Equation 5.4 survives, and it can subsequently be simplified to yield the exact equation

$$-2Q \frac{d^2\Phi_{bc}}{dy^2} + \frac{E}{R_o} \frac{d^4\Phi_{bc}}{dy^4} = 0. \quad (5.7)$$

The solution to this is

$$\Phi_{bc} = -y + \frac{\sinh \Gamma y}{\Gamma \cosh \Gamma y}, \quad (5.8)$$

where

$$\Gamma \equiv \sqrt{\frac{2Q}{E/R_o}}. \quad (5.9)$$

The boundary-layer thickness is  $O(1/\Gamma) = O(E^{1/4})$ , and the problem is equivalent to that examined by Stewartson (1957). The resulting basic state velocity profile is then given by

$$U_{bc} = \frac{-\partial \Phi_{bc}}{\partial y} = 1 - \frac{\cosh \Gamma y}{\cosh \Gamma} \quad (5.10)$$

and can be normalized by the factor  $1/(1 - (\cosh \Gamma)^{-1})$  so that the maximum velocity in the channel is 1. For large  $\Gamma$ , the profile is essentially unity, except near the meridional boundaries where the velocity must approach zero; for  $\Gamma \approx O(1)$ , the profile more resembles that of a parabola. The velocity profile is shown in Figure 5.1 for three values of  $\Gamma$ :  $\sqrt{10}$ ,  $\sqrt{100}$ , and  $\sqrt{1000}$ .

It should be noted that plausible values of  $\Gamma$  are physically constrained. In terms of the fundamental physical parameters,

$$\Gamma^2 = 2 \frac{L}{H} \frac{L}{\sqrt{\nu/\Omega}}. \quad (5.11)$$

The first term,  $L/H$ , is much greater than  $O(1)$  for geophysical flows and is approximately  $O(1)$  for laboratory experiments. The second term is the ratio of the horizontal length scale of the flow to the Ekman layer thickness, a ratio whose value

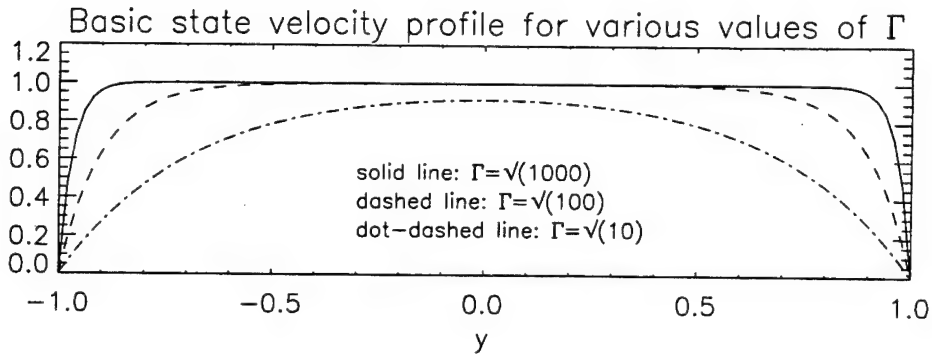


Figure 5.1. Basic state velocity profiles for  $\Gamma = \sqrt{10}$  (dot-dashed line),  $\sqrt{100}$  (dashed line), and  $\sqrt{1000}$  (solid line).

is always much greater than one. Thus  $\Gamma^2$ , and subsequently  $\Gamma$ , should be much greater than one to be physically reasonable.

### 5.3 Zonal Flow Boundary Conditions

The boundary conditions on the zonal flow are obtained in a manner similar to that followed for the slippery model. As with the slippery model, the mass must be conserved, so that Equation B.3 holds. In addition, an appeal must again be made to the zonally-averaged momentum equation at the walls. Equations B.7,8 give this relation in terms of the perturbation layer streamfunctions, where the perturbation is defined to be the total streamfunction minus the basic state. Converting these into relations for the total barotropic and baroclinic streamfunctions, and noting that the velocity at the walls is zero for the rigid case, one obtains

$$\frac{\partial^2}{\partial y^2} \bar{u}_{bc} = \Gamma^2, \quad (5.12)$$

$$\frac{\partial^2}{\partial y^2} \bar{u}_{bt} = 0. \quad (5.13)$$

Here the quantities  $\bar{u}_{bc}$  and  $\bar{u}_{bt}$  are the total velocities (basic state plus perturbations). The right hand side of Equations 5.13 is zero as shown if no basic zonal barotropic flow exists. If instead a zonal, barotropic basic state is included, then the

right hand side of Equation 5.13 must equal  $\Gamma^2/2$ . The basic-state solution given by Equation 5.10 already satisfies the conditions 5.12,13, so any perturbations to the basic state must satisfy

$$\frac{\partial^2}{\partial y^2} \bar{u}'_{bc} = 0, \quad (5.14)$$

$$\frac{\partial^2}{\partial y^2} \bar{u}'_{bt} = 0, \quad (5.15)$$

with the ' indicating a perturbation quantity. The above condition is analogous to that imposed by Equations B.7,8 for the slippery model, the difference being that the requirement applies to the velocity itself for the slippery implementation.

#### 5.4 Linear Theory

The linear theory for the rigid code is approached in the same manner as that for the slippery model (see Section 1.4), but the details are somewhat different. Consequently, it is useful to briefly summarize the methodology. Linearizing Equations 5.3,4 yields the following relations:

$$\begin{aligned} & \left[ \frac{\partial}{\partial t} + U_{bt} \frac{\partial}{\partial x} \right] q_{bt} + U_{bc} \frac{\partial}{\partial x} q_{bc} + \frac{\partial \phi_{bt}}{\partial x} \frac{\partial \Pi_{bt}}{\partial y} + \frac{\partial \phi_{bc}}{\partial x} \frac{\partial \Pi_{bc}}{\partial y} = \\ & -Q \nabla^2 \phi_{bt} + \frac{E}{R_o} \nabla^4 \phi_{bt}, \end{aligned} \quad (5.16)$$

$$\begin{aligned} & \left[ \frac{\partial}{\partial t} + U_{bt} \frac{\partial}{\partial x} \right] q_{bc} + U_{bc} \frac{\partial}{\partial x} q_{bt} + \frac{\partial \phi_{bc}}{\partial x} \frac{\partial \Pi_{bt}}{\partial y} + \frac{\partial \phi_{bt}}{\partial x} \frac{\partial \Pi_{bc}}{\partial y} = \\ & -2Q \nabla^2 \phi_{bc} + \frac{E}{R_o} \nabla^4 \phi_{bc}. \end{aligned} \quad (5.17)$$

Similar to the results presented in Section 1.4,  $q_{bt}$  and  $q_{bc}$  are, respectively, the barotropic and baroclinic perturbation potential vorticities and are defined as

$$q_{bt} = \nabla^2 \phi_{bt}, \quad (5.18)$$

$$q_{bc} = \nabla^2 \phi_{bc} - 2F \phi_{bc}, \quad (5.19)$$

$\Pi_{bt}$  and  $\Pi_{bc}$  are the potential vorticities of the basic state and have gradients given by

$$\frac{\partial \Pi_{bt}}{\partial y} = -\frac{\partial^2 U_{bt}}{\partial y^2}, \quad (5.20)$$

$$\frac{\partial \Pi_{bc}}{\partial y} = -\frac{\partial^2 U_{bc}}{\partial y^2} + 2FU_{bc} = (1 - U_{bc})\Gamma^2 + 2FU_{bc}, \quad (5.21)$$

and  $U_{bt}$  and  $U_{bc}$  are, respectively, the barotropic and baroclinic basic state zonal velocities.  $U_{bc}$  is given by Equation 5.8, while  $U_{bt}$  is generally chosen to be zero for the computations presented here. Equation 5.21 is obtained with the use of Equation 5.10.

For the slippery model, the governing equations have constant coefficients, since  $U_{bc} = \text{constant}$ . As a result, the form indicated by Equation 1.22 is an exact solution of the equations and is therefore eliminated upon substitution into Equations 1.13,14 (this situation also necessitates that the  $y$ -dependence of  $\phi_n$ , denoted as  $f_n(y)$ , be such that  $f_n''(y) = -C f_n(y)$ , where  $C$  is an arbitrary constant). For the rigid model, the meridional dependence of the stream functions (i.e. pressure) is given by a family of functions,  $g_n(y)$ ,  $n = 0, 1, 2, \dots$ , where

$$g_n(y) = T_{n+4}(y) - \frac{2n+4}{n+1}T_{n+2}(y) + \frac{n+3}{n+1}T_n(y) \quad (5.22)$$

and

$$T_n(y) = \cos[n \cos^{-1} y] \quad (5.23)$$

is a Chebyshev polynomial of the first kind. The functions  $g_n(y)$  have the property that  $g_n(\pm 1) = g'_n(\pm 1) = 0$  so that the boundary conditions on the velocity are satisfied (see Figure 5.2).

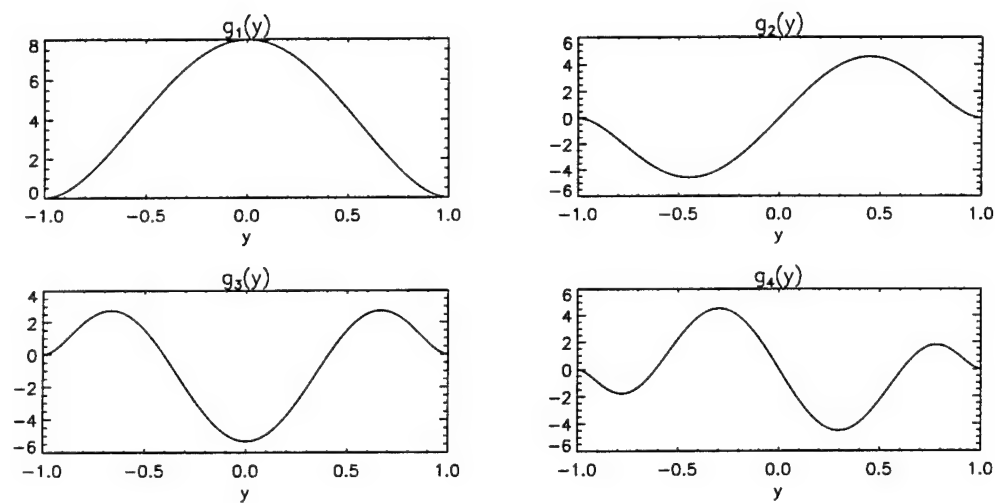


Figure 5.2. First four basis functions  $g_i(y)$ ,  $i = 1, 2, 3, 4$ , for the rigid, linear instability problem.

A disturbance  $\{\phi_{bt}, \phi_{bc}\}$  is taken to be

$$\phi_{bt} = Re \sum_{n=0}^{M-1} a_n g_n(y) e^{ik(x-ct)}, \quad (5.24)$$

$$\phi_{bc} = Re \sum_{n=0}^{M-1} b_n g_n(y) e^{ik(x-ct)} \quad (5.25)$$

where  $\{\phi_{bt}, \phi_{bc}\} = \{\phi'_{bt}, \phi'_{bc}\} = 0$  at  $y = \pm 1$  (the prime denotes differentiation with respect to  $y$ ). The expressions given in Equations 5.24,25 are substituted into Equations 5.16,17 and the resulting equations are projected back onto the basis functions  $g_n(y)$  via a Galerkin projection. This results in a set of linear, homogeneous equations for the  $a_n$  and  $b_n$  yielding an eigenvalue problem where  $c$  plays the role of the eigenvalue and the corresponding eigenvector yields the meridional structure of the disturbance. The parameter  $M$  is increased to include successively more modes until the results display convergent behavior.

In order to be consistent with the stability calculations for the slippery configuration, the basic velocity is re-scaled (as previously discussed) in order to achieve a flow velocity of unity at  $y = 0$ . In addition, because  $\Gamma$  is the relevant parameter in shaping the basic flow profile, this quantity is kept fixed for stability calculations; a choice for  $Q$  then automatically determines the value of  $E/R_o$  that is to be used. The critical value of  $F$  required for instability can then be calculated in a straightforward manner for a particular  $(\Gamma, Q, E/R_o)$  trio.

## 5.5 Results

**5.5.1  $U_{bc} \neq 0, U_{bt} = 0$ :** With the barotropic basic state equal to zero, the system has top-bottom symmetry. Therefore, the growing wavy modes are non-propagating ( $c_r = 0$ ) and the critical layers are at the wall. Figures 5.3,4,5 display the stability curves, for the rigid case, for  $M = 20$  (i.e. 11 even modes) with  $\Gamma$  equal to  $\sqrt{10}$ ,  $\sqrt{100}$ , and  $\sqrt{1000}$ , respectively. Because the initial instability entrains only the

even Chebyshev modes (i.e. those which are symmetric about  $y = 0$ ), the odd basis functions were not included in the calculations. The average difference in calculated values of  $F_c$  using  $M = 18$  instead of  $M = 20$  was found to be 0.33%, where the differences were calculated for all curves in Figures 5.3,4,5. Moreover, the largest errors, which are about 3%, occur only when  $\Gamma$  is large and  $Q$  is small. Therefore, a resolution of  $M = 20$  was deemed to give adequately-resolved results (valid results at higher values of  $M$  are difficult to achieve because of round-off errors that occur in the evaluation of integrals of products of Chebyshev functions and the basic state when high-order Chebyshev polynomials are included). The counterintuitive effect that rigid-wall flows are more unstable for small dissipation is not an artifact of the resolution used. Also plotted are the results for the slippery model (with the domain rescaled to  $0 \leq x \leq 8, -1 \leq y \leq 1$ ). For all three values of  $\Gamma$ , the rigid model is more stable at large values of  $Q$  (i.e., the bottom friction parameter) but less stable at small values of  $Q$ . In addition, the lowering of  $F_c$  with decreasing  $Q$  is more pronounced for smaller values of  $\Gamma$ .

Insight as to the cause of the relative destabilization of the rigid-wall flow for small  $Q$  can be obtained analytically. We first assume that the perturbation boundary layer, which brings tangential velocities to zero at the walls, is much thinner than the zonal-flow boundary layer, which has a thickness of  $1/\Gamma$ . Due to this constraint,  $U_{bc} \approx 0$  in the wave boundary layer that is attached to the no-slip sidewall. We also note that the numerical results reveal that the meridional dependences of  $\phi_{bt}$  and  $\phi_{bc}$  are such that one is purely real and the other is purely imaginary, which allows us to denote the barotropic meridional function as  $f(y)$  and the baroclinic function as  $g(y)$ , where  $f$  and  $g$  are either purely real or purely imaginary functions. For  $y \approx \pm 1$ , then, Equations 5.16,17 simplify to yield boundary-layer equations near

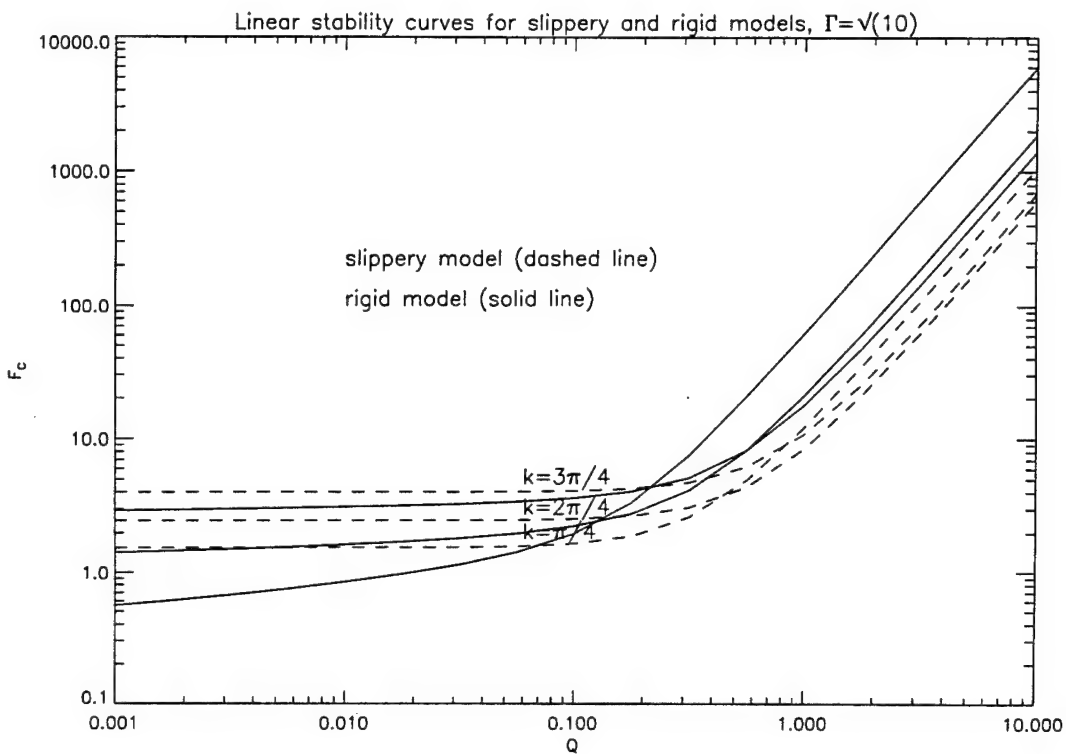


Figure 5.3: Linear stability curves for slippery and rigid models,  $\Gamma = \sqrt{10}$ .

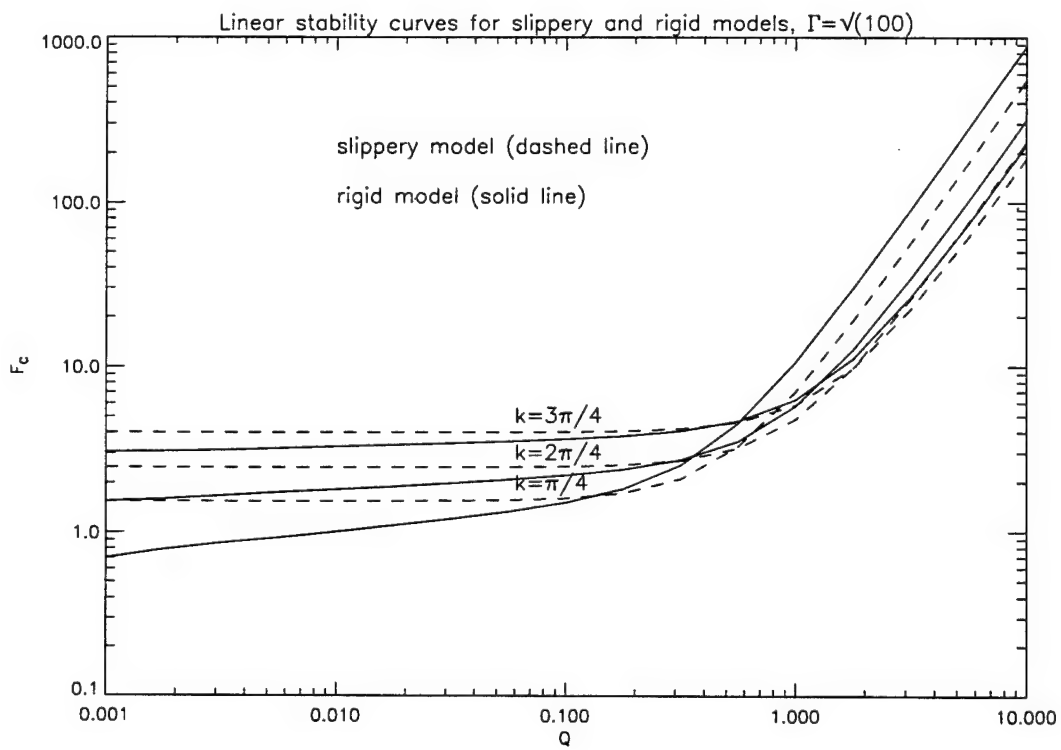


Figure 5.4: Linear stability curves for slippery and rigid models,  $\Gamma = \sqrt{100}$ .

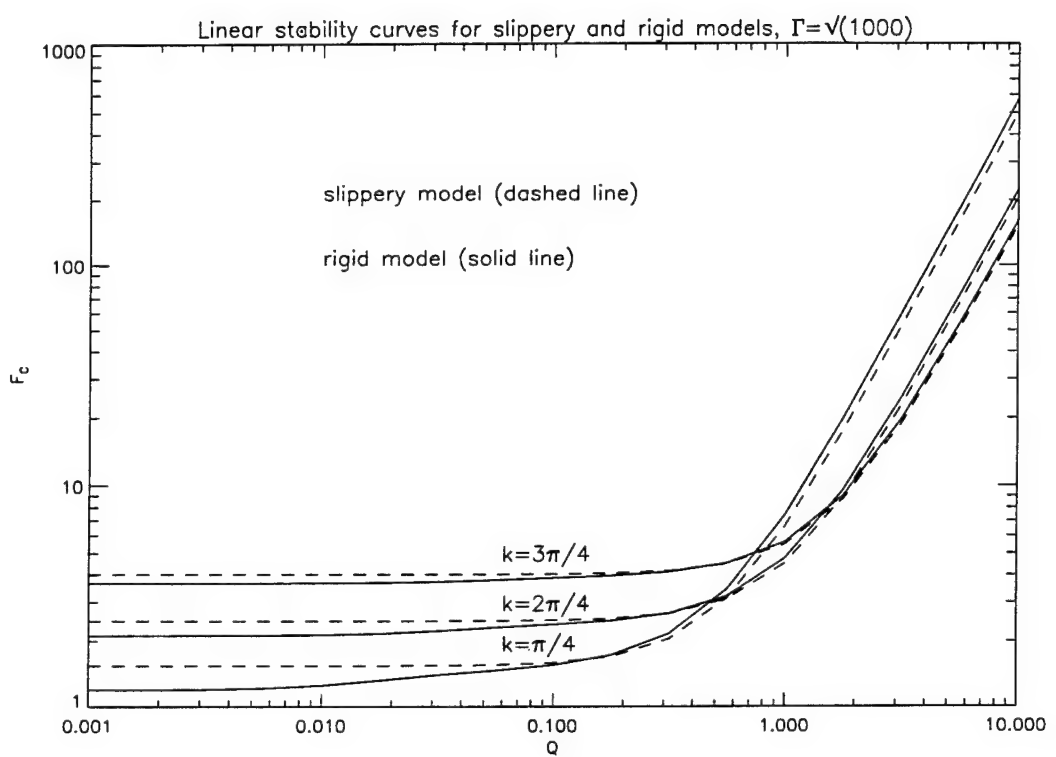


Figure 5.5: Linear stability curves for slippery and rigid models,  $\Gamma = \sqrt{1000}$ .

the walls:

$$ik\Gamma^2 g(y) = \frac{E}{R_o} f''''(y), \quad (5.26)$$

$$ik\Gamma^2 f(y) = \frac{E}{R_o} g''''(y), \quad (5.27)$$

so that the meridional advection of basic-state vorticity is balanced by the dissipation of vorticity due to lateral friction. The wave boundary layer thus has a thickness

$$\lambda \equiv \left( \frac{E/R_o}{\Gamma^2} \right)^{1/4} = \frac{(2Q)^{1/4}}{\Gamma} \quad (5.28)$$

given that  $k \approx O(1)$ . Therefore, the ratio of the wave boundary layer thickness to the zonal boundary layer thickness is  $(2Q)^{1/4}$ , so that our initial assumption of a small relative boundary-layer thickness is consistent for a parameter setting  $Q \ll 1$ .

If the dissipation parameters  $(Q, E/R_o)$  are small, the functions  $f(y)$  and  $g(y)$  outside the wave boundary layer should be similar to those obtained by examining the inviscid form of Equations 5.16,17, where  $Q$  and  $E/R_o$  terms are neglected. An exact solution of these inviscid equations which satisfies no normal flow through the walls at  $y = \pm 1$  is

$$f = U_{bc}, \quad (5.29)$$

$$g = 0, \quad (5.30)$$

a result identical to that found by Pedlosky and Klein (1991) (who impose rigid-sidewall conditions on the basic state but not on the wavy perturbations). This solution requires that  $F_c = k^2/2$ . The dissipative terms are assumed only to give rise to a passive boundary layer of thickness  $\lambda$  (given by Equation 5.28) so that the no-slip boundary conditions at  $y = \pm 1$  are satisfied. At best a weak boundary

suction velocity will occur to modify slightly the boundary conditions on the interior solution shown in Equations 5.29,30. We can ask when the solution given by Equations 5.29,30 is expected to be applicable. Roughly, the solution is valid when it consistently predicts the dissipative terms to be small compared to the other terms in the equations. A scale analysis reveals that this occurs when

$$Q \ll \frac{1}{\Gamma^4}, \quad (5.31)$$

where Equation 5.28 is used as an estimate of the boundary-layer thickness for  $f(y)$ . The details of obtaining Equation 5.31 are shown in Appendix H. For values of  $Q$  that do not satisfy Equation 5.31, there will be departures from the behavior of Equations 5.29,30, and the slippery solution itself is a candidate when  $1/\Gamma^4 \leq Q \ll 1$  (this is the case because in this region,  $Q$  is small enough so that dissipative terms can be neglected, and  $\Gamma$  may be large enough so that the flow appears largely uniform in the meridional direction).

These predictions are borne out by numerical calculations of the meridional eigenfunctions of the wavy perturbations. Using up to  $M = 20$  modes (only the 11 even modes were included), the eigenfunctions were calculated for  $Q = 10^{-4}$  and  $\Gamma = \sqrt{10}$ , where the corresponding value of  $F_c$  is 0.428, slightly larger than the theoretical limit of  $F_c = k^2/2 = 0.308$  for  $k = \pi/4$ . The barotropic meridional mode (normalized so that its maximum amplitude is 1) is shown in Figure 5.6, along with the basic state velocity profile. Except for the requisite boundary layers on the barotropic mode at  $y = \pm 1$ , there is very close agreement between the two shapes. In addition, the analysis that yields Equation 5.31 also predicts that the baroclinic amplitude (relative to the  $O(1)$  barotropic amplitude) should be  $O(Q^{1/2}\Gamma^2) = O(10^{-1})$  when  $Q \ll \Gamma^{-4}$ . The numerical results yield an amplitude ratio of 0.135, which is in agreement with the prediction.

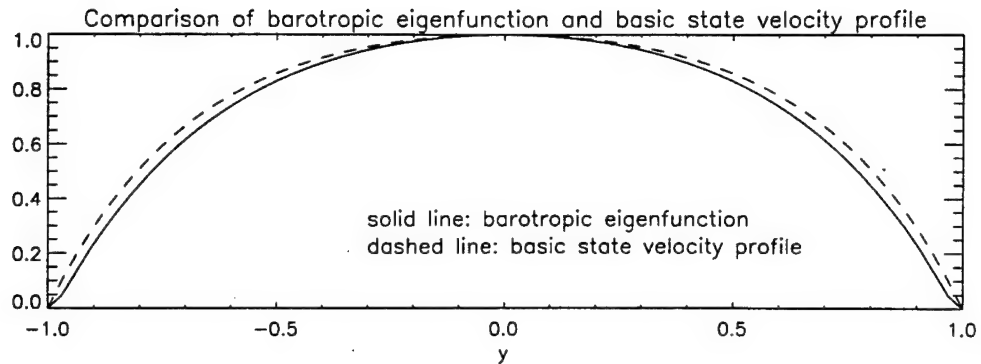


Figure 5.6. Comparison of barotropic eigenfunction with basic state velocity profile,  $Q = 10^{-4}$ ,  $\Gamma = \sqrt{10}$ . Both profiles are normalized to a maximum value of 1 for comparison.

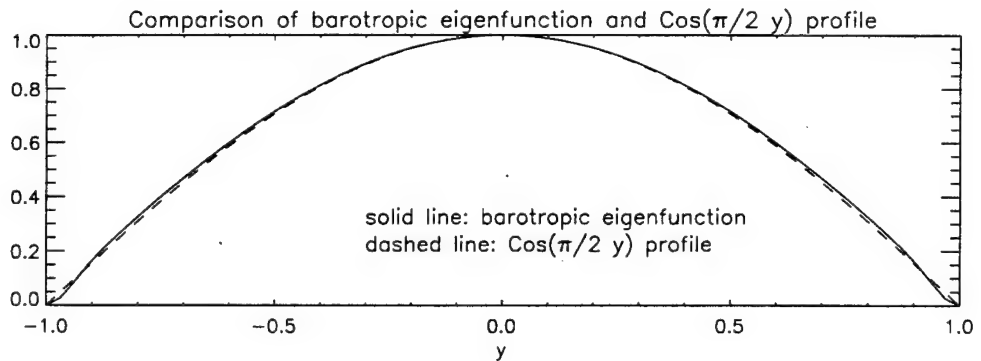


Figure 5.7. Comparison of barotropic eigenfunction with slippery case eigenfunction (i.e.  $\cos(\pi y/2)$ ),  $Q = 10^{-1}$ ,  $\Gamma = \sqrt{1000}$ . Both profiles are normalized to a maximum value of 1 for comparison.

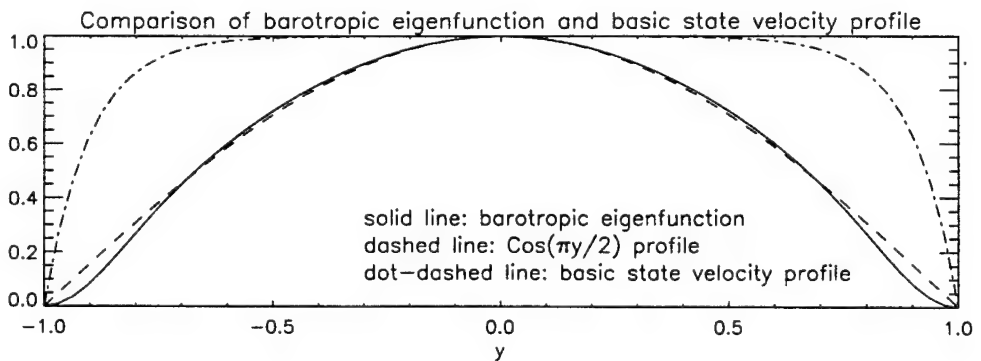


Figure 5.8. Comparison of barotropic eigenfunction with slippery case eigenfunction (i.e.  $\cos(\pi y/2)$ ) and basic state velocity profile,  $Q = 10^{-1}$ ,  $\Gamma = \sqrt{100}$ . All profiles are normalized to a maximum value of 1 for comparison.

Eigenfunctions were also calculated for  $Q = 10^{-1}$  and  $\Gamma = \sqrt{1000}$ , again using  $M = 20$  Chebyshev modes. For this case,  $F_c = 1.556$ , while the slippery value is  $F_c = 1.593$  when one includes frictional effects which are small but nonzero. The rigid-case barotropic eigenfunction and the slippery case profile, which is  $\cos(\pi y/2)$ , are shown in Figure 5.7. For comparison, the rigid-case profile is again normalized so that its maximum value is 1. Except for the boundary layers near  $y = \pm 1$  for the rigid solution, there is almost exact agreement in the shapes of the profiles. Additionally, the linearized equations predict a baroclinic eigenfunction amplitude of  $O(Q) = O(10^{-1})$ , while the numerical results yield a value of 0.185, so that the baroclinic eigenfunction is again consistent with the asymptotic analytical predictions. For comparison, the barotropic eigenfunction obtained for  $Q = 10^{-1}$  and  $\Gamma = \sqrt{100}$  is shown in Figure 5.8, along with the cosine and basic state profiles. At this parameter setting, which lies in between the two extremes discussed above, the barotropic eigenfunction is very similar to that obtained for the slippery case (i.e. a cosine solution).

The above results indicate that there are two very different solutions for small  $Q$ , depending on the relative sizes of  $Q$  and  $\Gamma$ . For  $\Gamma^{-4} \ll Q \ll 1$ , the solution approaches that of the slippery case and  $F_c = (k^2 + l^2)/2$ , where  $l$  is the meridional wavenumber of the barotropic wavy perturbation. For  $Q \ll \Gamma^{-4}$ , the solution approaches that given by Pedlosky and Klein (1991), where the barotropic wavy streamfunction is equal to  $U_{bc}$  while the baroclinic streamfunction is zero. The establishment of these two solutions as different limits of the nearly-inviscid case helps to provide an explanation of the lower stability threshold of the rigid case compared to the free-slip situation. In both limits, the absence of viscosity, coupled with the stipulation that  $U_{bt} = 0$ , leads to the result that  $\phi_{bc} = q_{bc} = 0$  at  $F = F_c$ .

Therefore, at  $F_c$  Equation 5.16 vanishes, and Equation 5.17 reduces to

$$U_{bc} \frac{\partial}{\partial x} q_{bt} + \frac{\partial \phi_{bt}}{\partial x} \frac{\partial \Pi_{bc}}{\partial y} = 0. \quad (5.32)$$

Thus, at the onset of instability, the zonal advection of the relative vorticity of the barotropic wavy perturbation by the basic-state zonal flow balances the meridional advection of the basic-state potential vorticity by the meridional velocity of the barotropic perturbation. In the slippery case, the basic-state potential vorticity gradient reduces to  $2F$ , while in the rigid case, there is a nonzero curvature to  $U_{bc}$  which gives the basic state the relative vorticity gradient shown in Equation 5.21. In the limit  $Q \ll \Gamma^{-4}$ , the meridional advection of the relative vorticity of the basic state by the perturbation meridional flow completely cancels the zonal advection of the  $\partial u / \partial y$  portion of the perturbation relative vorticity by the basic flow (more specifically, it is the portion of the perturbation relative vorticity that gives rise to the  $l^2/2$  term in the free-slip case). In between the limits where the two solutions are rigorously applicable, these two advective terms partially cancel so that  $k^2/2 < F_c < (k^2 + l^2)/2$ .

In the intermediate region where  $\Gamma^{-4} < Q \ll 1$  but  $\Gamma$  is relatively small, the slippery solution is not a good approximation to the rigid-case result. The decrease of  $F_c$  with decreasing  $\Gamma$  can be explained by appealing to the energy equation for the perturbations, which is given in Pedlosky (1987) and can be recast in terms of barotropic and baroclinic quantities to yield

$$\begin{aligned} \frac{dE'}{dt} = \frac{dK'}{dt} + \frac{dP'}{dt} &= \int_{-1}^1 \frac{\partial U_{bc}}{\partial y} \left[ \frac{\partial \phi_{bt}}{\partial x} \frac{\partial \phi_{bc}}{\partial y} + \frac{\partial \phi_{bc}}{\partial x} \frac{\partial \phi_{bt}}{\partial y} \right] dy + \\ &\quad \int_{-1}^1 \frac{\partial U_{bt}}{\partial y} \left[ \frac{\partial \phi_{bt}}{\partial x} \frac{\partial \phi_{bt}}{\partial y} + \frac{\partial \phi_{bc}}{\partial x} \frac{\partial \phi_{bc}}{\partial y} \right] dy - \\ &\quad 2F \int_{-1}^1 U_{bc} \left[ \phi_{bt} \frac{\partial \phi_{bc}}{\partial x} \right] dy - \end{aligned}$$

$$\begin{aligned}
& Q \int_{-1}^1 \left( \frac{\partial \phi_{bt}}{\partial x} \right)^2 + \left( \frac{\partial \phi_{bt}}{\partial y} \right)^2 dy - \\
& 2Q \int_{-1}^1 \left( \frac{\partial \phi_{bc}}{\partial x} \right)^2 + \left( \frac{\partial \phi_{bc}}{\partial y} \right)^2 dy - \\
& \frac{E}{R_o} \int_{-1}^1 \left( \frac{\partial^2 \phi_{bt}}{\partial x^2} \right)^2 + 2 \left( \frac{\partial^2 \phi_{bt}}{\partial x \partial y} \right)^2 + \left( \frac{\partial^2 \phi_{bt}}{\partial y^2} \right)^2 dy - \\
& \frac{E}{R_o} \int_{-1}^1 \left( \frac{\partial^2 \phi_{bc}}{\partial x^2} \right)^2 + 2 \left( \frac{\partial^2 \phi_{bc}}{\partial x \partial y} \right)^2 + \left( \frac{\partial^2 \phi_{bc}}{\partial y^2} \right)^2 dy. \tag{5.33}
\end{aligned}$$

The left hand side of the equation is the time rate of change of perturbation energy, partitioned into the perturbation kinetic energy ( $K'$ ) and the perturbation potential energy ( $P'$ ). The right hand side is comprised of several terms. The first two are the barotropic energy transfer terms. These depend on the meridional structure of the basic state. For our purposes,  $U_{bt}$  is zero and the second term thus vanishes. The first term represents the conversion of the basic-state kinetic energy directly into perturbation energy and will be referred to as  $\mathcal{X}_{bt}$ . The third term is the baroclinic transfer term, which converts available potential energy of the basic state into perturbation energy and depends only on the vertical structure of the basic state. This term is denoted as  $\mathcal{X}_{bc}$ . The fourth and fifth terms denote the energy loss due to bottom friction and are denoted summarily as  $\mathcal{F}_B$ . Similarly, the last two terms represent the dissipation from lateral friction and are denoted as  $\mathcal{F}_L$ .

Three values of  $\Gamma$  are examined:  $\Gamma = \sqrt{10}$ ,  $\Gamma = \sqrt{100}$ , and  $\Gamma = \sqrt{1000}$ . The friction parameter,  $Q$ , is set equal to 0.001, and the zonal wavenumber,  $k$ , is set to  $\pi/4$ , the longest allowable and most unstable wave at these parameter settings. The critical Froude numbers for the respective  $\Gamma$  values listed above are 0.558, 0.698, and 1.19. Once the critical values of  $F$  were determined for each case, energy fluctuations were calculated at the onset of instability (to within some small numerical error). The results are easily visualized via a box diagram, a template of which is shown in

Figure 5.9. In this diagram, the value of the box is zero as shown. Energy is input via the barotropic and baroclinic energy transfers, while friction drains energy from the system. The output is the perturbation energy, subdivided again into potential and kinetic energies. Since we are examining the system at the critical Froude number, the time rate of change of energy is identically zero.

Figure 5.10 shows the results for  $\Gamma = \sqrt{1000}$ . In all of the cases to be presented, the equation has been normalized by the magnitude of the baroclinic energy transfer term. In this case,  $\mathcal{X}_{bc}$  itself is positive. The barotropic term is negative and is about 37% of  $\mathcal{X}_{bc}$ . The size of  $\mathcal{X}_{bt}$  indicates that even for relatively thin boundary layers, the barotropic energy transfer term is of a significant magnitude. However, the sign of the term is **negative**, which indicates that it acts to stabilize the flow.

The next case, at  $\Gamma = \sqrt{100}$ , is shown in Figure 5.11, and it shows substantial differences with the previous scenario. The barotropic transfer term, still negative, is now about 72% of the size of  $\mathcal{X}_{bc}$ , which is positive. In addition, the friction is approximately 1/3 that of  $\mathcal{X}_{bt}$  and is dominated by  $\mathcal{F}_L$ . Thus, the decrease in  $\Gamma$  has increased the magnitude of the barotropic energy transfer but has actually made it more **negative**.

The final situation,  $\Gamma = \sqrt{10}$ , is shown in Figure 5.12. The ratio  $\|\mathcal{X}_{bt}/\mathcal{X}_{bc}\|$  has decreased slightly from the previous case and is now about 0.71. The dissipative terms are again 1/3 as large as the barotropic term, as they must be to balance the equation. As is the case for  $\Gamma = \sqrt{100}$ ,  $\mathcal{F}_L$  is an order of magnitude larger than  $\mathcal{F}_B$ .

The preceding results show that as the horizontal shear layer of the mean flow widens (i.e.  $\Gamma$  decreases), there is a marked increase in the magnitude of the barotropic energy transfer term. However, this term is negative for all the cases considered here, which indicates that the barotropic transfer term is taking energy from the perturbations and placing it back in the basic  $U_{bc}$  profile. The barotropic energy transfer is thus not responsible for the lowering of  $F_c$  with decreasing  $\Gamma$  and

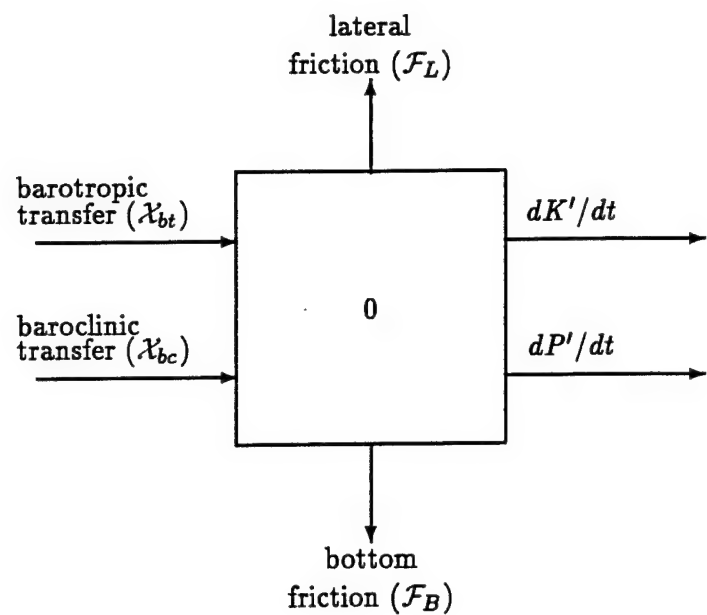
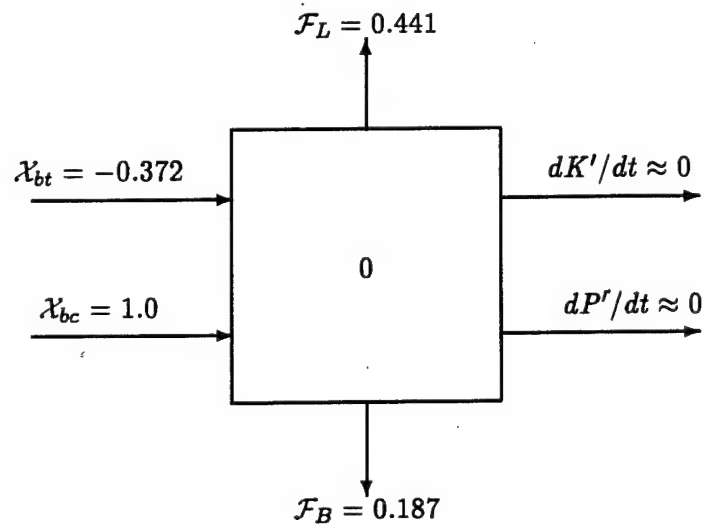


Figure 5.9: Generic energy transfer diagram for fluctuations.

Figure 5.10: Energy transfer diagram for fluctuations,  $\Gamma = \sqrt{1000}$ ,  $Q = 0.001$ .

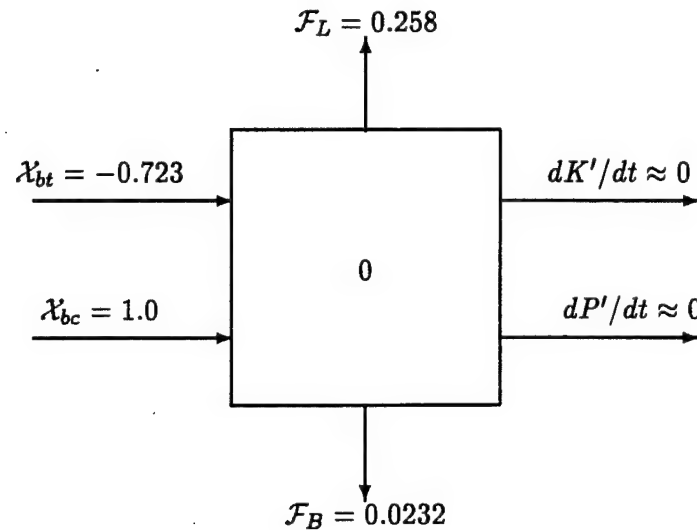


Figure 5.11: Energy transfer diagram for fluctuations,  $\Gamma = \sqrt{100}$ ,  $Q = 0.001$ .

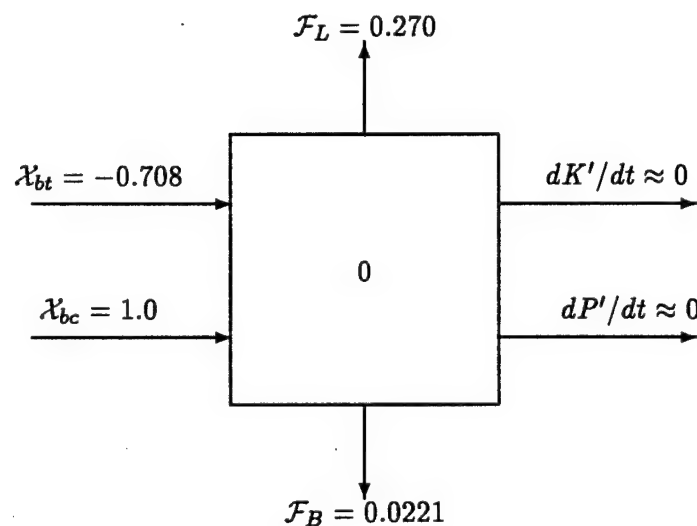


Figure 5.12: Energy transfer diagram for fluctuations,  $\Gamma = \sqrt{10}$ ,  $Q = 0.001$ .

in fact produces a stabilizing effect. However, the frictional terms in Equation 5.33 become smaller as  $\Gamma$  decreases and in fact more than offset the barotropic transfer, resulting in a decrease of  $F_c$ . To see this more clearly, we first define

$$\hat{\mathcal{X}}_{bc} \equiv \frac{-\mathcal{X}_{bc}}{F}. \quad (5.34)$$

At the onset of instability,  $dE'/dt = 0$  in Equation 5.33, and we can therefore write

$$F_c = \frac{\mathcal{X}_{bt}}{\hat{\mathcal{X}}_{bc}} - \frac{\mathcal{F}_B}{\hat{\mathcal{X}}_{bc}} - \frac{\mathcal{F}_L}{\hat{\mathcal{X}}_{bc}}. \quad (5.35)$$

Thus, the critical Froude number can be written in terms of the ratios of the barotropic energy transfer, the bottom friction, and the lateral friction to the baroclinic energy transfer (divided by  $F_c$ ). Table 5.1 shows the magnitudes of these terms for  $\Gamma = \sqrt{1000}$ ,  $\sqrt{100}$ , and  $\sqrt{10}$ . The table shows that as  $\Gamma$  decreases, the total dissipation also decreases, and the reduction in the frictional terms more than offsets any increase in the barotropic transfer. Figure 5.13 shows the meridional structures of the barotropic and baroclinic wavy perturbation for the three values of  $\Gamma$  studied. While the shape of the barotropic eigenfunction does not change substantially, the baroclinic eigenfunction is significantly affected by changes in  $\Gamma$ . In addition, for all three cases, the barotropic wavy amplitude ( $A_{bt}$ ) is substantially larger than the baroclinic wavy amplitude ( $A_{bc}$ ). The ratio  $A_{bt}/A_{bc}$  is approximately 5.1, 5.4, and 110, for  $\Gamma = \sqrt{10}$ ,  $\sqrt{100}$ , and  $\sqrt{1000}$ , respectively. The change in  $F_c$  between  $\Gamma = \sqrt{10}$  and  $\Gamma = \sqrt{100}$  is largely due to changes in the shapes of the eigenfunctions, since the relative amplitudes change very little. However, since the ratio of the dissipative terms to the baroclinic transfer term scales as  $A_{bt}/A_{bc}$  when  $A_{bt} \gg A_{bc}$ , the change in  $F_c$  between  $\Gamma = \sqrt{100}$  and  $\Gamma = \sqrt{1000}$  is due to changes in the relative amplitudes of the two eigenfunctions. In the intermediate  $Q$  region, then, the change

in  $F_c$  versus  $\Gamma$  for a specific value of  $Q$  is due both to changes in the shapes of the eigenfunctions and in their relative amplitudes.

Table 5.1. Contributions from the barotropic transfer term and the dissipative terms to  $F_c$  versus  $\Gamma$  for  $\Gamma = \sqrt{1000}$ ,  $\sqrt{100}$ , and  $\sqrt{10}$ .  $Q = 0.001$ .

$\Gamma$	$F_c$	$\mathcal{X}_{bt}/\hat{\mathcal{X}}_{bc}$	$-\mathcal{F}_B/\hat{\mathcal{X}}_{bc}$	$-\mathcal{F}_L/\hat{\mathcal{X}}_{bc}$	$-(\mathcal{F}_B + \mathcal{F}_L)/\hat{\mathcal{X}}_{bc}$
$\sqrt{1000}$	1.19	0.444	0.223	0.526	0.749
$\sqrt{100}$	0.698	0.504	0.0162	0.177	0.193
$\sqrt{10}$	0.558	0.395	0.0123	0.151	0.163

Finally, the behavior of the flow at large  $Q$  merits a brief discussion. Referring to Figures 5.3, 4, 5, the large- $Q$  solutions obtained for smaller  $\Gamma$  indicate that the flow is noticeably more stable than the free-slip case, while solutions for larger  $\Gamma$  approach the slippery results. This phenomenon can be understood by again appealing to the energy transfers occurring within the system. The energetics are quite different from those seen at small  $Q$ . Table 5.2 displays the normalized energy transfers (similar to that shown in Table 5.1). The barotropic transfer is essentially zero for all values of  $\Gamma$  considered. Thus, at  $F = F_c$  there is a balance between baroclinic energy conversion and dissipation. Moreover, as  $\Gamma$  increases, the magnitude of the lateral dissipation decreases with respect to that of the bottom friction (which is not unexpected, since  $E/R_o$  is decreasing), and the overall magnitudes of both friction terms decrease, thus lowering  $F_c$ . In the large- $Q$  limit, the free-slip solution is the same as that for small  $Q$ , i.e. the barotropic eigenfunction is  $\cos(\pi y/2)$  and the baroclinic eigenfunction is  $Q \cos(\pi y/2)/k$ . Now, however, the baroclinic wave dominates the dissipation, and the ratio of the frictional terms to the baroclinic conversion term scales as  $\mathcal{A}_{bc}/\mathcal{A}_{bt}$ . For  $Q = 10$ , this ratio is calculated to be 59.8, 17.3, and 13.6 for  $\Gamma = \sqrt{10}$ ,  $\sqrt{100}$ , and  $\sqrt{1000}$ , respectively, while the slippery-case value ( $Q/k$ ) is 12.7. Thus, for smaller  $\Gamma$  the free-slip solution is not a good approximation due to the large boundary layers in the basic flow, and the actual solution results in a diminution of the barotropic perturbation amplitude relative to the baroclinic amplitude.

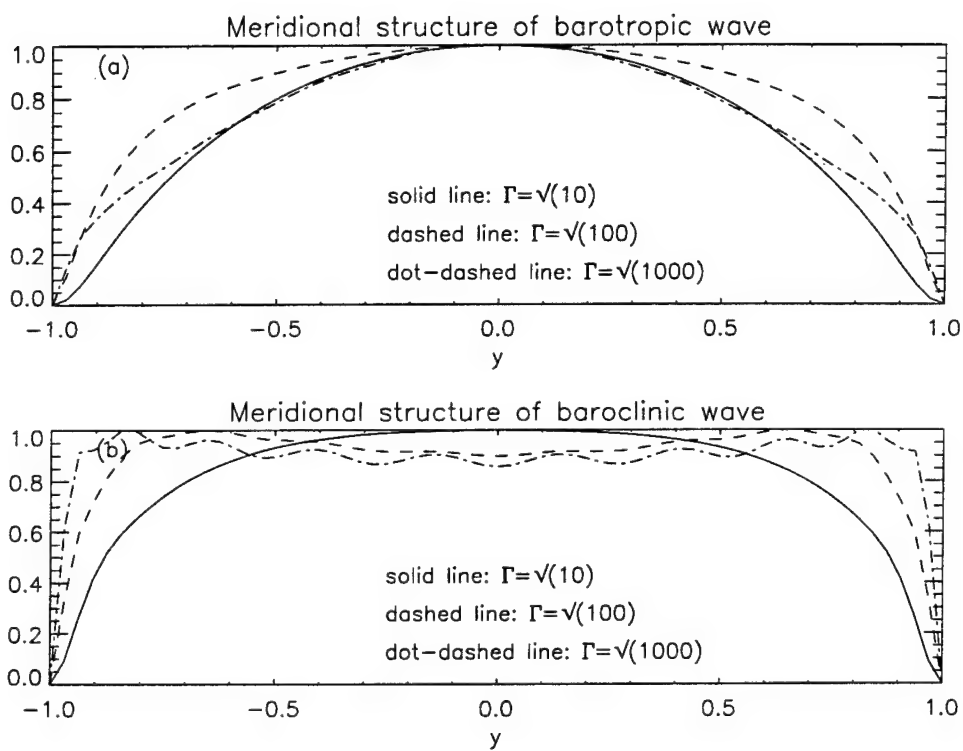


Figure 5.13. (a) Meridional structure of barotropic wavy perturbations for  $\Gamma = \sqrt{1000}$ ,  $\sqrt{100}$ , and  $\sqrt{10}$ .  $Q = 0.001$ . The amplitudes of the meridional functions are independently normalized to 1 for comparison. (b) Same as in (a) but for the baroclinic wavy perturbations.

This results in an increase in  $F_c$  from the free-slip value. The eigenfunctions for all three values of  $\Gamma$  at  $Q = 10$  are shown in Figure 5.14. In this figure, the amplitudes of all the eigenfunctions are normalized to one for comparison, and the  $\cos(\pi y/2)$  profile is also shown. As  $\Gamma$  decreases, the wave boundary layer grows thicker and both the barotropic and baroclinic profiles depart from the slippery case solution, although the overall shape change is not overwhelmingly large. In summary, then, it is largely the change in the relative amplitudes of the eigenfunctions, along with the corresponding change in  $E/R_o$ , that causes  $F_c$  to increase as  $\Gamma$  is decreased.

Table 5.2. Contributions from the barotropic transfer term and the dissipative terms to  $F_c$  versus  $\Gamma$  for  $\Gamma = \sqrt{1000}$ ,  $\sqrt{100}$ , and  $\sqrt{10}$ .  $Q = 10$ .

$\Gamma$	$F_c$	$\mathcal{X}_{bt}/\hat{\mathcal{X}}_{bc}$	$-\mathcal{F}_B/\hat{\mathcal{X}}_{bc}$	$-\mathcal{F}_L/\hat{\mathcal{X}}_{bc}$	$-(\mathcal{F}_B + \mathcal{F}_L)/\hat{\mathcal{X}}_{bc}$
$\sqrt{1000}$	578	0	561	16.5	578
$\sqrt{100}$	885	0	781	104	885
$\sqrt{10}$	5998	0	3011	2987	5998

The results presented above indicate a substantial difference in the stability curves for the rigid-wall and free-slip cases at extreme small or large values of  $Q$ . For  $Q \approx O(1)$ , however, the differences can be rather small. Hart (1972) found that the stability curves of the free-slip model agreed well with those obtained from laboratory experiments in a cylinder (which necessarily has a single rigid wall). These laboratory results were obtained in the range  $O(10^{-1}) < Q < O(1)$  and with  $\Gamma \approx \sqrt{200}$ . As is evident from Figure 5.4, this is indeed the region where the two types of solutions closely coincide, so that the agreement found between experiment and free-slip theory is an artifact of being in a regime where stabilization due to rigid no-slip boundary conditions on the waves, and destabilization due to the presence of a  $y$ -dependent basic state, roughly balance.

**5.5.2  $U_{bc} \neq 0$ ,  $U_{bt} \neq 0$ :** A final modification that can be made in order to better compare with experiment is to introduce a nonzero value of  $U_{bt}$ . In the laboratory, the upper layer is given a nondimensional velocity of 3, while the

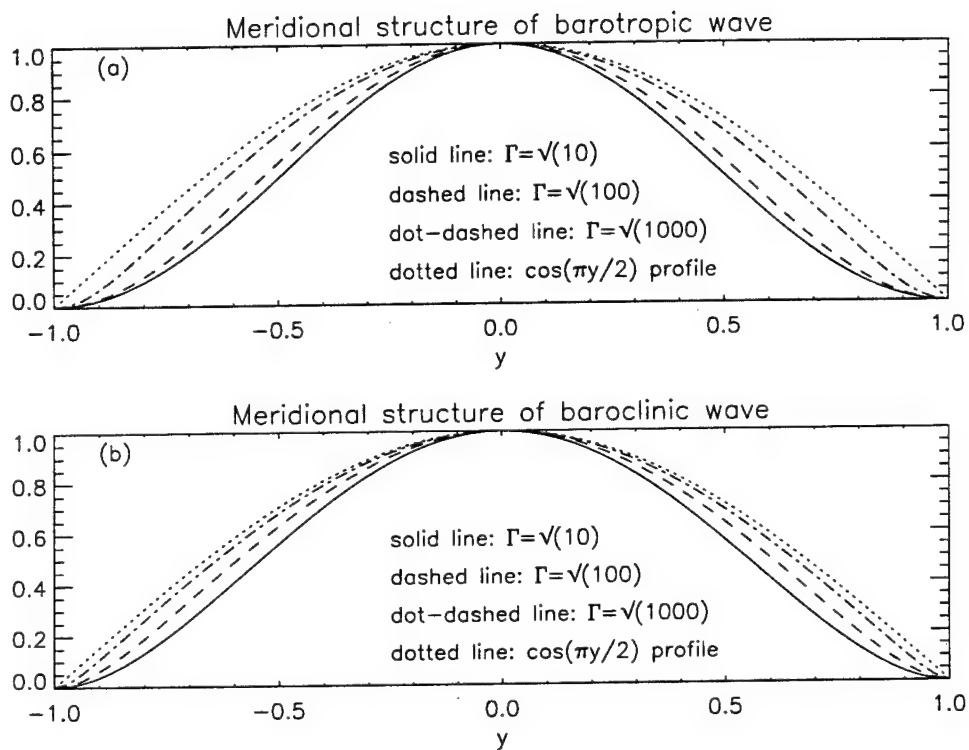


Figure 5.14. (a) Meridional structure of barotropic wavy perturbations for  $\Gamma = \sqrt{1000}$ ,  $\sqrt{100}$ , and  $\sqrt{10}$ .  $Q = 10$ . The amplitudes of the meridional functions are independently normalized to 1 for comparison. (b) Same as in (a) but for the baroclinic wavy perturbations.

lower layer has a nondimensional velocity of 1. This yields  $U_{bt} = 2$ ,  $U_{bc} = 1$  in the interior of the flow. This problem differs fundamentally from that previously discussed because a barotropic basic state allows critical layers in the flow. In other words, the vertical asymmetry of the problem causes the wavy perturbations to have a phase speed which is approximately equal to  $U_{bt}$ . Therefore, since the velocity must approach zero near the walls, in the upper layer only there will be a value of  $y$  for which  $U_1 = c_r$ , where  $c_r$  is the phase speed of the wavy perturbation. At the onset of instability,  $c_i = 0$ , so that the inviscid form of the equations contains a singularity. Although the presence of dissipation avoids a singular set of equations, we may still expect significant changes in the eigenfunctions near the critical layer for small to moderate values of  $Q$ .

To investigate this problem, a barotropic basic state of the form

$$\Phi_{bt} = 2 \left[ -y + \frac{\sinh \hat{\Gamma} y}{\hat{\Gamma} \cosh \hat{\Gamma} y} \right], \quad (5.36)$$

is added, where

$$\hat{\Gamma} \equiv \sqrt{\frac{Q}{E/R_o}} = \Gamma/\sqrt{2}. \quad (5.37)$$

The barotropic basic state velocity profile is

$$U_{bt} = \frac{-\partial \Phi_{bt}}{\partial y} = 2 \left[ 1 - \frac{\cosh \hat{\Gamma} y}{\sinh \hat{\Gamma} y} \right]. \quad (5.38)$$

Linear stability curves for  $0.01 \leq Q \leq 10$  and  $\Gamma = \sqrt{10}$ ,  $\sqrt{100}$ , and  $\sqrt{1000}$  are shown in Figures 5.15, 5.16, and 5.17. A value of  $M = 20$  cross-stream modes (again including only the even eigenfunctions) was used for all calculations. Stability curves were also found using  $M = 18$  and  $M = 24$ , and noticeable differences were found only for  $Q \approx 0.01$ .

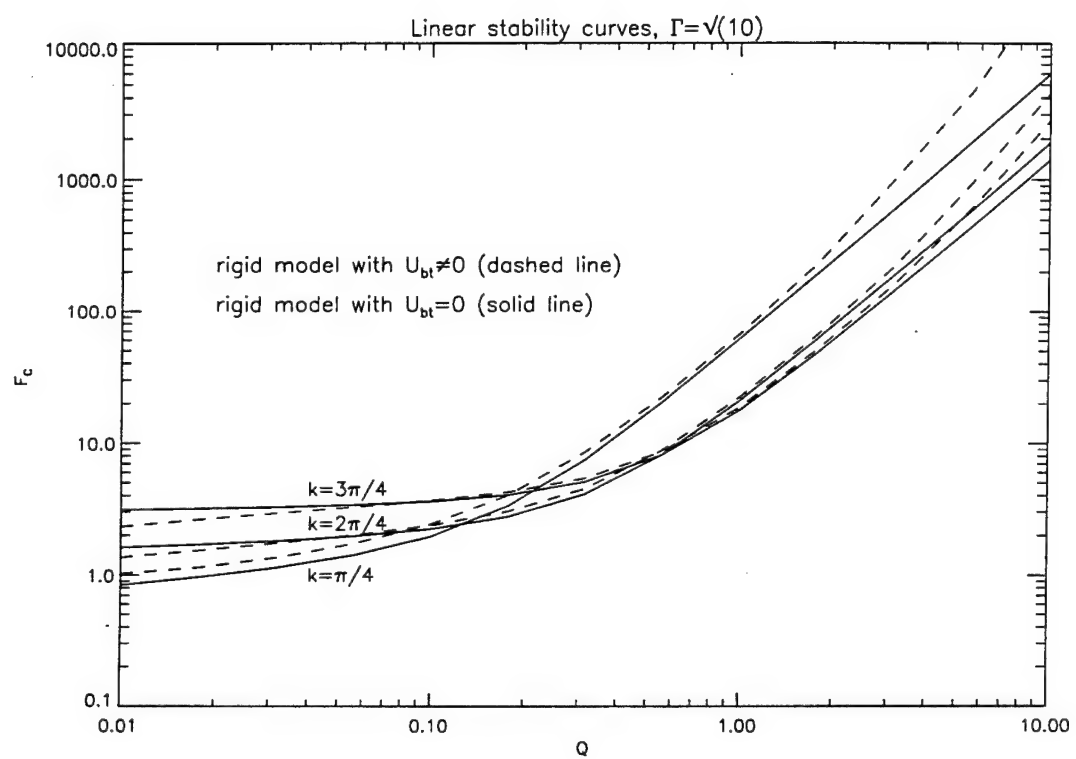


Figure 5.15. Linear stability curves for rigid model with  $U_{bt} = 0$  and  $U_{bt} \neq 0$ ,  $\Gamma = \sqrt{10}$ .

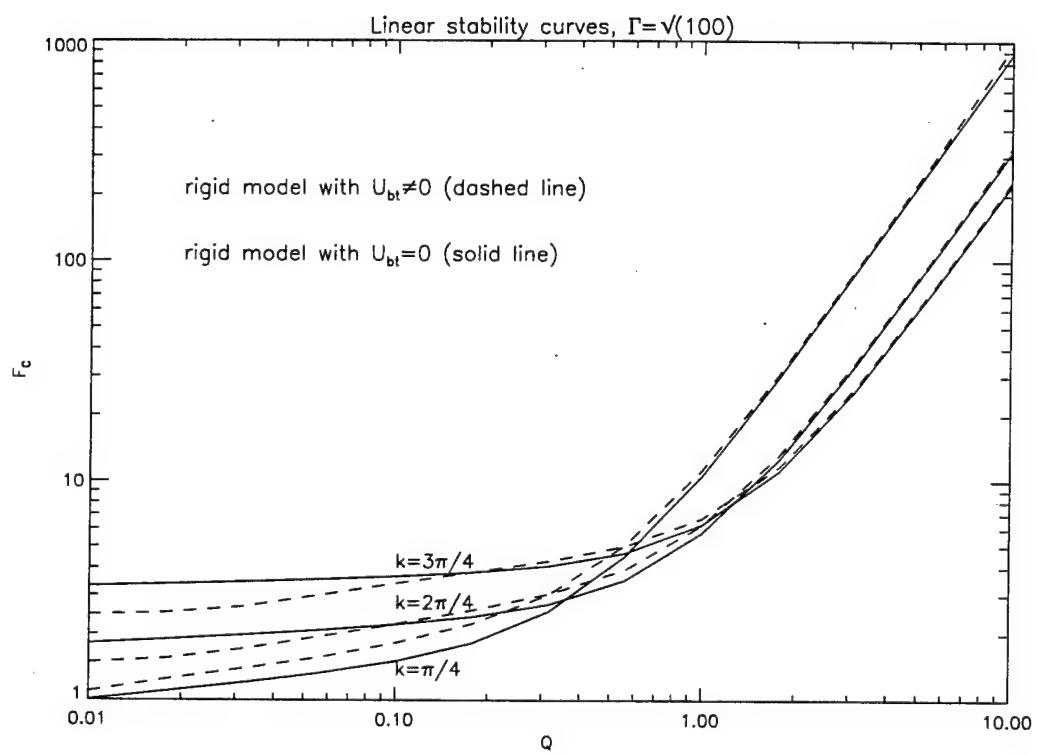


Figure 5.16. Linear stability curves for rigid model with  $U_{bt} = 0$  and  $U_{bt} \neq 0$ ,  $\Gamma = \sqrt{100}$ .

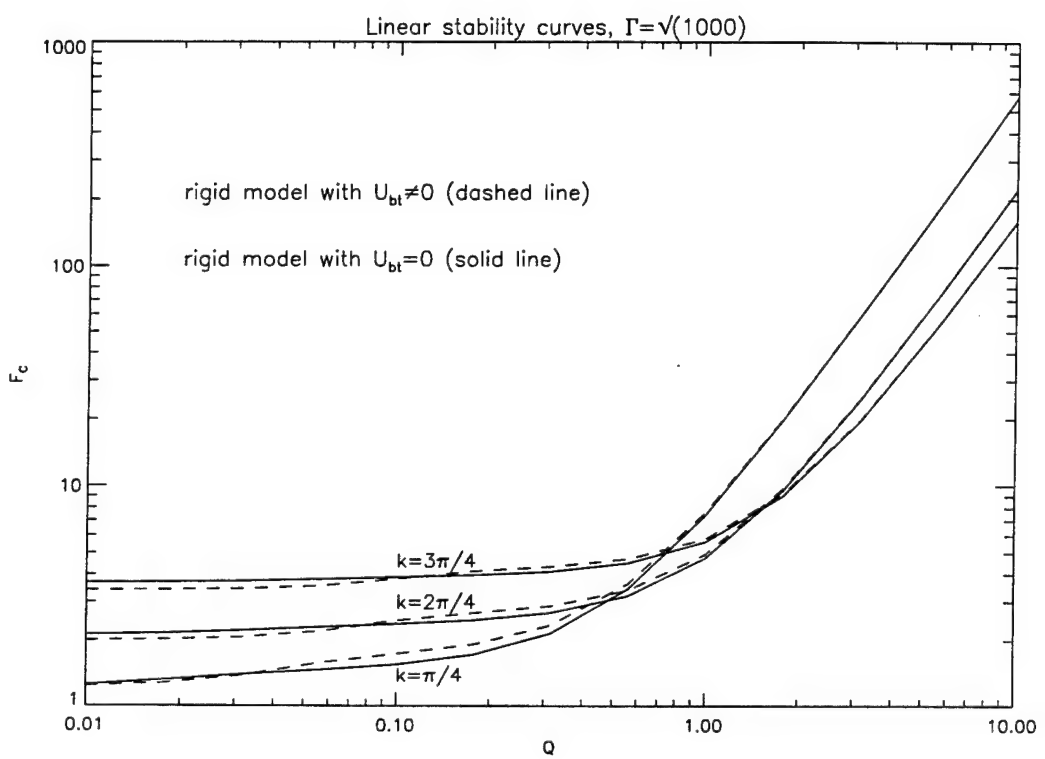


Figure 5.17. Linear stability curves for rigid model with  $U_{bt} = 0$  and  $U_{bt} \neq 0$ ,  $\Gamma = \sqrt{1000}$ .

For  $\Gamma = \sqrt{10}$ , there are substantial differences in the stability curves between the two rigid-wall cases. The case with  $U_{bt} \neq 0$  is generally more stable for  $Q \geq 1$ . For small values of  $Q$ , however, the  $k = 2\pi/4$  and  $3\pi/4$  waves are less stable than their  $U_{bt} = 0$  counterparts. For  $\Gamma = \sqrt{100}$ , shown in Figure 5.16, the situation is much the same. However, for large  $Q$ , the two cases agree much better. Finally, for  $\Gamma = \sqrt{1000}$ , where the zonal shear layers are trapped in a thin viscous region near the wall, the curves agree almost exactly for large  $Q$ . For intermediate values of  $Q$ , the situation with  $U_{bt} \neq 0$  is more stable for all  $k$ , and for small  $Q$ ,  $F_c$  values are slightly lower when  $U_{bt} \neq 0$ .

In order to more quantitatively assess the effect of including a barotropic basic state, energy balances were calculated for both rigid-wall cases for  $Q = 0.1$  and  $\Gamma = \sqrt{10}$ ,  $\sqrt{100}$ , and  $\sqrt{1000}$ . Table 5.3 shows the contribution to  $F_c$  from the various energy terms for the case where  $U_{bt} = 0$ , while Table 5.4 displays the same quantities when  $U_{bt}$  is nonzero. At these parameter settings,  $F_c$  is always higher in the latter case than in the former. In addition, the proportional contribution to  $F_c$  from the barotropic transfer term is enhanced when  $U_{bt} \neq 0$ . The eigenfunctions also show some differences between the two cases. Figure 5.18 shows the imaginary part of the barotropic eigenfunction for both situations for  $\Gamma = \sqrt{100}$ . In the figure, the eigenfunctions have both been normalized to 1, and the critical layer (i.e. the value of  $y$  for which  $U_{bt} = c_r$ ) for the second case is shown by the dashed vertical lines. When  $U_{bt} \neq 0$ , the eigenfunction undergoes substantial variation as it passes through the critical layer. This does not occur when  $U_{bt} = 0$ . A similar variation in the eigenfunction when  $y$  is at or near the critical layer is observed for all values of  $\Gamma$ .

The same analysis was also performed at  $Q = 10$  in order to compare with the results for small friction. Table 5.2 shows the contributions to  $F_c$  from the various energy terms when  $U_{bt} = 0$ , while the results for  $U_{bt} \neq 0$  are shown in Table 5.5. The

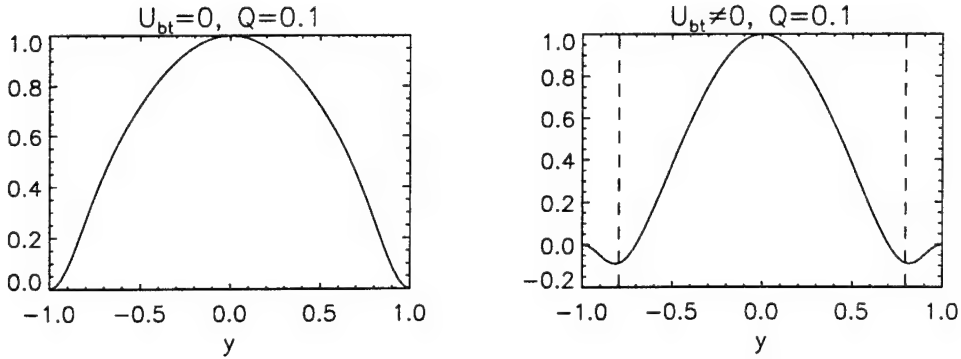


Figure 5.18. Imaginary parts of eigenfunctions of barotropic perturbations with  $U_{bt} = 0$  and  $U_{bt} \neq 0$ ,  $\Gamma = \sqrt{100}$ ,  $Q = 0.1$ . The dashed lines show the critical layer where  $U_{bt} = c_r$ .

Table 5.3. Contributions from the barotropic transfer term and the dissipative terms to  $F_c$  versus  $\Gamma$  for  $\Gamma = \sqrt{1000}$ ,  $\sqrt{100}$ , and  $\sqrt{10}$ .  $Q = 0.1$ ,  $U_{bt} = 0$ .

$\Gamma$	$F_c$	$\mathcal{X}_{bt}/\hat{\mathcal{X}}_{bc}$	$-\mathcal{F}_B/\hat{\mathcal{X}}_{bc}$	$-\mathcal{F}_L/\hat{\mathcal{X}}_{bc}$	$-(\mathcal{F}_B + \mathcal{F}_L)/\hat{\mathcal{X}}_{bc}$
$\sqrt{1000}$	1.56	0.120	1.14	0.298	1.44
$\sqrt{100}$	1.51	0.179	0.819	0.510	1.33
$\sqrt{10}$	1.96	0.144	0.681	1.14	1.82

Table 5.4. Contributions from the barotropic transfer term and the dissipative terms to  $F_c$  versus  $\Gamma$  for  $\Gamma = \sqrt{1000}$ ,  $\sqrt{100}$ , and  $\sqrt{10}$ .  $Q = 0.1$ ,  $U_{bt} \neq 0$ .

$\Gamma$	$F_c$	$\mathcal{X}_{bt}/\hat{\mathcal{X}}_{bc}$	$-\mathcal{F}_B/\hat{\mathcal{X}}_{bc}$	$-\mathcal{F}_L/\hat{\mathcal{X}}_{bc}$	$-(\mathcal{F}_B + \mathcal{F}_L)/\hat{\mathcal{X}}_{bc}$
$\sqrt{1000}$	1.73	0.378	1.12	0.235	1.36
$\sqrt{100}$	1.82	0.578	0.796	0.450	1.25
$\sqrt{10}$	2.42	0.421	0.764	1.24	2.00

energetics are much the same for the two cases, and the barotropic transfer term is essentially zero for all the situations listed. Only at  $\Gamma = \sqrt{10}$  is there a noticeable difference in  $F_c$  and hence in the eigenfunctions.

In summary, then, the presence of a barotropic basic state results in critical layers in the flow. These critical layers in turn affect the meridional eigenfunctions of the wavy perturbations, especially at or near the actual critical value of  $y$ . The extent of the effect on  $F_c$  depends on the particular  $\Gamma, Q$  combination under consideration. However, in regions of parameter space most relevant to experiment, the changes in the stability curves are minimal.

Table 5.5. Contributions from the barotropic transfer term and the dissipative terms to  $F_c$  versus  $\Gamma$  for  $\Gamma = \sqrt{1000}, \sqrt{100}$ , and  $\sqrt{10}$ .  $Q = 10, U_{bt} \neq 0$ .

$\Gamma$	$F_c$	$\mathcal{X}_{bt}/\hat{\mathcal{X}}_{bc}$	$-\mathcal{F}_B/\hat{\mathcal{X}}_{bc}$	$-\mathcal{F}_L/\hat{\mathcal{X}}_{bc}$	$-(\mathcal{F}_B + \mathcal{F}_L)/\hat{\mathcal{X}}_{bc}$
$\sqrt{1000}$	578	0	562	16	578
$\sqrt{100}$	967	2	845	120	965
$\sqrt{10}$	28580	20	6550	22010	28560

## 5.6 Discussion

The stability curves for a rigid-wall model have been obtained numerically. Because the basic flow must necessarily be a function of  $y$ , a series solution in Chebyshev polynomials is used to find both the meridional dependence of the perturbations and the resulting values of  $F_c$ . For the parameter range of interest,  $M = 20$  cross-stream modes gives reasonably accurate results. Furthermore, the critical Froude number ( $F_c$ ) required for instability is found to vary substantially with  $\Gamma$ . For  $Q \ll \Gamma^{-4}$ , the barotropic eigenfunction at  $F_c$  is equal to  $U_{bc}$  while the baroclinic eigenfunction is essentially 0. In this situation, the advection of the perturbation vorticity by the basic-state velocity partially cancels the advection of basic-state vorticity by the perturbation velocity, resulting in  $F_c \approx k^2/2$ .

For  $\Gamma^{-4} < Q \ll 1$ , the solution approaches that of the free-slip case, so that

the barotropic eigenfunction is approximately equal to  $\cos(\pi y/2)$  and the baroclinic eigenfunction is approximately  $Q \cos(\pi y/2)/k$ . In this case,  $F_c = (k^2 + l^2)/2$ . In between the two analytically-obtainable solutions, the eigenfunctions are more complicated and  $k^2/2 < F_c < (k^2 + l^2)/2$ . For a fixed value of  $Q \ll 1$ ,  $F_c$  decreases as  $\Gamma$  decreases and an examination of the energy balances reveals that this is due to both shape and amplitude changes in the eigenfunctions. At large values of  $Q$ , the physics governing  $F_c$  are different from those seen at small  $Q$ . In this situation, the barotropic transfer of energy is zero, and a large baroclinicity in the neutral wave is necessary to provide sufficient energy to balance the dissipation. Thus, at  $F = F_c$  there is a balance between baroclinic energy conversion and dissipation. Moreover, for large values of  $\Gamma$ , the solutions are nearly those of the free-slip case. However, for small  $\Gamma$ , the decreased relative amplitude of the barotropic eigenfunction causes an increase in  $F_c$  relative to the slippery solution. An investigation of previous experimental findings, which are in good agreement with analytical calculations using a free-slip assumption, show that they lie in the parameter range where both the rigid-wall and slippery-wall models yield similar results.

Finally, the analysis of the linear stability problem was expanded to include a nonzero value of the barotropic basic state, the purpose of which is to better simulate laboratory conditions that have a critical layer in the upper fluid near the outer wall. The results show that there are generally only minor differences between the two cases. Depending on the parameter setting, the case with  $U_{bt} \neq 0$  may be more or less stable than its counterpart with no barotropic basic flow, but the differences are only about 15% when  $Q = 0.1, \Gamma = \sqrt{100}$ , similar to laboratory settings. An analysis of the energetics reveals a somewhat enhanced barotropic energy transfer at  $F_c$  when  $U_{bt} \neq 0$ , and the eigenfunctions in this situation show rapid variations in amplitude as they cross the critical layer. In the region applicable to experimental findings (i.e.  $0.1 \leq Q \leq 1$ ) the results for the two cases are similar.

## CHAPTER 6

### A RIGID-WALL MODEL OF BAROCLINIC INSTABILITY: NUMERICAL RESULTS

This chapter examines the solutions of a high-resolution numerical model with rigid sidewalls. The investigation of such an implementation is important for several reasons. First, due to the presence of viscosity at the walls, the behavior may be expected to deviate significantly from that seen in the slippery-wall model. In addition, laboratory experiments conducted in a cylinder necessarily possess a rigid sidewall, and the inclusion of such effects in the model will hopefully result in better agreement between theory and experiment. Finally, while the atmosphere has no “walls”, the ocean certainly possesses the equivalent of sidewalls in the form of land. Thus, the investigation of a rigid-wall model may have particular applications to baroclinic instability in the ocean. The chapter is organized as follows. The numerical method used to obtain the solutions is briefly explained. Next, the validation of the model is discussed. The salient results are then summarized, and an effort is made to understand the physics underlying the observed behavior. This is done both by appealing to EOF-based surrogate models and also by quasi-analytical methods.

#### 6.1 Numerical Method

The numerical method is similar to that used for the slippery model. A pseudo-spectral approach is again implemented, so that the linear terms are computed in spectral space, while the nonlinear terms are computed in physical space. Unlike the slippery code, however, the spatial discretization in the two directions

is different. In the zonal direction, Fourier modes are again used, but the meridional dependence is now represented in terms of Chebyshev polynomials. Since the Chebyshev functions do not individually satisfy the boundary conditions (i.e. no-slip and impenetrable), they are combined using a “tau” method in order to meet the necessary requirements (Canuto et al., 1988). Also unlike the slippery case, in the rigid-wall formulation there are no boundary conditions on the vorticity for the wavy portions of the flow. To overcome this problem, a modification of the influence matrix technique (Kleiser and Schumann, 1980) is used. A full description of this method by the author of the code (Brummell, 1993) is outlined in Appendix I.

## 6.2 Validation of Model

The model was run at two different resolutions: 64x33 and 128x65. The complexity of the code prevented runs at higher resolutions due to excessive computational times. The higher-resolution runs were compared to those performed at lower resolution near transition points in parameter space, especially near the onset of chaos. No substantial difference in results was found between the two resolutions. Consequently, a resolution of 64x33 was deemed adequate to provide convergent results.

In order to validate the code itself, critical values of  $F_c$  obtained using the method outlined in Chapter 5 were used to test the onset of instability found in the numerical code. In all cases, the actual onset of instability was equal to the predicted value (within the numerical error expected from the quasi-analytical prediction). In addition, the linear eigenfunctions calculated from the linear model were compared to the eigenfunctions of the full model. Figure 6.1 displays the eigenfunctions obtained via both methods for  $F = 1.68$ ,  $Q = 0.15$ , and  $E/R_o = 0.001$ . For this case,  $F_c = 1.67$ , so we are just above the onset of instability. The shapes of the predicted eigenfunctions agree almost exactly with those observed in the numerical model.

In addition, the amplitude ratios of the barotropic and baroclinic eigenfunctions calculated with the two methods agree to within less than 1%. Finally, energetics of the flow were calculated at chosen parameter settings, and the results show that the energies balance to within a small numerical error. In combination, these results instill confidence that the code is operating properly.

### 6.3 Results

The model was run for a variety of parameter values, and both  $Q$  and  $F$  were varied. The parameter  $E/R_o$  was kept fixed at 0.001 for all runs, so that changes in  $Q$  also changed the value of  $\Gamma$  used. Generally, a value of  $Q$  was chosen and  $F$  was successively increased until the system became chaotic. However, some runs were made with  $F$  fixed and  $Q$  variable. The regime diagrams are shown in Figures 6.2,3.

Numerical runs were made for variable  $F$  with  $Q=0.08, 0.10, 0.125, 0.15$ , and 0.20. The critical values of  $F$  for the above parameter settings are approximately 1.44, 1.52, 1.60, 1.67, and 1.81, respectively. One run was also made for variable  $Q$  with  $F = 1.90$ . Solutions for variable  $F$  were initially obtained by starting just above  $F_c$  and sequentially increasing  $F$  to examine any changes in behavior. These results are shown in Figure 6.2. For  $Q = 0.2$ , the bifurcation structure is similar to that seen in the slippery model, i.e.  $S \rightarrow PAV \rightarrow C$ , with the exception of a missing quasi-periodic regime. In this model, the quasi-periodic behavior is transient since two instabilities grow simultaneously from the PAV solution at the same parameter setting. For  $0.08 \leq Q \leq 0.15$ , however, the initial behavior is not steady, but rather periodic or chaotic. The fact that the amplitudes of these motions does not approach 0 at  $F_c$  further indicates that the instabilities born at  $F_c$  are subcritical. Because of this, one should be able to observe non-trivial behavior below  $F_c$ ; this indeed occurs, and the results are summarized in Figure 6.3. In this figure, the solutions at fixed  $Q$

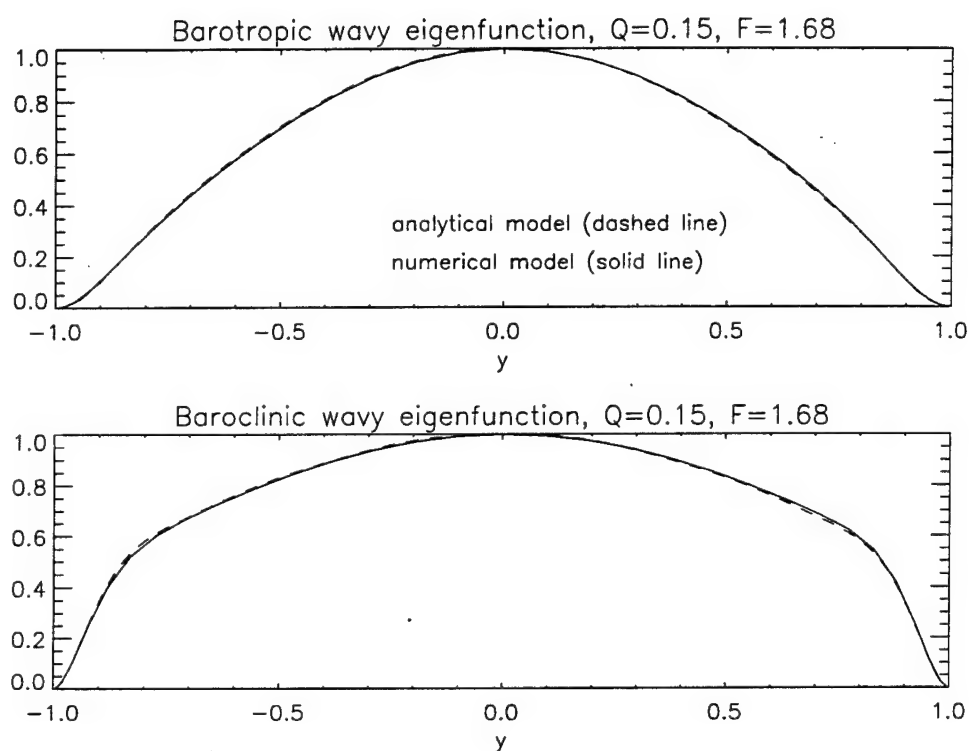


Figure 6.1. Calculated and observed linear eigenfunctions,  $F = 1.68$ ,  $Q = 0.15$ . The predicted eigenfunctions are shown by the solid lines, while the dashed lines show the actual eigenfunctions.

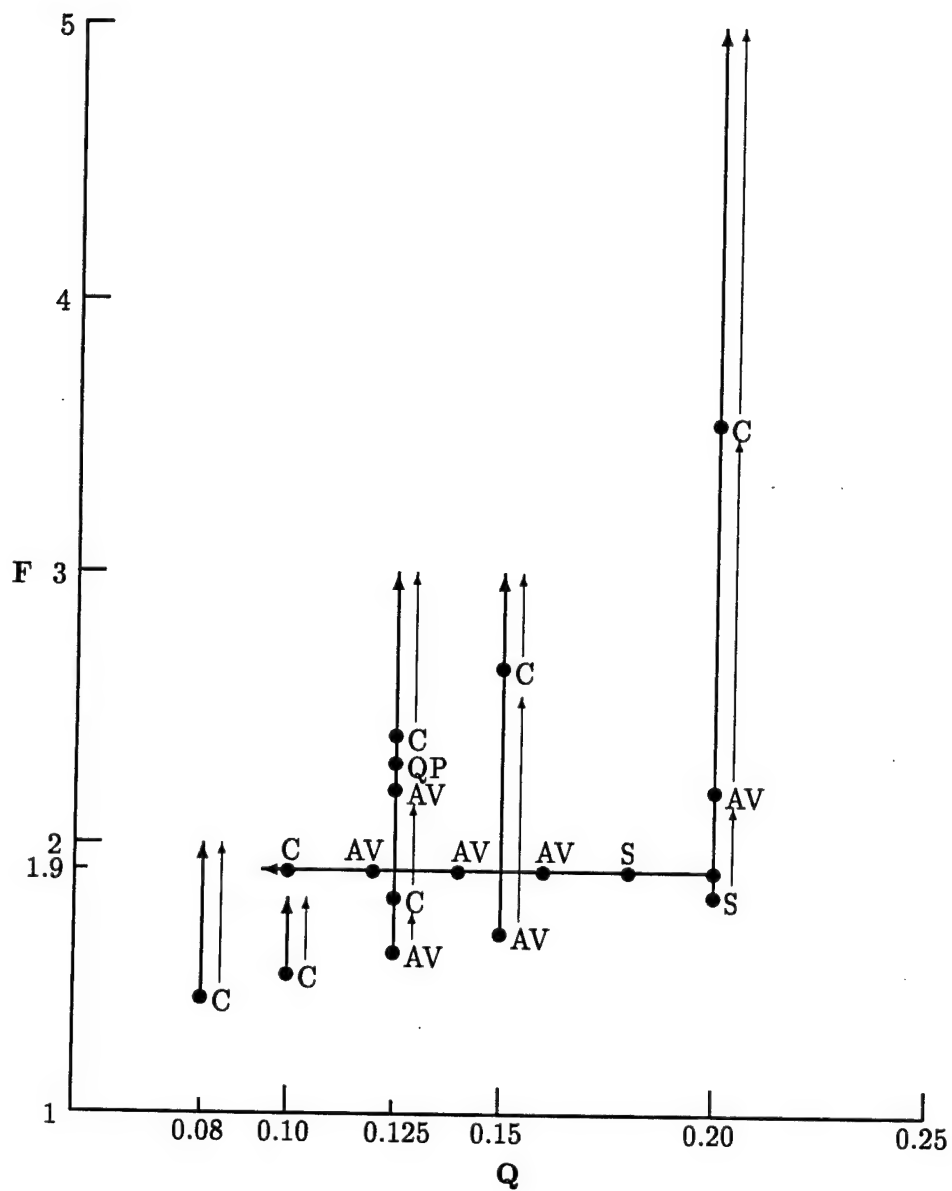


Figure 6.2. Regime diagram for rigid-wall model with increasingly supercritical parameters. The solutions are obtained by following the arrows in the direction indicated in the  $F$ - $Q$  plane. 0 denotes the basic-state solution, S denotes steady behavior, AV denotes periodic amplitude vacillation, QP denotes quasi-periodicity, and C denotes chaos.

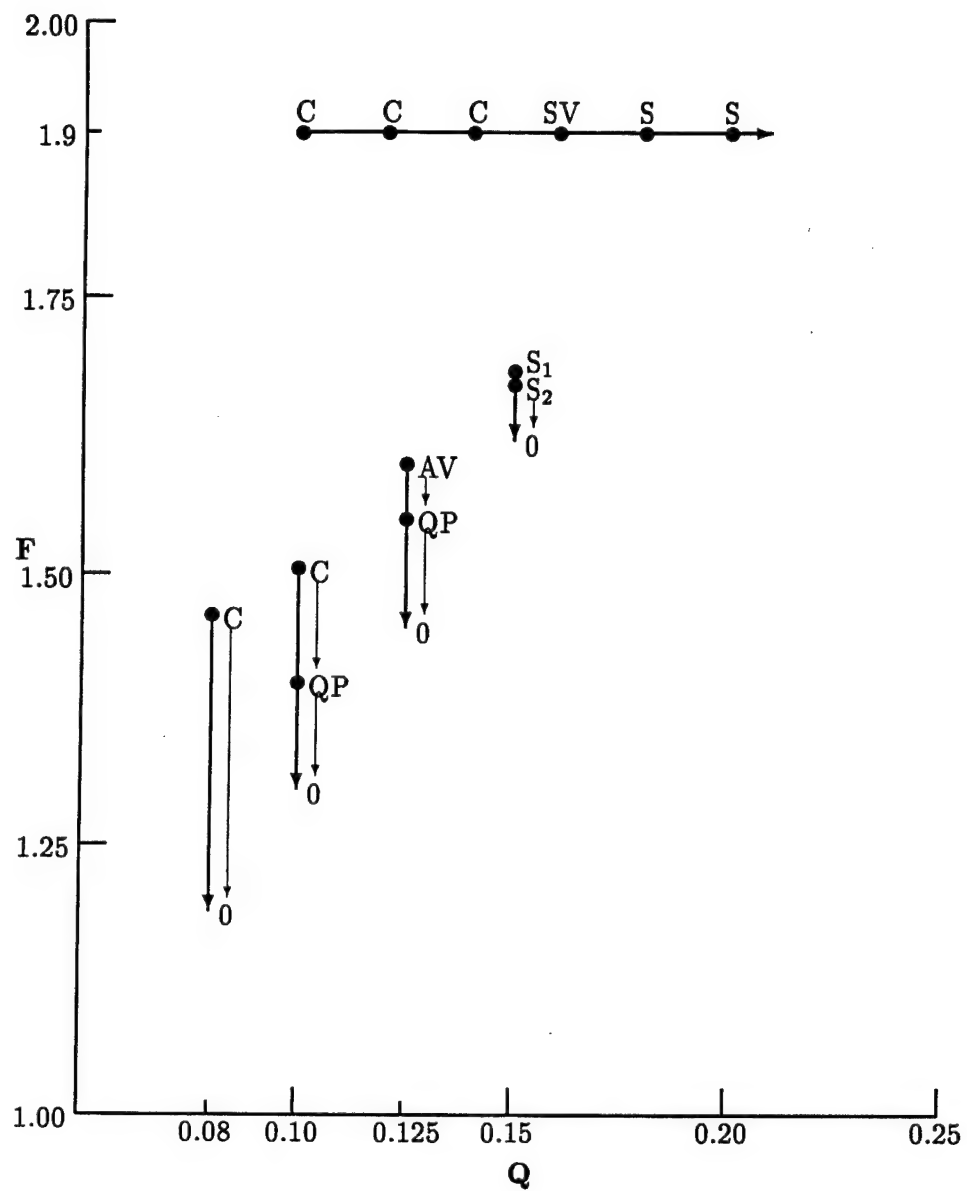


Figure 6.3. Regime diagram for rigid-wall model with decreasingly supercritical and subcritical parameters. The solutions are obtained by following the arrows in the direction indicated in the  $F$ - $Q$  plane. Note that the directions followed are opposite those seen in Figure 6.1. The symbols are the same as indicated in Figure 6.1, with the addition that  $SV$  denotes periodic structural vacillation.

are obtained by starting with a solution for  $F > F_c$  and using this as an initial state to find a solution for  $F < F_c$ . The subcritical region is quite large for  $Q = 0.08$  and nearly disappears for  $Q = 0.15$ . The cause of this behavior will be discussed in detail shortly. Hysteresis also occurs in the investigations made for  $F = 1.9$  with variable  $Q$ . Referring to Figure 6.2, there is a transition (as  $Q$  decreases) from steady flow to PAV to chaos. Using the solution at  $Q = 0.1$  as an initial condition and increasing  $Q$ , however, the solution stays chaotic until  $Q \approx 0.16$ , then enters a region of periodic structural vacillation. It eventually returns to a steady-wave state when  $Q \approx 0.18$ . Although not shown in Figures 6.2,3, a set of runs was performed for  $Q = 0.5$ . The results displayed only steady behavior until  $O(10)$  supercriticality and thus will not be discussed further.

The behavior at  $Q = 0.1$  is especially interesting because of the subcritical behavior at  $F_c = 1.52$  and also due to the fact that the asymptotic state of the system is chaotic at  $F_c$ . Small, random initial conditions quickly settle into a symmetric, PAV regime with no barotropic zonal corrections. A time trace of the lowest symmetric, baroclinic zonal correction, calculated at  $F = 1.53$ , is shown in Figure 6.4. However, once the flow enters PAV, the asymmetric, barotropic zonal correction (also shown in Figure 6.4), which was zero during the initial growth of the wavy perturbations, grows to finite amplitude. This instability, whose dominant frequency is slightly less than  $1/2$  that of the amplitude vacillation, appears to result in an immediate transition to chaos. This, however, is illusory, for the chaotic transients eventually yield to a complex, quasi-periodic solution. The transients are so long, though, that the remaining two growing instabilities (i.e. the asymmetric baroclinic and symmetric barotropic, shown in Figure 6.4) reach finite amplitude just after the system has settled into a QP state. It in fact appears that these two instabilities are induced to grow by the new behavior exhibited by the system. Figure 6.5 shows the lowest asymmetric, baroclinic zonal correction and the lowest symmetric, barotropic

zonal correction at  $F = 1.60$ . These modes have now both grown to finite amplitude, and the system behaves chaotically.

As with the slippery case, an effort was made to ascertain the underlying dimension of the attractor in the chaotic regime. However, attempts to calculate the correlation dimension were again inconclusive, evidently owing to the lack of extreme low-dimensionality seen in the system's behavior. A maximum return map calculated from the lowest symmetric, baroclinic zonal mode, shown in Figure 6.6, shows no evidence of structure when embedded in two dimensions. In addition, the power spectrum of the same quantity, displayed in Figure 6.7, shows a distinct peak at the dominant PAV frequency (approximately 0.12 freq. units) and its first harmonic, but exhibits broad-band noise elsewhere. Thus, we can conclude that the succession of instabilities seen at  $F_c$  eventually causes chaotic behavior, and the asymptotic state of the flow is not characterized by extremely low-dimensional chaos (i.e. dimension  $\leq 3$ ). This is not surprising, since the two-torus motion is destroyed by two simultaneous instabilities. For this reason, we may anticipate that the solution moves on an attractor with dimension  $\approx 4$ .

Figure 6.2 shows that at  $Q = 0.08$  the flow also becomes chaotic immediately. In this situation, there is an initial onset of PAV, just as for  $Q = 0.10$ . Subsequent to this, however, all of the remaining zonal modes, i.e. symmetric barotropic, asymmetric barotropic, and asymmetric baroclinic, grow and reach finite amplitude nearly simultaneously. Thus, in this situation all the remaining symmetries of the problem are broken simultaneously. The end result is chaotic behavior similar to that seen at  $Q = 0.10$ . For  $Q = 0.15$  and  $Q = 0.20$  there exist stable PAV regimes over a finite range of  $F$ . In both situations, an asymmetric barotropic instability eventually grows and reaches finite amplitude, causing quasi-periodicity. The quasi-periodic solution is not asymptotically stable, however, as symmetric barotropic and asymmetric baroclinic instabilities reach finite amplitude shortly thereafter, resulting

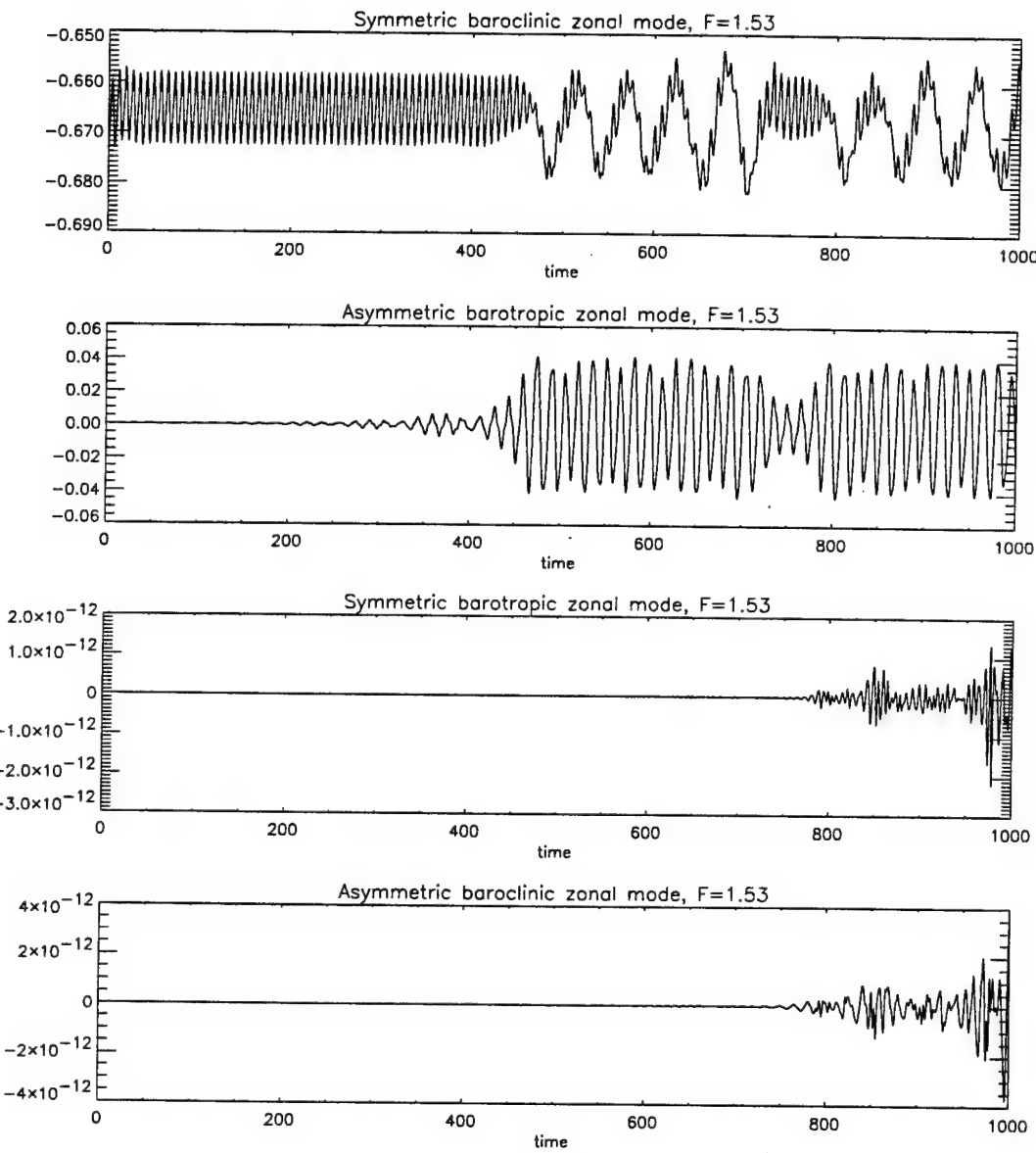


Figure 6.4: Time traces of lowest zonal-correction modes,  $F = 1.53$ ,  $Q = 0.10$ .

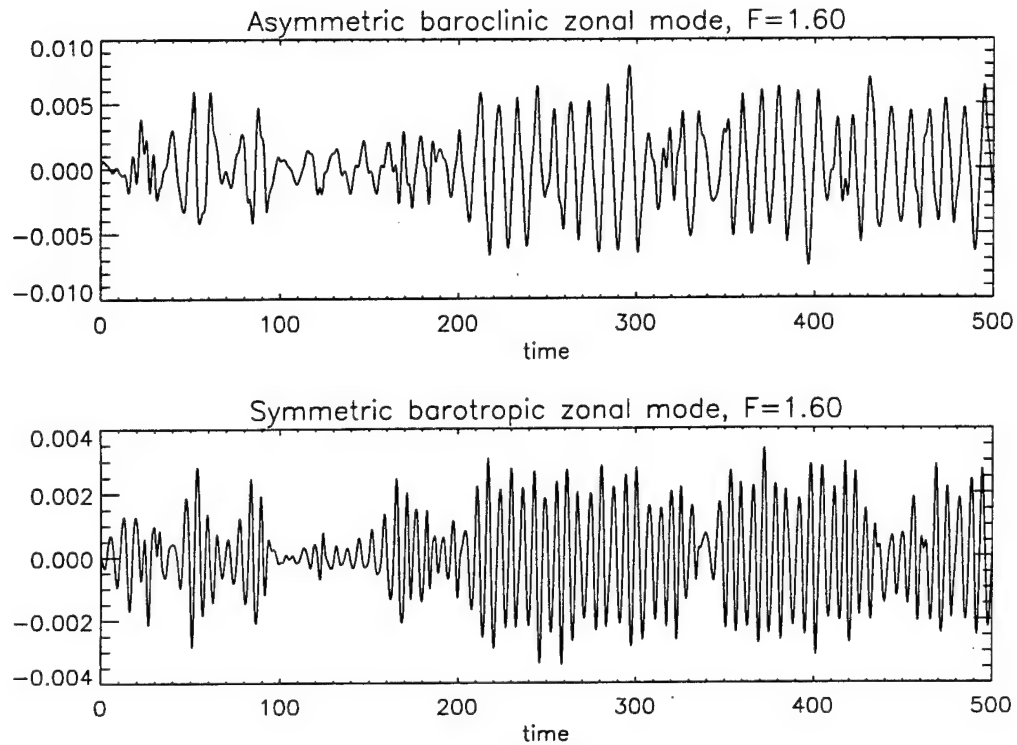


Figure 6.5. Time traces of selected lowest zonal-correction modes,  $F = 1.60$ ,  $Q = 0.10$ .

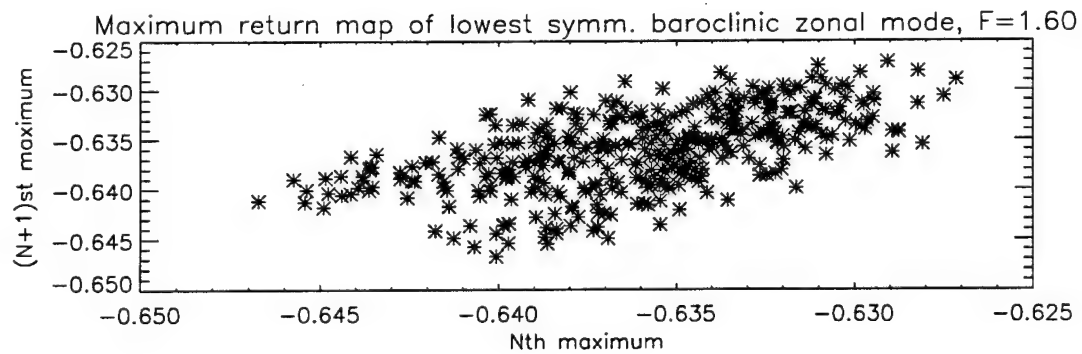


Figure 6.6. Maximum return map of lowest symmetric baroclinic zonal correction,  $F = 1.60$ .

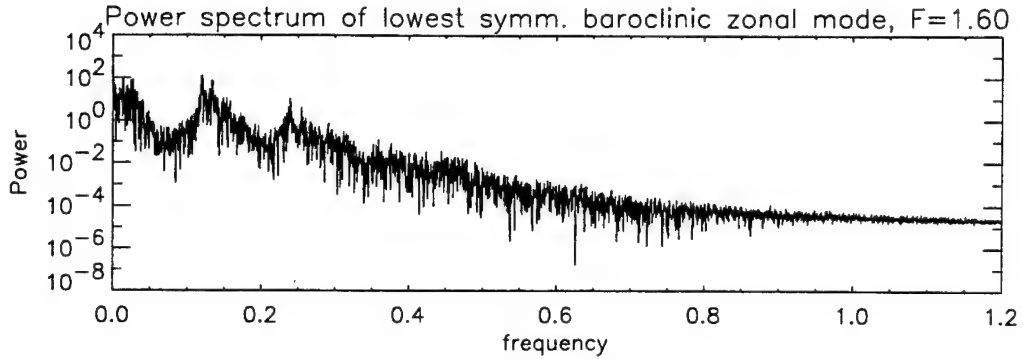


Figure 6.7. Power spectrum of lowest symmetric baroclinic zonal correction,  $F = 1.60$ .

in chaos. Thus, in all cases previously mentioned, both the shift-reflect symmetry and the vertical symmetry are broken via an asymmetric, barotropic instability, the asymptotic result of which is chaos.

At  $Q = 0.125$ , the bifurcation sequence is slightly different. At  $F_c = 1.60$ , there is a transient PAV regime that is annihilated by the familiar asymmetric, barotropic instability. However, the flow remains in a periodic state largely characterized by the PAV behavior until  $F = 1.80$ . At this point, the symmetric, barotropic and asymmetric, baroclinic modes grow to finite amplitude, eventually causing chaos. At  $F = 2.20$ , the PAV regime returns and is stable until  $F = 2.30$ , at which point a symmetric, barotropic instability grows and causes the flow to become quasi-periodic. The quasi-periodic solution is stable until  $F = 2.40$ , when both asymmetric modes grow and again cause chaos. These solutions appear to bridge the gap between those seen at  $Q = 0.10$  and those observed for  $Q = 0.15$  or  $0.20$ . At these larger values of  $Q$ , there is a standard transition from periodic solutions at lower values of  $F$  to chaotic solutions at higher values of  $F$ . At the lower values of  $Q$ , chaos is immediate. At  $Q = 0.125$ , the instabilities waver in strength as  $F$  is altered, thus resulting in intermittent chaos (in parameter space).

One set of runs was done for  $F$  fixed at  $F = 1.9$  with variable  $Q$ , the results of which are displayed in Figures 6.2,3. This was done in order to ensure

the continuity of solutions in parameter space as  $Q$  was varied. The results did indeed agree with those done at constant  $Q$ . At  $Q = 0.2$ , a symmetric, steady solution is obtained. This persists until  $Q \approx 0.16$ , at which point a symmetric PAV instability occurs. The PAV regime gives way to chaos at  $Q = 0.10$  in a manner consistent with the results presented for  $Q = 0.10$  previously. As  $Q$  is now increased back towards its original value, however, the solutions are different (see Figure 6.3). The chaos persists until  $Q \approx 0.16$ ; at this point, the asymmetric modes die altogether and the system enters a symmetric PSV state. Thus, the system possesses multiple stable states in this parameter range. The behavior seen upon increasing  $Q$  from its value of 0.10 was also observed by perturbing the symmetric solutions with asymmetric initial conditions. The final state is thus dependent on the symmetry of the initial perturbations. The PSV behavior is curious because it is the only instance of PSV seen over the range of parameter values examined. Since the appearance of a symmetric barotropic instability superimposed on a symmetric baroclinic instability occurs quite frequently in the model without causing PSV, this particular state must have a rather small basin of attraction (i.e. must require very special initial conditions to be realized).

The dominant frequencies of the particular instabilities seen in this model differ somewhat from those seen in the slippery case. The dominant PAV frequency (caused by a symmetric, baroclinic instability) is essentially the same in both models and has a value of approximately 0.12-0.13 frequency units. However, in the slippery case, the barotropic instabilities generally possess dominant frequencies about twice that of the PAV frequency. In the rigid case, when  $\Gamma$  is relatively large, the frequencies of the barotropic instabilities are indeed 1.3-2 times larger than the PAV frequency. However, as  $\Gamma$  is decreased, these frequencies also decrease, until at  $Q = 0.10$ , the asymmetric barotropic instability has a frequency about half that of the PAV solution. This alteration in time scales in the higher instabilities will greatly affect the

structure of the resulting solution, since the instabilities interact nonlinearly. On a more physical level, changes in the basic flow must affect the nature of some of the instabilities in an  $O(1)$  manner.

Finally, it is important to note that the results discussed in this chapter were obtained by changing  $F$  and  $Q$  for a fixed value of  $E/R_o$ . An alteration of  $Q$  thus effects an alteration of  $\Gamma$ . One can imagine fixing  $Q$  and varying  $E/R_o$ , so that an increase (decrease) in  $E/R_o$  would decrease (increase)  $\Gamma$ . Thus, one would expect the subcritical behavior to occur as  $E/R_o$  is increased, and supercritical behavior to return for  $E/R_o$  adequately small. Of course, changes in  $E/R_o$  also affect the magnitude of the dissipation, so that these effects would have to be accounted for in the limit  $E/R_o \rightarrow 0$  or when  $E/R_o \rightarrow O(1)$ .

#### 6.4 Discussion

The results discussed above are profoundly different from the behavior seen in the slippery model. First of all, for similar values of  $Q$  and  $E/R_o$ , the rigid model becomes chaotic much sooner than the slippery case (unit supercriticality versus order four supercriticality). In this respect, the model results agree much better with experiments, which also become chaotic at unit supercriticality. Additionally, the rigid model displays subcritical behavior, so that a stable state obtained just above  $F_c$  is, for some values of  $Q$ , realizable below  $F_c$  as well. Furthermore, the amount of subcritical behavior can be quite large, as Figure 6.3 shows. Also evident from the figure is the fact that the subcritical region disappears for  $Q > 0.15$ .

The existence of the subcritical behavior indicates a fundamental difference between the slippery and rigid models. Certain nonlinearities in the rigid case must be enhancing the initial instabilities near  $F_c$ . The physical basis of such a situation warrants investigation. To understand the cause of the subcritical behavior, surrogate EOF models were utilized. These proved especially useful because of their

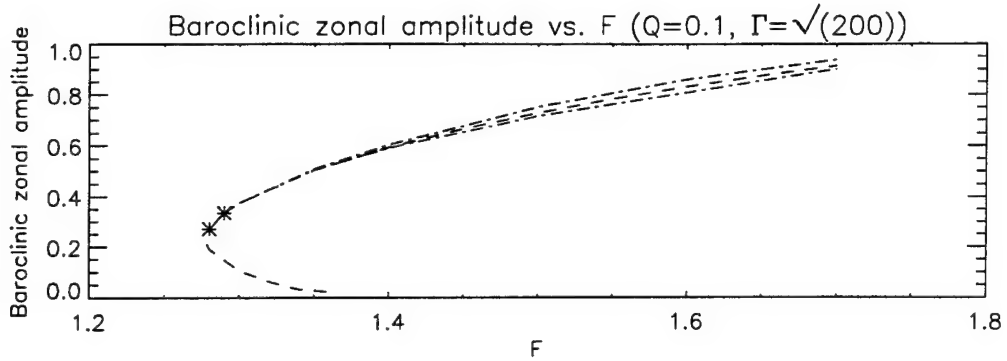


Figure 6.8. Bifurcation structure near  $F_c = 1.52$  for  $Q = 0.1, \Gamma = \sqrt{200}$ . The solid line shows a stable fixed point (in this case demarcated by asterisks), the dashed lines reflect unstable fixed points, and the dot-dashed lines show the approximate envelope of the stable periodic solution.

ability to accurately model the relatively complex spatio-temporal behavior with a small number of equations. Models were constructed at  $Q = 0.10, F = 1.55$ , and also at  $Q = 0.2, F = 2.50$ . These parameter settings were chosen in order to obtain one model representative of the subcritical region and one reflective of the supercritical regime. For both sets of parameter settings, the EOFs were obtained in a PAV regime. Although for  $Q = 0.10$  this behavior is transient, the spatial fields were sampled well before the other instabilities reached a measurable amplitude. In both cases, 4 barotropic wavy EOFs, 4 baroclinic wavy EOFs, and 3 baroclinic zonal EOFs were necessary to meet the 99% variance threshold. The resulting sets of ODEs were then used to find the fixed points of the system, and their stability, near  $F_c$  via the method outlined in Chapter 3. The results are shown in Figures 6.8,9, where the amplitude of the baroclinic zonal correction is shown versus  $F$ .

At  $Q = 0.1$ , there is a clear subcritical bifurcation with an unsteady, subcritical fixed-point branch emanating from near  $F_c$  (numerical errors prevented the resolution of the unstable fixed-point branch near the origin for  $F > 1.36$ ), a small region in which there is a stable fixed point (near  $F = 1.27$ ) and a supercritical fixed-point branch which is unstable to a Hopf bifurcation (the approximate amplitude of

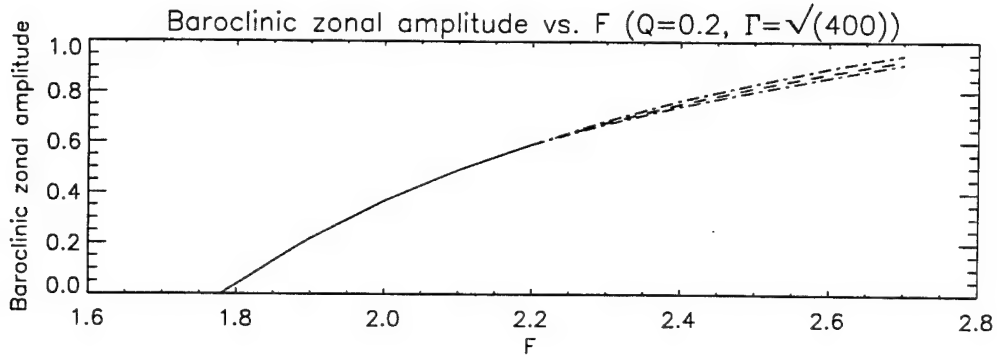


Figure 6.9. Bifurcation structure near  $F_c = 1.81$  for  $Q = 0.2$ ,  $\Gamma = \sqrt{400}$ . The lines have the same meaning as in Figure 6.8.

which is also shown). In contrast, for  $Q = 0.2$ , there is a supercritical, stable fixed-point branch that begins at  $F \approx 1.8$  and becomes unstable to a Hopf bifurcation at  $F \approx 2.2$ . The surrogate EOF models therefore show that the bifurcation structure is subcritical for  $Q = 0.10$  and supercritical for  $Q = 0.20$ , and it therefore must change from one to the other somewhere in the region  $0.10 < Q < 0.20$ . One other interesting item that can be gleaned from the surrogate models is the behavior of the eigenvalues of the various instabilities. More specifically, Figure 6.8 shows that the value of  $F$  at which the stable steady state first appears almost coalesces with the point at which the Hopf bifurcation comes into existence. However, an examination of the eigenvalues at these two parameter values indicates that they do not coalesce. The saddle-node instability has a purely real eigenvalue, while the Hopf bifurcation possesses a complex eigenvalue whose imaginary part does not approach zero as it nears the saddle-node bifurcation. It is reasonable to assume that the instabilities will collide for some value of  $Q$ , and the resulting co-dimension two bifurcation can then generate complicated dynamics (see Guckenheimer and Holmes (1983)).

The surrogate models offer little assistance in understanding the physical origin of the observed subcritical behavior because they are really just a shorthand method for representing the full numerical results. In order to gain this insight, a

perturbation method was used. The goal of this approach was to find the value of  $Q$  at which the cubic term in the Landau equation, which describes the evolution of the amplitude of the linear eigenfunctions near  $F = F_c$ , changes sign. If the bifurcation is supercritical, then we expect that this equation, which can be written as

$$dA/dt = A - \gamma A^3 + h.o.t., \quad (6.1)$$

where  $A$  is the amplitude of the wavy perturbation and  $h.o.t.$  indicates "higher-order terms", will have  $\gamma > 0$ . However, a subcritical bifurcation will have  $\gamma < 0$  so that the lowest nonlinearity of the equation actually destabilizes the steady-state, requiring a higher-order nonlinearity (e.g.  $A^5, A^7, \dots$ ) to bring the system to equilibration.

If we expand the perturbation series in terms of  $A$ , then we can write

$$\phi_{bt} = A(\phi_{bt}^{(1)} + A\phi_{bt}^{(2)} + A^2\phi_{bt}^{(3)} + \dots), \quad (6.2)$$

$$\phi_{bc} = A(\phi_{bc}^{(1)} + A\phi_{bc}^{(2)} + A^2\phi_{bc}^{(3)} + \dots), \quad (6.3)$$

where the superscript indicates the order and  $\phi_{bt}^{(i)}$  and  $\phi_{bc}^{(i)}$  are all  $O(1)$  variables. We also stipulate that

$$\partial/\partial t = \partial/\partial t_1 + A\partial/\partial t_2 + A^2\partial/\partial t_3 + \dots, \quad (6.4)$$

$$F = F_0 + AF_1 + A^2F_2 + \dots, \quad (6.5)$$

where the  $t_i$  and  $F_i$  are also  $O(1)$ . Isolating all terms of  $O(A)$ , we obtain

$$\mathbf{L}[\phi_{bt}^{(1)}\phi_{bc}^{(1)}]^T = 0. \quad (6.6)$$

Here,  $\mathbf{L}$  is a linear differential operator matrix. Solving this equation yields  $F_c$  and the linear eigenfunctions, just as in Chapter 5. At  $O(A^2)$ , the following equation

arises:

$$\mathbf{L}[\phi_{bt}^{(2)} \phi_{bc}^{(2)}]^T = [R_1^{(2)} R_2^{(2)}]^T. \quad (6.7)$$

The right-hand side consists of the nonlinear interactions of the  $O(A)$  solution. From this equation, we obtain two particular solutions—one that is proportional to  $e^{2ikx}$  and one that is a function of  $y$  only. These are the second zonal harmonic and the mean-flow correction generated directly by the nonlinear interactions of the linear eigenfunctions. Finally, at third order, we obtain the following equation:

$$\mathbf{L}[\phi_{bt}^{(3)} \phi_{bc}^{(3)}]^T = [R_1^{(3)} R_2^{(3)}]^T. \quad (6.8)$$

In this case the right-hand side contains terms that resonate with the left-hand side. In order that the solution is valid, these terms must not project onto the original eigenfunctions, which are proportional to  $e^{ikx}$ . This creates a solvability condition that yields the Landau equation, allowing us to determine whether  $\gamma$  is positive or negative. The results of this analysis are shown in Figure 6.10. The coefficient is indeed negative for  $Q < 0.13$ , rendering the instability subcritical. In addition, it is the wave-mean flow interaction that yields a negative  $\gamma$ , as the wave-wave interactions are stabilizing for all  $Q$ . The results agree quite well with the full numerical solutions. However, the numerical results indicate that the transition from  $\gamma < 0$  to  $\gamma > 0$  occurs for  $Q \approx 0.15$ . Upon further examination, the full numerical code revealed that supercritical solutions do indeed exist near the origin, but that subcritical behavior exists for larger amplitudes. This situation may occur if the  $A^3$  term is stabilizing, but the  $A^5$  term is de-stabilizing, requiring a stabilizing  $A^7$  term to bring the system to eventual equilibration. These various scenarios are best

understood visually, as shown in Figure 6.11. Figure 6.11a shows the subcritical bifurcation diagram that exists for  $Q \approx 0.10$ , similar to that shown in Figure 6.8. In this case, the  $A^3$  term is destabilizing and requires a higher order correction for equilibration. In Figure 6.11b, we see the situation when the  $A^3$  term is stabilizing but the  $A^5$  term is destabilizing. This is applicable for  $Q \approx 0.15$ . In this case, small initial conditions started near  $F_c$  will evolve to the small supercritical branch near the origin. However, if the initial perturbation is too large or  $F$  is large enough so that the supercritical branch cannot be reached, then the solution will jump up to the subcritical branch. Finally, for  $Q \approx 0.20$ , Figure 6.11c is the applicable bifurcation diagram (compare to Figure 6.9), and in this case the instability is purely supercritical, with no hysteresis or multiple solutions observed.

The final task is to identify the physical mechanism responsible for the negative Landau coefficient. To accomplish this, the nonlinear terms that combine to yield the wave-mean portion of the Landau coefficient (i.e., the destabilizing part) were compared with their counterparts in the fully slippery case, in which the wave-mean portion of the Landau coefficient is positive and thus stabilizing. Figure 6.12 displays the contributions from the various nonlinear terms for the slippery case, while those for the rigid solution are displayed in Figure 6.13. The  $J_i$  terms are defined as follows:

$$J_1 = \int_{-1}^1 \tilde{\phi}_{bt} \left( -\bar{U}_{bc} \frac{\partial}{\partial x} \nabla^2 \phi'_{bc} \right) dy, \quad (6.9)$$

$$J_2 = \int_{-1}^1 \tilde{\phi}_{bt} \left( -v'_{bc} \frac{\partial}{\partial y} \bar{\omega}_{bc} \right) dy, \quad (6.10)$$

$$J_3 = \int_{-1}^1 \tilde{\phi}_{bc} \left( -v'_{bt} \frac{\partial}{\partial y} \bar{\omega}_{bc} \right) dy, \quad (6.11)$$

$$J_4 = \int_{-1}^1 \tilde{\phi}_{bc} \left( -\bar{U}_{bc} \frac{\partial}{\partial x} \nabla^2 \phi'_{bt} \right) dy, \quad (6.12)$$

$$J_5 = \int_{-1}^1 \tilde{\phi}_{bc} \left( -v'_{bt} 2F \frac{\partial}{\partial y} \bar{\phi}_{bc} \right) dy, \quad (6.13)$$

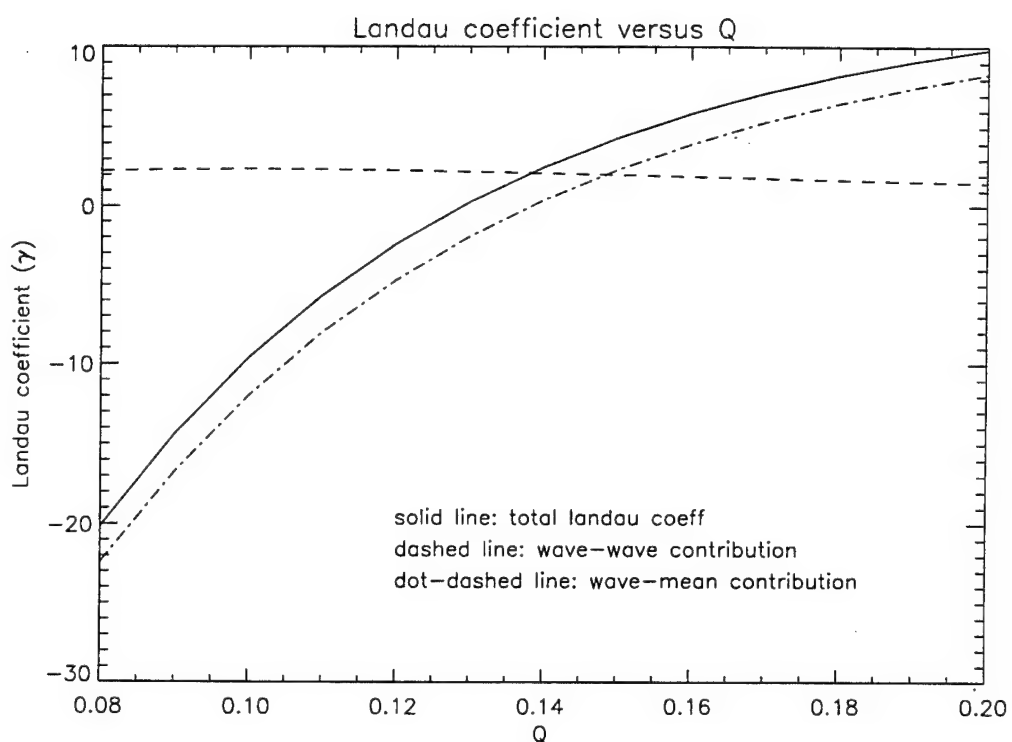


Figure 6.10. Landau coefficient ( $\gamma$ ) versus  $Q$ . The solid line shows the overall coefficient, while the dashed and dot-dashed lines show the wave-wave and wave-mean contributions, respectively.

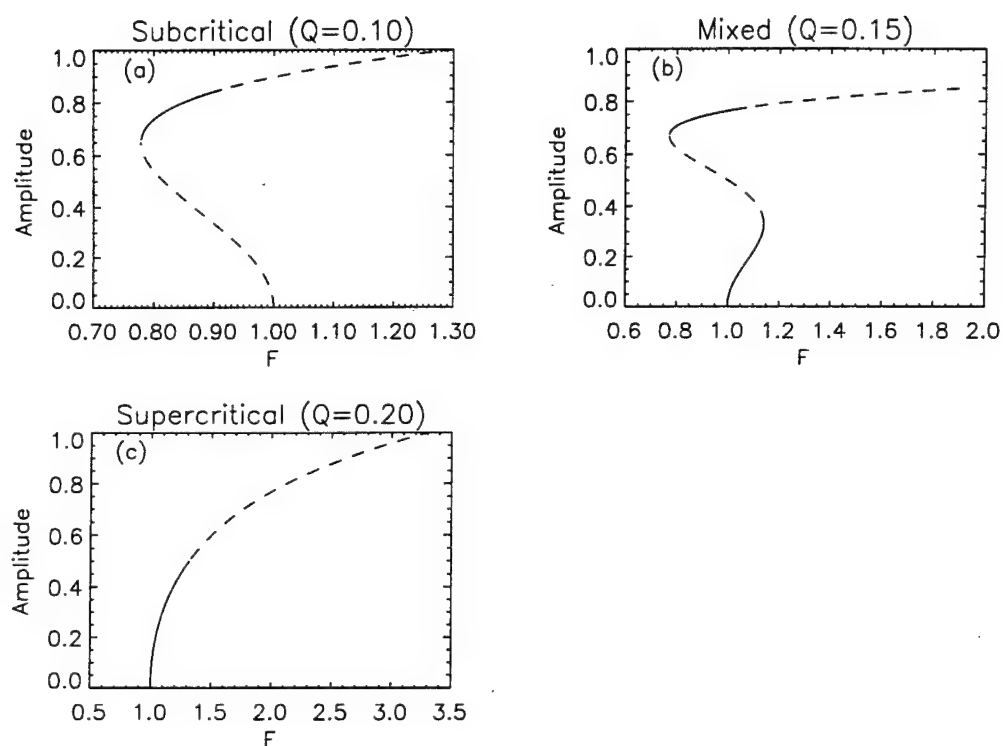


Figure 6.11. Various bifurcation structures seen in the rigid model. (a) purely subcritical bifurcation. (b) mixed bifurcation. (c) purely supercritical bifurcation. In all cases,  $F_c = 1$ , and the amplitudes are arbitrary.

$J_1$  is the zonal advection of wavy baroclinic relative vorticity by the zonal flow,  $J_2$  is the meridional advection of zonal relative vorticity by the baroclinic wavy perturbation,  $J_3$  is the meridional advection of zonal relative vorticity by the barotropic wavy perturbation,  $J_4$  is the zonal advection of wavy barotropic relative vorticity by the zonal flow, and  $J_5$  is the meridional advection of zonal baroclinic vorticity due to interface stretching by the barotropic wavy perturbation. In addition, the  $\sim$  indicates the adjoint solutions, the  $'$  indicates wavy quantities, and the overbar indicates zonally-averaged variables. In the figures, the plots are normalized by the total contribution to the Landau coefficient at  $Q = 0.08$ . Although the respective magnitudes of the  $J_i$  are different between the two cases, only  $J_3$  in the rigid case possesses a sign opposite its slippery counterpart. Thus, the wavy barotropic field advects zonal vorticity in such a way that it enhances its own growth rate against the background state.

The quantity  $J_3$ , which has an  $O(1)$  stabilizing effect in the free-slip case, has an  $O(1)$  de-stabilizing contribution in the rigid formulation. In fact, the change of sign of  $J_3$  coincides closely with the change of sign of the entire contribution from the wave-mean interactions to the Landau coefficient. This is not simply a fortuitous occurrence. If one examines the slippery case for  $Q \ll 1$ , then  $J_1$  and  $J_2$  can be shown to be  $O(Q^2)$  with respect to the remaining  $J_i$ . In addition, although  $J_4$  and  $J_5$  are  $O(1)$ , their difference is also  $O(Q^2)$ . Therefore,  $J_3$  is left as the only remaining  $O(1)$  contribution to the Landau coefficient. Moreover, the difference between  $J_3$  in the slippery and rigid cases can be traced to a single term in  $J_3$ ,  $\partial \bar{\omega}_{bc} / \partial y = \partial^3 \bar{\phi}_{bc} / \partial y^3$  (since the product of the other two terms has almost the same shape in both the rigid and slippery cases, as Figure 6.14 shows). These are shown (for  $Q = 0.08$ ) in Figure 6.15 for the slippery and rigid case, respectively, and the amplitudes are normalized to 1 for convenience. In the rigid case, the large amplitude deviations near the walls, which correspond to large vorticity gradients, change the sign of  $J_3$ .

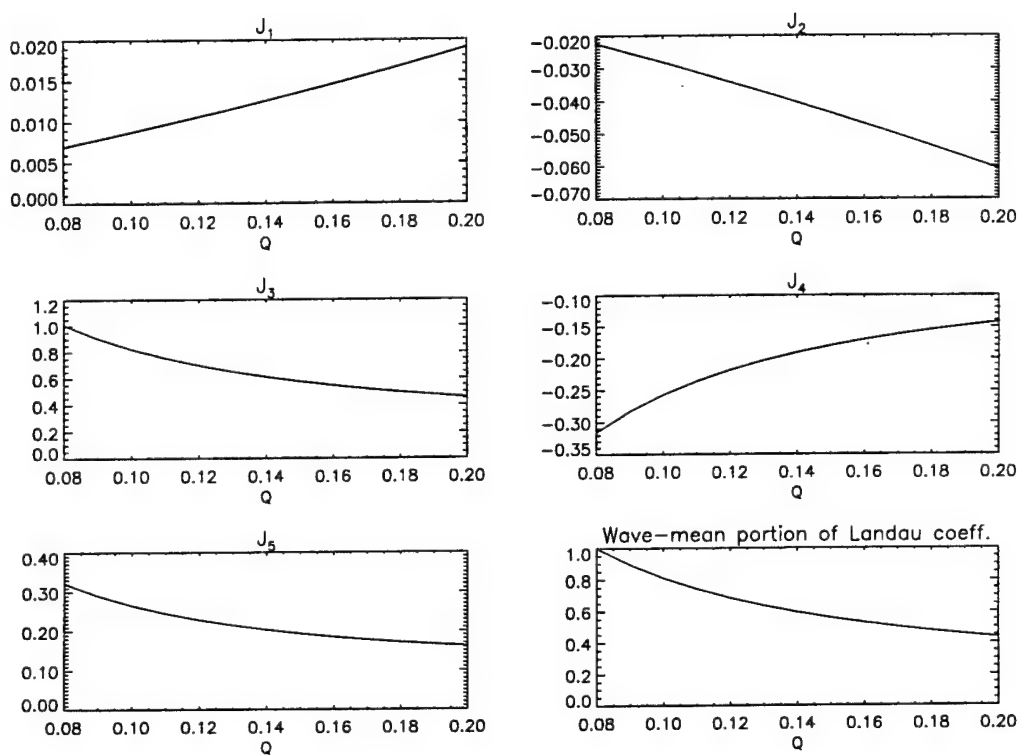


Figure 6.12. Contribution by nonlinear wave-zonal interactions to Landau coefficient, slippery case. The plots have been normalized by the total wave-mean contribution to the Landau coefficient at  $Q = 0.08$ . The  $J_i$  terms are defined in the text.

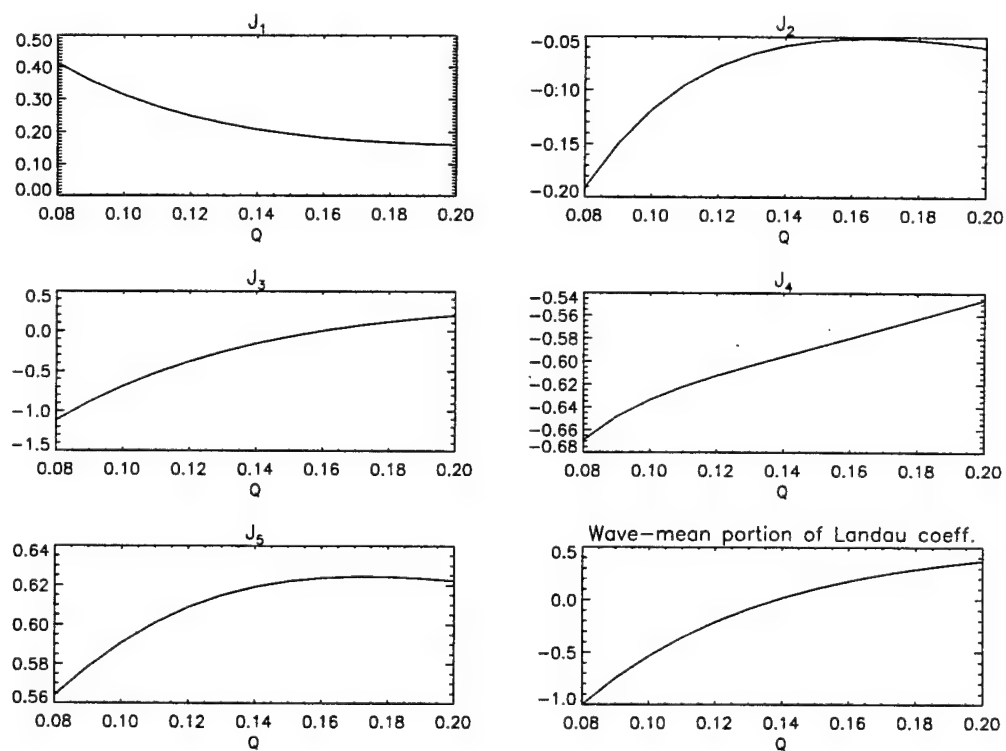


Figure 6.13. Contribution by nonlinear wave-zonal interactions to Landau coefficient, rigid case. The plots have been normalized by the total wave-mean contribution to the Landau coefficient at  $Q = 0.08$ . The  $J_i$  terms are defined in the text.

from positive to negative for certain values of  $Q$ . Thus, the subcritical instability owes its existence entirely to the presence of rigid sidewalls. As  $Q$  increases and the basic profile approaches that of the free-slip case,  $J_3$  becomes positive and the instability becomes supercritical. However, as just discussed, for some values of  $Q$ , higher-order terms act in such a manner as to make the solutions still exhibit subcritical behavior, even though the initial instability is supercritical.

The profound differences in the vorticity gradients shown in Figure 6.15 can be traced back to the shapes of the linearly unstable wavy eigenfunctions. The equation for the baroclinic zonal correction can be written schematically as

$$Q \frac{\partial^2 \bar{\phi}_{bc}^{(2)}}{\partial y^2} - \frac{E}{R_o} \frac{\partial^4 \bar{\phi}_{bc}^{(2)}}{\partial y^4} = \text{RHS}, \quad (6.14)$$

where  $\bar{\phi}_{bc}^{(2)}$  is the second-order, baroclinic zonal correction term. The equation is dominated on the left-hand side by the fourth derivative term, and the right-hand side is a result of the nonlinear interactions of the first-order terms. These nonlinear terms give rise to large derivatives near the walls, thus causing the shape of the zonal correction to deviate significantly from the free-slip case. The right-hand side is in fact dominated by the term  $-k f_1 g_1'''/2$ , where  $f_1$  is the barotropic meridional eigenfunction and  $g_1$  is the baroclinic eigenfunction. The functions  $f_1$ ,  $g_1$ ,  $g_1'''$ , and  $-k f_1 g_1'''/2$  for  $Q = 0.08$  are shown in Figure 6.16. The shape of the nonlinear term is similar to that of the vorticity gradient for the rigid case shown in Figure 6.15 and thus reveals the origin of the zonal correction's shape (in fact, the antiderivative of  $-k f_1 g_1'''/2$  is approximately the vorticity gradient). In contrast, the eigenfunctions and nonlinear terms in the slippery case are sine and cosine functions.

## 6.5 Conclusions

Results for a rigid-wall model were obtained at many points in  $F - Q$  parameter space, and the bifurcation structure of the flow is found to be fundamentally

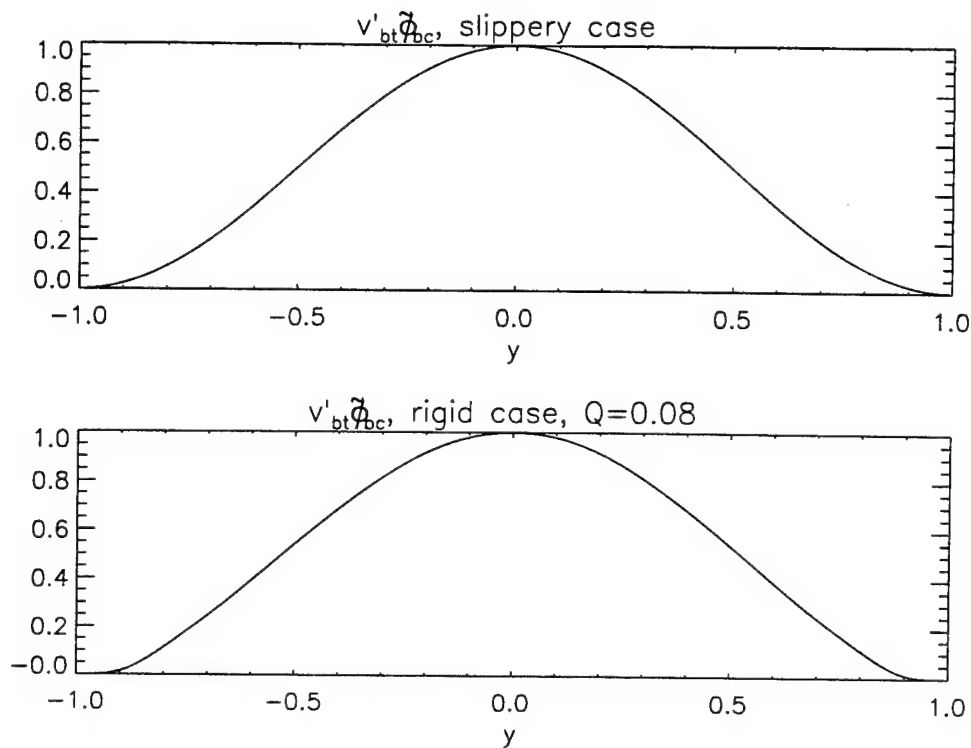


Figure 6.14:  $v'_{bt} \tilde{\phi}_{bc}$  versus  $y$  for slippery and rigid cases,  $Q = 0.08$ .

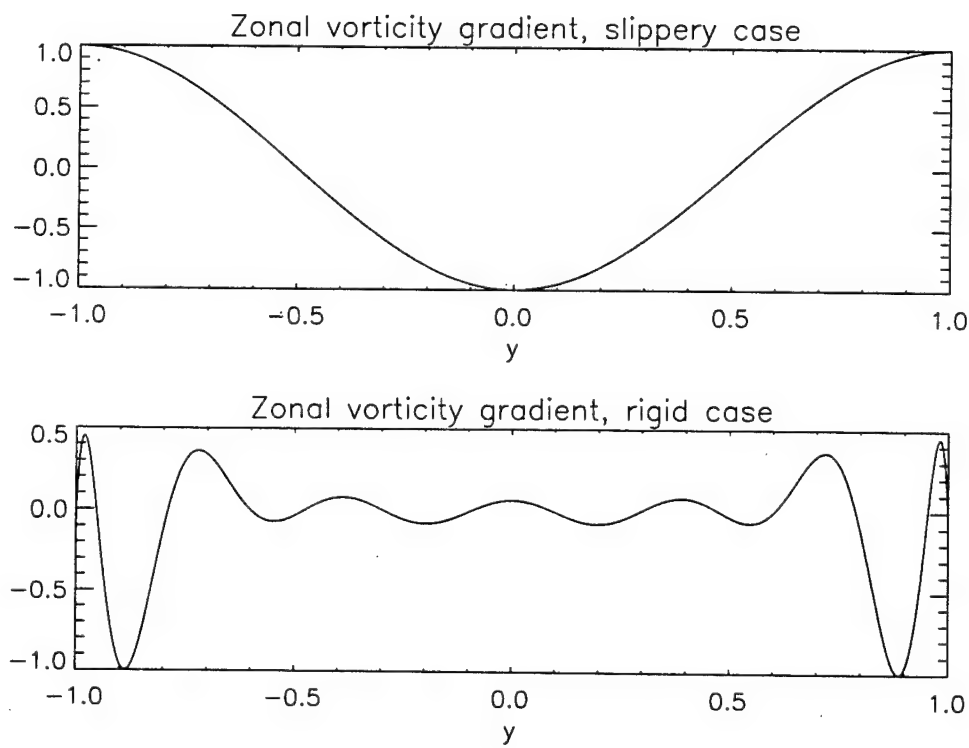


Figure 6.15. Zonal vorticity gradients versus  $y$  for slippery and rigid cases,  $Q = 0.08$ .

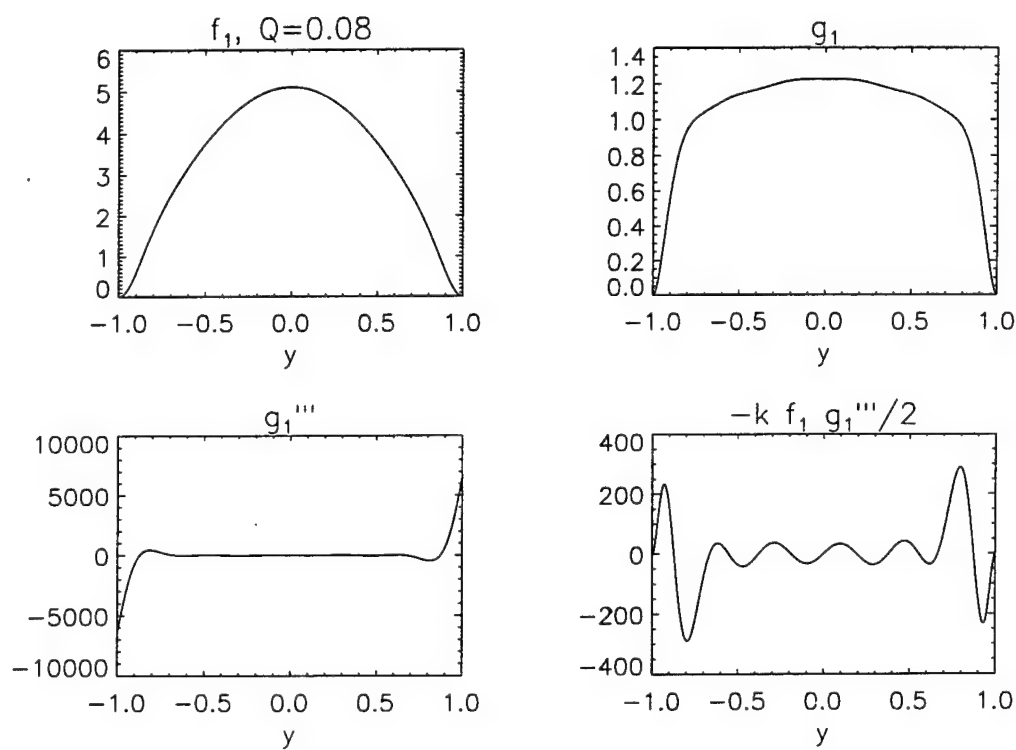


Figure 6.16. Contributions to forcing of zonal correction equation, rigid case,  $Q = 0.08$ .

different from that seen in the slippery-wall implementation. The transition to chaos in the rigid-wall model is abrupt and occurs at  $F_c$  in some instances. Even for larger values of  $Q$  (e.g.  $Q = 0.2$ ), chaos occurs when the supercriticality is  $O(1)$ . Generally, the chaos is caused when an asymmetric barotropic instability grows on top of a secondary, oscillatory baroclinic instability, and asymmetric baroclinic and symmetric barotropic instabilities are entrained in the process. The actual route to chaos is observed to be the breakdown of a torus, just as in the slippery model. For certain values of  $Q$  (corresponding to particular values of  $\Gamma$ ), the initial instability at  $F = F_c$  is subcritical, i.e. the nonlinearities enhance the instability. Because of this, hysteresis exists and finite-amplitude solutions can be found below  $F_c$ . For larger values of  $\Gamma$ , the initial instability is supercritical. The subcritical behavior was investigated via both surrogate EOF models and also using a perturbation analysis. The surrogate models confirm the presence of subcritical bifurcation diagrams for the proper values of  $Q$ . The perturbation analysis indicates that the behavior is caused by wave-mean flow interactions. Specifically, the meridional advection of the relative vorticity of the zonal baroclinic correction by the meridional velocity of the barotropic wave is found to be the main contributor to the subcritical behavior observed.

## CHAPTER 7

### CONCLUSIONS

In this thesis, we have examined the behavior of a two-layer model of quasi-geostrophic flow in a channel. Solutions were obtained both for free-slip walls (which neglect viscous effects) and also rigid walls (which arise from the inclusion of viscosity at the boundaries). Both situations were investigated via the use of high-resolution numerical models.

The fully-slippery case was formulated in order to correct the deficiencies in previous models, which use inconsistent boundary conditions on the zonal flow. Solutions were obtained both for a symmetric wave state and an asymmetric solution. The symmetric wave state exhibits a transition from steady to periodic to quasi-periodic flow over the range of  $F$  studied. However, the symmetric state is unstable over a large range of  $F$  and is therefore not physically realizable. The asymmetric solution shows a clear transition from steady flow to periodic flow to quasi-periodicity and finally to chaos. Periodic solutions can take the form of periodic amplitude vacillation (PAV), in which the energy transfers are largely baroclinic, or they can alternately be in the form of periodic structural vacillation (PSV), where the transfers of energy are primarily barotropic. The quasi-periodic solutions are found to be caused by the interactions of two competing instabilities. This phenomenon occurs between instabilities of differing symmetries. When three time-dependent instabilities are simultaneously present, the system breaks down into chaos. In addition, the evidence of a low-dimensional attractor on which the system evolves quickly disappears as  $F$  is increased beyond the threshold for chaos. Numerical runs at values of  $F$  much greater than the critical value for chaos reveal that the flow eventually reaches

a point of presumed "geostrophic turbulence", although the scaling relations differ from the classic signature of geostrophic turbulence. Nonetheless, in this situation the spatial and temporal power spectra exhibit the beginnings of self-similarity (as in fully-developed turbulence) and the attractor of the flow becomes large. The results are disappointing in comparison to laboratory experiments, since the simulations produce chaos at  $F \approx 5F_c$ , while laboratory flows become chaotic for  $F \approx 1.6F_c$ .

In order to better understand the results from the slippery model, a quasi-analytical method was invoked in order to find the steady states of the system and also any secondary instabilities that may be present. Despite the fact that the resolution of the quasi-linear model is limited to  $O(10^2)$  degrees of freedom in comparison to the full model (with  $O(10^4)$  degrees of freedom), the results are consistent with the behavior of the large numerical simulations. Applying the technique to the symmetric solution, the onset of the various instabilities in the quasi-analytical model agrees with that seen in the numerical results. In addition, the predicted frequencies of the barotropic and baroclinic disturbances match extremely well with the actual frequencies observed in the simulations. Moreover, the actual spatial structures of the growing eigenfunctions corresponding to PAV and PSV behavior correlate very highly with the dominant structures in the full flow in the respective regimes. This indicates that the PAV and PSV vacillations originate as simple instabilities of the steady-state solution. For the asymmetric case, the predicted sequence of secondary bifurcations also agrees with the behavior of the full numerical code. The observed PSV frequency corresponds to that predicted by the quasi-analytical method. As in the symmetric solution, the eigenfunctions calculated analytically correlate highly with the observed spatial structures of the flow in the applicable regimes. Finally, since the mean fields in the flow are much larger than their respective rms deviations, the mean quantities approximate well the steady state of the system (and vice versa). As a result, this implies that the steady-state solutions can be approximately

extracted by simply measuring the mean quantities.

The solutions observed in the slippery model were also investigated by extracting the Empirical Orthogonal Functions (EOFs) of the system in various regimes. This method was employed for two reasons. First, the EOFs themselves can reveal a great deal of information regarding the underlying complexity of the flow, and in some instances it can also reveal physical processes. In addition, the EOFs can be used to generate approximate dynamical systems of the model in question, thus allowing one to (possibly) forge a link between low-dimensional systems and the behavior of complex numerical simulations. For both the symmetric and asymmetric solutions, the number of EOFs needed to adequately represent the flow is proportional to its temporal complexity, indicating that the spatial and temporal characteristics of the system are inextricably linked. In periodic regimes,  $O(10)$  total fields are adequate to describe the behavior accurately; however, for quasi-periodic flows, the required number is  $O(50)$ , and for chaotic flows,  $O(100)$ . Not surprisingly, the number of EOFs needed to adequately represent the vorticity at a chosen value of  $F$  is more (by a factor of 4 or so) than the number required to represent the streamfunction. The number of modes needed to replicate the flow indicates that, although the temporal behavior of the system sometimes indicates low-dimensional evolution, the entire spatio-temporal field is far too complex to be described by a few equations. Despite the caveats, dynamical systems were constructed using the EOFs in several regimes. For purely periodic and simple quasi-periodic flows, the method works well, generating results very similar to the original solutions. In more complicated spatio-temporal regimes, the number of EOFs required forced severe truncations of the spatial fields. Nonetheless, the resulting systems yield qualitatively accurate representations of the original flows.

Turning to the rigid-wall model, the linear stability curves were calculated

using a numerical approach. Numerical solutions are necessary because of the non-uniform nature of the basic state. The critical Froude number is found to depend greatly on  $\Gamma$ , where  $\Gamma \equiv \sqrt{2Q/(E/R_o)}$ . For  $Q \ll \Gamma^{-4}$ , the solution matches that predicted by Pedlosky and Klein (1991), i.e. the barotropic eigenfunction at  $F_c$  is essentially equal to  $U_{bc}$  and the baroclinic eigenfunction is nearly 0. When the above relation between  $Q$  and  $\Gamma$  holds, the advection by the basic-state velocity of the perturbation vorticity cancels the advection of basic-state vorticity by the perturbation velocity, resulting in  $F_c \approx k^2/2$ . In the region where  $\Gamma^{-4} < Q \ll 1$  and  $\Gamma$  is relatively large, the solution is nearly identical to the free-slip results. The barotropic eigenfunction is approximately equal to  $\cos(\pi y/2)$  while the baroclinic eigenfunction is  $Q \cos(\pi y/2)/k$ , and  $F_c = (k^2 + l^2)/2$ . Between these two limits,  $k^2/2 < F_c < (k^2 + l^2)/2$  and the eigenfunctions are more complicated and must be obtained numerically. At large values of  $Q$  and  $\Gamma$ , the solutions are nearly equivalent to those of the free-slip case, while for large  $Q$  and smaller  $\Gamma$  there is an increase in  $F_c$  over the slippery-model results. The analysis was also expanded to include the situation with a basic-state barotropic flow,  $U_{bt}$ . The inclusion of nonzero  $U_{bt}$  introduces the presence of critical layers into the interior of the flow, and it thus may be expected to alter  $F_c$  substantially. The results indicate that, while the  $U_{bt} \neq 0$  case may be more or less stable than its counterpart with  $U_{bt} = 0$ , the differences in  $F_c$  are only about 15% in the region applicable to laboratory results. Finally, an examination of the energy transfers in the flow shows that the presence of a barotropic basic state enhances the barotropic energy transfer at  $F_c$ , and the eigenfunctions show substantial shape variations as they move through the critical layers.

Finally, solutions of the rigid-wall model were obtained numerically. Results were generated by fixing  $E/R_o = 0.001$  and varying  $F$  and  $Q$ . A constant

value for  $E/R_o$  indicates that changes in  $Q$  effect changes in  $\Gamma$  as well, thus altering the basic-state profile. The results are profoundly different from the slippery model. The observed route to chaos is generally through the break-up of a transient two-torus, and for certain values of  $Q$  chaos occurs at  $F_c$ . This phenomenon is due to the generation of multiple instabilities simultaneously in parameter space. Even for larger values of  $Q$ , the flow becomes chaotic at  $O(1)$  supercriticality. In this manner, the results are in much better agreement with laboratory experiments (which exhibit chaos at similar supercriticality). Also observed for relatively small values of  $Q$  is subcritical behavior (and thus hysteresis) near  $F = F_c$ . The cause of this behavior was investigated via the use of surrogate EOF models and also by using a perturbation analysis. The surrogate models confirm the presence of a subcritical instability by yielding appropriate bifurcation diagrams. The physical cause of the subcritical behavior, found by the perturbation method, is determined to be wave-mean flow interactions. The primary component of the wave-mean interaction responsible for the behavior is the meridional advection of the relative vorticity of the zonal baroclinic correction by the meridional velocity of the barotropic wavy perturbation. Slight discrepancies were found between the results of the perturbation analysis and the full numerical solutions. The discrepancy is due to the presence of a mixed bifurcation state, over a small range of  $Q$ , where the third-order terms in the Landau equation are stabilizing (supercritical) but the fifth-order terms are destabilizing (subcritical). The presence of this situation was confirmed in the full numerical solutions.

A logical extension of the analyses presented in this thesis is to examine the results in a cylindrical domain. A rigid-wall model with such a geometry would hopefully allow quantitative agreement with experiment and would presumably explain the discrepancies found between experiment and previous numerical results using free-slip sidewalls. Another topic of interest would be to extend the EOF

analyses to more realistic models of geophysical flows. This, however, would require a more detailed understanding of the problems associated with using approximate dynamical systems to replicate complex spatio-temporal behavior. In particular, the parameterization of low-energy modes needs to be accounted for in a systematic, physical manner before the method can be considered viable.

## BIBLIOGRAPHY

Aubry, N., P. Holmes, J. L. Lumley, and E. Stone, The Dynamics of Coherent Structures in the Wall Region of a Turbulent Boundary Layer, *J. Fluid Mech.*, **192**, 115–173, 1988.

Aubry, N., P. Holmes, J. L. Lumley, and E. Stone, Application of Dynamical System Theory to Coherent Structures in the Wall Region, *Physica D*, **37**, 1–10, 1989.

Baker, G. L. and J. P. Gollub, *Chaotic Dynamics: An Introduction*, Cambridge University Press, Cambridge, 1990.

Berge, P., Y. Pomeau, and C. Vidal, *Order Within Chaos*, John Wiley, New York, 1984.

Boville, B. A., Amplitude Vacillation on an  $f$ -Plane, *J. Atmos. Sci.*, **37**, 1413–1423, 1980.

Boville, B. A., Amplitude Vacillation on a  $\beta$ -Plane, *J. Atmos. Sci.*, **38**, 609–618, 1981.

Boville, B. A., Strongly Nonlinear Vacillation in Baroclinic Waves, *J. Atmos. Sci.*, **39**, 1227–1240, 1982.

Brandstater, A. and H. L. Swinney, Strange Attractors in Weakly Turbulent Couette Flow, *Phys. Rev. A.*, **35**, 2207–2220, 1987.

Brummell, N. H., unpublished manuscript, 1993.

Busse, F. H. and A. C. Or, Convection in a Rotating Cylindrical Annulus: Thermal Rossby Waves, *J. Fluid Mech.*, **166**, 173–187, 1986.

Buzyna, G., R. L. Pfeffer, and R. Kung, Transition to Geostrophic Turbulence in a Rotating Differentially Heated Annulus of Fluid, *J. Fluid Mech.*, **145**, 377–403, 1984.

Canuto, C., M. Y. Hussaini, A. Quarteroni, and T. A. Zang, *Spectral Methods in Fluid Dynamics*, Springer-Verlag, New York, 1988.

Cattaneo, F. and J. E. Hart, Multiple States for Quasi-Geostrophic Channel Flows, *Geophys. Astrophys. Fluid Dyn.*, **54**, 1–33, 1990.

Charney, J. G., The Dynamics of Long Waves in a Baroclinic Westerly Current, *J. Meteorol.*, **4**, 135–162, 1947.

Davey, M. K., Recycling Flow over Bottom Topography in a Rotating Annulus, *J. Fluid Mech.*, **87**, 497-520, 1978.

Davey, M. K., A Quasi-Linear Theory for Rotating Flow Over Topography. Part 1: Steady  $\beta$ -Plane Channel, *J. Fluid Mech.*, **99**, 267-292, 1980.

Deane, A. E. and L. Sirovich, A Computational Study of Rayleigh-Benard Convection. Part 2. Dimension Considerations, *J. Fluid Mech.*, **222**, 251-265, 1991.

Deane, A. E., I. G. Kevrekidis, G. E. Karniadakis, and S. A. Orszag, Low-Dimensional Models for Complex Geometry Flows: Application to Grooved Channels and Circular Cylinders, *Phys. Fluids A*, **3**, 2337-2354, 1991.

Drazin, P. G. and W. H. Reid, *Hydrodynamic Stability*, Cambridge University Press, Cambridge, 1981.

Eady, E. T., Long Waves and Cyclone Waves, *Tellus*, **1**, 35-52, 1949.

Eckmann, J.-P., S. O. Kamphorst, D. Ruelle, and S. Ciliberto, Liapunov Exponents from Time Series, *Phys. Rev. A.*, **34**, 4971-4979, 1986.

Eckmann, J.-P. and D. Ruelle, Fundamental Limitations for Estimating Dimensions and Lyapunov Exponents in Dynamical Systems, *Physica D*, **56**, 185-187, 1992.

Farmer, D., J. Hart, and P. Weidman, A Phase Space Analysis of Baroclinic Flow, *Phys. Lett. A*, **91**, 22-24, 1982.

Farmer, J. D. and J. J. Sidorowich, Predicting Chaotic Time Series, *Phys. Rev. Lett.*, **59**, 845-848, 1987.

Feigenbaum, M. J., Quantitative Universality for a Class of Nonlinear Transformations, *J. Stat. Phys.*, **19**, 25-52, 1978.

Flierl, G. R., Models of Vertical Structure and the Calibration of Two-Layer Models, *Dyn. Atmos. Oceans*, **2**, 341-381, 1978.

Guckenheimer, J., and P. Holmes, *Nonlinear Oscillations, Dynamical Systems, and Bifurcations of Vector Fields*, Volume 42 of *Applied Mathematical Sciences*, Springer-Verlag, New York, 1983.

Grassberger, P., and I. Procaccia, Characterization of Strange Attractors, *Phys. Rev. Lett.*, **50**, 346-349, 1983a.

Grassberger, P., and I. Procaccia, Measuring the Strangeness of Strange Attractors, *Physica D*, **9**, 189-208, 1983b.

Greenside, H. S., A. Wolf, J. Swift, and Pignataro, T., Impracticality of a Box-Counting Algorithm for Calculating the Dimensionality of Strange Attractors, *Phys. Rev. A.*, **25**, 3453-3456, 1982.

Guckenheimer, J. and G. Buzyna, Dimension Measurements for Geostrophic Turbulence, *Phys. Rev. Lett.*, **51**, 1438–1441, 1983.

Hart, J. E., A Laboratory Study of Baroclinic Instability, *Geophys. Fluid Dyn.*, **3**, 181–209, 1972.

Hart, J. E., The Modulation of an Unstable Baroclinic Wave Field, *J. Atmos. Sci.*, **33**, 1874–1889, 1976.

Hart, J. E., Finite Amplitude Baroclinic Instability, *Ann. Rev. Fluid Mech.*, **11**, 147–172, 1979.

Hart, J. E., Wavenumber Selection in Nonlinear Baroclinic Instability, *J. Atmos. Sci.*, **38**, 400–408, 1981.

Hart, J. E., A Laboratory Study of Baroclinic Chaos on the *f*-Plane, *Tellus*, **37A**, 286–296, 1985.

Hart, J. E., A Model for the Transition to Baroclinic Chaos, *Physica D*, **20**, 350–362, 1986.

Hide, R. and P. J. Mason, Sloping Convection in a Rotating Fluid, *Adv. Phys.*, **24**, 57–100, 1975.

Holland, W. R., The Role of Mesoscale Eddies in the General Circulation of the Ocean—Numerical Experiments Using a Wind-Driven Quasi-Geostrophic Model, *J. Phys. Ocean.*, **8**, 363–392, 1978.

Holton, J. R., *An Introduction to Dynamic Meteorology*, Academic Press, New York, 1972.

Hurlburt, H. E. and J. D. Thompson, A Numerical Study of Loop Current Intrusions and Eddy Shedding, *J. Phys. Ocean.*, **10**, 1611–1651, 1980.

Klein, P. and J. Pedlosky, A Numerical Study of Baroclinic Instability at Large Supercriticality, *J. Atmos. Sci.*, **43**, 1243–1262, 1986.

Klein, P. and J. Pedlosky, The Role of Dissipation Mechanisms in the Nonlinear Dynamics of Unstable Baroclinic Waves, *J. Atmos. Sci.*, **49**, 29–48, 1992.

Kleiser, L. and Schumann, U., in *Proceedings of the 3<sup>rd</sup> Gesellschaft für Angewandte Mathematik and Mechanik Conference: Numerical Methods in Fluid Mechanics*, ed. E.H. Hirschel, Vieweg, Braunschweig, 165, 1980.

Loeve, M. M., *Probability Theory*, van Nostrand, Princeton, 1955.

Lorenz, E. N., Deterministic Nonperiodic Flow, *J. Atmos. Sci.*, **20**, 130–141, 1963.

Lumley, J. L., The Structure of Inhomogeneous Turbulent Flows, in *Atmospheric Turbulence and Radio Wave Propagation*, A. M. Yaglom and V. I. Tatarsky, eds., pp. 166-178, NAUKA, Moscow, 1967.

Lumley, J. L., *Stochastic Tools in Turbulence*, Academic Press, New York, 1970.

Nerenberg, M. A. H. and C. Essex, Correlation Dimension and Systematic Geometric Effects, *Phys. Rev. A.*, 42, 7065-7074, 1990.

Ohlsen, D. R. and J. E. Hart, The Transition to Baroclinic Chaos on the  $\beta$ -Plane, *J. Fluid Mech.*, 203, 23-50, 1989a.

Ohlsen, D. R. and J. E. Hart, Nonlinear Interference Vacillation, *Geophys. Astrophys. Fluid Dyn.*, 45, 213-235, 1989b.

Oort, A. H. and J. P. Peixoto, The Annual Cycle of the Energetics of the Atmosphere on a Planetary Scale, *J. Geophys. Res.*, 79, 2705-2719, 1974.

Or, A. C. and F. H. Busse, Convection in a Rotating Cylindrical Annulus. Part 2. Transitions to Asymmetric and Vacillating Flow, *J. Fluid Mech.*, 174, 313-326, 1987.

Orlanski, I. and M. D. Cox, Baroclinic Instability in Ocean Currents, *Geophys. Fluid Dyn.*, 4, 297-332, 1973.

Packard, N. H., J. P. Crutchfield, J. D. Farmer, and R. S. Shaw, Geometry from a Time Series, *Phys. Rev. Lett.*, 45, 712-716, 1980.

Pedlosky, J., Finite-Amplitude Baroclinic Waves, *J. Atmos. Sci.*, 27, 15-30, 1970.

Pedlosky, J., Finite-Amplitude Baroclinic Waves with Small Dissipation, *J. Atmos. Sci.*, 28, 587-597, 1971.

Pedlosky, J., Limit Cycles and Unstable Baroclinic Waves, *J. Atmos. Sci.*, 29, 53-63, 1972.

Pedlosky, J., *Geophysical Fluid Dynamics*, 2nd Ed., Springer-Verlag, New York, 1987.

Pedlosky, J. and C. Frenzen, Chaotic and Periodic Behavior of Finite-Amplitude Baroclinic Waves, *J. Atmos. Sci.*, 37, 1177-1196, 1980.

Pedlosky, J. and L. M. Polvani, Wave-Wave Interaction of Unstable Baroclinic Waves, *J. Atmos. Sci.*, 44, 631-647, 1987.

Pedlosky, J. and P. Klein, The Nonlinear Dynamics of Slightly Supercritical Baroclinic Jets, *J. Atmos. Sci.*, 48, 1276-1286, 1991.

Pfeffer, R. L. and Y. Chiang, Two Kinds of Vacillation in Rotating Laboratory Experiments, *Mon. Weather Rev.*, 95, 75-82, 1967.

Pfeffer, R. L. and W. W. Fowlis, Wave Dispersion in a Rotating, Differentially Heated Cylindrical Annulus of Fluid, *J. Atmos. Sci.*, **25**, 361–371, 1968.

Pfeffer, R., G. Buzyna, and W. W. Fowlis, Synoptic Features and Energetics of Wave-Amplitude Vacillation in a Rotating, Differentially-Heated Fluid, *J. Atmos. Sci.*, **31**, 622–645, 1974.

Pfeffer, R. L., G. Buzyna, and R. Kung, Time-Dependent Modes of Behavior of Thermally Driven Rotating Fluids, *J. Atmos. Sci.*, **37**, 2129–2149, 1980.

Phillips, N. A., Energy Transformations and Meridional Circulations Associated with Simple Baroclinic Waves in a Two-Level, Quasi-Geostrophic Model, *Tellus*, **6**, 273–286, 1954.

Priesendorfer, R. W., *Principal Component Analysis in Meteorology and Oceanography*, Elsevier, Amsterdam, 1988.

Rasband, N. S., *Chaotic Dynamics of Nonlinear Systems*, John Wiley, New York, 1990.

Read, P. L., Applications of Singular Systems Analysis to 'Baroclinic Chaos', *Physica D*, **58**, 455–568, 1992.

Read, P. L., M. J. Bell, D. W. Johnson, and R. M. Small, Quasi-Periodic and Chaotic Flow Regimes in a Thermally Driven, Rotating Fluid Annulus, *J. Fluid Mech.*, **238**, 599–632, 1992.

Rodriguez, J. D. and L. Sirovich, Low-Dimensional Dynamics for the Ginzburg-Landau Equation, *Physica D*, **43**, 77–86, 1990.

Ruelle, D. and F. Takens, On the Nature of Turbulence, *Commun. Math. Phys.*, **20**, 167–192, 1971.

Sano, M. and Y. Sawada, Measurement of the Lyapunov Spectrum from a Chaotic Time Series, *Phys Rev. Lett.*, **55**, 1082–1085, 1985.

Schuster, H. G., *Deterministic Chaos*, 2nd Ed., Physik Verlag, Weinheim, FRG, 1989.

Sirovich, L., Turbulence and the Dynamics of Coherent Structures. Part I: Coherent Structures, *Quar. Appl. Math.*, **45**, 561–571, 1987.

Sirovich, L., Chaotic Dynamics of Coherent Structures, *Physica D*, **37**, 126–145, 1989.

Sirovich, L., Empirical Eigenfunctions and Low Dimensional Systems, in *New Perspectives in Turbulence*, Springer-Verlag, New York, 1991.

Sirovich, L. and J. D. Rodriguez, Coherent Structures and Chaos: A Model Problem, *Phys. Lett. A*, **120**, 211–214, 1987.

Sirovich, L., M. Kirby, and M. Winter, An Eigenfunction Approach to Large Scale Transitional Structures in Jet Flow, *Phys. Fluids A*, **2**, 127–136, 1990a.

Sirovich, L., K. S. Ball, and L. R. Keefe, Plane Waves and Structures in Turbulent Channel Flow, *Phys. Fluids A*, **2**, 2217–2226, 1990b.

Sirovich, L., B. W. Knight, and J. D. Rodriguez, Optimal Low-Dimensional Dynamical Approximations, *Quar. Appl. Math.*, **48**, 535–548, 1990c.

Smith, G. R., E. D. Boerner, R. H. Cohen, and W. A. Newcomb, *Empirical Orthogonal Functions and Spectral Models of the Atmosphere*, presented at the 1991 AGU Fall Meeting, December 9–13, 1991.

Stewartson, K., On Almost Rigid Rotations, *J. Fluid Mech.*, **3**, 17–26, 1957.

Takens, F., Detecting Strange Attractors in Turbulence, in *Dynamical Systems and Turbulence*, Vol. 898 of Lecture Notes in Mathematics, edited by D. A. Rand and L. S. Young, pp. 366–381, Springer, New York, 1981.

Theiler, J., Some Comments on the Correlation Dimension of  $1/f^\alpha$  Noise, *Phys. Lett. A*, **155**, 480–493, 1991.

Webster, P. J. and J. L. Keller, Atmospheric Variations: Vacillations and Index Cycles, *J. Atmos. Sci.*, **32**, 1283–1300, 1975.

Weng, H.-Y., A. Barcilon, and J. Magnan, Transitions between Baroclinic Flow Regimes, *J. Atmos. Sci.*, **43**, 1760–1777, 1986.

Wolf, A., J. B. Swift, H. L. Swinney, and J. A. Vastano, Determining Lyapunov Exponents from a Time Series, *Physica D*, **16**, 285–317, 1985.

Wolfram, S., *Mathematica: A System for Doing Mathematics by Computer*, 2nd Ed., Addison-Wesley, Redwood City, 1991.

Yoshida, A. and J. E. Hart, A Numerical Study of Baroclinic Chaos, *Geophys. Astrophys. Fluid Dyn.*, **37**, 1–56, 1986.

## APPENDIX A

### QUANTITIES OF FLOW ENERGETICS

Equations 1.31-34 describe the evolution of the zonal and wavy potential and kinetic energies. It is useful to briefly list the form of each term on the right-hand sides of the energy equations. In the following equations,  $\bar{w}_{int}$  denotes the vertical velocity of the fluid interface, and the  $x$  and  $y$  subscripts denote partial differentiation with respect to that particular variable.

$$\{\bar{K} \cdot \bar{P}\} = \iint \bar{w}_{int} (\bar{P}_2 - \bar{P}_1) dx dy, \quad (A.1)$$

$$\{P' \cdot \bar{P}\} = F \iint (\bar{P}_2 - \bar{P}_1) J(P'_2, P'_1) dx dy, \quad (A.2)$$

$$\{K' \cdot \bar{K}\} = - \iint [\bar{P}_1 J(P'_1, P'_{1yy}) + \bar{P}_2 J(P'_2, P'_{2yy})] dx dy, \quad (A.3)$$

$$\{K' \cdot P'\} = \iint w'_{int} (P'_2 - P'_1) dx dy, \quad (A.4)$$

$$\begin{aligned} \bar{F} = & -Q \iint \bar{P}_{1y} \bar{P}_{2y} dx dy + \frac{3Q}{2} \iint (\bar{P}_{1y}^2 + \bar{P}_{2y}^2) dx dy + \\ & \frac{E}{R_o} \iint (\bar{P}_{1yy}^2 + \bar{P}_{2yy}^2) dx dy, \text{ and} \end{aligned} \quad (A.5)$$

$$\begin{aligned} F' = & -Q \iint (P'_{1z} P'_{1y} + P'_{2z} P'_{2y}) dx dy + \\ & \frac{3Q}{2} \iint (P'_{1z}^2 + P'_{1y}^2 + P'_{2z}^2 + P'_{2y}^2) dx dy + \\ & \frac{E}{R_o} \iint (P'_{1yy}^2 + P'_{1yy}^2 + P'_{2yy}^2 + P'_{2yy}^2 \\ & + 2P'_{1yy}^2 + 2P'_{2yy}^2) dx dy. \end{aligned} \quad (A.6)$$

The equation describing the energy input depends on the specific model implementation. However, it is useful to briefly describe the result obtained for the model to

be discussed in Chapter 2. Equations B.4,5 describe the evolution of the zonally-averaged flow at the walls, *minus* the basic-state flow. If the basic-state terms are included (i.e.  $\bar{u}_1 = 1, \bar{u}_2 = -1$ ), and the flow is assumed steady (which is of course the case in the basic flow regime), then the equations are inconsistent unless a  $+2Q$  term is added onto Equation B.4 and a  $-2Q$  term is added onto Equation B.5. Then, multiplying Equation B.4, modified by the  $+2Q$  term, by  $-\bar{u}_1$ , and multiplying Equation B.5, augmented by a  $-2Q$  term, by  $-\bar{u}_2$ , one obtains equations for the rate of change of zonal kinetic energy. If the resulting equations are integrated over the domain of the fluid, an energy input term materializes, and it is given by

$$\overline{EI} = 8Q(2 + \mathcal{U}_2(t) - \mathcal{U}_1(t)). \quad (\text{A.7})$$

The quantities  $\mathcal{U}_2(t)$  and  $\mathcal{U}_1(t)$  are zonal correction terms specific to the slippery model presented in Chapter 2 and are discussed further there.

## APPENDIX B

### DERIVATION OF ADDITIONAL CONDITIONS

Appendix B contains the derivation of the additional conditions required for the slippery model.

The first additional condition that must be satisfied is that of mass conservation. If one imposes the reasonable requirement that the mass in each layer be constant for all time, then

$$\int_0^1 \int_0^4 h(x, y) dx dy = C, \quad (B.1)$$

where  $h(x, y)$  is the height of the interface between the two layers and  $C$  is a constant.

Using Equation 1.11, this can be written as

$$\int_0^1 \int_0^4 R_o F(P_2 - P_1) dx dy = C, \quad (B.2)$$

or

$$\frac{d}{dt} \int_0^1 \int_0^4 R_o F(P_2 - P_1) dx dy = 0. \quad (B.3)$$

The wavy terms for both the semi-slippery and slippery models trivially satisfy this condition, but the zonal terms are somewhat more problematic. For the semi-slippery model, the use of cosine functions for the zonal flow also trivially satisfies the above requirement, but the sine function expansion used in the stress-free model does not. More specifically, zonal terms of the form  $\sin(j' \pi y)$ , with  $j' = 1, 3, 5, \dots$  (which are

zero in the symmetric state but nonzero in the asymmetric case) yield a nonzero value when integrated across the channel. As a result, an extra term must be added that will allow the mass conservation condition to be satisfied for all solutions. The exact implementation of this condition will be addressed once the circulation condition has been examined.

The circulation condition can be obtained by appealing to the original momentum equations for the two-layer flow. If one writes down the zonal momentum equation for the upper layer (i.e. layer 1),

$$\frac{\partial u_1}{\partial t} + \vec{u}_1 \cdot \nabla u_1 - v_1^{(1)} = -\partial p_1^{(1)}/\partial x + \frac{E}{R_o} \nabla^2 u_1, \quad (\text{B.4})$$

(where the <sup>(1)</sup> superscripts indicate ageostrophic quantities) and then takes a zonal average by performing the following operation on Equation B.4,

$$\frac{1}{L} \int_0^L (\cdot) dx, \quad (\text{B.5})$$

one finally obtains a zonally-averaged momentum equation,

$$\frac{\partial \bar{u}_1}{\partial t} + \frac{\partial}{\partial y} (\bar{u}_1 \bar{v}_1) - \bar{v}_1^{(1)} = \frac{E}{R_o} \frac{\partial^2}{\partial y^2} \bar{u}_1. \quad (\text{B.6})$$

The term  $\bar{v}_1^{(1)}$  is the ageostrophic meridional velocity and its x-average therefore does not necessarily vanish. Now, near the wall at  $y=1$ , there will be a meridional flux directed toward the wall in the upper Ekman layer. This flux is proportional to  $\bar{v}_1^{(1)}$  and subsequently to  $\bar{u}_1$ , a result derivable from an analysis of Ekman layers (see Pedlosky, 1987). However, because the wall is impermeable, the mass flux must be returned into the interior flow (via a thin boundary layer whose effects are not explicitly included), so that  $\bar{v}_1^{(1)} \propto -\bar{u}_1$  near  $y=1$ . This condition must hold for all the

Ekman layers, and it also is valid at  $y=0$ . Thus, after implementing this condition at both walls, and noting that  $\frac{\partial}{\partial y}(\bar{u}_1 \bar{v}_1) = 0$  at  $y=0,1$ , the zonal momentum equations can be written for the two layers as

$$\frac{\partial \bar{u}_1}{\partial t} = -\frac{3Q}{2}\bar{u}_1 + \frac{Q}{2}\bar{u}_2 + \frac{E}{R_o} \frac{\partial^2}{\partial y^2} \bar{u}_1, \quad y = 0, 1, \quad (B.7)$$

$$\frac{\partial \bar{u}_2}{\partial t} = \frac{Q}{2}\bar{u}_1 - \frac{3Q}{2}\bar{u}_2 + \frac{E}{R_o} \frac{\partial^2}{\partial y^2} \bar{u}_2, \quad y = 0, 1. \quad (B.8)$$

This is equivalent to the circulation condition derived by Davey (1978, 1980) for barotropic quasi-geostrophic flow and is a consequence of closing the secondary circulation (induced by the Ekman layers) in terms of the geostrophic variables. It should be noted that Equations B.7,8 are valid only in the equal-viscosity case (i.e.  $\chi = 1$ ). For  $\chi \neq 1$ , the frictional terms involving  $Q$  would have different coefficients, but the approach would be identical to that presented here.

The above result is obtained by appealing to the original zonal momentum equation and by making a heuristic conservation of mass argument regarding the return of mass flux into the interior. It is useful to compare this to constraints derivable directly from the vorticity equations. If one takes the vorticity equation for layer 1, which is given by Equation 1.3, and integrates over the area of the channel, then one obtains.

$$\begin{aligned} \frac{\partial}{\partial t} \int_0^1 \int_0^4 \nabla^2 P_1 \, dx \, dy + F \frac{d}{dt} \int_0^1 \int_0^4 (P_2 - P_1) \, dx \, dy + \\ \int_0^1 \int_0^4 J(P_1, \nabla^2 P_1) \, dx \, dy = \int_0^1 \int_0^4 \left[ -\frac{3Q}{2} \nabla^2 P_1 + \frac{Q}{2} \nabla^2 P_2 + \frac{E}{R_o} \nabla^4 P_1 \right] \, dx \, dy. \end{aligned} \quad (B.9)$$

Utilizing Equation B.3 and noting that the nonlinear term given by  $J( \cdot, \cdot )$  is zero when averaged over the area of the channel, Equation B.9 becomes

$$\frac{\partial}{\partial t} (\bar{P}_{1,y})_0^1 = -\frac{3Q}{2} (\bar{P}_{1,y})_0^1 + \frac{Q}{2} (\bar{P}_{2,y})_0^1 + \frac{E}{R_o} (\nabla^2 \bar{P}_{1,y})_0^1, \quad (B.10)$$

where the limits are taken in the  $y$  direction. Finally, noting that  $\bar{u}_i = -\partial \bar{P}_i / \partial y$ , Equation B.10 can be written as

$$\frac{\partial}{\partial t}(\bar{u}_1)_0^1 = -\frac{3Q}{2}(\bar{u}_1)_0^1 + \frac{Q}{2}(\bar{u}_2)_0^1 + \frac{E}{R_o}(\nabla^2 \bar{u}_1)_0^1, \quad (\text{B.11})$$

while the corresponding equation for layer 2 can be written as

$$\frac{\partial}{\partial t}(\bar{u}_2)_0^1 = -\frac{3Q}{2}(\bar{u}_2)_0^1 + \frac{Q}{2}(\bar{u}_1)_0^1 + \frac{E}{R_o}(\nabla^2 \bar{u}_2)_0^1. \quad (\text{B.12})$$

Equations B.11 and B.12 are just the differences of Equations B.7 and B.8 evaluated at the two walls,  $y=0$  and  $y=1$ . Because these conditions are derivable from the vorticity equations, they should already be satisfied, without appeal to another external relation, by solving the vorticity equations. However, it should be noted that Equations B.11,12 are less generic and therefore are not completely equivalent to Equations B.7,8, so that there it is still necessary to satisfy Equations B.7,8 separately.

In order to do this, in addition to satisfying Equation B.3, the functional expansion shown in Equation 2.7 is used. In particular, the  $\mathcal{U}_k(t)$  terms are coupled to a  $(y - 1/2)$  spatial term, which is antisymmetric about  $y = 1/2$ . This first additional term is introduced in order to satisfy the circulation condition. The second additional term is purely temporal and is represented by  $\mathcal{D}(t)$ ; it is used to satisfy conservation of mass.

If one takes Equations B.7,8, evaluates them at both  $y = 0$  and  $y = 1$ , and adds the two resulting equations for each layer separately, the following results:

$$\begin{aligned} \partial \mathcal{U}_1 / \partial t + \sum_{j'=1}^{\infty} j' \pi \partial \hat{\phi}_{1,j'} / \partial t &= -\frac{3Q}{2} \left( \sum_{j'=1}^{\infty} j' \pi \hat{\phi}_{1,j'} + \mathcal{U}_1 \right) + \\ \frac{Q}{2} \left( \sum_{j'=1}^{\infty} j' \pi \hat{\phi}_{2,j'} + \mathcal{U}_2 \right) - \frac{E}{R_o} \left( \sum_{j'=1}^{\infty} (j' \pi)^3 \hat{\phi}_{1,j'} \right), \quad j' \text{ even,} \end{aligned} \quad (\text{B.13})$$

$$\begin{aligned} \partial \mathcal{U}_2 / \partial t + \sum_{j'=1}^{\infty} j' \pi \partial \hat{\phi}_{2,j'} / \partial t &= -\frac{3Q}{2} \left( \sum_{j'=1}^{\infty} j' \pi \hat{\phi}_{2,j'} + \mathcal{U}_2 \right) + \\ \frac{Q}{2} \left( \sum_{j'=1}^{\infty} j' \pi \hat{\phi}_{1,j'} + \mathcal{U}_1 \right) - \frac{E}{R_o} \left( \sum_{j'=1}^{\infty} (j' \pi)^3 \hat{\phi}_{2,j'} \right), \quad j' \text{ even,} \end{aligned} \quad (B.14)$$

where the  $\hat{\phi}_{1,j'}$  coefficients correspond to layer 1 and the  $\hat{\phi}_{2,j'}$  coefficients correspond to layer 2. These equations give two additional constraints to the system described by Equation 1.3. Note that the above equations couple the zonal harmonics which comprise the symmetric state with the  $\mathcal{U}_k(t)$  terms, while the  $\mathcal{D}(t)$  term is absent. This directly implies that  $\mathcal{D}(t)$  is zero for the symmetric solutions, which is reasonable since the symmetric zonal flow trivially satisfies conservation of mass.

As noted before, if one instead subtracts the relations obtained by evaluating Equations B.7,8 at the walls, Equations B.11,12 are obtained. This indicates that these constraints should be redundant statements of the vorticity equations. It can be shown that, if mass conservation is satisfied, this is indeed the case, so that additional terms need not be added to satisfy the circulation condition for the asymmetric zonal terms.

Finally, by substituting the expansion for  $P_1$  and  $P_2$  (given by Equation 2.7) into Equation B.3, one obtains the mass conservation equation, which can be written as

$$\frac{\partial \mathcal{D}}{\partial t} + \sum_{j'=1}^{\infty} \frac{2}{j' \pi} \frac{\partial}{\partial t} (\hat{\phi}_{2,j'} - \hat{\phi}_{1,j'}) = 0. \quad (B.15)$$

This ensures that mass is conserved in each layer for all time. In summary, then, the circulation condition is not necessarily satisfied for the symmetric state, and it requires the introduction of an additional term to see that this happens. The extra term also allows a full set of eigenfunctions (in terms of cosines) for the velocity fields of the two layers. The portion of the circulation condition that couples to the

asymmetric zonal terms is already satisfied if the vorticity equations and the mass conservation equation are solved simultaneously.

As a final exercise, it is interesting to examine the effect on the circulation condition with no lateral friction, since this is the scenario assumed by the semi-slippery model. If we return to Equations B.7 and B.8 and let  $\frac{E}{R_o} = 0$ , then at either wall,

$$\frac{\partial \bar{u}_1}{\partial t} = -\frac{3Q}{2}\bar{u}_1 + \frac{Q}{2}\bar{u}_2, \quad (B.16)$$

$$\frac{\partial \bar{u}_2}{\partial t} = -\frac{3Q}{2}\bar{u}_2 + \frac{Q}{2}\bar{u}_1, \quad (B.17)$$

for the upper and lower layers, respectively. Assuming solutions of the form  $e^{\lambda t}$ , an eigenvalue problem results, with the corresponding solution being  $\lambda = -Q, -2Q$ . Thus, in the absence of lateral friction, the zonally-averaged zonal velocity at both walls decays to zero within the order of a spin-up time (i.e.  $t_{spinup} \sim 1/Q$ ). This is a generalization of the results presented by Pedlosky (1987), who derived similar results for two-layer flows without interfacial friction. Thus, if lateral friction is excluded, then the semi-slippery model's functional expansion becomes valid, although it is not at all clear that the semi-slippery model is asymptotically valid for  $\frac{E}{R_o} \rightarrow 0$  (but not exactly zero), since the neglect of viscous effects is a singular perturbation of the vorticity equations.

## APPENDIX C

### RESULTS FOR SLIPPERY MODEL-SYMMETRIC STATE

The symmetric solution displays steady behavior for  $8 \leq F < 12$ , periodic amplitude vacillation for  $12 \leq F < 24$ , periodic structural vacillation for  $24 \leq F < 34$ , and finally quasi-periodic behavior for  $34 \leq F < 40$ . Figure C.1 shows the transfer of energy for  $F = 8$ . The energy conversion process is primarily baroclinic, with the energy primarily flowing from  $\bar{K}$  to  $\bar{P}$  to  $P'$  to  $K'$ . The barotropic conversion term,  $\{K', \bar{K}\}$  is small and is about 4.3% of the baroclinic conversion terms (i.e.  $\{\bar{K}, \bar{P}\}$ ,  $\{\bar{P}, P'\}$ , and  $\{P', K'\}$ ). However, the sign of  $\{K', \bar{K}\}$  is negative, which indicates that the waves are extracting kinetic energy directly from the mean flow. This situation occurs for all parameter settings examined in this thesis. Although the diagram shown in Figure C.1 is of great value in displaying the mean transfer of energy through the system, the important quantities in understanding the behavior in various regimes are the relative sizes of the rms deviations of the energy transfer terms. Thus, the box diagram is not of much practical value, and for the sake of brevity, any important results contained in these diagrams will simply be stated in the text rather than graphically illustrated.

For  $F = 12$ , the system has entered a PAV state, similar to that seen in the CH model. The barotropic energy transfer term is approximately 12% of the baroclinic transfer terms, indicating that the barotropic mechanism is becoming more important as the flow becomes more supercritical. Figure C.2 shows the energy fluctuations as a function of time. As discussed in Chapter 1, periodic amplitude vacillation essentially involves periodic exchanges of energy between the wavy and zonal portions of the flow. The zonal available potential energy and zonal kinetic

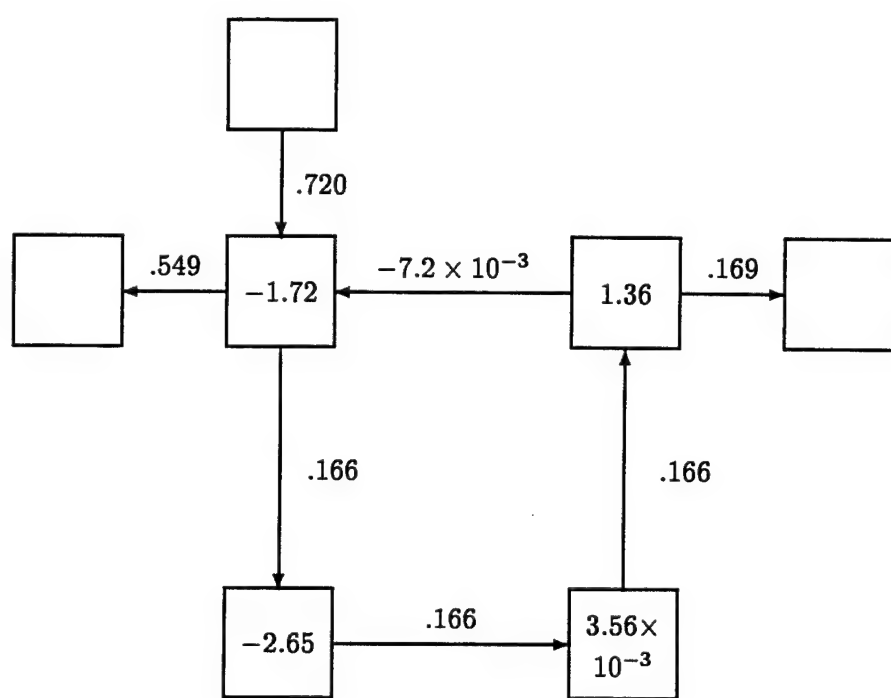


Figure C.1: Energy Flow Diagram for symmetric state,  $F = 8$ .

energy appear to be in phase with one another and 180 degrees out of phase with the wavy kinetic energy, so that the zonal energies reach a maximum as the wavy kinetic energy reaches a minimum (and vice versa). However, the wavy available potential energy reaches a maximum when the zonal energies are decreasing most rapidly and the wavy kinetic energy is increasing most rapidly. This is due to the fact that the phase lag of the upper layer wave with respect to the lower layer wave is greatest when the waves are growing most rapidly (and the zonal energies are, correspondingly, decreasing most rapidly).

The fluctuations of the energy appear to be dominated by two terms,  $\{\bar{P} \cdot P'\}$  and  $\{P' \cdot K'\}$ , which have rms deviations that are five to ten times larger than the rms deviations of the other two energy transfer terms. This suggests that the energy cycle can primarily be described as a transfer from zonal potential energy to wavy potential energy to wavy kinetic energy, the classic signature of baroclinic instability. Additionally, as noted in Section 1.5.2, amplitude vacillation is characterized by a spatial structure that is essentially constant with time. Figure C.3 displays the upper-layer, zonally-integrated, wavy kinetic energy as a function of  $y$  for eight time steps (which comprise one vacillation period). The quantity shown is the energy *minus* its mean value, which allows the fluctuations to be seen more readily. It is evident that the meridional distribution of energy is essentially constant and is characterized by the  $\sin(2\pi y)$  cross-stream mode. Additionally, for the purpose of later comparison with the PSV regime, the dominant temporal frequency of the system, as measured from the upper layer  $\sin(2\pi y)$  zonal correction term, is 0.125 nondimensional frequency units.

Figures D.1,2 show the baroclinic and barotropic wavy streamfunction fields, respectively, over one period. In these figures,  $F = 20$ , a value which is chosen to accommodate comparison with later results. However, the behavior shown is indicative of the PAV regime in general. For all of the spatio-temporal sequences

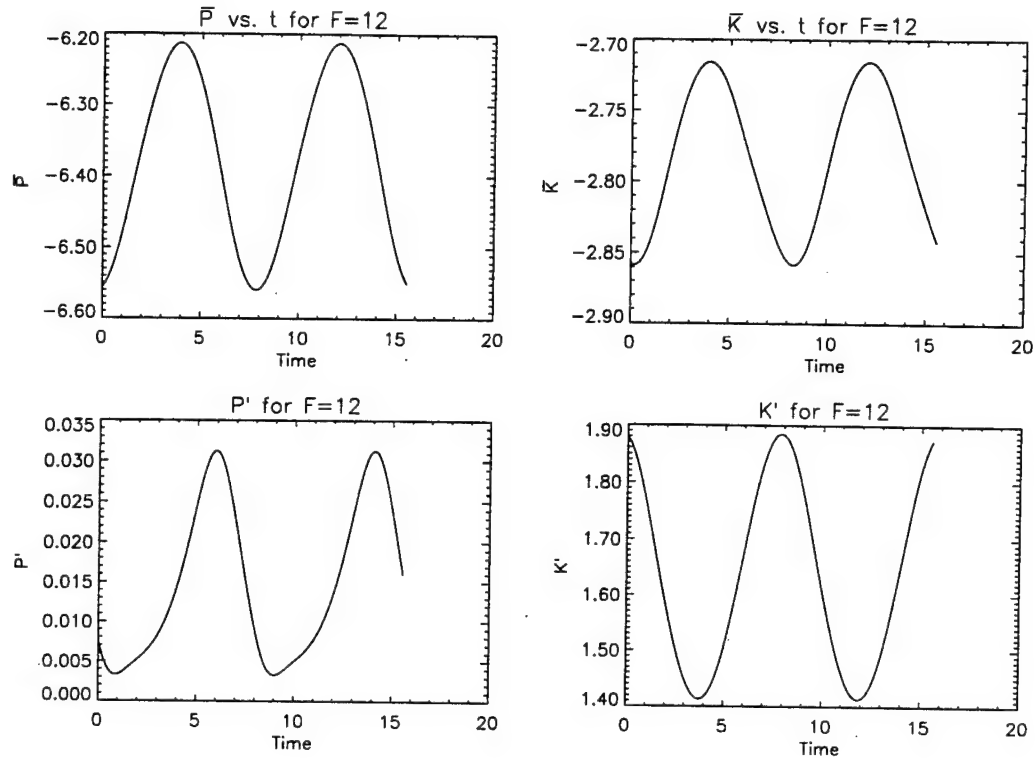


Figure C.2: Energy fluctuations vs. time for symmetric state,  $F = 12$

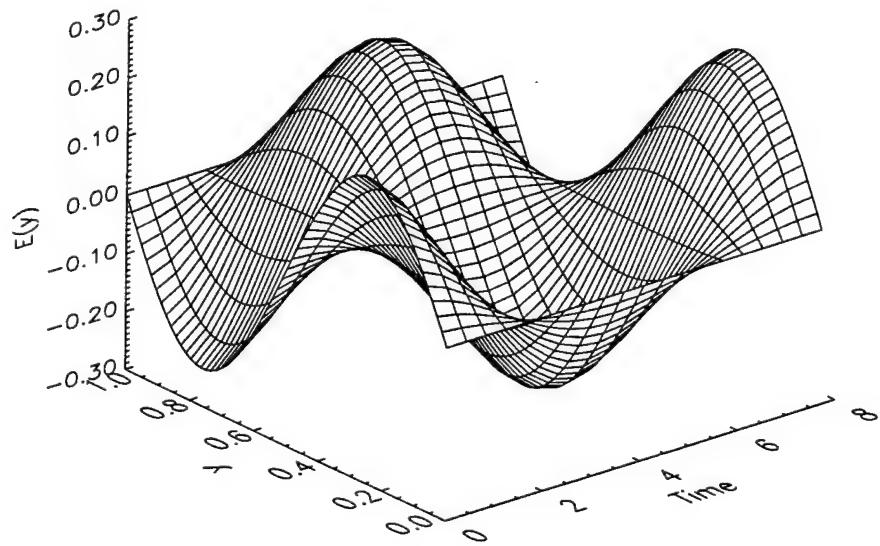


Figure C.3:  $E(y)$  vs.  $y$  for several times,  $T$ , over one cycle,  $F = 12$

shown in Appendix D, the time-averaged spatial mean has been removed. It is evident from Figures D.1,2 that there occur intricate and complex spatial patterns. Both barotropic and baroclinic fields are alternately dominated by several different waves. The multiplicity of waves involved is shown in Figure C.4, which displays the spatial power spectra (for the first 20 wavenumbers in each direction) for the barotropic and baroclinic wavy fields at a selected time. The barotropic field is dominated by just a few waves, but the baroclinic field spectrum shows significant power at many wavenumbers. This effectively negates the accuracy of low-order models based on single-wave hypotheses, even for relatively simple temporal behavior.

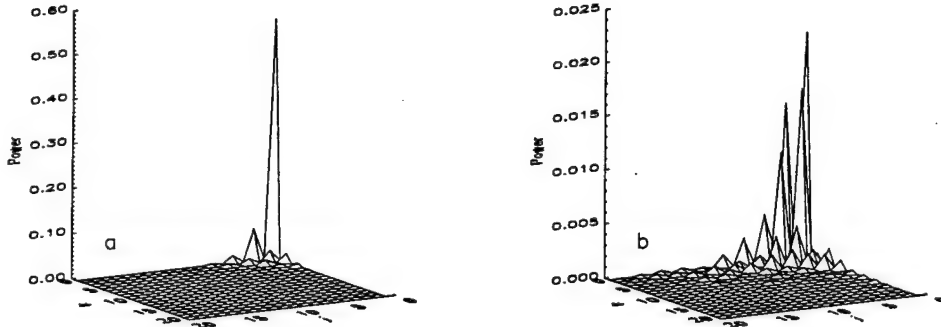


Figure C.4. (a) Spatial power spectrum of barotropic wavy field. (b) Spatial power spectrum of baroclinic wavy field.  $F = 20$ , symmetric case. Only the first 20 wavenumbers in each direction are shown.

The transition to periodic structural vacillation occurs, for the symmetric state, at about  $F = 24$ . The energetics are examined at  $F = 26$ , just after the system has entered the PSV state. In terms of mean quantities, little is changed from the results at  $F = 22$ , in the PAV regime. The only significant difference is in the average value of  $P'$ , which is only about 40% of its mean for  $F = 22$ . The barotropic transfer term, on average, is still about 25% of the mean value of the baroclinic quantities, which is equal to that found at  $F = 22$ . Figure C.5 displays the zonally-integrated, meridional wavy kinetic energy for several times over the course of one vacillation cycle. As before, the mean value has been subtracted out in order to better show the

fluctuations. In contrast to the PAV regime, the meridional distribution of energy undergoes dramatic changes during one oscillation period. This is consistent with the findings of Pfeffer et al. (1980), who found that structural vacillation can be characterized by a periodic radial re-distribution of energy with little variation in the total wave energy.

The oscillations in energy are found to be the same as in the PAV regime. However, the disparity between the behavior of the two vacillation types becomes clear when one examines Figure C.6, which shows the energy transfer terms. The rms deviation of all four quantities are reduced from their magnitudes at  $F = 22$ , but the barotropic transfer term,  $\{\bar{K} \cdot K'\}$ , now has an rms deviation that is about three times larger than the largest deviation of the remaining transfer terms. This implies that the onset of PSV can be directly traced to the growth of a barotropic instability, which has superseded the largely baroclinic fluctuations that occur in the PAV regime. The hypothesis is corroborated when one considers the barotropic zonal kinetic energy. For the steady and PAV regimes, this quantity is zero. However, the barotropic zonal kinetic energy is now a small, but certainly finite, quantity. This suggests that for  $F < 24$ , the system is both barotropically and baroclinically unstable, but the baroclinic instability "wins" in the sense that it determines, and indeed dictates, the behavior of the two-layer model. However, for  $F > 24$ , the barotropic instability of the wavy and zonal flow becomes the dominant instability in the system, and it becomes the governing mechanism for energy fluctuations. The barotropic zonal kinetic energy must necessarily become nonzero when this occurs.

The frequency of oscillations is much higher in the PSV regime than for PAV. The peak frequency of the oscillation is about .381 nondimensional time units, which is about 3.4 times the frequency found in the PAV regime at  $F = 22$  (which has a nondimensional dominant frequency of about .113 nondimensional frequency units, slightly lower than that found at  $F = 12$ ).

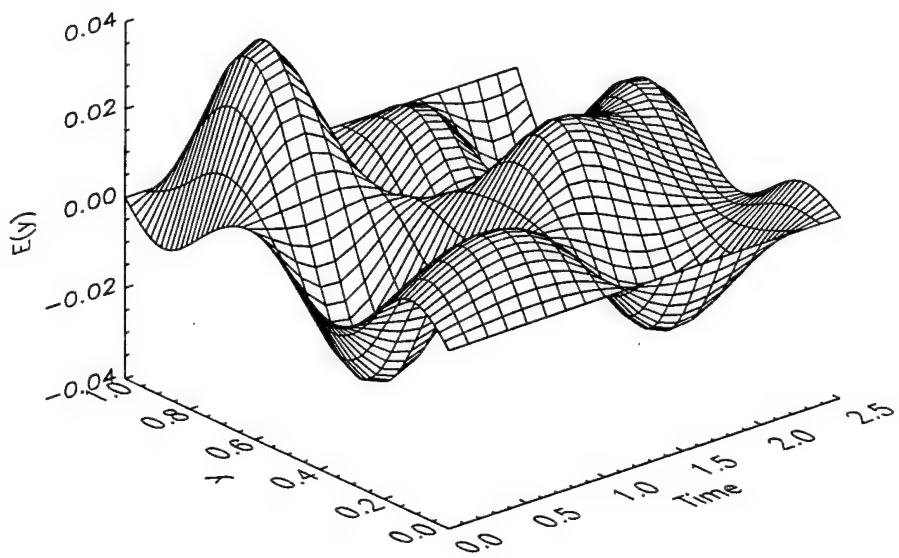


Figure C.5:  $E(y)$  vs.  $y$  for several times,  $T$ , over one cycle,  $F = 26$

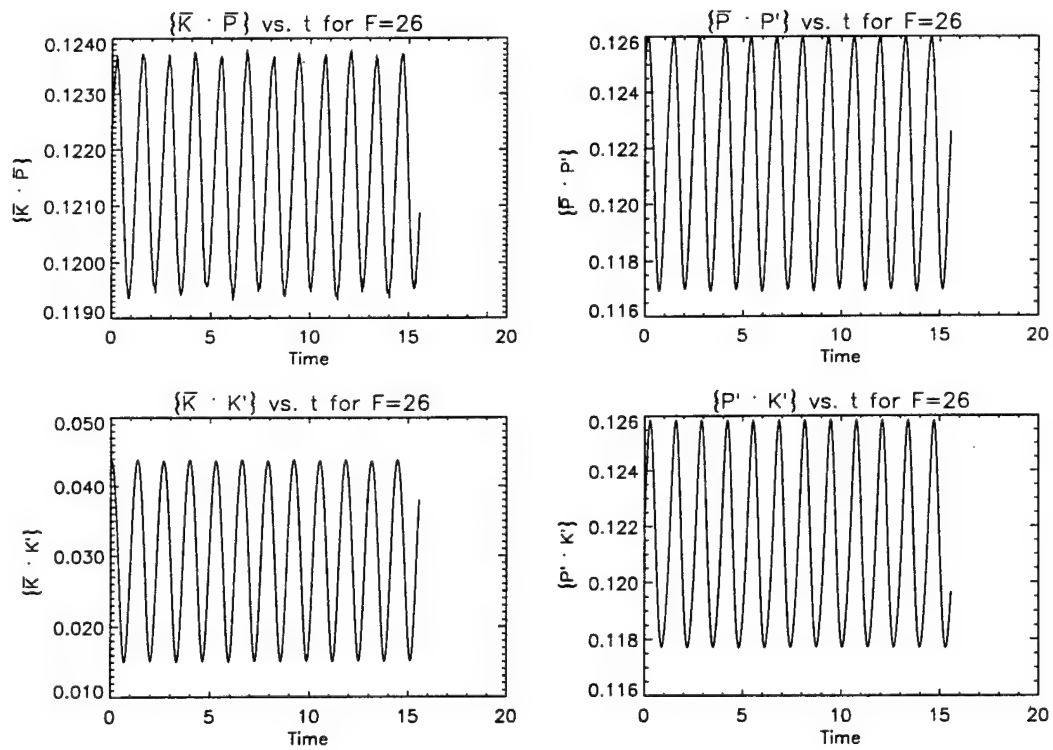


Figure C.6: Energy transfers vs. time for symmetric state,  $F = 26$

As is the case for the asymmetric solution, the PAV→PSV transition is abrupt, with no mixed vacillation occurring between the two. In a low-order model, Weng et al. (1986) observed a slow transition between the two states, with a mixed vacillation occurring between PAV and PSV. However, no mention of whether this vacillation is periodic or quasi-periodic is made.

The baroclinic and barotropic streamfunction fields in the PSV regime are shown in Figures D.3,4, respectively. The behavior is clearly much different than that in the PAV regime. First of all, the characteristic spatial scale of the system has become smaller, with a corresponding increase in the spatial intricacy. In addition, it is evident, upon some scrutiny, that the temporal behavior of both wavy fields is actually comprised on two counter-rotating “eddies”. In the top half of the flow domain, the blue and yellow “blobs” rotate counter-clockwise but remain in the top half of the flow field, while those in the bottom half rotate clockwise, again staying within their domain. This is consistent with the observation that the PSV behavior reflects a periodic meridional transport of energy with little change in the overall energy. The wavy fields in this instance tend to transport energy from “equator to pole” and back again. The approximate location of the center of a chosen eddy in the baroclinic wavy field is shown in Figure C.7. The center moves clockwise in an approximate circle over the course of two periods (the eddy moves only halfway around in one period since the field possesses particular symmetries).

At  $F = 36$ , the symmetric state is quasi-periodic. At this parameter value, the mean barotropic energy transfer is now about 30% of the baroclinic quantities, a slight increase from  $F = 26$ . Figure C.8a displays the upper layer  $\sin(2\pi y)$  coefficient, which consists of the same oscillation as seen for  $F = 32$ , but which is now modulated by a lower frequency oscillation. Two observations indicate that the flow is indeed quasi-periodic, as opposed to chaotic. First, Figure C.8b displays the power spectrum of the data from Figure C.8a. There are several peaks, each of which correspond

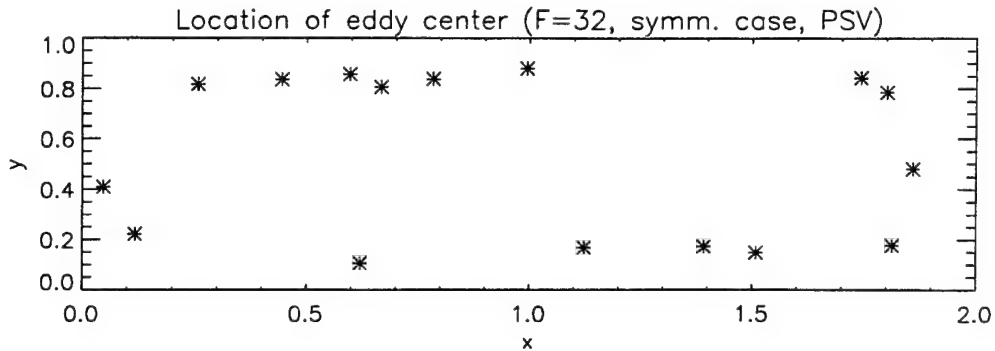


Figure C.7. Approximate location of eddy center (in baroclinic wavy field) over two periods,  $F=32$ , symmetric case, PSV regime. The eddy moves clockwise as time proceeds and reaches its starting point after two periods.

to the different combinations of frequencies that naturally arise in a quasi-periodic system (Berge et al., 1984), but there is no broad-band noise associated with a chaotic time series. In addition, Figure C.9 shows a maximum return map of the same time series (for the uninitiated reader, Appendix E presents a brief introduction to return maps and other measures of chaos discussed in this thesis). The Poincaré section clearly shows a one-dimensional loop, indicating that the full temporal behavior occurs on a 2-torus.

The energetics, on average, are only slightly different from those at  $F = 32$ . However, an examination of the energy fluctuations and transfers as a function of time reveals profound differences between the PSV and quasi-periodic states. In Figure C.10, the various energies, instead of being plotted as functions of time, are plotted versus each other. Clearly, there no longer exists a simple phase lag between various energy quantities. Instead, the energies assume a complicated functional relationship with one another.

Also, the rms deviation of the barotropic transfer term,  $\{\bar{K} \cdot K'\}$ , is still the dominant fluctuation, but both the  $\{\bar{P} \cdot P'\}$  and  $\{P' \cdot K'\}$  terms now have rms deviations that are about 70-75% of the barotropic transfer term. This is very different from the situation at  $F = 32$ , where the baroclinic terms had rms deviations only

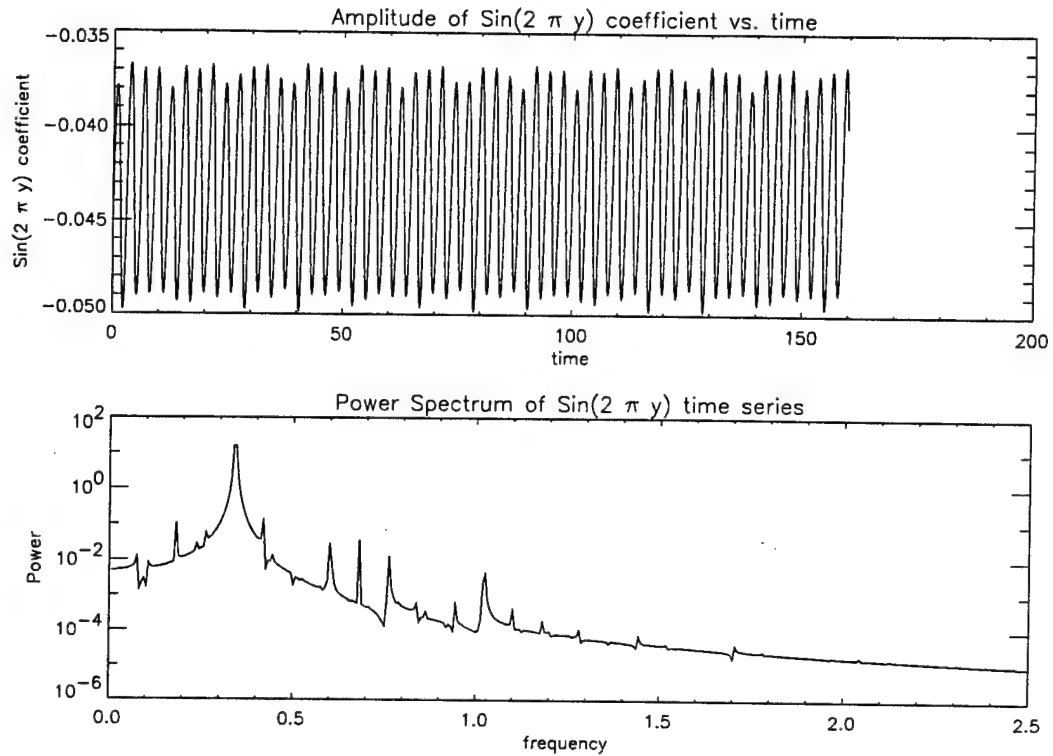


Figure C.8:  $\sin(2\pi y)$  coefficient and power spectrum for layer 1,  $F = 36$

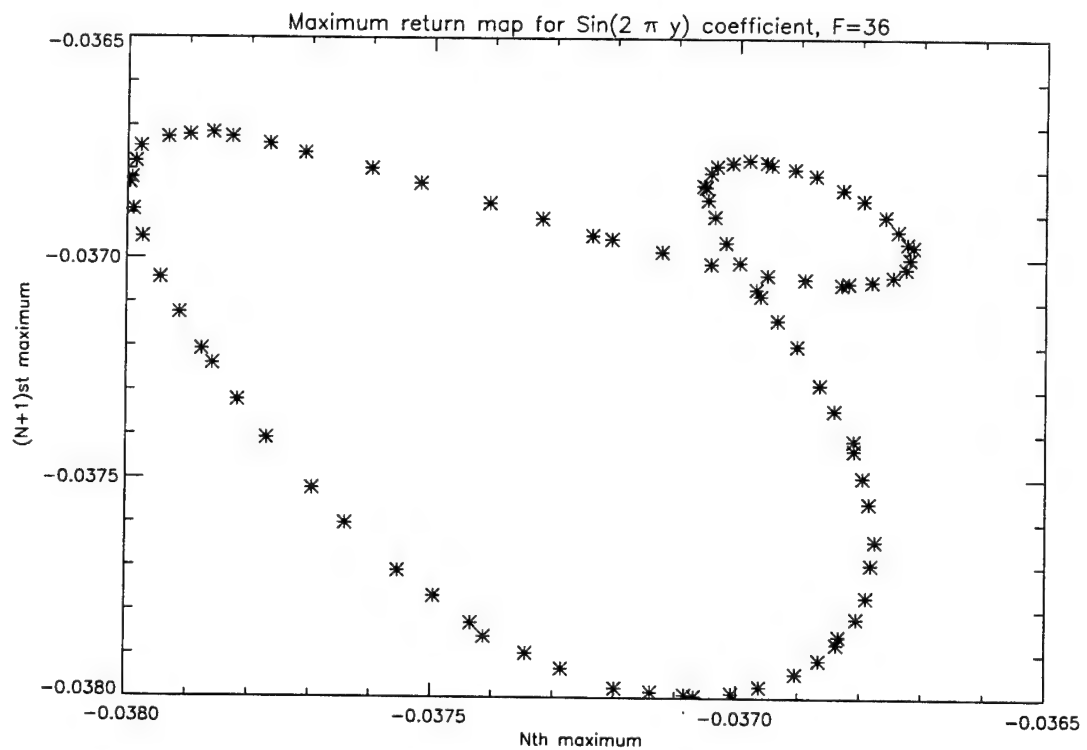


Figure C.9: Poincaré section of  $\sin(2\pi y)$  coefficient for layer 1,  $F = 36$

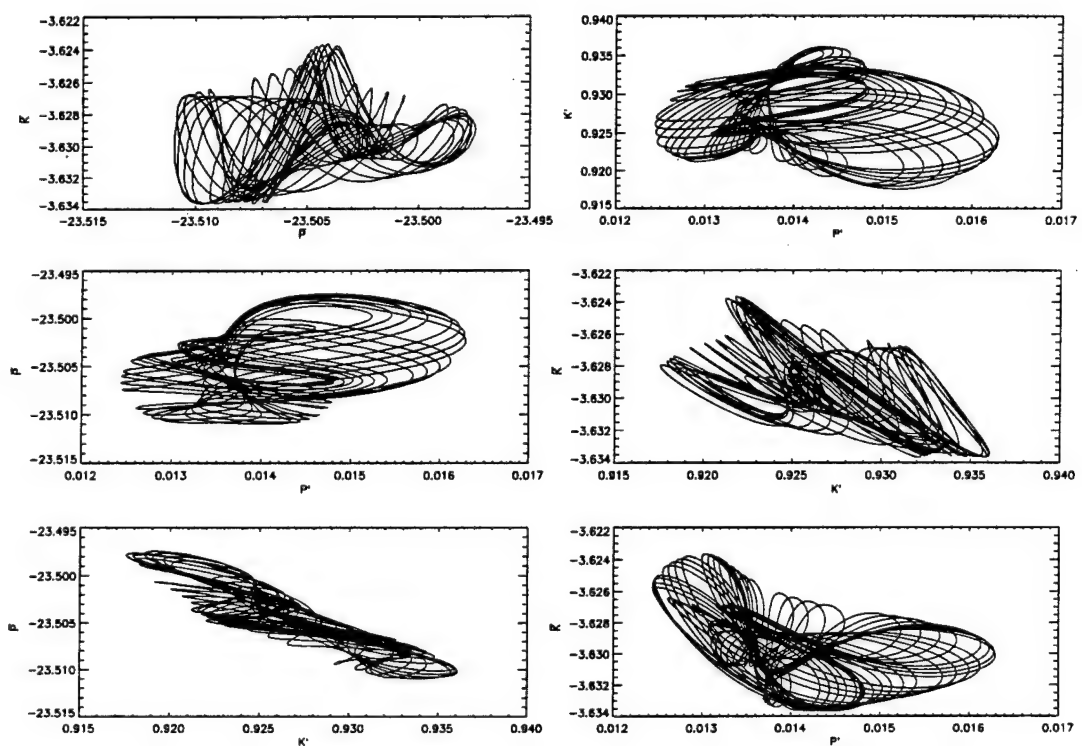


Figure C.10: Phase-space plots of energy fluctuations,  $F = 36$

about 1/3 the magnitude of the barotropic fluctuation. Consequently, it appears that the quasi-periodic behavior arises as a result of a mixing between the barotropic and baroclinic instabilities, each of which at lower Froude numbers is able to essentially dominate the system's behavior. The power spectrum shown in Figure C.8b supports this hypothesis. The peak in the spectrum occurs at a non-dimensional frequency of about 0.34, which shall be denoted as  $f_1$ . However, there is a small peak at about 0.077 frequency units, which shall be denoted as  $f_2$ . In addition, the other peaks can be explained in terms of linear combinations of  $f_1$  and  $f_2$ . This suggests that these two frequencies are the fundamental frequencies in this quasi-periodic system, and a glance at Figure C.8a confirms that the fast oscillation is indeed modulated by a slower oscillation that repeats every 4-5 fast oscillation cycles ( $f_1/f_2 \approx 4.4$ ). Clearly,  $f_1$  corresponds to the barotropic instability, since it is nearly the same as the oscillation frequency for  $F = 32$ . It seems reasonable to assume, then, that  $f_2$  corresponds to the amplitude vacillation, since the oscillation frequency at  $F = 22$  is approximately 0.13 frequency units and the trend in the PAV regime is for the oscillation frequency to decrease with increasing  $F$ . In an attempt to more quantitatively determine the change in vacillation frequency with  $F$ , the dominant frequencies for six values of  $F$  in the PAV regime were calculated ( $F = 12$  to 22 in increments of 2). Then a least-squares fit was attempted in order to determine the frequency for PAV (at  $F = 36$ ) by extrapolation. Since one would not expect that the dominant frequency (denoted as  $f_d$ ) would ever become negative, a plausible functional form would, at worst, allow  $f_d$  to asymptotically approach zero for large  $F$ , ruling out polynomial fits between  $f_d$  and  $F$ . Instead, to satisfy the asymptotic condition, the following fit was performed:

$$\log(f_d) = c_1[\log(F)]^2 + c_2\log(F) + c_3, \quad (C.1)$$

which is equivalent to

$$f_d = D e^{\log(F)[c_1 \log(F) + c_2]} \quad (C.2)$$

where  $D = e^{c_3}$ . In addition, a fit to a cubic in  $\log(F)$  was attempted, with the results being almost identical. The result, shown in Figure C.11, is that the extrapolated value of  $f_d$  at  $F = 36$  is approximately 0.085, which is reasonably close to the observed value of 0.077, although extrapolation is, admittedly, not a very robust method of approximation. Nonetheless, the result is consistent in supporting the notion that the low-frequency component of the quasi-periodicity results from a renewed baroclinic instability exhibiting itself via a relatively low-frequency amplitude vacillation.

Finally, one can again examine the temporal evolution of the wavy fields in order to better understand the nature of the quasi-periodic behavior. The baroclinic and barotropic fields are shown, respectively, in Figures D.5,6 for 16 uncorrelated times. The behavior looks much like the PSV regime shown in Figures D.3,4. However, there is some added complexity to the fields which is presumably due to the PAV influence. Nonetheless, the behavior is not fundamentally different from that observed at  $F = 32$ , so that the presence of the lower frequency serves simply to modulate the PSV-type fields in time.

In summary, the evolution of the symmetric state can be characterized as follows. The initial transition from the basic zonal flow to a steady-wave state is via baroclinic instability. This is to be expected, since the lack of a horizontal shear necessarily deprives the flow of an initial barotropic energy-transfer mechanism. However, once the steady-state flow is established, the wave interaction produces a small but finite transport of kinetic energy directly from the zonal flow to the waves. At larger  $F$ , the steady-state becomes unstable to periodic amplitude vacillation, which

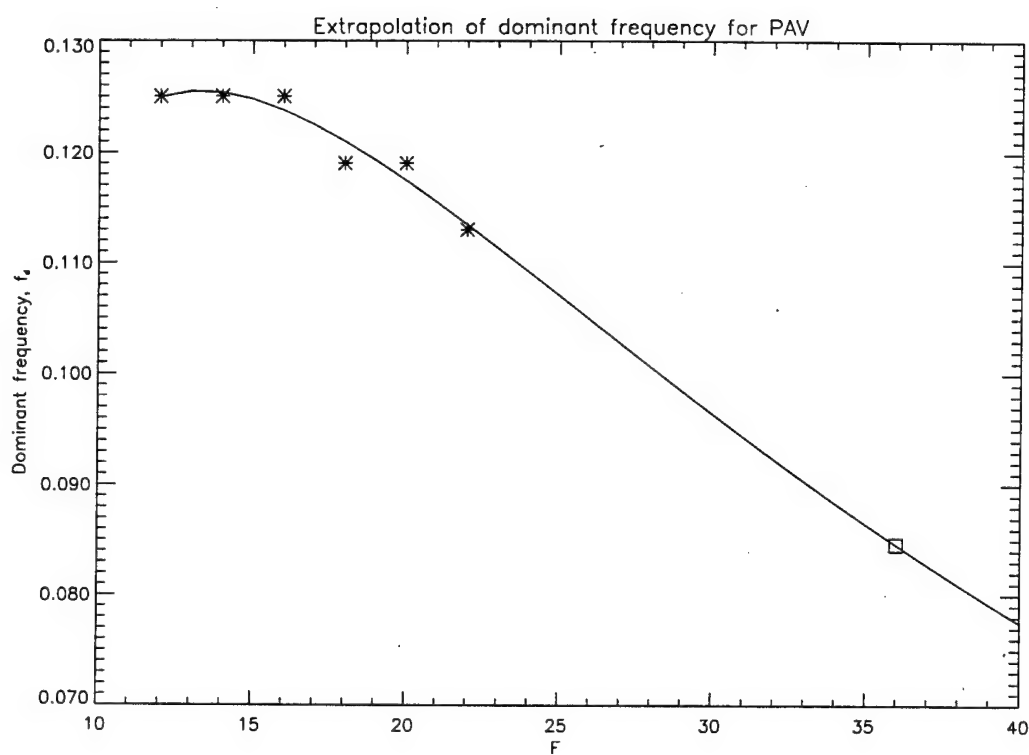


Figure C.11: Estimation of dominant PAV frequency at  $F = 36$

persists for  $12 \leq F < 24$ . The barotropic energy transfer has continued to grow and contributes substantially to the mean energetics of the system. Nonetheless, the PAV regime is characterized essentially as a baroclinic phenomenon, since the fluctuations of the baroclinic transfers are several times larger than the barotropic term. For values of  $F$  between 24 and 34, the barotropic instability becomes dominant, and the system enters a state of periodic structural vacillation. In this regime, the amplitudes of the wave fields do not fluctuate much, but rather the shapes of the waves undergo substantial changes throughout a cycle. In the PSV regime, the fluctuation of the barotropic energy transfer term is about three times larger than the baroclinic terms. Additionally, the vacillation frequency is about three to four times that found for PAV. Finally, for  $34 < F \leq 40$ , the flow becomes quasi-periodic. The quasi-periodicity arises from a mixing between the structural vacillation caused by a barotropic instability and a renewed amplitude vacillation that is ostensibly the result of a baroclinic instability.

## APPENDIX D

### SPATIAL SNAPSHOTS OF FULL SOLUTIONS OF SLIPPERY MODEL

Appendix D contains snapshots of the barotropic and baroclinic wavy fields for various solutions of the fully slippery model.

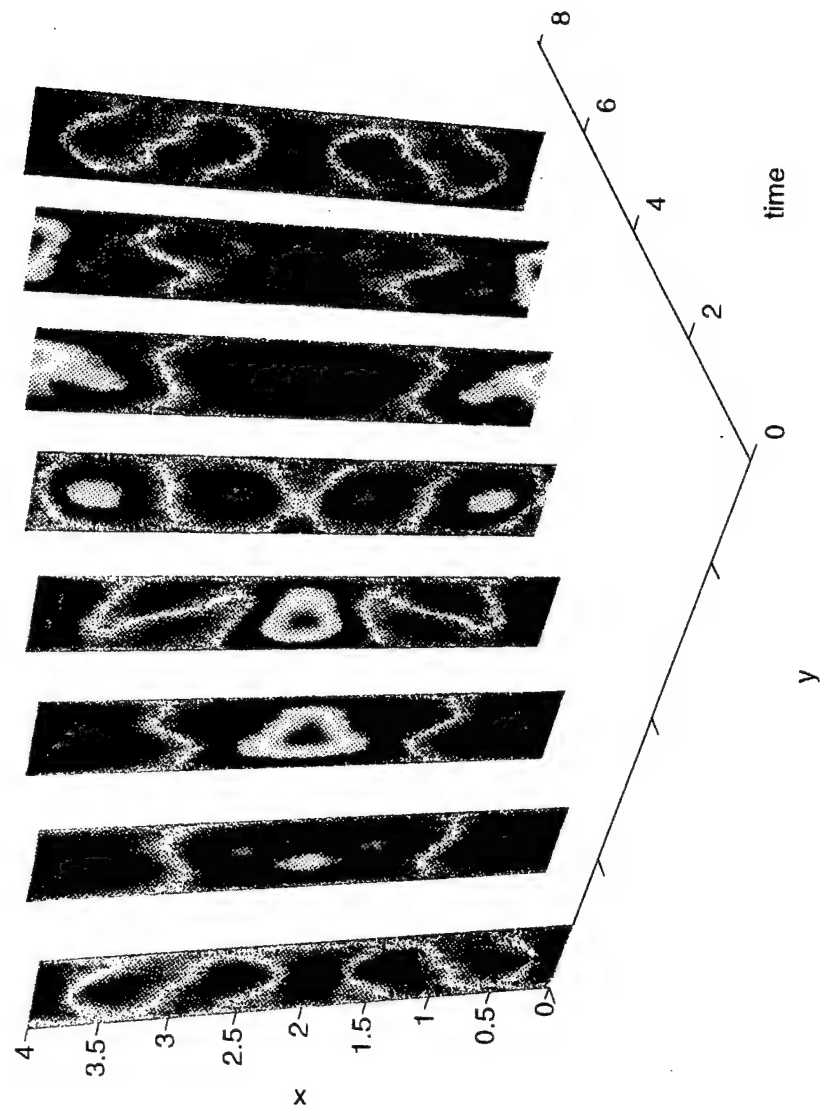


Figure D.1. Temporal snapshots of baroclinic wavy field over one period.  $F = 20$ ,  
symmetric solution, PAV regime.

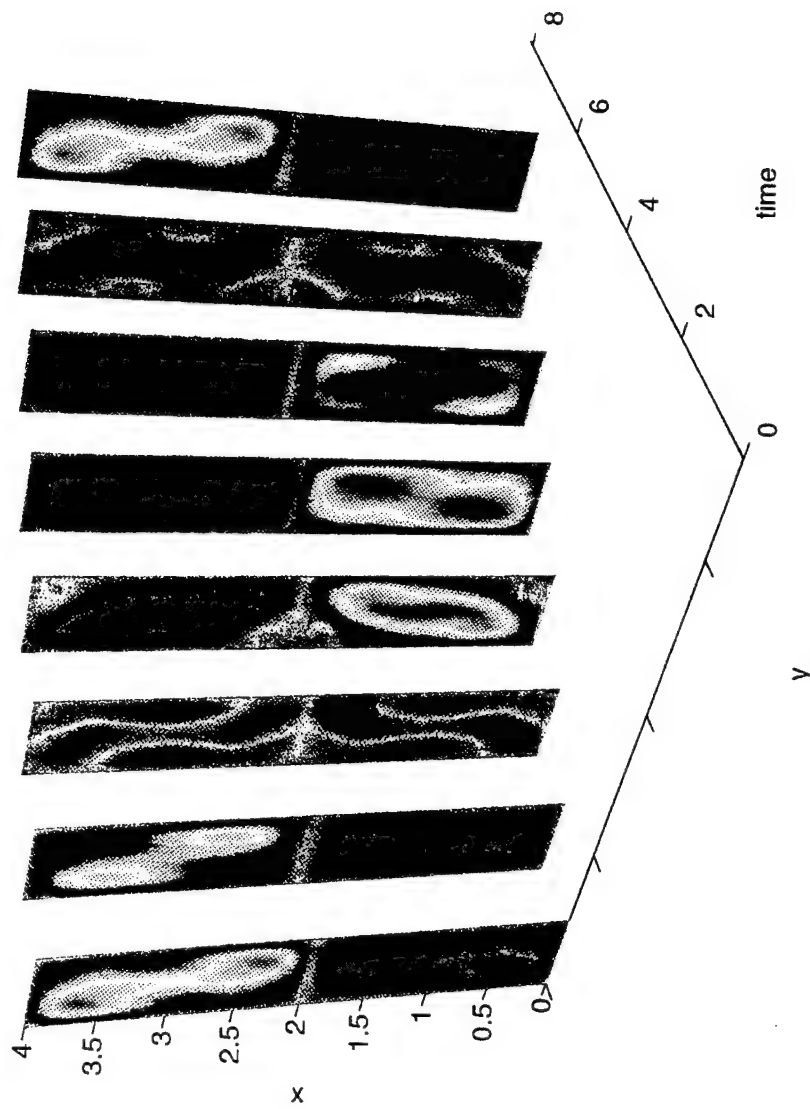


Figure D.2. Temporal snapshots of barotropic wavy field over one period.  $F = 20$ ,  
symmetric solution, PAV regime.

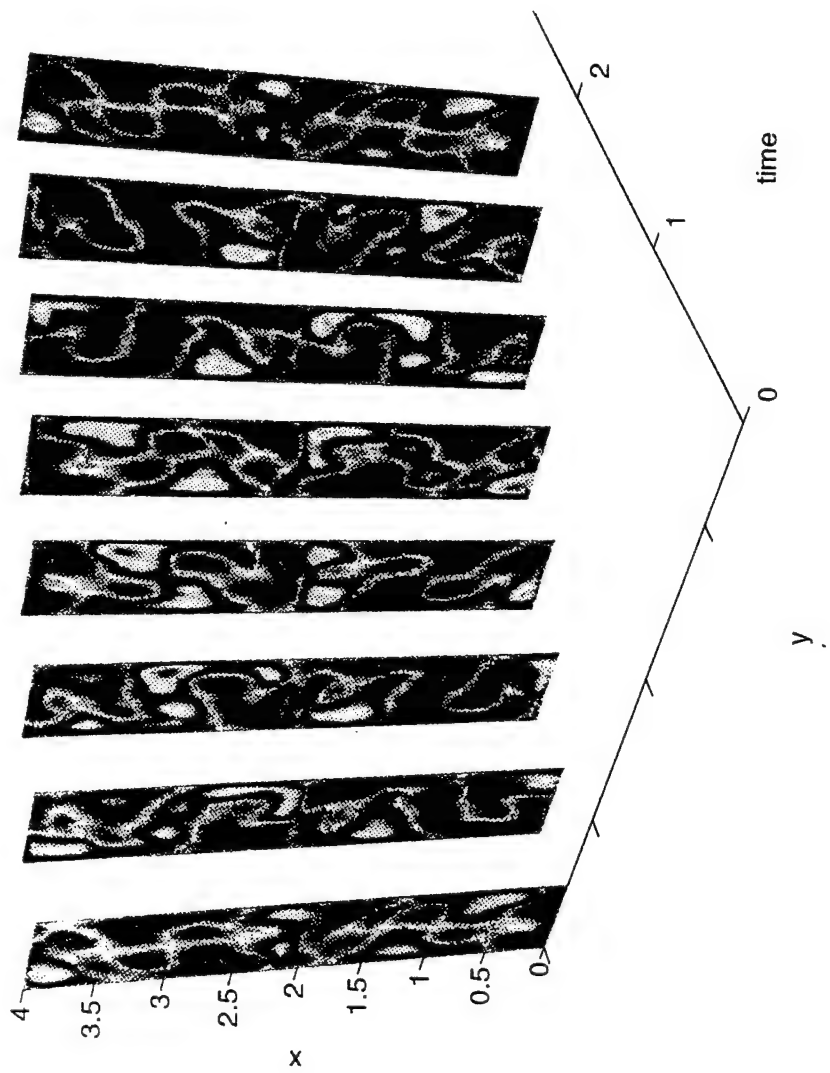


Figure D.3. Temporal snapshots of baroclinic wavy field over one period.  $F = 32$ , symmetric solution, PSV regime.

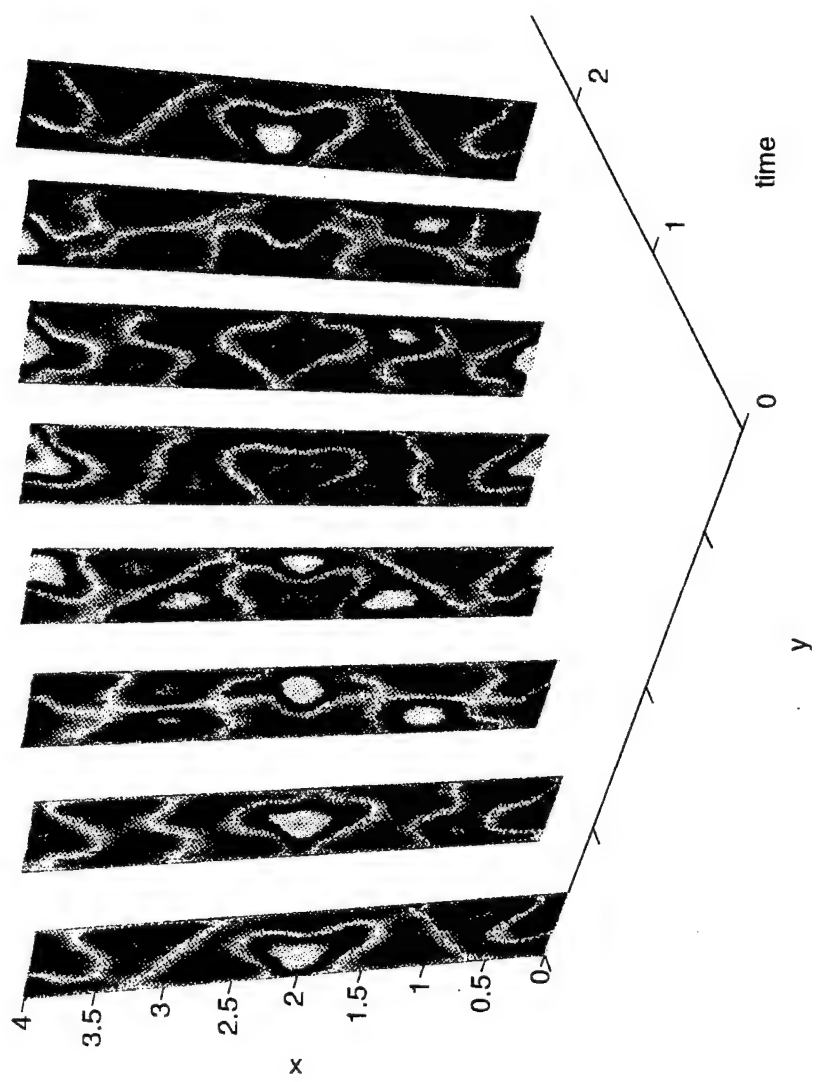


Figure D.4. Temporal snapshots of barotropic wavy field over one period.  $F = 32$ , symmetric solution, PSV regime.

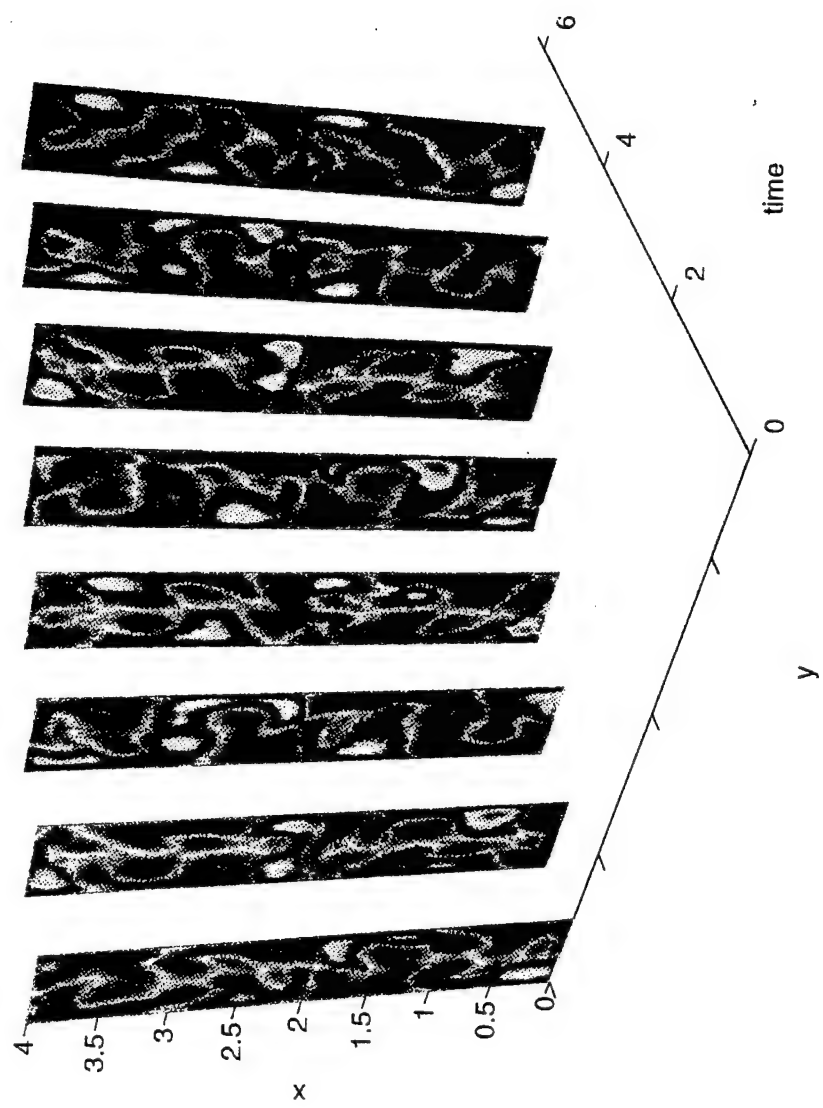


Figure D.5. Temporal snapshots of baroclinic wavy field at temporally uncorrelated times.  $F = 36$ , symmetric solution, quasi-periodic regime.

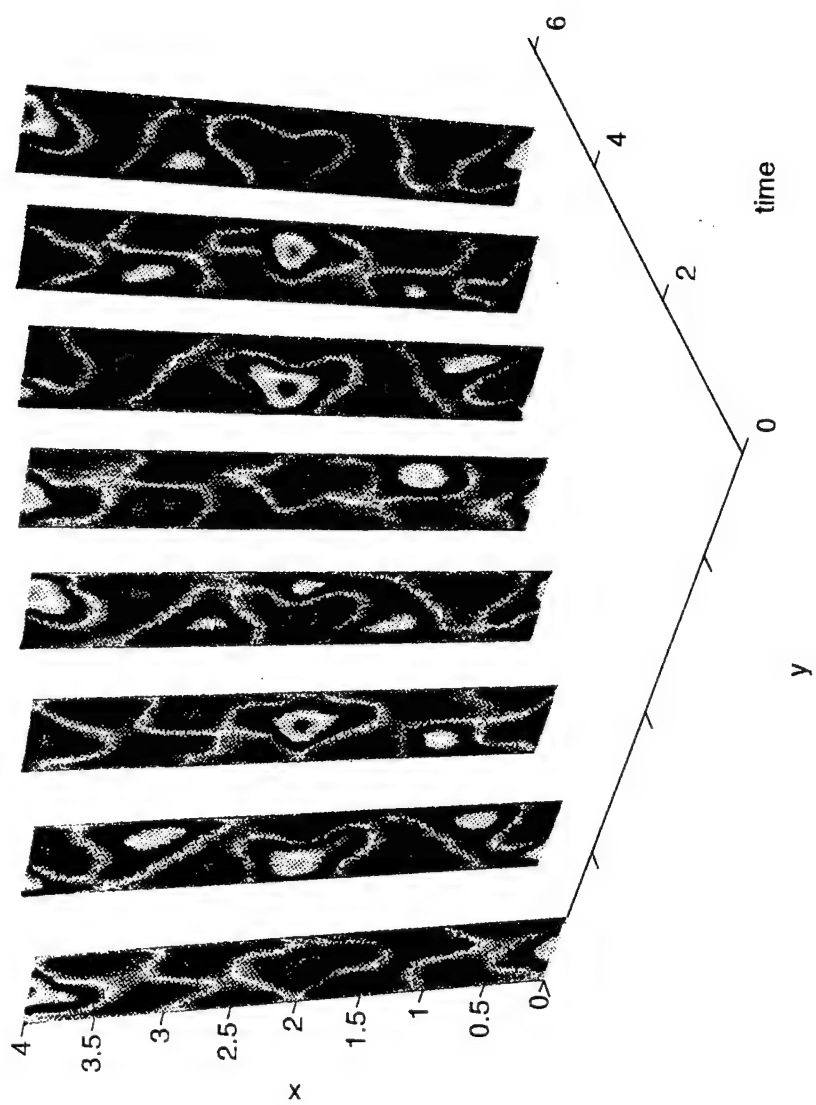


Figure D.6. Temporal snapshots of barotropic wavy field at temporally uncorrelated times.  $F = 36$ , symmetric solution, quasi-periodic regime.

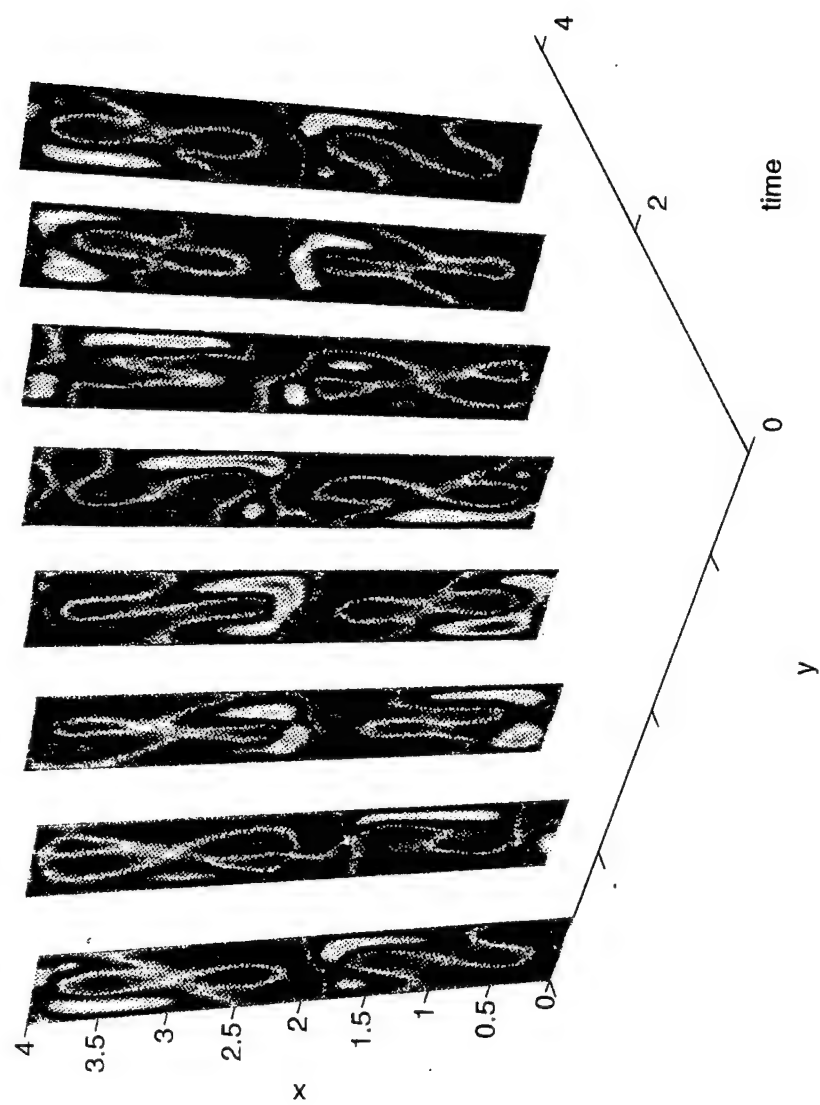


Figure D.7. Temporal snapshots of baroclinic wavy field over one period.  $F = 20$ , asymmetric solution, PSV regime.

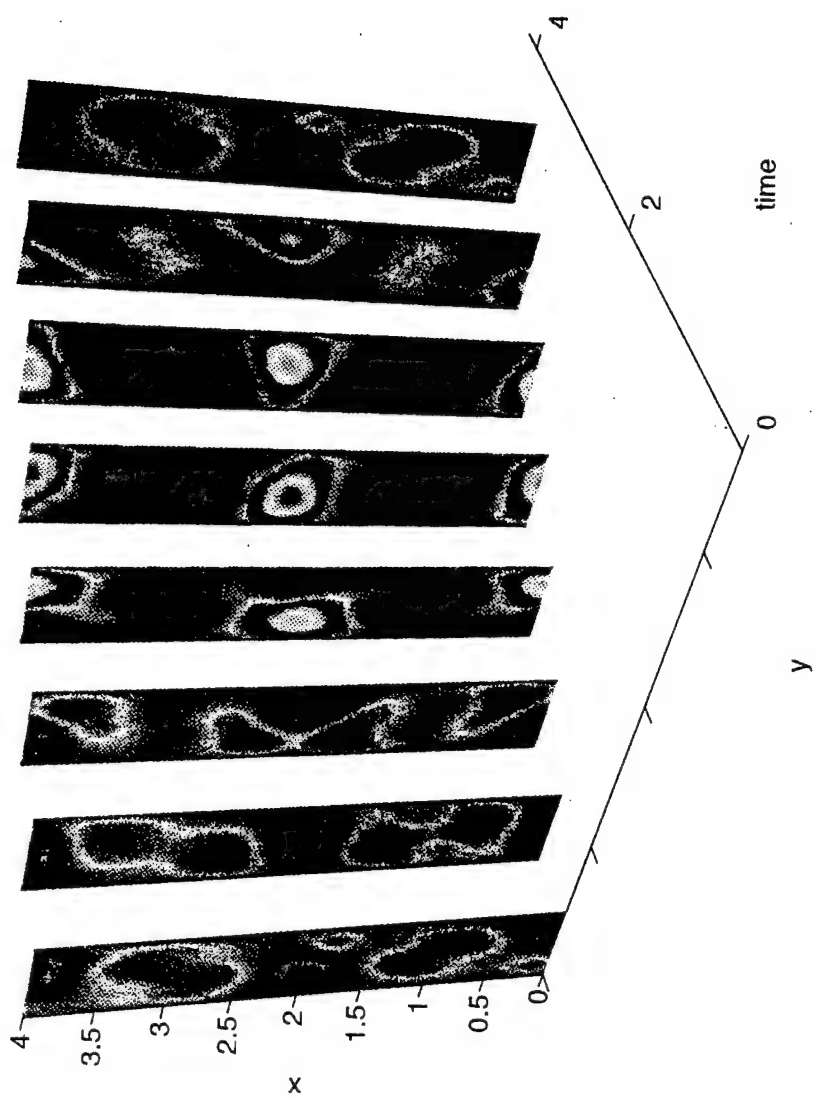


Figure D.8. Temporal snapshots of barotropic wavy field over one period.  $F = 20$ , asymmetric solution, PSV regime.

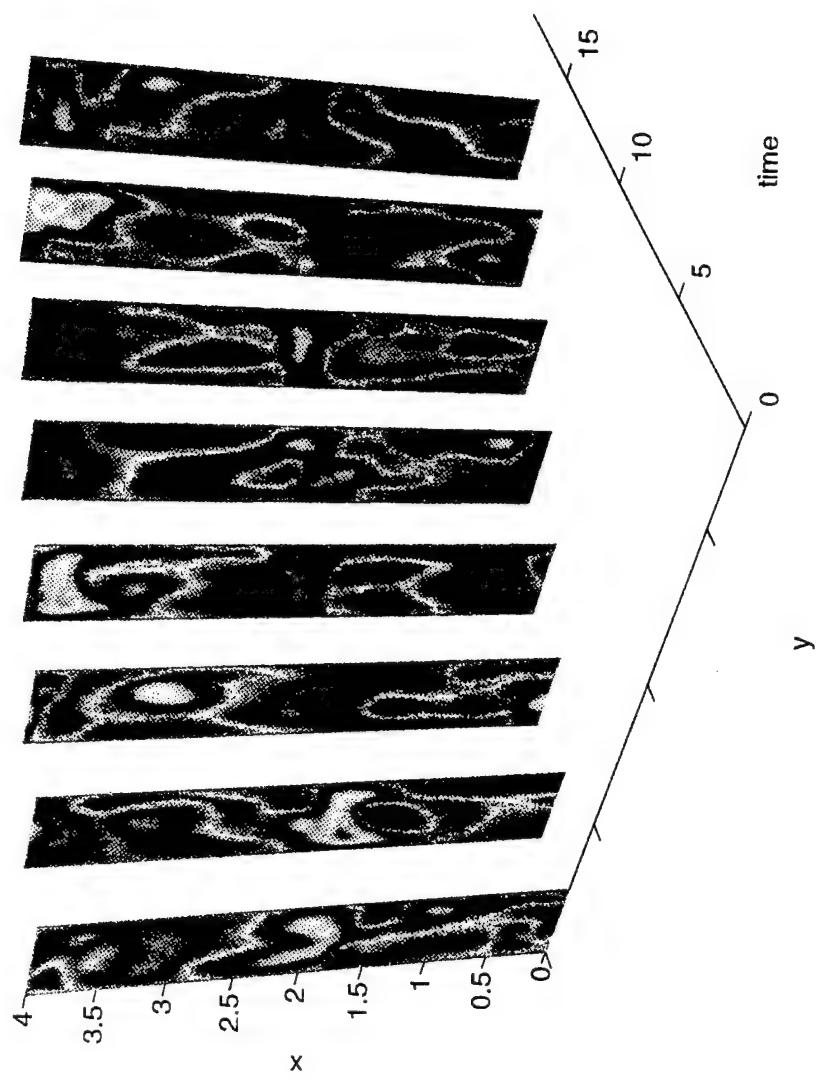


Figure D.9: Temporal snapshots of baroclinic wavy field at uncorrelated times.  
 $F = 28$ , asymmetric solution, quasi-periodic regime.

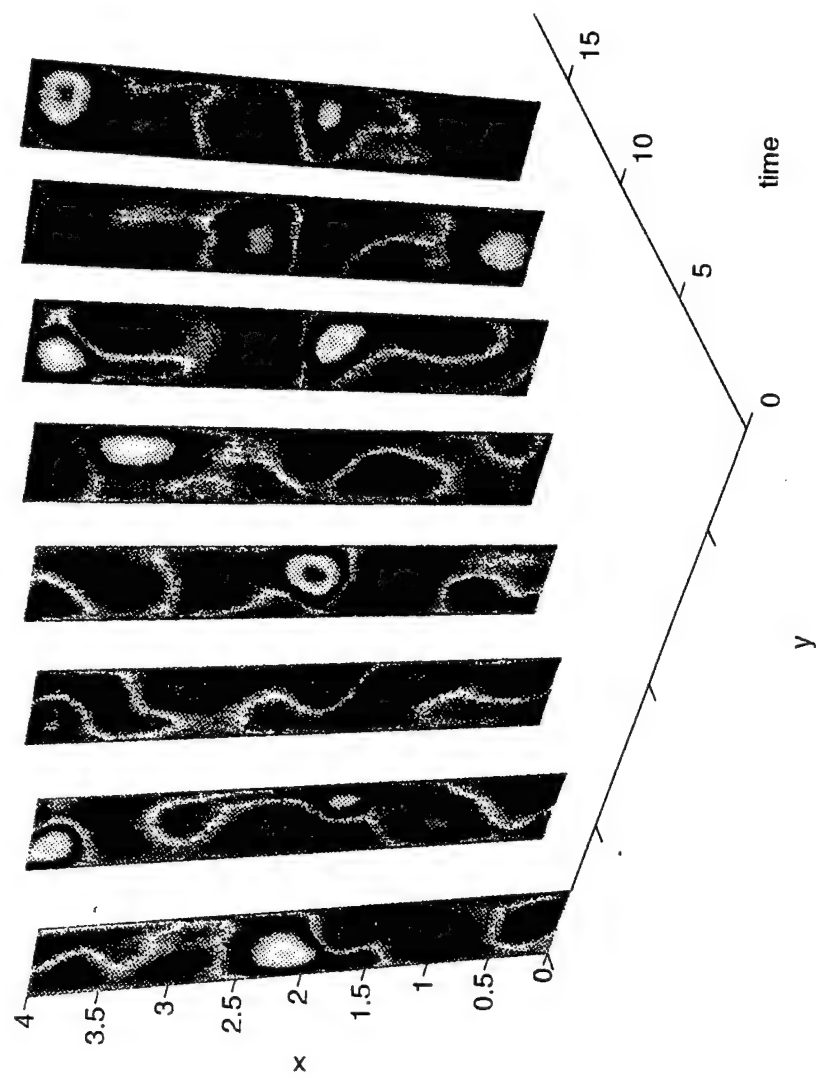


Figure D.10. Temporal snapshots of barotropic wavy field over one period.  $F = 28$ , asymmetric solution, quasi-periodic regime.

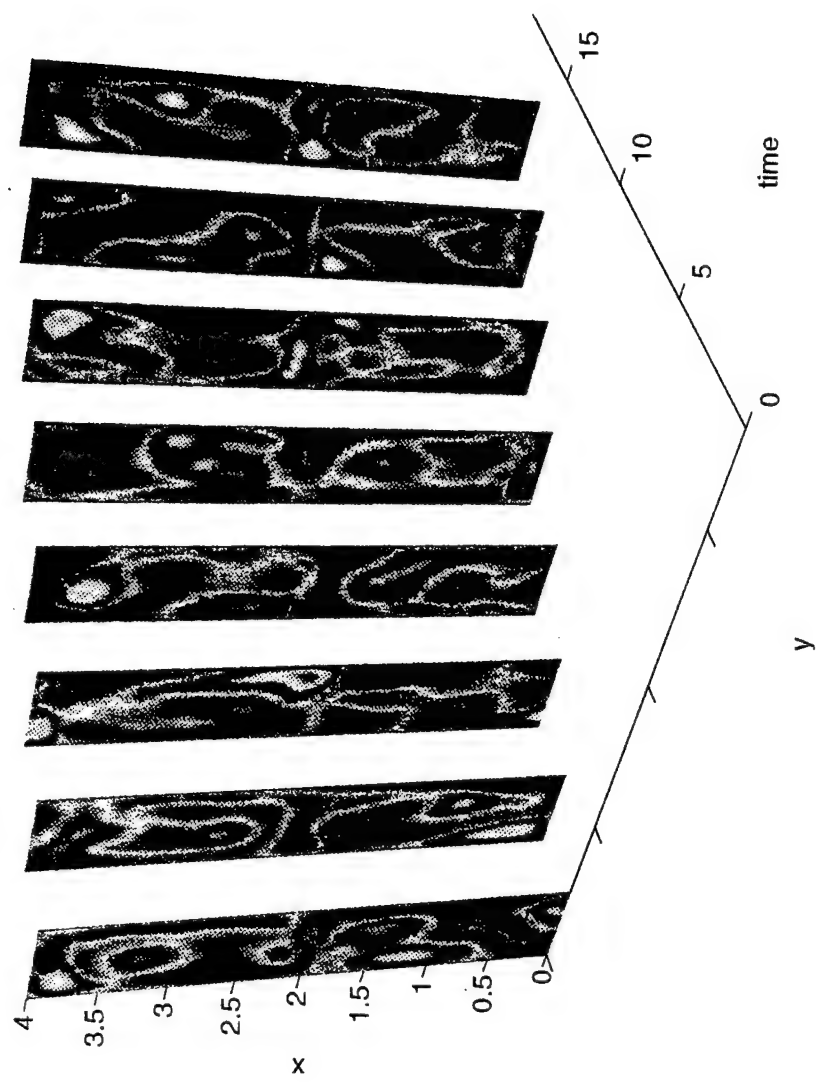


Figure D.11. Temporal snapshots of baroclinic wavy field at temporally uncorrelated times.  $F = 32$ , asymmetric solution, chaotic regime.

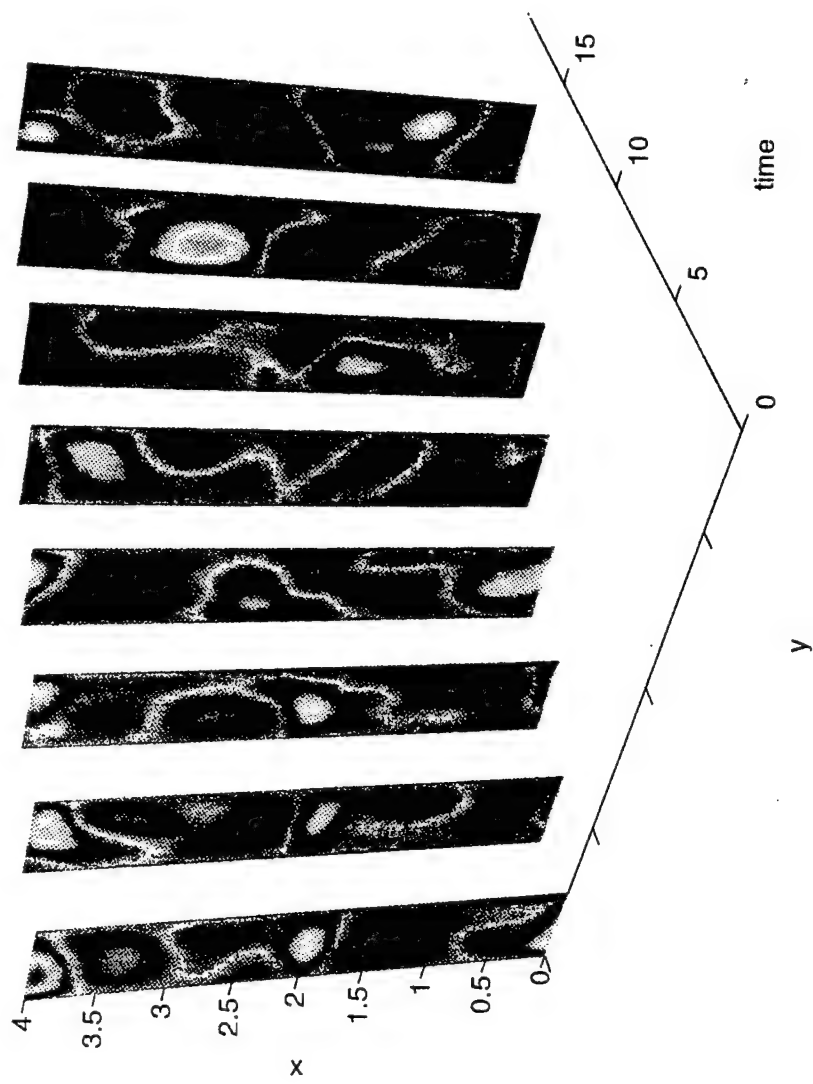


Figure D.12. Temporal snapshots of barotropic wavy field at temporally uncorrelated times.  $F = 32$ , asymmetric solution, chaotic regime.

## APPENDIX E

### SPATIAL SNAPSHOTS OF APPROXIMATE SOLUTIONS OF SLIPPERY MODEL

Appendix E contains snapshots of the barotropic and baroclinic wavy fields for the reconstructed, approximate systems (of the fully slippery model) at various parameter settings.

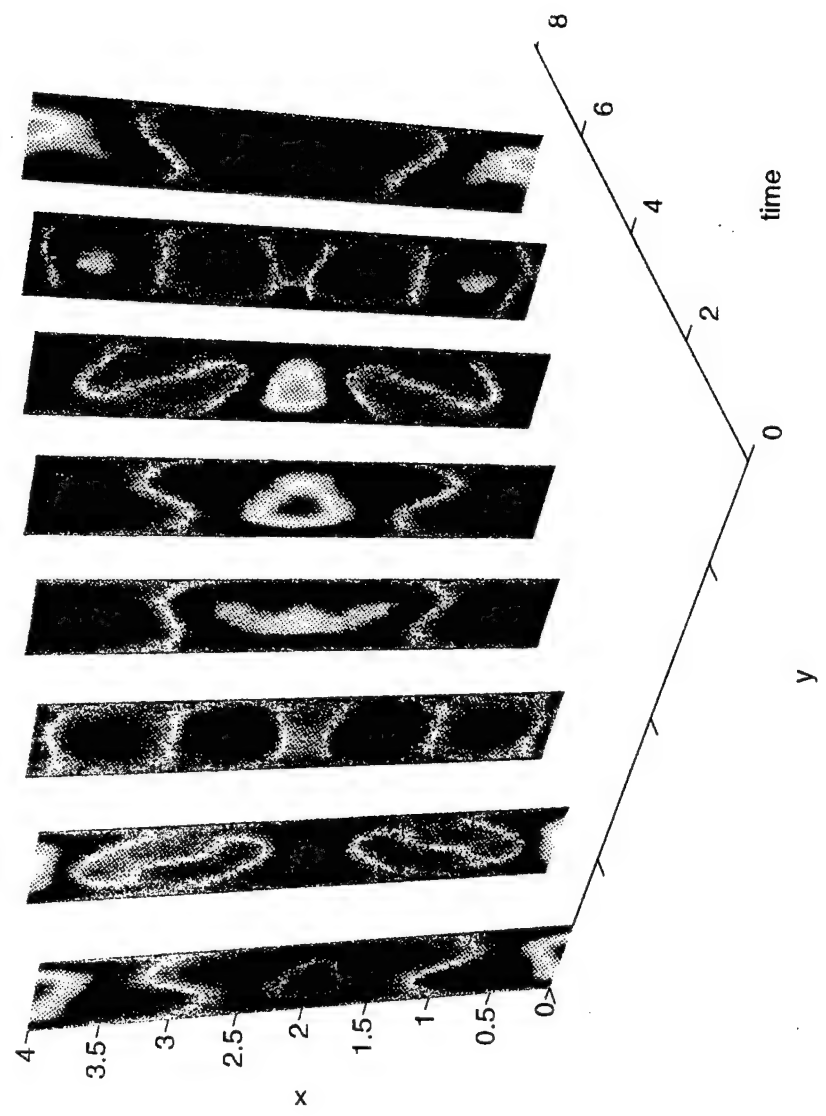


Figure E.1. Temporal snapshots of approximate baroclinic wavy field over one period.  
 $F = 20$ , symmetric solution, PAV regime.

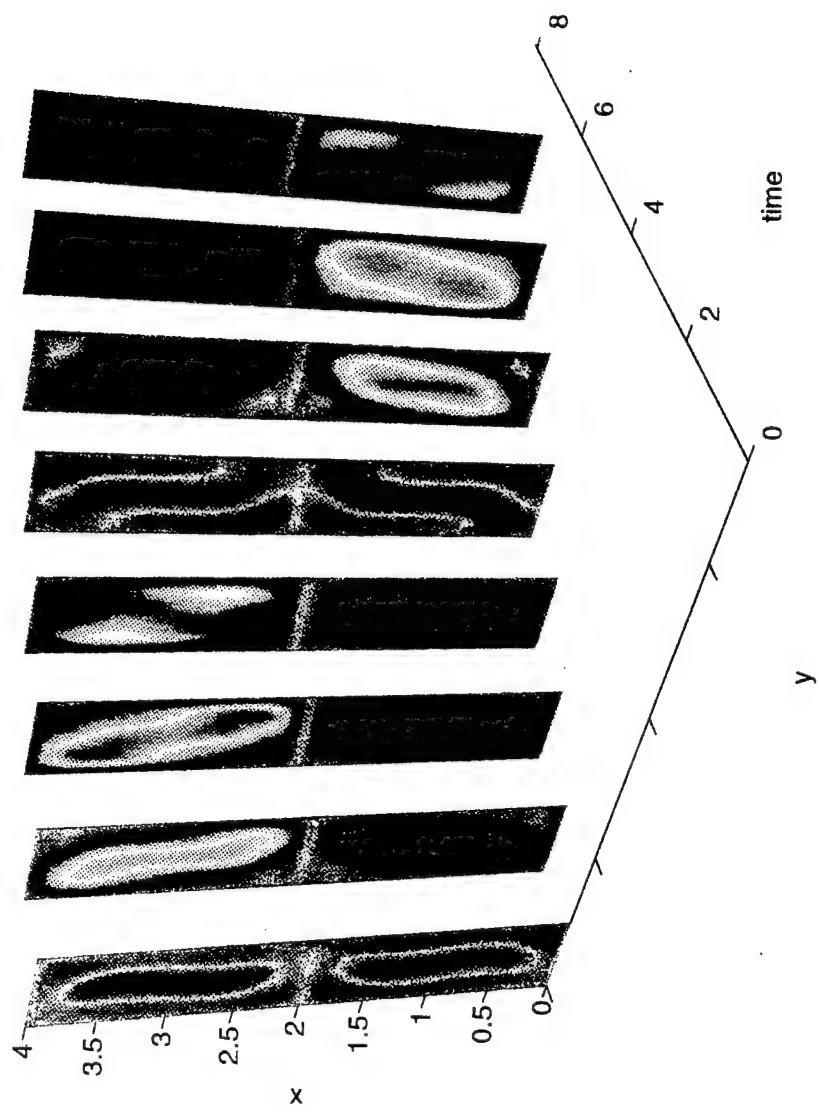


Figure E.2. Temporal snapshots of approximate barotropic wavy field over one period.  $F = 20$ , symmetric solution, PAV regime.

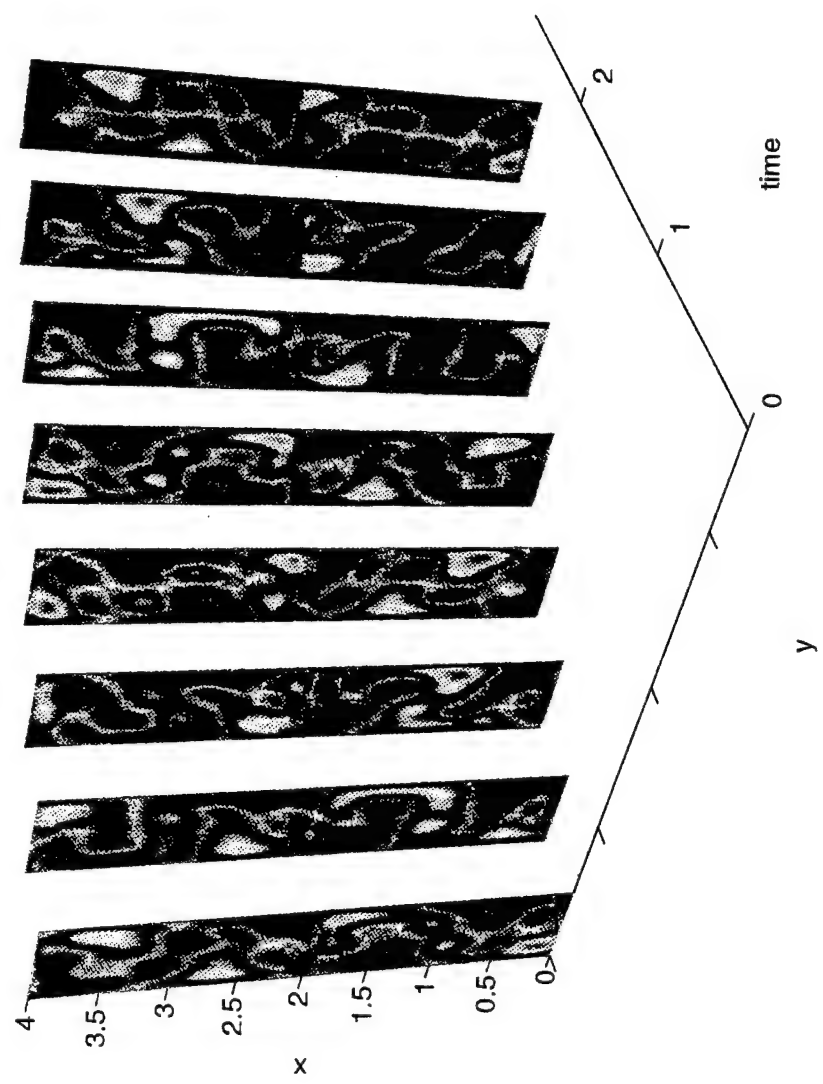


Figure E.3. Temporal snapshots of approximate baroclinic wavy field over one period.  
 $F = 32$ , symmetric solution, PSV regime.

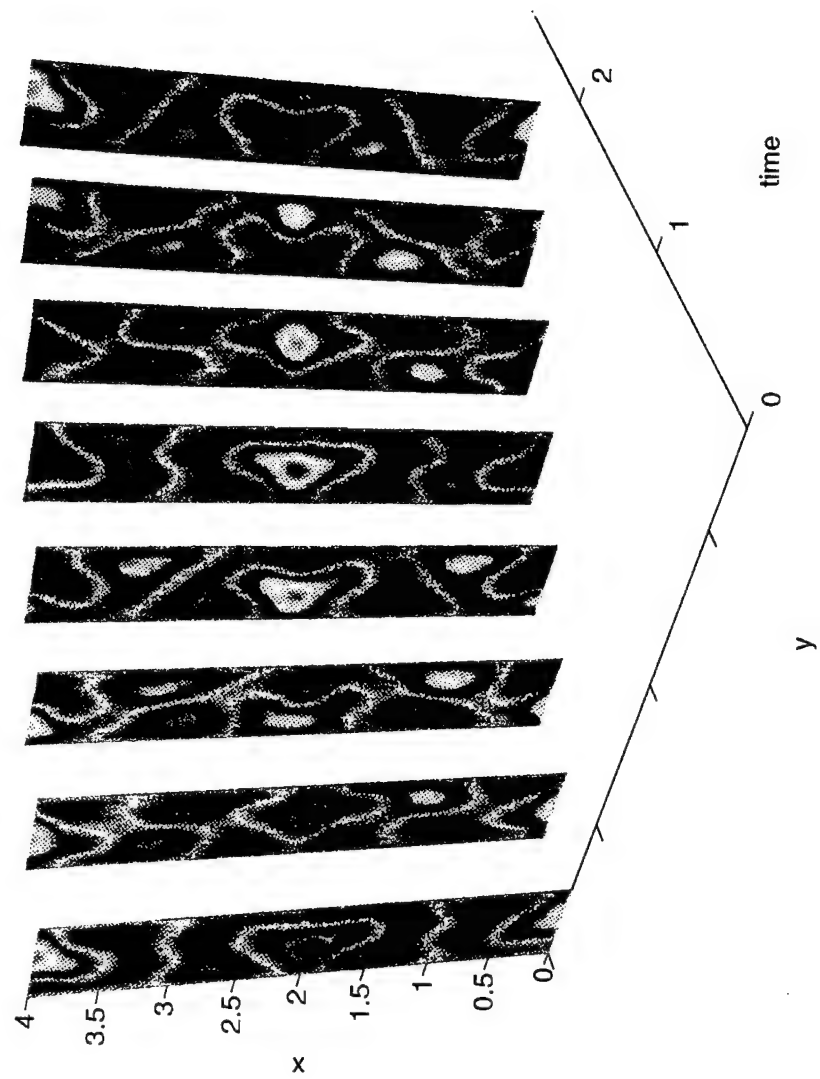


Figure E.4. Temporal snapshots of approximate barotropic wavy field over one period.  $F = 32$ , symmetric solution, PSV regime.

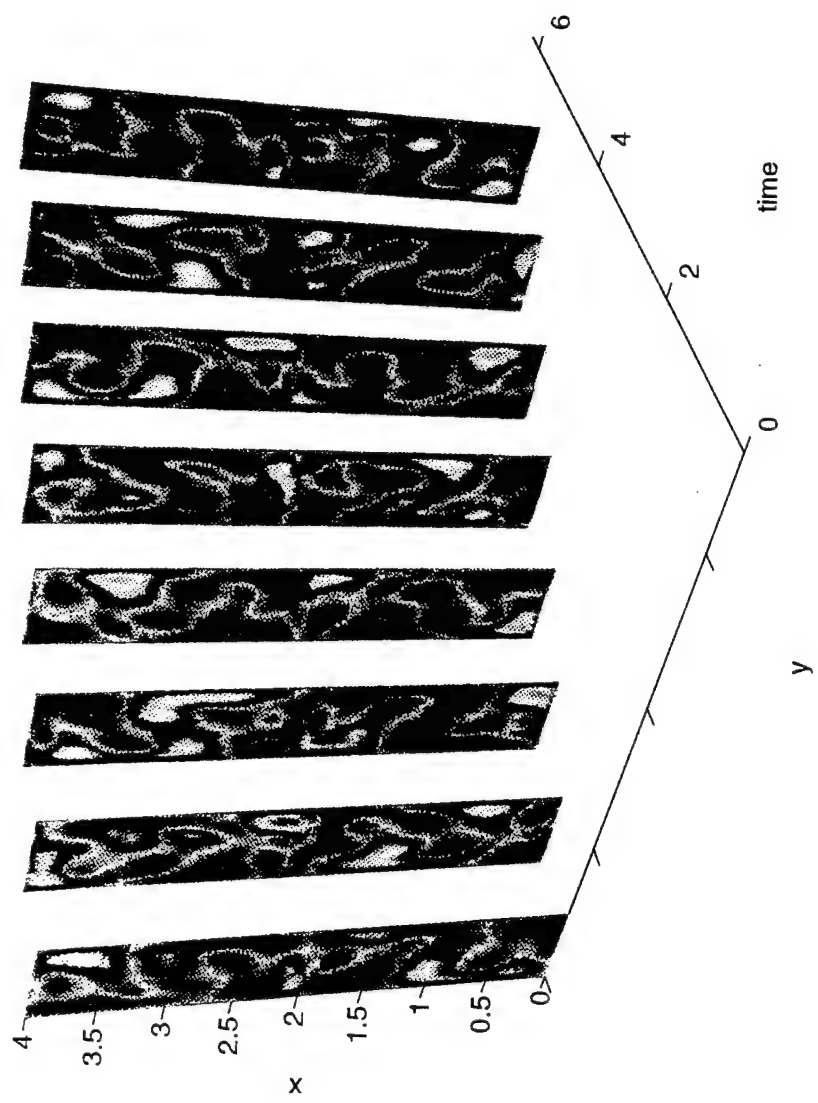


Figure E.5. Temporal snapshots of approximate baroclinic wavy field at temporally uncorrelated times.  $F = 36$ , symmetric solution, quasi-periodic regime.

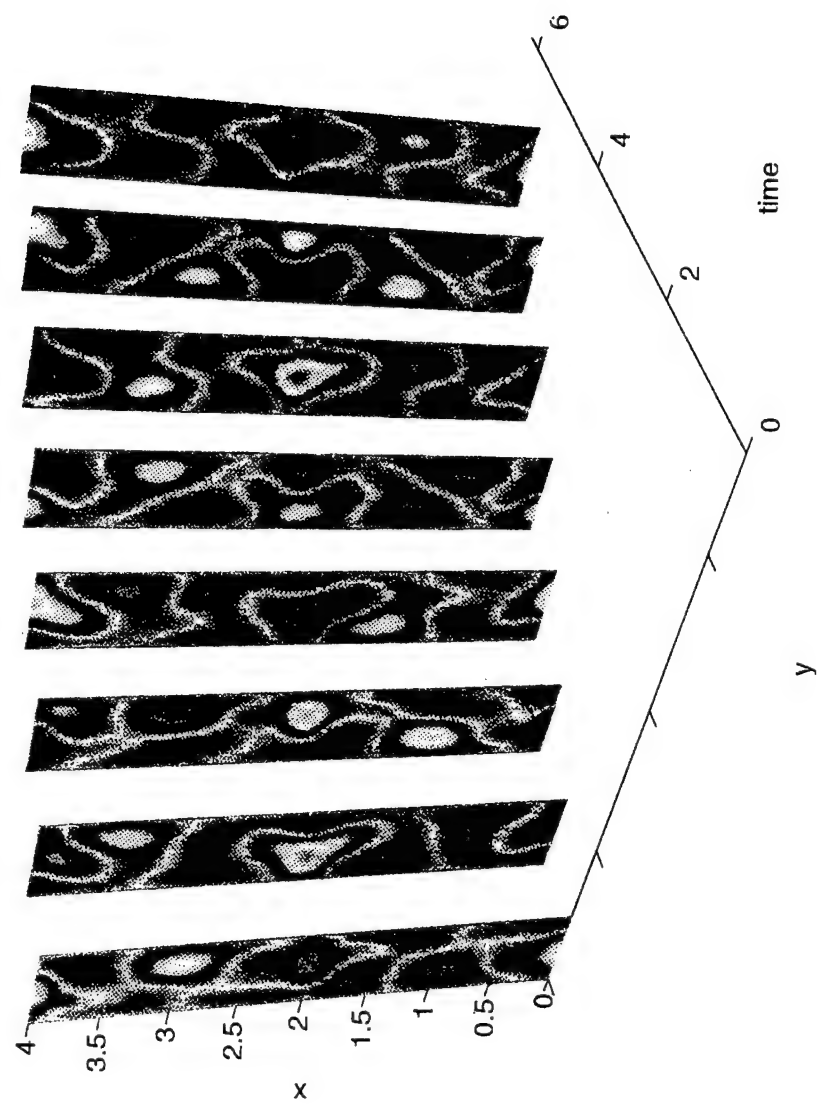


Figure E.6. Temporal snapshots of approximate barotropic wavy field at temporally uncorrelated times.  $F = 36$ , symmetric solution, quasi-periodic regime.

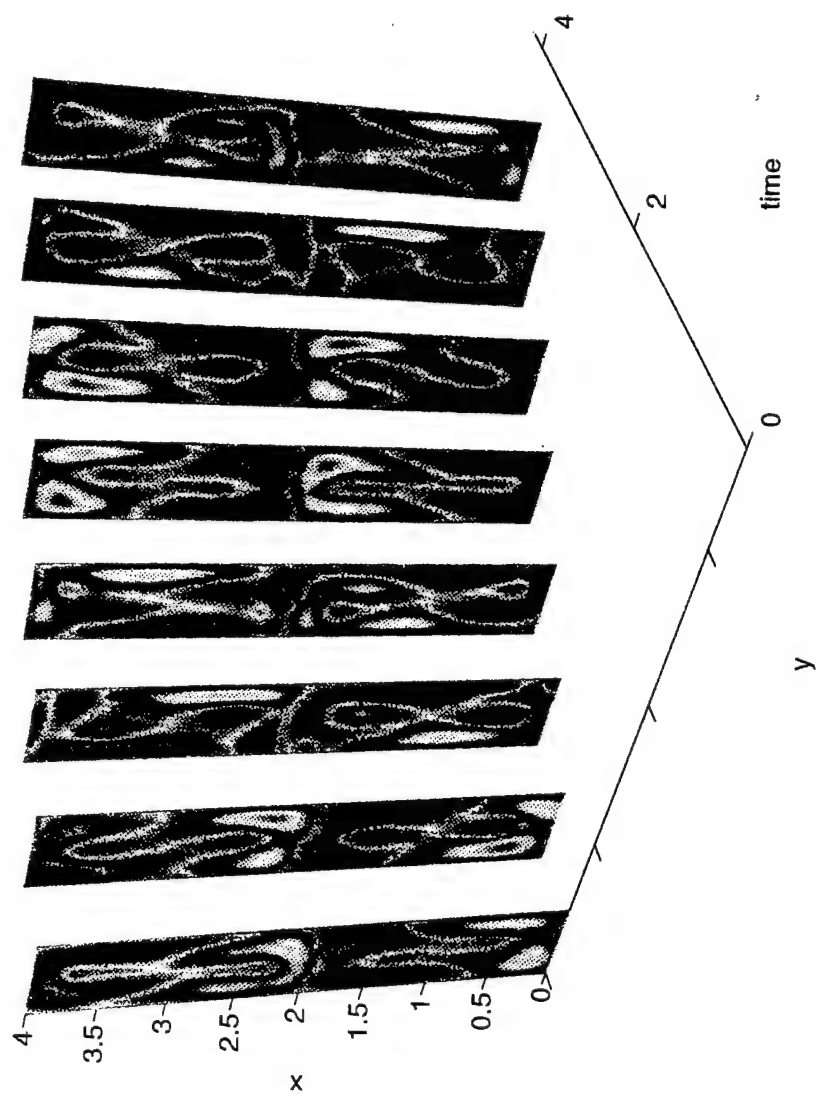


Figure E.7. Temporal snapshots of approximate baroclinic wavy field over one period.  
 $F = 20$ , asymmetric solution, PSV regime.

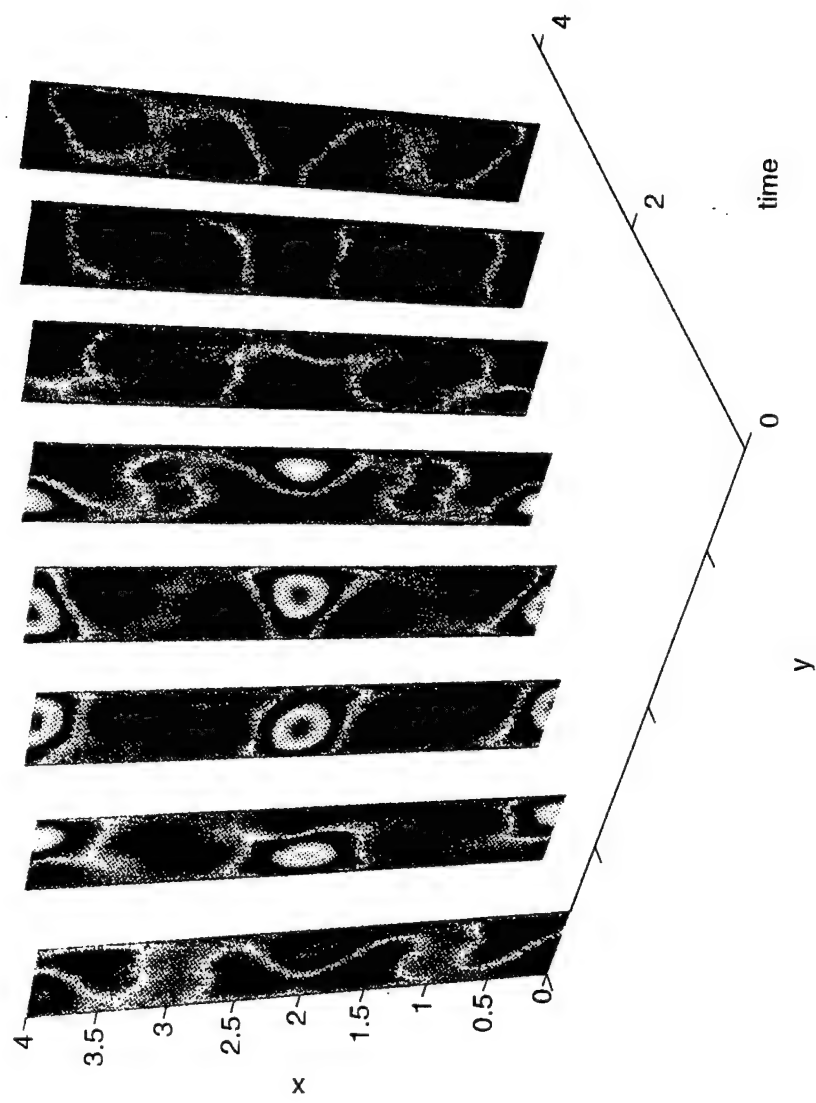


Figure E.8. Temporal snapshots of approximate barotropic wavy field over one period.  $F = 20$ , asymmetric solution, PSV regime.

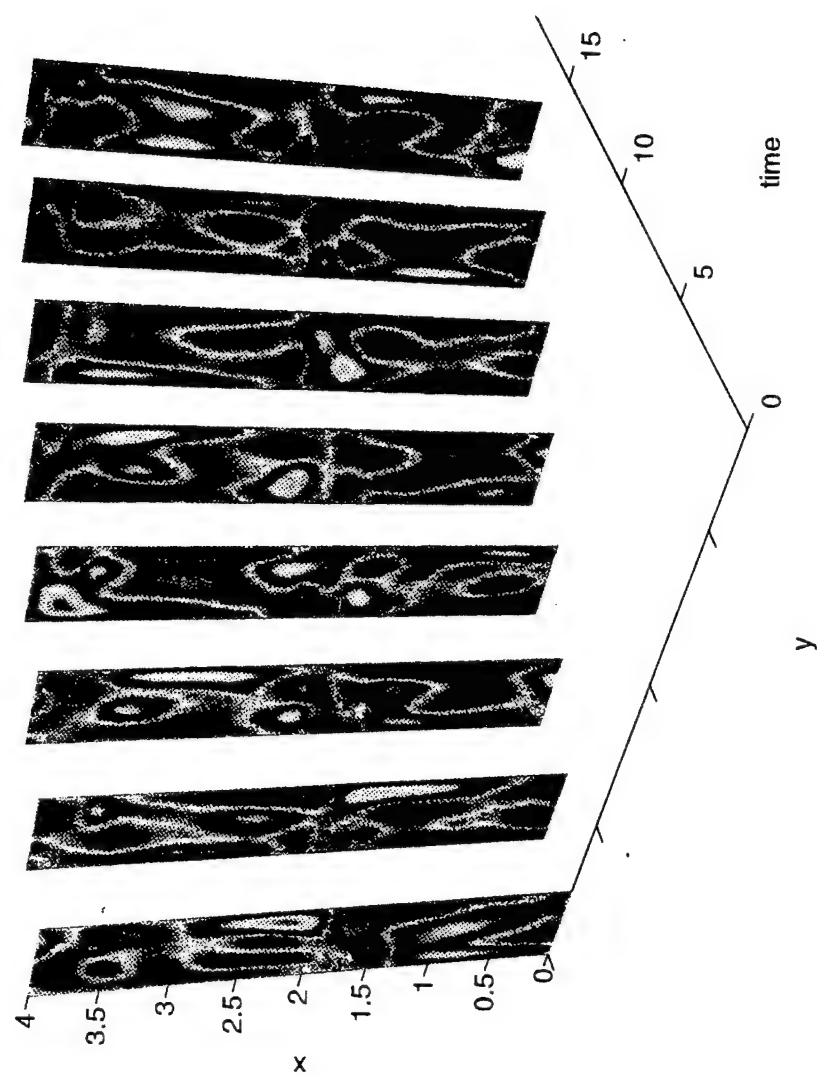


Figure E.9. Temporal snapshots of approximate baroclinic wavy field at uncorrelated times.  $F = 28$ , asymmetric solution, quasi-periodic regime.

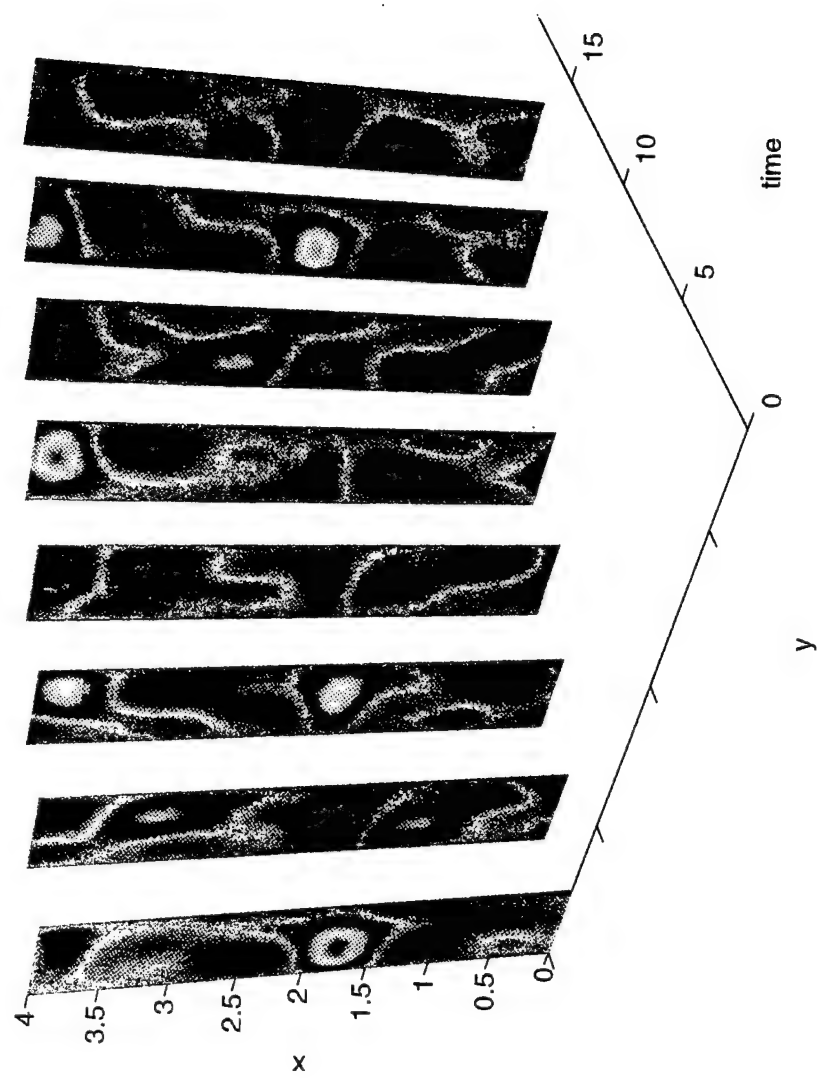


Figure E.10. Temporal snapshots of approximate barotropic wavy field at uncorrelated times.  $F = 28$ , asymmetric solution, quasi-periodic regime.

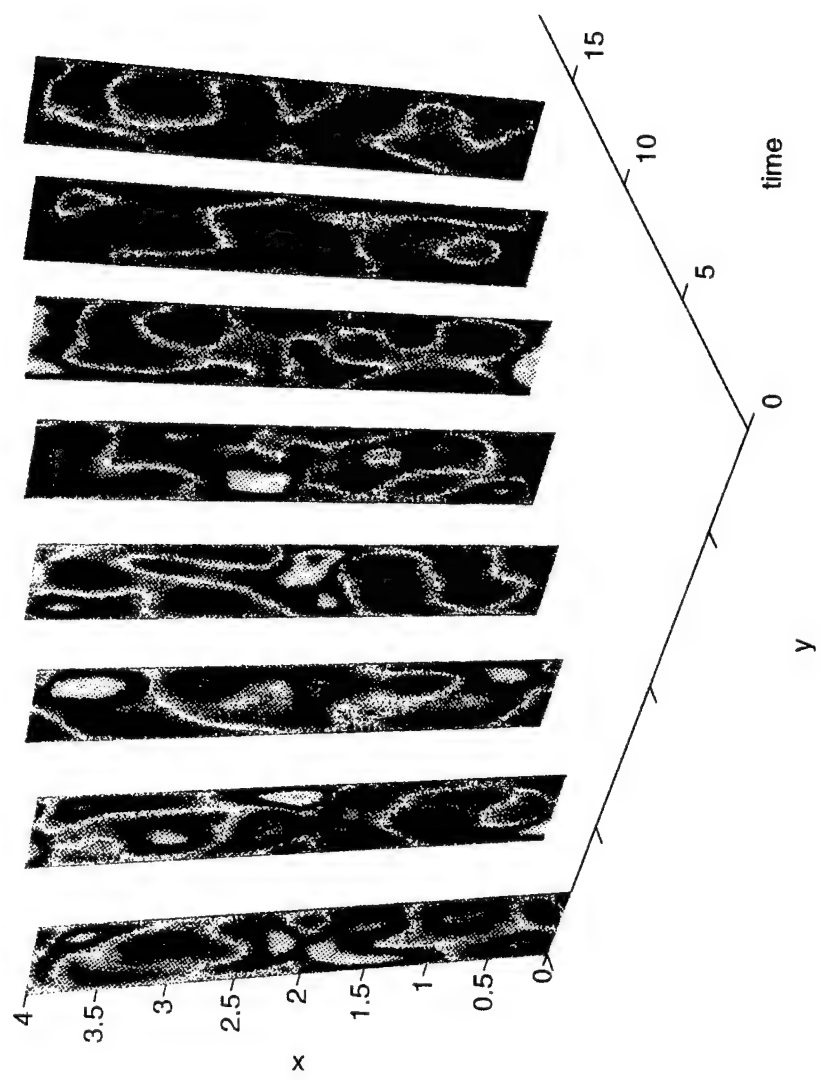


Figure E.11. Temporal snapshots of approximate baroclinic wavy field at temporally uncorrelated times.  $F = 32$ , asymmetric solution, chaotic regime.

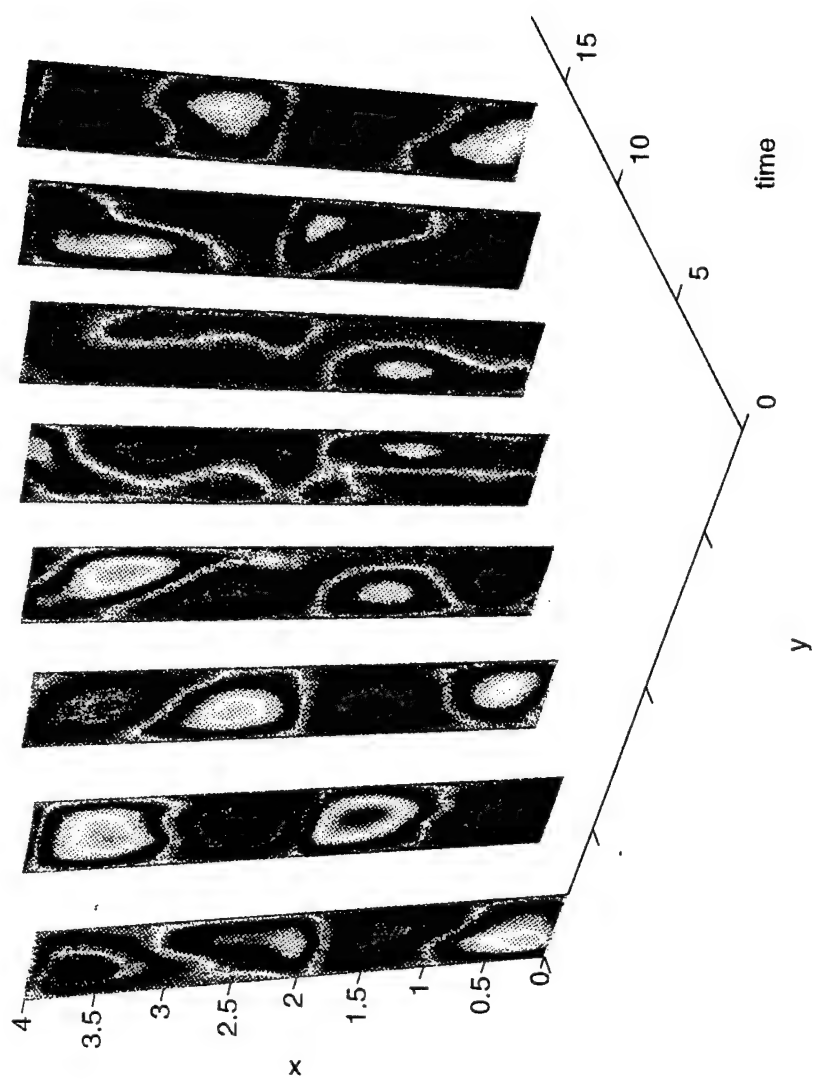


Figure E.12. Temporal snapshots of approximate barotropic wavy field at temporally uncorrelated times.  $F = 32$ , asymmetric solution, chaotic regime.

## APPENDIX F

### MEASURES OF CHAOS

There are several methods by which to test the existence of chaotic behavior in nonlinear systems, whether the data is obtained numerically or experimentally. A comprehensive explanation of these methods is given in textbooks (see Berge et al., 1984; Schuster, 1989; and Rasband, 1990), and only a brief overview will be presented here.

A simple method by which to determine the existence of chaos is to examine the power spectrum of some measured output of the system in question. A periodic signal will, of course, show one or more well-defined peaks at particular frequencies, with some lower level of background noise permeating the remaining frequencies. A chaotic signal, conversely, will produce a power spectrum that exhibits broad-band noise with no necessarily-dominant frequencies. The power spectrum, then, is a first arbiter of distinguishing a periodic or noisy-periodic signal from a nonperiodic one. However, since the spectral representation of a chaotic signal resembles that of a random time series, the power spectrum alone is insufficient to distinguish deterministic, nonperiodic behavior from stochastic time evolution. For this, one must resort to geometric properties of the system.

To understand the geometric measures of chaotic behavior that have historically been implemented, it is necessary to first introduce the idea of state-space (alternately referred to as phase space). Given an  $N$ -dimensional dynamical system, one can completely specify the state of the system (at a particular time) with the values of the  $N$  variables at that time. This can be thought of as plotting a point in an  $N$ -dimensional space, defined as a state space, where the various axes represent

the values of the  $N$  variables. Time evolution of the system, then, is represented by tracing a trajectory in state space, which for dissipative systems evolves on the system's attractor (an attractor is simply the manifold to which initial conditions eventually become attracted). The difficulty with implementing this for experimental data, obviously, lies in the fact that it is essentially impossible to know all of the variables that comprise the system under scrutiny. However, Packard et al. (1980) and Takens (1981) described a method by which the state space could be reconstructed using only one measured variable; the reconstructed state space exhibits the same properties as the original state space. The technique, known as the method of time-delay coordinates, is implemented as follows. First, presume that one possesses a signal from some dynamical system, either numerical or experimental, and that the time series can be denoted as  $\{x(t_i)\}$ ,  $i = 1, \dots, M$ , where  $M$  is the length of the data set. One can then reconstruct an attractor in  $D_E$  dimensions whose coordinates are given by the state-space vector

$$\vec{y}_i = (x(t_i), x(t_i + \tau), \dots, x(t_i + [D_E + 1]\tau)). \quad (F.1)$$

The variable  $\tau$  is the delay time, and its proper value has been the subject of much controversy. However, a generally-accepted estimate is to use the correlation time of the data set, so that the axes of the pseudo-state space are linearly independent. Additionally, Takens (1981) showed that using an embedding dimension  $D_E = (2D_T + 1)$ , where  $D_T$  is the topological dimension of the manifold containing the attractor, is sufficient but not always necessary to recover the original dynamics of the system. The strength of the above method is clearly that it allows one to reconstruct the attractor of a system (assuming one exists), and thus measure its properties, without actually knowing the plethora of variables that define the dynamical system in question.

Due to dissipative influences (among others), dynamical systems often evolve on an attractor that has a much lower dimension than the state space of the system. This can be exemplified by considering that hydrodynamic systems, which exist in an infinite-dimensional state space due to the fact that they are described by partial differential equations (and are generally equivalent to an infinite set of ordinary differential equations), can exhibit steady-state behavior, which evolves on an attractor of dimension zero, or periodic behavior, which evolves on an attractor of dimension one. Chaotic systems evolve on attractors that are of non-integer, or fractal, dimension. The measurement of the fractal attractor dimension is impractical due to the large data requirements even for low-dimensional attractors (Greenside et al., 1982). However, Grassberger and Procaccia (1983a,b) introduced a practical method by which a lower bound on the fractal dimension, known as the correlation dimension, could be calculated. In order to calculate the correlation dimension, a correlation integral, defined as  $C(r)$ , was introduced, where

$$C(r) = \sum_{i=1}^M \sum_{j=1}^M \Theta(r - \|\vec{y}_i - \vec{y}_j\|), \quad i \neq j, \quad (F.2)$$

where  $\Theta(x)$  is the Heaviside step function ( $\Theta(x) = 1$  for  $x > 0$ , 0 otherwise),  $\vec{y}_i$  and  $\vec{y}_j$  are given by Equation 1.38, and  $M$  is the size of the data set. For  $r \rightarrow 0$ ,  $C(r)$  will (hopefully) scale as a power of  $r$  as follows:

$$C(r) = r^{D_C}, \quad (F.3)$$

where  $D_C$  is the correlation dimension of the attractor and is a lower bound on (but usually a good approximation to) the fractal dimension.

In order to compute the correlation dimension, the correlation integral must

be computed for successively larger values of  $D_E$ . The scaling behavior should become independent of the embedding dimension for sufficiently large  $D_E$ , implying that  $D_C$  approaches a constant value and shows no further increase with increasing values of  $D_E$  (from the theorem of Takens outlined above,  $D_E$  should not need to be larger than  $\approx (2D_C + 1)$ ). The asymptotic value of  $D_C$  is then the correlation dimension, and the effective number of degrees of freedom of the system is given approximately by the lowest embedding dimension required to achieve a saturated value of  $D_C$ . Dimension estimates obtained via this method have been the subject of much controversy in recent years. Random data sets of finite length often yield a spurious, finite value of  $D_C$  despite the fact that random noise is infinite-dimensional (Theiler, 1991). Eckmann and Ruelle (1992) have shown that a given data set, regardless of its actual dimension, will yield a maximum value of correlation dimension that is approximately given by  $D_{C_{\max}} = 2 \log_{10} M$ , where  $M$  is the number of points in the data set given that the delay time,  $\tau$ , is equal to one. This latter stipulation ensures that one does not artificially increase the length of the data set by oversampling, a practice which obviously does not increase the amount of information present in the data. The above data requirement implies that dimension estimates that are not substantially less than  $2 \log_{10} M$  are suspect. If one inverts the above relationship, it is clear that the required number of points scales as  $10^{D_C/2}$ , although Nerenberg and Essex (1990), using a more refined analysis, report that the number of required points is smaller for lower-dimensional systems.

The other standard measure of chaotic systems is the Lyapunov exponent spectrum. Although there is no precise definition of "chaos", the standard view, and the one adopted here, is that for a system to be chaotic, it must possess at least one positive Lyapunov exponent, which results in the afore-mentioned "sensitive dependence on initial conditions." To define the Lyapunov exponents, imagine an infinitesimal hypersphere of initial conditions in a  $D$ -dimensional phase space, noting

that there will be one Lyapunov exponent for each degree of freedom. The evolution of the hypersphere with time is then observed; this hypersphere will be deformed into a hyper-ellipsoid as time passes. The  $j$ th Lyapunov exponent can then be defined in terms of the length of the  $j$ th principal axis,  $p_j$ , of the ellipsoid by

$$\lambda_j = \lim_{t \rightarrow \infty} \frac{1}{t} \ln \frac{p_j(t)}{p_j(0)} \quad (\text{F.4})$$

where the  $\lambda_j$ 's are ordered from largest to smallest in an algebraic sense (Wolf et al., 1985). A minimum condition for chaos, then, is that  $\lambda_1$  be positive. Wolf et al. (1985) developed a method of determining  $\lambda_1$  from a time series using a relatively simple procedure in both concept and practice. Eckmann et al. (1986) and Sano and Sawada (1985) independently developed a more complicated algorithm that is theoretically capable of computing all the Lyapunov exponents of the system. However, the ability of the algorithm to determine the values of  $\lambda_2, \lambda_3, \dots, \lambda_D$  diminishes substantially in the presence of noisy data and also for small data sets. This is further exacerbated by the fact that the negative Lyapunov exponents characterize the decay of transients or small perturbations in the system, making them difficult to accurately determine. The main item of interest in this study is the calculation of the positive Lyapunov exponents, since these in turn yield the predictability time scale of the system. To facilitate this task, both algorithms will be used and their results compared, a procedure which will hopefully allow more robust estimates of the Lyapunov spectrum.

It should be noted that, armed with the governing equations of a particular dynamical system, it is possible to compute all of the Lyapunov exponents. Wolf et. al (1985) describe the general method for ordinary differential equations, and assuming that partial differential equations can be cast in the form of a large set of ordinary differential equations, the method is applicable to PDEs as well. However,

to solve for all of the Lyapunov exponents of an  $N$ -dimensional system requires the integration of  $O(N^2)$  equations, rendering this procedure impractical for systems with large  $N$ .

A qualitative, and relatively new, method of testing for chaos is the use of nonlinear forecasting algorithms (Farmer and Sidorowich, 1987). The given data can be used in order to predict future states of the system by reconstructing the attractor and exploiting its geometric properties. If the predictions degrade with time, this indicates the system is chaotic (or worse), while forecasting errors that do not grow with time indicate a periodic or quasi-periodic system.

One final tool for measuring the chaotic nature of a system is also qualitative rather than quantitative, but it is nonetheless quite useful in assessing the dynamical character of the given flow. This is the first return map, which is constructed directly from a Poincaré surface of section. A comprehensive discussion of surfaces of section and return maps is given by Berge et al. (1984) and Rasband (1990), and only a cursory summary will be given here. Given an attractor in  $D$ -dimensional space, one can imagine a  $(D - 1)$ -dimensional hyper-plane (denoted as  $\Sigma$ ) that intersects the attractor. The hyperplane  $\Sigma$  is then the surface of section. If one records the locations of the successive intersections of an attractor trajectory with  $\Sigma$ , these locations can then be plotted against each other (e.g. one can plot the distance, from some arbitrary origin, of the  $n$ th crossing vs. the distance of the  $(n - 1)$ st crossing). This is known as a first return map. The effective result of this is to create a discrete map of fractal dimension  $(D_F - 1)$ , where  $D_F$  is the fractal dimension of the original attractor. For attractors with  $2 < D_F < 3$ , the first return map then possesses a dimension between 1 and 2, allowing it to be visualized on a two-dimensional plane. Therefore, the qualitative nature of the flow can be gleaned from a time series without the need to resort to dimension or Lyapunov exponent calculations. For higher-dimensional flows, of course, the first return map loses its effectiveness

and one must resort to more computationally-intensive measures in order to assess the complexity of the flow.

## APPENDIX G

### THE RELATIONSHIP BETWEEN SPATIAL AND TEMPORAL COMPLEXITY

A concern of some importance is the relationship between the temporal behavior and the spatial behavior of the system in question. For instance, one can construct low-order models by assuming some simple spatial dependence for the flow, such as a single wave. Then the spatial structure is implicitly fixed for all time, and the temporal behavior of the resulting ODEs dictates the system's actions. However, the models in this thesis involve the actions of many waves and are thus spatially complex. Conversely, an examination of either a time series taken at some point in the flow or else a temporal coefficient of some spatial mode often indicates low-dimensional (e.g. periodic, quasi-periodic, or chaotic) behavior; this fact indicates that the flow may be describable by a relatively small set of ODEs. To answer this question, a simple model was constructed, the purpose of which is to examine the role temporal and spatial dynamics, and their coupling, play in influencing the EOF spectrum.

The model chosen is one-dimensional in both space and time. The field  $\Phi$  is thus written as

$$\Phi = \sum_{i=1}^N \phi_i(x) \psi_i(t), \quad (G.1)$$

where  $N$  the number of modes chosen for inclusion. This is a very general representation and the critical portion of the problem arises from choosing the functional representation properly. For the present purposes, it was decided that choosing random spatial fields would be appropriate; this approach assumes that real dynamical

systems, while their behavior is certainly deterministic, often exhibit sufficient complexity that their behavior can be considered random. In addition, it was deemed appropriate to choose the temporal behavior to be periodic; this choice then allows one to fully observe the discrepancy between spatial and temporal complexity. To effect these choices, the following parameterization was made: the spatial functions were chosen to be sums of sines and cosines, so that

$$\phi_i(x) = \sum_{n=0}^{N/2} A_{in} \cos(n\pi x) + B_{in} \sin(n\pi x), \quad (G.2)$$

and the temporal functions were chosen similarly, i.e.,

$$\psi_i(t) = \sum_{n=1}^{N/2} C_{in} \cos(n\pi t) + D_{in} \sin(n\pi t). \quad (G.3)$$

The only difference between Equations G.2 and G.3 is that the spatial fields allow mean values, while the temporal fields do not. This is to eliminate the tedious process of first removing the temporal mean from the spatial field, a quantity which does not reflect the dynamical complexity of the system.

The final quantities to be chosen are the coefficients of the trigonometric functions, and these reflect the random nature of the system. It has been observed that the slippery model discussed in Chapter 2 exhibits the beginnings of spatial self-similarity. To simulate this, the amplitude,  $\mathcal{A}(k)$ , as a function of wavenumber,  $k$ , is chosen to scale as

$$\mathcal{A}(k) \sim k^{-\alpha}, \quad (G.4)$$

where  $\alpha$  is some positive number (but necessarily an integer). In addition, periodic, temporal signals exhibit discrete spikes at the fundamental frequency of oscillation,

denoted as  $f$ , and its higher harmonics (given by  $nf$ , where  $n$  is some integer), and the amplitude of these also typically decrease with a power law, so that

$$\mathcal{A}(f) \sim f^{-\beta}, \quad (G.5)$$

where  $\beta$  is also a positive number but not necessarily an integer. These two heuristic rules furnish sufficient information to complete the choices for the coefficients. For the spatial modes, the amplitude for each wavenumber is given by

$$\mathcal{A}(k) = \sqrt{A_{in}^2 + B_{in}^2} \quad (G.6)$$

and is normalized so that  $\mathcal{A}(1) = 1$ . The relative sizes of  $A_{in}$  and  $B_{in}$  are chosen at random by using the relation

$$\begin{aligned} A_{in} &= \cos(2\pi Z_{in}), \\ B_{in} &= \sin(2\pi Z_{in}), \end{aligned} \quad (G.7)$$

where  $Z_{in}$  is a random variable distributed uniformly on  $[0, 1]$  and is selected anew for each pair of  $i$  and  $n$ . Thus, the power law distribution of amplitudes is maintained, but the phases are chosen randomly in order to represent random fields. The effective result of this is to create data sequences of "colored" noise, the exact color depending on the scaling exponents  $\alpha$  and  $\beta$ .

The intent of this particular construct is to qualitatively replicate the statistical nature of the spatio-temporal behavior observed in the quasi-geostrophic models. The main limitation of this parametrization is its simplicity. With the simple scaling laws invoked, the dominant temporal frequency and spatial wavenumber will always be the lowest of the set used. This does not always seem to be the case in the model. Similarly, although the scaling behavior is observed in the fluid model

for relatively high frequencies and wavenumbers, there are departures from this behavior at longer temporal and larger spatial scales. Nonetheless, given that only an understanding of the intricacies involved is desired, and not a rigorous quantitative analysis, the above model was deemed satisfactory.

There are two limits under which the field  $\Phi$  can be trivially decomposed. The first is when  $\alpha$  becomes large. Then the spatial fields are all essentially comprised of three functions: a constant,  $\cos(\pi x)$  and  $\sin(\pi x)$ , since the amplitudes of the higher harmonics are much smaller than these fundamental waves. In this case, three pairs of temporal and spatial functions are able to essentially describe the entire variability of  $\Phi$ . The other limit, by symmetry considerations, is when  $\beta$  approaches  $\infty$ . Since no mean is allowed for the temporal fields, the time variability is dominated by the  $\sin(\pi t)$  and  $\cos(\pi t)$  modes. The field  $\Phi$  can then be represented by two pairs of spatial modes and temporal coefficients. These results indicate that it is not simply temporal or spatial complexity that results in the requirement of a large number of EOFs for adequate representation. Rather, it is the coupling between the two, which is generally reflective of the coherence or slaving between scales, that is the governing factor in determining the number of EOFs that will be required. This will be borne out by the following numerical examples.

Numerical runs were made at all  $\alpha, \beta$  pairs for  $\alpha = 0, 1, , \dots, 5, \beta = 0, 1, , \dots, 5$ . As expected, for  $\alpha = 5$  or  $\beta = 5$ , the first two or three EOFs essentially capture all the variance of the original field. To analyze the more interesting parameter settings, the cumulative variance function,  $\mathcal{C}(n)$ , is used, and

$$\mathcal{C}(n) = \sum_{i=1}^n \lambda_i, \quad (G.8)$$

where the  $\lambda_i$ 's are the eigenvalues normalized such that their sum is equal to one.  $\mathcal{C}(n)$  then measures the percent of total variance captured by the first  $n$  EOFs.

Figure G.1 displays  $\mathcal{C}(n)$  versus  $n$  for  $\beta = 2$  and  $\alpha = 0, 1, \dots, 5$ . Note that  $\beta=2$  is the smallest value for which the temporal fields are continuously differentiable. It is clear from the figure that, as  $\alpha$  becomes larger, the cumulative variance asymptotes to 1 more quickly. Figure G.2 displays  $\mathcal{C}(3)$  vs.  $\alpha$ , which also shows that the cumulative variance increases for fixed  $n$  as  $\alpha$  increases. The results shown in the figures can be anticipated intuitively, since as  $\alpha \rightarrow \infty$ , the number of EOFs needed should be three, or alternatively,  $\mathcal{C}(3)$  should approach one. The results for other values of  $\beta$  are similar.

To see if  $\mathcal{C}(n)$  observes any scaling laws, the mean wavenumber,  $\bar{k}$ , can be introduced, where

$$\bar{k} = \sum_{k=1}^{N/2} k \mathcal{A}(k) / \sum_{k=1}^{N/2} \mathcal{A}(k) = \sum_{k=1}^{N/2} k^{-\alpha+1} / \sum_{k=1}^{N/2} k^{-\alpha}. \quad (\text{G.9})$$

One can then define a length scale,  $\bar{X}$ , as  $\bar{X} \equiv \bar{k}^{-1}$ . A point of minor importance is that the sums diverge when the exponent greater than -2. ( $\alpha \leq 3$ ). However, since we are using only finite sums, the mean wavenumber is always finite. The conjecture is that as  $\bar{k}$  becomes smaller ( $\bar{X}$  becomes larger),  $\mathcal{C}(n)$  will increase (for some fixed  $n$ ). This is borne out in Figure G.3, which displays  $\log[\mathcal{C}(3)]$  vs.  $\log(\bar{k})$ . The relation is nearly linear, indicating that there is an approximate scaling relation between the mean length scale of the spatial field and the convergence of  $\mathcal{C}(n)$ . Alternatively, the relation can be taken to imply that as the length scale becomes smaller, more and more EOFs will be required to meet a particular variance threshold.

In order to compare with results for a more complicated temporal field, the  $\psi_i(t)$  functions were replaced with data from the Lorenz system (Lorenz, 1963) in a chaotic region of parameter space. The phase of the signal was chosen at random by choosing a relatively small time series from a much larger, contiguous data set. The values of  $\alpha$  again varied from 0 to 5. Figure G.4 displays  $\mathcal{C}(3)$  vs.  $\alpha$ . The general

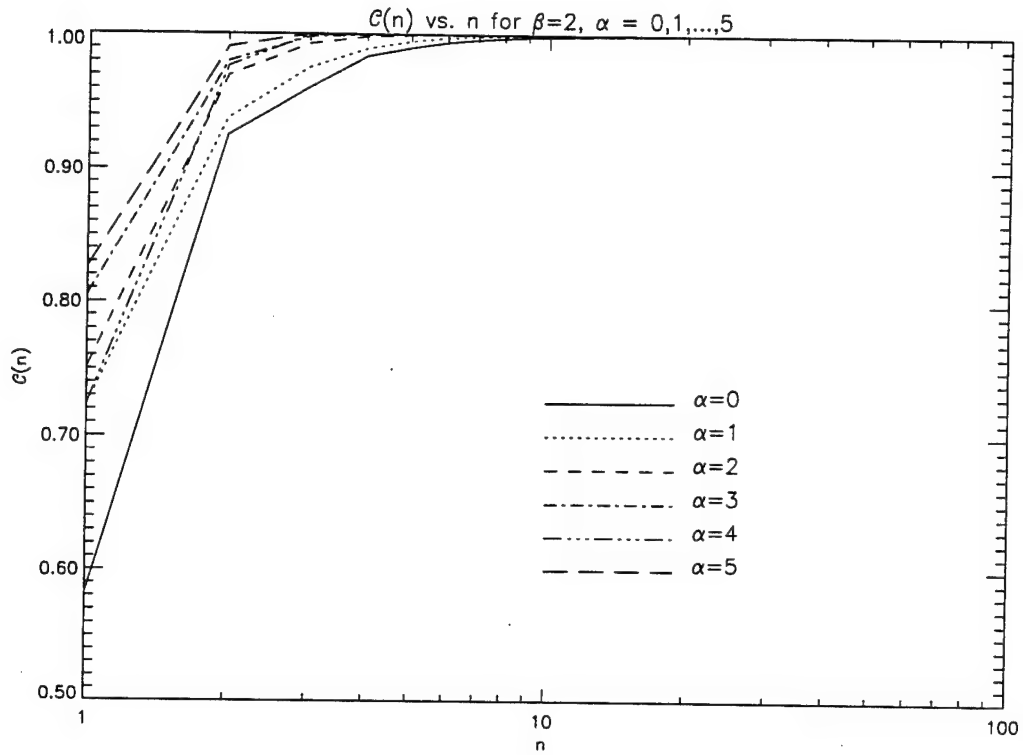


Figure G.1. Cumulative variance functions,  $C(n)$ , for  $\beta=2$ ,  $\alpha = 0, 1, \dots, 5$ , periodic temporal behavior.

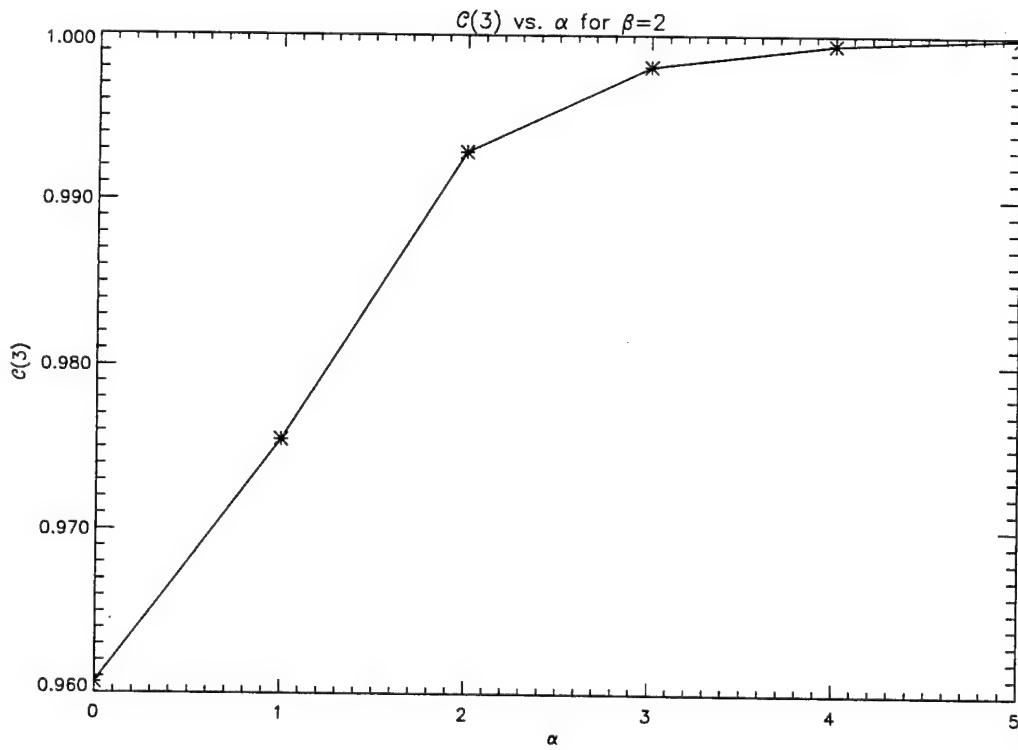


Figure G.2:  $C(3)$  versus  $\alpha$  for  $\beta=2$ , periodic temporal behavior.

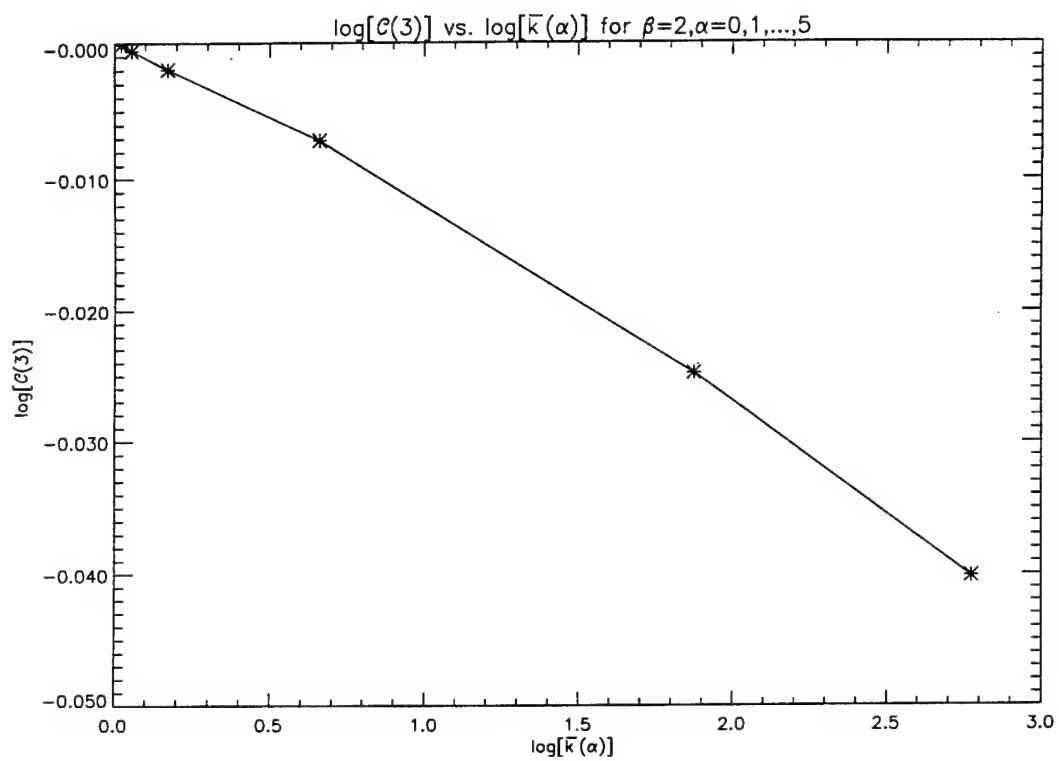


Figure G.3. Scaling behavior of  $\mathcal{C}(3)$  versus mean wavenumber,  $\bar{k}$ , for  $\beta = 2$ , periodic temporal behavior.

behavior is much the same as for the periodic time series. Differences, arise, however, in scaling behavior, as is evident in Figure G.5.  $C(3)$  now varies with  $\exp(\gamma \bar{k})$ , where  $\gamma$  is some constant. This is at odds with the power-law behavior observed above. The origin of the difference is not quite clear, but it may be related to the differences in temporal power spectra. Whereas for the periodic case the temporal power spectrum scales as some power of the frequency, for the Lorenz system the temporal power spectrum decays exponentially (Brandstater and Swinney, 1987). Despite the differences, it appears that the convergence of the cumulative variance depends directly on the characteristic scales in the problem.

In summary, this simplified model makes the important point that the results obtained by the EOF analysis depend on the coupling between spatial and temporal complexity. When either the spatial or temporal complexity is null, the number of EOFs needed to represent the spatio-temporal variability is also small. It is the combination of variability in the two domains that necessitates a large number of time-space mode pairs. In addition, there seem to exist some rough scaling relations that are affected by the particular representation of the spatial and temporal fields. This will not be investigated further here but is certainly a subject of some interest. Finally, the basic mechanism used in the above model to change the "complexity" are the scaling exponents, which affect the length and time scales of the system. Another possible avenue of investigation (but much more complicated) would be to keep the scaling exponent fixed, but to "color" the randomness in the phases shown in Equation G.7. In other words, it would be possible to correlate the various length and time scales by some amount. Intuitively, one would expect that the number of EOFs required would be inversely proportional to the correlation between scales. However, the basic results presented here would likely not be altered.

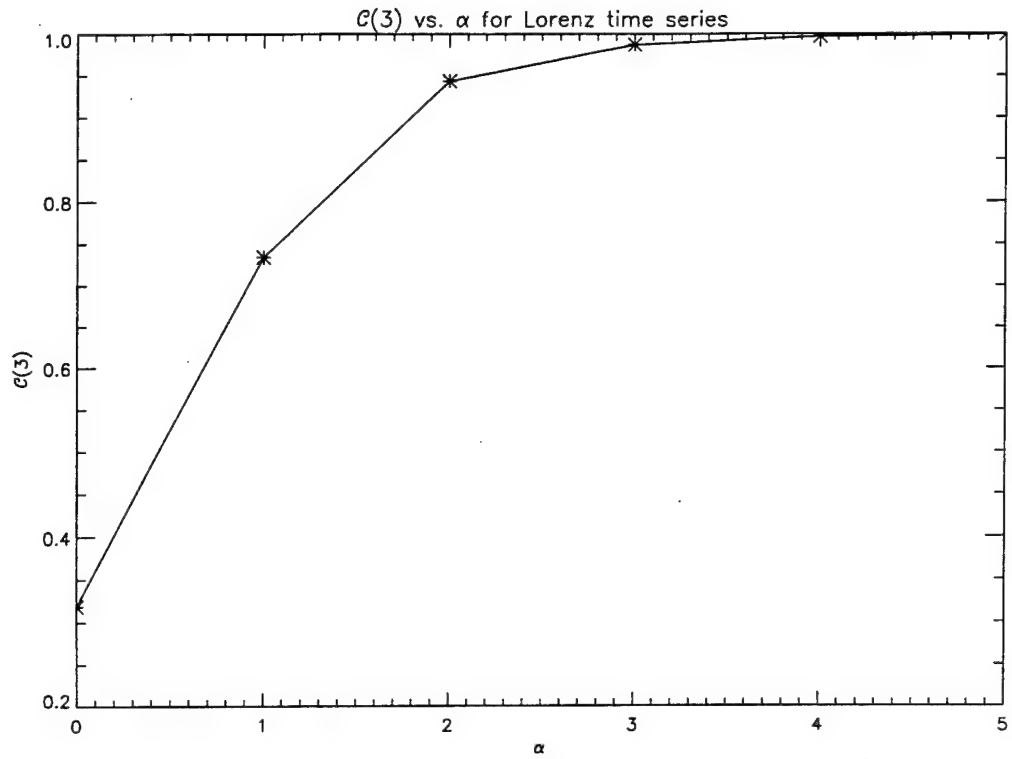


Figure G.4:  $C(3)$  versus  $\alpha$  for Lorenz time series.

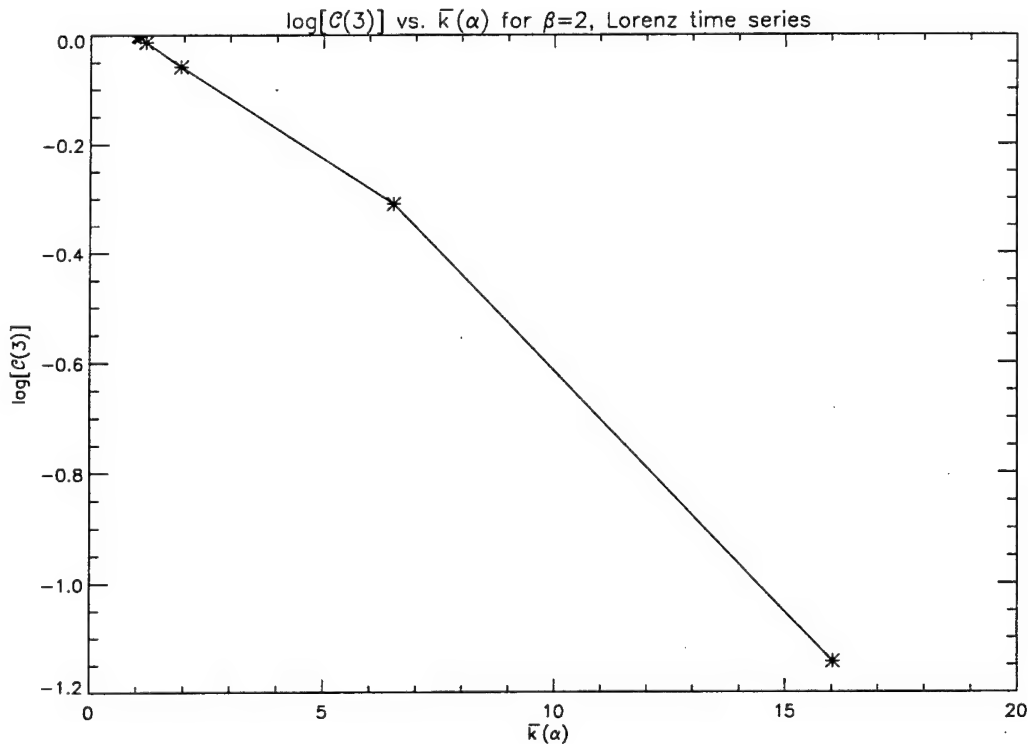


Figure G.5. Scaling behavior of  $C(3)$  versus mean wavenumber,  $\bar{k}$ , for Lorenz time series.

## APPENDIX H

### SOME DERIVATIONS CONCERNING THE RIGID-WALL, LINEAR INSTABILITY PROBLEM

In this appendix we derive the condition given by Equation 5.31 such that Equations 5.29,30 are valid, i.e. the relation between the parameters  $Q$  and  $\Gamma$  such that  $f = U_{bc}$ ,  $g = 0$  is a solution for  $F_c = k^2/2$ .

If we write the perturbation streamfunctions as

$$\phi_{bt} = \text{Re } f(y)e^{ik(x-ct)}, \quad (\text{H.1})$$

$$\phi_{bc} = \text{Re } g(y)e^{ik(x-ct)}, \quad (\text{H.2})$$

then by substitution into Equations 5.16,17, the following relations are obtained:

$$\begin{aligned} ikU_{bc}g'' + ik[\Gamma^2 - (k^2 + \Gamma^2)U_{bc}]g = \\ -(Q + 2k^2E/R_o)f'' + (Qk^2 + E/R_0k^4)f + E/R_0f''', \end{aligned} \quad (\text{H.3})$$

$$\begin{aligned} ikU_{bc}f'' + ik[\Gamma^2 + (2F - k^2 - \Gamma^2)U_{bc}]f = \\ -(2Q + 2k^2E/R_o)g'' + (2Qk^2 + E/R_0k^4)g + E/R_0g'''. \end{aligned} \quad (\text{H.4})$$

The solution given by Equations 5.29,30 is obtained by neglecting the terms on the right hand sides of Equations H.3,4. We expect that these terms are only important in giving rise to a boundary layer (of thickness  $\lambda$  as defined in Equation 5.28) that brings the waves' zonal velocity to zero at the walls. We can then ask when this constraint is broken, i.e. when the solution given by Equations 5.29,30 does not consistently yield terms on the right hand sides of Equations H.3,4 that are indeed

small outside the wave boundary layer. We therefore choose to examine the sidewall at  $y = -1$  (the results are invariant with respect to the wall chosen) and consequently define

$$\tilde{y} = 1 + y, \quad (H.5)$$

so that  $\tilde{y}$  gives the distance away from the sidewall. Thus, using the fact that  $f = U_{bc}$ ,

$$f \approx \Gamma \tilde{y}, \quad (H.6)$$

$$f'' \approx -\Gamma^2, \quad (H.7)$$

$$\text{and } f''' \approx -\Gamma^4 \quad (H.8)$$

for  $\tilde{y} \ll 1$ . Furthermore, since the dissipative terms should be neglectable except inside the wave boundary layer, we set  $\tilde{y}$  equal to  $\lambda = (2Q)^{1/4}/\Gamma$  so that we evaluate the magnitudes of the terms at one  $e$ -folding distance from the sidewall. Finally, we expect that the baroclinic wave, which has an asymptotic amplitude of zero, will be small but nonzero and possesses an amplitude of  $O(g)$ . Making the above substitutions, Equations H.3,4 become

$$\begin{aligned} ik(2Q)^{1/4}O(g) + ik[\Gamma^2 - (k^2 + \Gamma^2)(2Q)^{1/4}]O(g) = \\ -Q\Gamma^2 + E/R_o\Gamma^4, \end{aligned} \quad (H.9)$$

$$\begin{aligned} ik(2Q)^{1/4}\Gamma^2 + [(2F - \Gamma^2 - k^2)(2Q)^{1/4} + \Gamma^2]ik(2Q)^{1/4} = \\ -2QO(g) + E/R_oO(g). \end{aligned} \quad (H.10)$$

In the above equations, only the dominant dissipative terms have been retained for simplicity. The two retained terms on the right hand side of Equation H.9 can be shown, with the aid of Equation 5.9, to always be the same order regardless of

the exact parameter values used, justifying the inclusion of both. Looking at the barotropic equation, the dissipative terms scale as  $Q\Gamma^2$ . Further assuming that the shape of the baroclinic perturbation is equivalent to  $U_{bc}$  (but with an unknown amplitude  $A_{bc}$ ), the terms on the left hand side of the barotropic equation are on the order of  $Q^{1/2}A_{bc}$  since the larger terms proportional to  $\Gamma^2$  tend to cancel each other. This immediately yields the relationship that

$$A_{bc} = O(Q^{1/2}\Gamma^2). \quad (\text{H.11})$$

With this knowledge, we can now turn to the baroclinic equation. In order for the baroclinic equation to yield  $F_c = k^2/2$ , the dissipative terms must be essentially zero outside the wave boundary layer. This requires that the dissipation, which with the use of Equation H.11 can be shown to be  $O(Q^{3/2}\Gamma^4)$ , must be much smaller than the relevant terms on the left hand side, which are  $O(Q^{1/2})$ . This results in the relation

$$Q \ll \Gamma^{-4}. \quad (\text{H.12})$$

If we return to Equation H.11 and make the additional requirement that  $A_{bc} \ll 1$  in order to maintain the approximate validity of Equation 5.30, we again obtain Equation H.12. There is thus consistency in the requirement on the parameters such that  $f \approx U_{bc}$ ,  $g \approx 0$ , and  $F_c \approx k^2/2$ . The relation given by Equation 6.12 offers the following physical interpretation if one takes the fourth root of each side. Doing this, we find that

$$Q^{1/4} \leq \Gamma^{-1}, \quad (\text{H.13})$$

which indicates that the ratio of the wave boundary layer thickness to the basic-flow

boundary layer thickness is less than the thickness of the basic-state boundary layer itself.

## APPENDIX I

### NUMERICAL METHOD FOR RIGID-WALL FORMULATION

This appendix summarizes the influence-matrix technique used in the numerical code for the rigid-wall model. The following synopsis is from Brummell (1993).

The problem for the rigid-wall streamfunction formulation, where there are no boundary conditions on the vorticity equation, is overcome by using a modification of the influence matrix technique (Kleiser and Schumann, 1980). First, some clarification of the standard influence matrix technique may be valuable.

Discretization of the governing equations leads to problems of the form

$$(D^2 - \lambda^2) \omega = R, \quad (I.1)$$

$$(D^2 - k^2) \psi = \omega, \quad (I.2)$$

where  $D \equiv \frac{\partial}{\partial y}$ ,  $\omega$  is the vorticity,  $\psi$  is a streamfunction,  $k$  is the horizontal wavenumber,  $\lambda$  is a constant depending upon the discretization, and  $R$  is a function of known quantities. An uncertainty arises since the boundary conditions for a rigid channel problem exist on  $\psi$  only:

$$\psi(\pm 1) = 0, \quad (I.3)$$

$$D\psi(\pm 1) = 0. \quad (I.4)$$

Since  $R$  is known, a normal method of proceeding would be to solve the first

equation for  $\omega$ , substitute into the second equation and solve for  $\psi$ . However, this is impossible because no boundary conditions exist for the first equation. Alternatively, the two equations could be combined into one biharmonic equation but this would require the inversion of a pentadiagonal problem for its solution.

The influence matrix technique instead takes the solutions of easily solved systems and then uses the linearity of the problem to construct the correct solution. Consider the solutions of a homogeneous problem with inhomogeneous boundary conditions ("+" and "−" problems) and an inhomogeneous problem with homogeneous boundary conditions ("p" problem) as follows:

*p* problem:

$$\begin{aligned} (D^2 - \lambda^2) \omega_p &= R, \\ (D^2 - k^2) \psi_p &= \omega_p, \\ \omega_p(1) = 0, \quad \omega_p(-1) &= 0, \\ \psi_p(1) = 0, \quad \psi_p(-1) &= 0. \end{aligned} \tag{I.5}$$

+ problem:

$$\begin{aligned} (D^2 - \lambda^2) \omega_+ &= 0, \\ (D^2 - k^2) \psi_+ &= \omega_+, \\ \omega_+(1) = 1, \quad \omega_+(-1) &= 0, \\ \psi_+(1) = 0, \quad \psi_+(-1) &= 0. \end{aligned} \tag{I.6}$$

− problem:

$$\begin{aligned} (D^2 - \lambda^2) \omega_- &= 0, \\ (D^2 - k^2) \psi_- &= \omega_-, \end{aligned}$$

$$\begin{aligned}\omega_-(1) &= 0, \quad \omega_(-1) = 1, \\ \psi_-(1) &= 0, \quad \psi_(-1) = 0.\end{aligned}\tag{I.7}$$

Notice that the + and - problems do not depend on  $R$  and therefore can be solved once at the beginning of the calculation (possibly even analytically) and used for all time, whereas the  $p$  problem must be solved at each time step, since  $R$  depends on quantities from the previous time step.

Now let

$$\begin{pmatrix} \omega \\ \psi \end{pmatrix} = \begin{pmatrix} \omega_p \\ \psi_p \end{pmatrix} + \delta_+ \begin{pmatrix} \omega_+ \\ \psi_+ \end{pmatrix} + \delta_- \begin{pmatrix} \omega_- \\ \psi_- \end{pmatrix}.\tag{I.8}$$

Obviously, boundary condition I.3 is automatically satisfied and so we are left to choose  $\delta_+$  and  $\delta_-$  in order to satisfy boundary condition I.4 i.e. choose  $\delta_+$  and  $\delta_-$  such that

$$\begin{pmatrix} D\psi_+(+1) & D\psi_-(-1) \\ D\psi_(-1) & D\psi_(-1) \end{pmatrix} \begin{pmatrix} \delta_+ \\ \delta_- \end{pmatrix} = - \begin{pmatrix} D\psi_p(+1) \\ D\psi_p(-1) \end{pmatrix}.\tag{I.9}$$

Having established  $\delta_+$  and  $\delta_-$ , there are two ways to proceed. The solution may be constructed as the sum of the various  $p$ , + and - solutions, or, notice that  $\delta_+$  and  $\delta_-$  are precisely the boundary conditions we were seeking on  $\omega$ , i.e.

$$\omega(+1) = \delta_+, \quad \omega(-1) = \delta_-,\tag{I.10}$$

and so the original equations may now be solved.

The methodology used in the current code is a little different to the general example given above. In the above, the  $p$ , + and - solutions were chosen to enforce

condition I.3 immediately. We find that enforcing I.4 in the sub-problems, i.e. using Neumann rather than Dirichlet boundary conditions on  $\psi$ , produces more accurate numerical representations. Also, the choice of  $\omega_p(\pm 1)$  is arbitrary, and the use of a more realistic value than zero, say the vorticity on the boundary from the previous time step, reduces numerical instability at the boundaries. We also chose the vorticity boundary conditions on the  $\pm$  problems to be either even or odd so that the boundary of each problem contains some vorticity at the walls for the same reasons. Notice that a problem of the above type must be solved for each  $k$ . For the system of equations under study here, the  $k = 0$  component has different boundary conditions from the  $k \neq 0$  i.e.

$$D\psi^{(k=0)}(\pm 1) = 0, \quad (I.11)$$

$$D^3\psi^{(k=0)}(\pm 1) \equiv D\omega^{(k=0)}(\pm 1) = Q^2, \quad (I.12)$$

where  $Q$  is a constant. Condition I.12 is actually a condition on the vorticity and hence the  $k = 0$  components can be solved immediately without recourse to the influence matrix technique. However, I.11 and I.12 place some integral constraints on the solution which we must ensure are captured by the numerical method.

First, for the barotropic streamfunction which is represented in discretized form exactly by Equations I.1 and I.2, substitution of I.2 into I.1 for  $k = 0$ , integration once with respect to  $y$  and use of condition I.12 leads to the conclusion that

$$\int_{-1}^{+1} R^{(k=0)} dy = 0. \quad (I.13)$$

Second, the baroclinic streamfunction solves a slightly modified equation

$$(D^2 - \lambda^2) \omega_{bc} + \alpha \psi_{bc} = R_{bc}, \quad (I.14)$$

$$(D^2 - k^2) \psi_{bc} = \omega_{bc}, \quad (I.15)$$

and so the constraint I.13 becomes

$$\int_{-1}^{+1} R_{bc}^{(k=0)} dy = \alpha \int_{-1}^{+1} \phi_{bc}^{(k=0)}. \quad (I.16)$$

$R$  contains terms from the previous time step which either have zero horizontal average (Jacobian terms) or are zero by the boundary conditions except for one term. This term involves the same integral as the right hand side of I.16 except that it is evaluated at the previous time step, and so  $\phi_{bc}^{(k=0)}$  will remain zero if originally set to zero.

The equations ultimately solved are as follows: Barotropic part  $k \neq 0$ :

$$\begin{aligned} (D^2 - \lambda^2) \omega_+ &= 0, \\ (D^2 - k^2) \psi_+ &= \omega_+, \\ \omega_+(1) = 1, \quad \omega_+(-1) &= 1, \\ D\psi_+(1) = 0, \quad D\psi_+(-1) &= 0. \end{aligned} \quad (I.17)$$

$$\begin{aligned} (D^2 - \lambda^2) \omega_- &= 0, \\ (D^2 - k^2) \psi_- &= \omega_-, \\ \omega_-(1) = 1, \quad \omega_-(-1) &= -1, \\ D\psi_-(1) = 0, \quad D\psi_-(-1) &= 0. \end{aligned} \quad (I.18)$$

$$\begin{aligned}
(D^2 - \lambda^2) \omega_p &= R_{bt}, \\
(D^2 - k^2) \psi_p &= \omega_p, \\
\omega_p(1) = +R_i, \quad \omega_p(-1) &= -R_i, \\
D\psi_p(1) = 0, \quad D\psi_p(-1) &= 0. \tag{I.19}
\end{aligned}$$

where

$$R_i = \frac{1}{2} \int_{-1}^{+1} R_{bt} dy, \tag{I.20}$$

and so in I.8

$$\delta_+ = -\frac{(\psi_p(1) + \psi_p(-1))}{2\psi_+(1)}, \tag{I.21}$$

$$\delta_- = -\frac{(\psi_p(1) - \psi_p(-1))}{2\psi_-(1)}. \tag{I.22}$$

$k = 0$ :

$$\begin{aligned}
(D^2 - \lambda^2) \omega &= R_{bt}, \\
(D^2 - k^2) \psi &= \omega, \\
D\omega(1) = Q_a^2, \quad D\omega(-1) &= Q_a^2, \\
D\psi(1) = 0, \quad D\psi(-1) &= 0. \tag{I.23}
\end{aligned}$$

Baroclinic part  $k \neq 0$ :

$$(D^2 - \lambda^2) \omega_+ + \alpha \psi_+ = 0,$$

$$\begin{aligned}
(D^2 - k^2) \psi_+ &= \omega_+, \\
\omega_+(1) = 1, \quad \omega_+(-1) &= 1, \\
D\psi_+(1) = 0, \quad D\psi_+(-1) &= 0. \tag{I.24}
\end{aligned}$$

$$\begin{aligned}
(D^2 - \lambda^2) \omega_- + \alpha \psi_- &= 0, \\
(D^2 - k^2) \psi_- &= \omega_-, \\
\omega_-(1) = 1, \quad \omega_-(-1) &= -1, \\
D\psi_-(1) = 0, \quad D\psi_-(-1) &= 0. \tag{I.25}
\end{aligned}$$

$$\begin{aligned}
(D^2 - \lambda^2) \omega_p + \alpha \psi_p &= R_{bt}, \\
(D^2 - k^2) \psi_p &= \omega_p, \\
\omega_p(1) = \omega^*(1), \quad \omega_p(-1) &= \omega^*(-1), \\
D\psi_p(1) = 0, \quad D\psi_p(-1) &= 0. \tag{I.26}
\end{aligned}$$

and so in I.8

$$\delta_+ = -\frac{(\psi_p(1) + \psi_p(-1))}{2\psi_p(1)}, \tag{I.28}$$

$$\delta_- = -\frac{(\psi_p(1) - \psi_p(-1))}{2\psi_p(-1)} \tag{I.29}$$

$k = 0$ :

$$\begin{aligned}
(D^2 - \lambda^2) \omega + \alpha \psi &= R_{bc}, \\
(D^2 - k^2) \psi &= \omega,
\end{aligned}$$

$$\begin{aligned} D\omega(1) &= Q_b^2, & D\omega(-1) &= Q_b^2, \\ D\psi(1) &= 0, & D\psi(-1) &= 0. \end{aligned} \tag{I.30}$$

Finally, the representation of the vertical dependences as Chebyshev polynomials reduces the differential operator in I.17–I.29 to a 3-point recurrence relation in the Chebyshev coefficients (Canuto et al., 1988) and the resulting algebraic matrix equations are solved by direct Gaussian elimination (individually for the uncoupled equations and by block elimination for the coupled).